

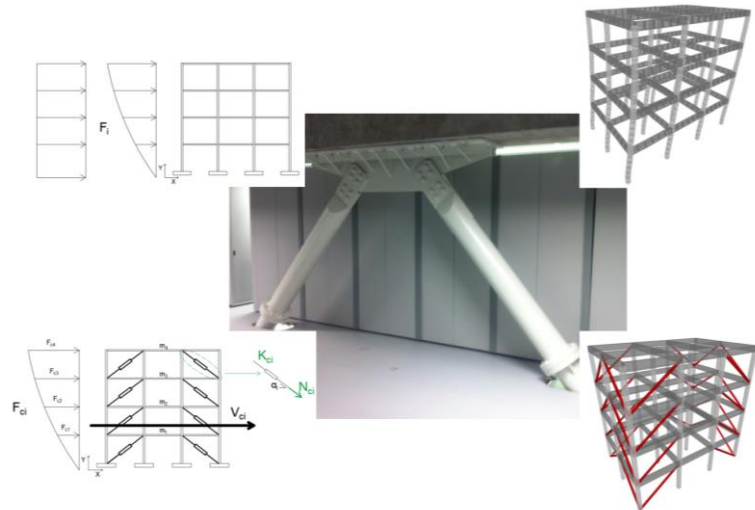


Dottorato di Ricerca in Architettura, Ingegneria delle costruzioni e Ambiente costruito

*Ph.D. Degree in Architecture, Built environment and Construction engineering*

Eleonora Bruschi

**Seismic retrofit of RC framed buildings with supplementary energy dissipation: modelling and application of a novel Lead Damper**







**POLITECNICO**  
MILANO 1863

DOCTORAL PROGRAMME IN ARCHITECTURE, BUILT  
ENVIRONMENT AND CONSTRUCTION ENGINEERING

---

# Seismic retrofit of RC framed buildings with supplementary energy dissipation: modelling and application of a novel Lead Damper

Doctoral Dissertation of:

**Eleonora Bruschi**

Supervisors:

**Prof. V. Quaglini**

**Prof. P.M. Calvi**

Tutor:

**Prof. S. Cattaneo**

Head of PhD:

**Prof. M. Scaioni**

December 2021 – Cycle XXXIV



# Ringraziamenti

*Giunta alla conclusione di questo percorso, vorrei ringraziare dal profondo del mio cuore la persona che più di tutte ha reso possibile questo traguardo, il Prof. Virginio Quaglini, che per me è un vero mentore, oltre che un grande amico.*

*Ringrazio il Prof. Paolo Calvi per avermi dato la possibilità di lavorare con lui all'Università di Washington, è stata un'esperienza importantissima per la mia vita personale e professionale.*

*Grazie alla mia tutor, la Prof. Sara Cattaneo, per tutti i consigli e il supporto che mi ha dato durante questi anni, il suo è stato un aiuto prezioso.*

*Un grazie sentito alla Ermenegildo Zegna Founder's Scholarship per aver creduto in me e avermi offerto l'opportunità di svolgere il programma di Visiting Student presso l'Università di Washington.*

*Ringrazio la mia famiglia per tutto l'amore, l'affetto e il supporto che mi hanno sempre dimostrato: se oggi sono la donna che sono lo devo soprattutto a loro.*

*Grazie a Gabriele per essere sempre al mio fianco, sostenendomi in modo costante e sincero in tutto ciò che faccio.*

*Infine, grazie a tutti i miei amici che arricchiscono la mia vita e mi fanno sentire davvero speciale e fortunata.*



# Abstract

---

The present work develops tools for the seismic retrofit of reinforced concrete (RC) structures provided with energy dissipation devices. This aim is pursued by means of different subgoals, namely (i) assessment of reliable concentrated plasticity models for dynamic non-linear analyses of RC framed buildings; (ii) experimental investigation of a novel damper proposed for retrofitting RC structures; (iii) formulation of an effective and affordable displacement-based design procedure for proportioning the damping system in RC buildings; and (iv) assessment of the proposed method.

The first part of the thesis presents a critical review of current material modelling for ductile RC frame structures, in the context of non-linear time-history analyses, focusing on concentrated plasticity. Four RC frames with increasing number of stories (2, 4, 8 and 12) subjected to a set of seven spectrum-compatible input ground motions are examined numerically and the structural response is evaluated in terms of engineering demand parameters like base reactions (shear force and moment), inter-story drift and peak floor accelerations. Results of analyses conducted by adopting a distributed plasticity model are used as benchmark, and the implications of adopting different modelling assumptions to implement concentrated plasticity models in non-linear time-history analyses of ductile RC frame buildings are eventually highlighted and discussed.

In the second part of the work, a novel Lead Damper (LED) is experimentally investigated. The device provides a resistive force by the friction created between a lead core and a shaft. This damper is expected to incorporate several desirable characteristics, namely high stiffness and damping capability in a compact design and low manufacturing cost, which make it suitable for social housing. A modelling procedure is suggested to represent the non-linear behavior of the LED in both static and dynamic analyses. In particular, for dynamic analyses, a finite element object of the LED is formulated in the structural software program OpenSees.

Then, an effective and computationally affordable displacement-based design procedure for seismic retrofit of RC framed structures equipped with hysteretic dampers, characterized by an elastic-perfectly plastic behavior, is proposed. The method aims at proportioning damped braces to attain a target performance level (for a specific level of seismic intensity), controlling the maximum inter-story drifts of the structure and, if needed, regularizing the stiffness and the strength of the building along its elevation. In order to demonstrate its effectiveness, the procedure is applied to the retrofit of two existing reinforced concrete buildings. For the validation of the design method, the seismic performance of the retrofitted structures is assessed in both static and dynamic non-linear analyses. In particular, for the dynamic analyses, structural models are formulated in the OpenSees finite element framework by adopting a concentrated plasticity approach, based on the results of Chapter 1.

In the last part of the study, the two RC structures are examined and retrofitted with the LED following the design procedure explained at Chapter 3. Two different design targets are considered: in the first case, the structure is retrofitted in order to maintain an elastic behavior, with no plastic hinges, during the earthquake,

while in the second case, a partial dissipative behavior of the structure is allowed, with formation of plastic hinges limited to a repairable limit state. Non-linear dynamic analyses are carried out in OpenSees, considering a suite of artificial ground motions whose response spectra match on average the target spectra according to NTC 2018 for the life-safety limit state. The results of the numerical study demonstrate both the effectiveness of the LED device and the viability of the design procedure.

## Keywords

---

Reinforced concrete frame; energy dissipation; hysteretic damper; experimental characterization; non-linear analyses; seismic retrofit

# Table of Contents

---

<b>Abstract .....</b>	<b>1</b>
<b>Introduction.....</b>	<b>3</b>
<b>1. Concentrated plasticity modelling of RC frames in time-history analyses .....</b>	<b>7</b>
1.1. Introduction.....	7
1.2. Review of the state of art .....	10
1.3. Numerical investigation .....	17
1.3.1. RC case-study frames.....	17
1.3.2. Numerical model of the RC case-study frames .....	20
1.4. Results.....	27
1.5. Discussion .....	36
1.6. Conclusions.....	39
1.7. Symbols.....	41
1.8. References.....	45
<b>2. Characterization and numerical assessment of Lead Damper .....</b>	<b>51</b>
2.1. State of art of energy dissipation devices .....	51
2.1.1. General introduction: principles of energy dissipation.....	51
2.1.2. Energy dissipation hardware: critical review of past studies.....	53
2.2. Lead extrusion dampers .....	64
2.2.1. Design modelling of lead extrusion dampers .....	67
2.2.2. Applications of lead extrusion dampers in real structures .....	71
2.3. Experimental investigation.....	75
2.3.1. Description of the LED prototype .....	75
2.3.2. Experimental protocol .....	76
2.4. Results.....	78
2.5. Modelling of LED in OpenSees.....	82
2.6. Conclusions.....	86
2.7. Symbols.....	87
2.8. References.....	90
<b>3. Design procedure for the seismic retrofit of RC framed structures .....</b>	<b>97</b>
3.1. Introduction.....	97
3.2. Design procedure of the damped brace system .....	102
3.3. Application of the design procedure .....	113
3.3.1. Numerical model of the RC case-study framed buildings.....	116
3.3.2. Case-study 1: building in Potenza .....	117
3.3.3. Case-study 2: building in Pordenone.....	125
3.4. Discussion and conclusions.....	130
3.5. Symbols.....	133
3.6. References.....	137

<b>4. Assessment of the Lead Damper for the seismic rehabilitation of RC framed structures .....</b>	<b>143</b>
4.1. Case-study 1: building in Potenza .....	143
4.1.1. Retrofit with elastic frame behavior.....	143
4.1.2. Retrofit with dissipative frame behavior.....	150
4.1.3. Comparison between LED- and SHD-DBS .....	157
4.2. Case-study 2: building in Pordenone .....	163
4.2.1. Retrofit with elastic frame behavior.....	163
4.2.2. Retrofit with dissipative frame behavior.....	165
4.2.3. Comparison between LED- and SHD-DBS .....	169
4.3. Discussions and conclusions.....	173
4.4. Symbols .....	175
4.5. References .....	177
<b>Conclusions.....</b>	<b>179</b>
Further developments and impacts .....	181
<b>Appendix A.....</b>	<b>183</b>
<b>Appendix B.....</b>	<b>189</b>

# Introduction

---

Italy is a country prone to earthquake activity, where strong events happen with a frequency of 4-5 years. Just in the last ten years, three strong earthquakes occurred with invaluable losses in terms of human life and with dramatic economic consequences: Aquila 2009, Emilia 2012 and Centro Italia 2016. The damages produced by these earthquakes are usually out of proportion with respect to their intensity, especially if compared to what usually happens in other seismically active countries, such as California or Japan [1]. This is due to the seismic vulnerability of the Italian building stock, which is characterized by a massive presence of historical buildings, a varied urban structure and a complex geomorphological system that characterize every Italian urban center [2]. Figure 1 shows that the construction development was concentrated especially between the '50s and the '80s. Except in the case of some noncompulsory provisions, released between the mid-60s and mid-70s, the first specific seismic provisions appeared in Italy in the early 90s, and internationally recognized modern seismic concepts, such as capacity design, were implemented only approximately 10 years ago [3]. Furthermore, a standardized classification of the national seismicity dates back to 2004.

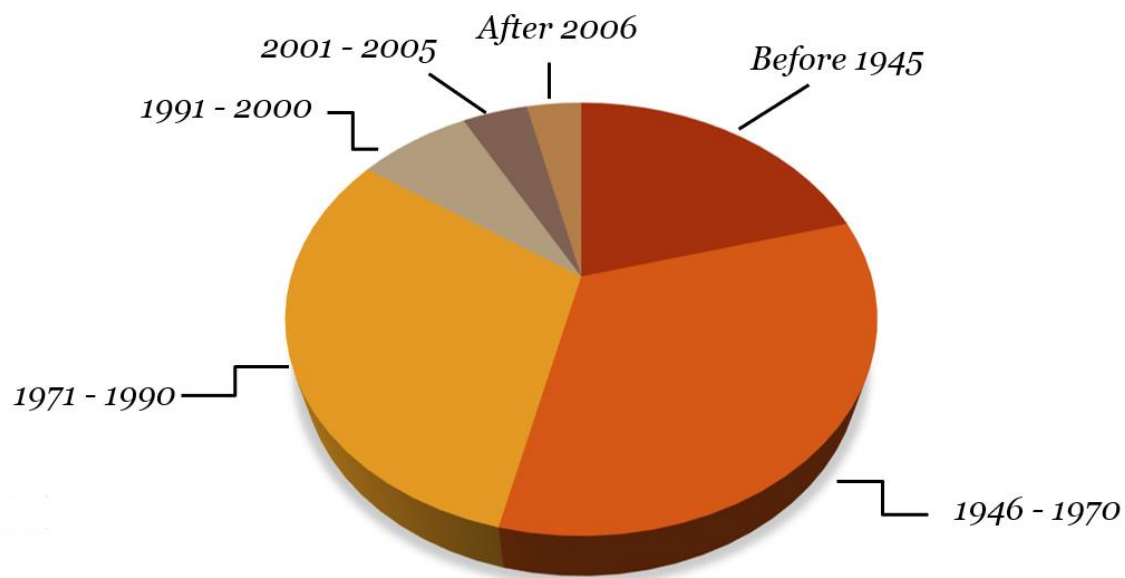


Figure 1: Year of construction of the Italian Building Stock (Ance elaboration based Dati ISTAT data – 2011 National Survey and Protezione Civile) [4]

Therefore, most of the Italian structures were built in compliance to old seismic standards; for this reason, they may be unable to survive ground motions, even of medium intensity.

Hence, the development of seismic rehabilitation technologies is a key step to pursue the target of reducing the failure probabilities and consequently increasing the resilience of the Italian community.

Many techniques are available for upgrading existing structures, which can be used alternatively or in combination to increase the capacity of the structure and/or to reduce the seismic demand (e.g., [5]-[7]).

## Introduction

---

Among them, supplementary energy dissipation is an appealing one, especially for reinforced concrete (RC) structures, which represent one of the most common structural typologies in Italy ([8], [4]). This technique can be applied to both new and retrofitted constructions in order to prevent structural damage, increase life-safety and achieve a desired level of performance ([9], [10]) appearing an appropriate and economically affordable solution to reduce the vulnerability of ordinary structures, such as residential, school and industrial buildings. Unfortunately, despite of remarkable improvements in dampers' technology, nowadays practitioners still have little confidence in implementing supplementary energy dissipation strategies due to lack of both design procedures to be easily adopted and seismic codes that properly address specific provisions [11].

The present work aims at presenting a design procedure for the seismic upgrade of RC frame structures equipped with hysteretic dampers. The primary goal is to define a simple and computationally affordable method, able to overcome the limits of the existing design procedures, in order to make more attractive the use of the supplementary energy dissipation strategy for the seismic protection of RC buildings.

In this light, the second goal of the work is to promote the use of a novel energy dissipation device, named LED (Lead Damper), which is characterized by valuable features, such as a consistent rigid-plastic behavior without strength degradation during repeated cycles, and a repeatable and robust seismic response, providing maintenance-free operation even in presence of repeated ground shakes.

The thesis consists of *Introduction* and five *Chapters*.

The *Introduction* declares the research objective and the related research questions, illustrating also the methodology adopted to reach the goal.

*Chapter 1* and *Chapter 2* are preparatory to the application of the design procedure for the seismic upgrade of RC frame structures, described in *Chapter 3*. In *Chapter 4*, the design procedure is applied to two existing RC structures and validated through the verifications prescribed by the current Italian Building Code. The seismic retrofit of the case-study buildings is performed considering two performance requirements: in one case, the structure is retrofitted in order to maintain an elastic behavior, when subjected to the design ground motions; in the second case, a partial dissipative behavior of the structure is allowed, with formation of plastic hinges limited to a repairable limit state. Finally, *Chapter 5* presents the main results of the work and the future developments.

Since the retrofit procedure is developed for RC structures, a fundamental aspect is the choice of the proper Finite Element model to reproduce the non-linear response of the case-study buildings. The selected model must combine a fairly accurate and reliable reproduction of the structural behavior with computational effectiveness and ease of application. As stated in the State of Art of *Chapter 1*, there are various modelling approaches, each one presenting advantages and drawbacks, and users are faced with a trade-off between refined models, at higher computational costs, and simpler, more practical models, that may imply higher approximation in the results. For this reason, an insight into the effects of the modelling decisions of RC structural members are investigated in *Chapter 1*, with the aim of defining convenient practices for structural

engineers who perform non-linear analyses on RC structures. Moreover, this investigation is useful to define the modelling choices adopted in *Chapter 3* and *Chapter 4*.

*Chapter 2* presents the experimental campaign conducted according to the European code on anti-seismic devices (EN 15129) on a novel energy dissipation device, named Lead Damper (LED), which provides a resistive force and dissipates energy by the friction activated between a lead core and a shaft. Starting from the results of the tests, the constitutive behavior of the LED device is implemented in the software program OpenSees to perform non-linear dynamic analyses.

*Chapter 3* is the core of the thesis, containing the proposal of the design procedure for the seismic retrofit of RC frame structures by means of supplementary energy dissipation damped brace systems (DBS). The method is step-by-step illustrated through the application of the procedure to two case-study structures, which are retrofitted by using a standard hysteretic damper.

Finally, in *Chapter 4*, the design method is applied to the two case-study structures of *Chapter 3* by inserting braces equipped with the LED device. Four design cases are presented, corresponding to two target performance levels of the frame after the retrofit for each structure: an elastic frame behavior and a partially dissipative frame behavior. The study is validated by performing non-linear analyses and checking the prescriptions of the current Italian Building Code. A direct comparison between the retrofit with the LED device and with a traditional steel hysteretic damper is performed as final step to demonstrate both the effectiveness of the LED device and the robustness of the design procedure.

## References

- [1] Dolce M, Zuccaro G. Strumenti aggiornati per la vulnerabilità sismica del patrimonio edilizio dei sistemi urbani, Gruppo Nazionale per la difesa dai terremoti, Programma quadro 2000-2002.
- [2] Mezzina M, Raffaele D, Uva G, Marano GC. Progettazione sismo-resistente di edifici in cemento armato, Città Studi Edizioni 2011.
- [3] Pampanin S. Chapter 13: Alternative performance-based retrofit strategies and solutions for existing RC buildings, *Seismic Risk Assessment and Retrofitting 2009*; DOI: 10.1007/978-90-481-2681-1\_13.
- [4] CRESME Ricerche, Incentivi e riduzione del rischio sismico in Italia, *Ingegneria Sismica Italiana*, 2020, in Italian.
- [5] Ilki A, Karadogan F, Pala S, Yuksel E. (Eds.) *Seismic risk assessment and retrofitting*, Geotechnical, Geological, and Earthquake Engineering 2009 (10); DOI:10.1007/978-90-481-2681-1\_13.
- [6] CEB state of the art report. Fastenings for seismic retrofitting, state-of-the-art report on design and application. Comité Euro-International du Béton (CEB), London, 1996.
- [7] Quaglino V, Pettoruso C, Bruschi E. Experimental and numerical assessment of prestressed lead extrusion dampers, *International Journal of Earthquake Engineering* 2021, Anno XXXVIII – Num.2, pp. 46-69.
- [8] Calderoni B, Cordasco EA, Sandoli A. Una classificazione tipologica strutturale degli edifici esistenti in muratura ed in CA finalizzata alla valutazione della vulnerabilità sismica su scala territoriale, *Progettazione sismica n.1*, IussPress 2016, Italy.
- [9] Di Cesare A, Ponzo FC, Nigro D. Assessment of the performance of hysteretic energy dissipation bracing systems. *Bulletin of Earthquake Engineering* 2014, 12(6):2777–2796; DOI: 10.1007/s10518-014-9623-z.
- [10] Di Cesare A, Ponzo FC. Seismic retrofit of reinforced concrete frame buildings with hysteretic bracing systems: design procedure and behaviour factor. *Hindawi, Shock and Vibration* 2017, Article ID 2639361, DOI: 10.1155/2017/2639361.
- [11] Nuzzo I, Losanno D, Caterino N. Seismic design and retrofit of frames structures with hysteretic dampers: a simplified displacement-based procedure, *Bulletin of Earthquake Engineering* 2019; 17: 2787-2819; DOI: 10.1007/s10518-019-00.

# 1. Concentrated plasticity modelling of RC frames in time-history analyses

---

The study aims at giving an insight into the effects of modelling decisions that are adopted in concentrated plasticity formulations used in time-history analyses to model the behavior of reinforced concrete frames, by investigating the sensitivity of the estimated structural response on the assumed length of the plastic hinge region  $L_{pl}$  and the effective area moment of inertia  $I_{eq}$  of the cracked concrete section. Four frames with 2, 4, 8 and 12 stories, designed in accordance with the Italian Building Code and characterized by a flexural behavior, are taken as case-studies. Structural models are coded in the OpenSees framework adopting various formulations of  $L_{pl}$  and  $I_{eq}$  taken both from the literature and the European and the Italian codes. The results of the analyses are compared to the ones provided by a distributed plasticity formulation and evaluated considering engineering demand parameters such as internal forces and deformations, and absolute accelerations. The main differences between the predictions provided from the distributed and the lumped inelasticity approaches regard the estimates of the inter-story drift ratio and the maximum base moment, while predictions of absolute acceleration and maximum base shear are found to be more consistent; a certain influence of the number of stories is also highlighted. Eventually, the agreement between concentrated and distributed plasticity formulations can be improved by adopting an effective area moment of inertia of concrete cracked section dependent on the axial load in the structural member.

## 1.1. Introduction

---

Static (Pushover) and dynamic (Time-History) non-linear analyses are used in design practice to assess the seismic vulnerability of reinforced concrete (RC) buildings. The analyses are performed using Finite Element Models (FEMs), and various software programs for structural calculation, like e.g., OpenSees [1], Abaqus [2], MidasGen [3] and SAP2000 [4] are available to the designers. Considering the structural non-linear response, there are two major sources of non-linearity, namely material and geometric non-linearity. Material non-linearity is considered the primary source of damage for low- and medium-rise building structures, while geometrical non-linearities should be accounted for in high-rise buildings with small aspect ratios subjected to large horizontal deflections that introduce P-Delta effects. For the non-linear material response, the Finite Element simulation falls into two main categories, namely distributed plasticity models and concentrated (or lumped) plasticity models

Concentrated plasticity formulations are easier to implement, computationally more effective and are able to provide fairly accurate and reliable predictions in most practical situations [5], [6]. There are different levels of complexity that can be taken into account to address material non-linearities. For instance, the length of a structural member affected by anelastic behavior can be represented either by means of a single rotational spring with assigned non-linear moment-curvature relationships, or by an element made of non-linear fiber sections [7]. Two important modelling decisions that have been shown to affect the accuracy of the model indeed concern: (i) the “plastic hinge length” ( $L_{pl}$ ), a fictitious length related with the extension of

the part of a structural member over which non-linear behavior is activated; and (ii) the flexural stiffness of the cracked concrete section, which is generally taken into account by introducing an artificially low effective area moment of inertia ( $I_{eq}$ ).

Several plastic hinge length formulations have been proposed in the literature (e.g., [8]-[21]) and later incorporated in seismic codes and guidelines (among the others, e.g., FEMA 356 [22], ACI 318 [23], Eurocode 8 Part 3 [24] and, with reference to the Italian scenario, the Explanatory Circular to the Italian Building Code [25]). To the Authors' knowledge, a comparative evaluation of concentrated plasticity models for non-linear dynamic analyses of RC structures has not been conducted yet, and the choice is ultimately left to the structural engineer. However, not negligible differences exist among the various formulations, which can lead to inconsistent approaches and possibly conflicting results, see e.g., references [26], [27].

In the same way, though cracking is noted to reduce the stiffness of RC members and it should be accounted for in numerical models ([28]-[30]), a common approach is missing. Modelling strategies based on the use of a reduced area moment of inertia with respect to the one of the gross cross-section have some merit ([24], [25], [31], [32]), but the coefficients of reduction proposed in the codes are mainly empirical rather than based on rigorous studies [33].

The present work aims at giving guidance to structural engineers who perform non-linear dynamic analyses on RC frames, by providing some insight into the effects of the modelling decisions on the plastic hinge length and the reduction of the area moment of inertia in lumped plasticity formulations. The study does not intend to provide an overview of all the available modelling choices for plasticity of RC columns and beams, but it focuses on modelling of structural elements where the non-linear behavior is activated at the end regions, while in the middle the behavior remains elastic.

The State of Art describes the significance and the hypotheses at the basis of the plastic hinge length formulation and provides a critical discussion of the various expressions proposed in research works and in the European and the Italian norms; some expressions for the effective area moment of inertia  $I_{eq}$  of cracked concrete section are presented and discussed as well.

A numerical investigation conducted on a set of four case-study RC frames is performed focusing on the effects of the modelling decisions. The structures, designed in compliance with the current code recommendations, are characterized by a flexural behavior and are respectful of the principles of the capacity design. Every structure has been modelled according to both distributed and concentrated plasticity formulations, and in each of them the inelasticity is defined at the sectional level, assigning a material uniaxial inelastic behavior to concrete and steel. The distributed plasticity models, where plasticity can spread across the whole length of each structural members, are expected to be able to capture the overall flexural behavior of the case-study frames ([34]-[36]), and therefore are assumed as the benchmark. Several concentrated plasticity models are formulated accounting for different expressions of the plastic hinge length  $L_{pl}$  and the effective area moment of inertia taken from the literature and the European and Italian norms. Non-linear time histories are performed according to the provisions of the Italian Code [37], and the models are compared in terms of predicted structural drifts and accelerations, and reactions (forces and moments) at

the base, which are the engineering demand parameters usually considered for the verification of RC structures.

### 1.2. Review of the state of art

---

In an RC frame designed according to capacity design principles, during a seismic event, plastic flexural mechanisms are expected to be activated at the end sections of the beams and at the basis of the columns of the first floor [14]. These dissipative zones, where non-linear mechanisms such as yielding of the longitudinal reinforcement, extensive spalling of concrete cover, diagonal cracking and crushing of concrete core, and buckling and fracture of longitudinal steel bars are engaged [38], represent the so-called *real* plastic hinge regions, also termed as *critical zones* in the Eurocode [24]. The curvature distribution inside the critical zones is very complex and case-dependent, as it is affected by the concrete compressive strength, the bottom/top reinforcement ratio, the transverse reinforcement ratio and the shear span to depth ratio [38], [39], and the maximum curvature may do not occur in the same section where the moment has its maximum [19].

In the framework of non-linear analyses, this complex behavior can be represented with fair accuracy by means of a concentrated plasticity formulation, i.e., assuming that the structure is composed of beam–column members made of an elastic core and “plastic hinges” of assigned length at both ends, where the plastic behavior can be activated. The concept of the plastic hinge length was initially introduced by Park and Paulay [40] who considered a cantilevered RC column subjected to a transversal force, and determined the ultimate top displacement according to the expression:

$$\delta = \frac{\varphi_y z^2}{3} + (\varphi_u - \varphi_y) L_{pl} (z - 0.5L_{pl}) \quad (1.1)$$

where  $z$  is the shear span of the column,  $\varphi_u$  is the ultimate curvature at failure and  $\varphi_y$  is the curvature at yielding. Within this simplification, which is rigorously valid only for members characterized by a purely flexural behavior, the plastic hinge length ( $L_{pl}$ ) does not correspond to the actual length of the critical zone over which the inelastic deformation actually spreads, but is instead the *effective* length [31] over which a given plastic curvature is assumed to be constant and is integrated to calculate the effective chord rotation, including shear and fixed-end rotation contributions, under the Bernoulli’s plane section assumption [41], [42]. All the analytical models developed after Park and Paulay are based on this fundamental hypothesis ([14]-[19]). Fardis [16] introduced an additional contribution to Eq. (1.1), representing the fixed-end rotation due to the slippage of the longitudinal bars from the anchorage zone  $a_{sl}(\theta_{u,slip} - \theta_{y,slip})$ , where  $a_{sl} = 0$  when the slippage is not physically possible and  $a_{sl} = 1$  otherwise, and  $\theta_{u,slip}$ ,  $\theta_{y,slip}$  are the rotations due to slippage at failure and at yielding, respectively.

Several studies have been conducted to formulate plastic hinge length expressions suitable for beams and columns, and a comprehensive list is reported in Table 1-1.

<i>Reference</i>	<i>Plastic Hinge Length (<math>L_{pl}</math>)</i>	<i>Element applicability</i>
Baker, 1956 <sup>[8]</sup>	$k_1 k_2 k_3 \left(\frac{z}{d}\right)^{1/4} d$	beams and columns
Mattock, 1964 <sup>[9]</sup>	$\frac{d}{2} \left[ 1 + \left( 1.14 \sqrt{\frac{z}{d}} - 1 \right) \left\{ 1 - \left( \frac{q-q'}{q_b} \right) \sqrt{\frac{d}{16.2}} \right\} \right]$	beams
Sawyer, 1964 <sup>[10]</sup>	$0.25d + 0.075z$	beams
Corley, 1966 <sup>[11]</sup>	$0.5d + 0.2\sqrt{d} \left(\frac{z}{d}\right)$	beams
Mattok, 1967 <sup>[12]</sup>	$0.5d + 0.05z$	beams
Priestley et al., 1987 <sup>[13]</sup>	$0.08z + 6d_b$	columns
Paulay et al., 1992 <sup>[14]</sup>	$0.08z + 0.022d_b f_y$	beams and columns
Panagiotakos et al., 2001 <sup>[15]</sup>	$0.12z + 0.014a_{sl} d_b f_y$	beams and columns
Fardis, 2007 <sup>[16]</sup>	$0.09z + 0.2h$	beams and columns
Priestley et al., 2007 <sup>[17]</sup>	$0.2 \left( \frac{f_u}{f_y} - 1 \right) z + 0.022d_b f_y$	beams and columns
Bae et al., 2008 <sup>[18]</sup>	$\left\{ \left[ 0.3 \left( \frac{P}{P_0} \right) + 3 \left( \frac{A_s}{A_g} \right) - 0.1 \right] \left( \frac{z}{h} \right) + 0.25 \right\} h \geq 0.25h$	columns
Elmenschawi et al., 2012 <sup>[19]</sup>	$[0.08z + 0.022d_b f_y + l_s]$	beams and columns
Mortezaei et al., 2013 <sup>[20]</sup>	for far-fault earthquakes: $\left\{ \left[ 0.4 \left( \frac{P}{P_0} \right) + 3 \left( \frac{A_s}{A_g} \right) - 0.1 \right] \left( \frac{z}{h} \right) + 0.6 \right\} h \geq 0.6h$ for near-fault earthquakes: $\left\{ \left[ 0.4 \left( \frac{P}{P_0} \right) + 3 \left( \frac{A_s}{A_g} \right) - 0.1 \right] \left( \frac{z}{h} \right) + 0.45 \right\} h \geq 0.45h$	columns
Ning et al., 2016 <sup>[21]</sup>	$z \left( 0.042 + 0.072 \frac{P}{P_0} \right) + 0.298h + 6.407d_b$	columns

Table 1-1: Plastic Hinge formulations proposed the literature

The expressions in Table 1-1 were mainly developed upon experimental investigations conducted on beam and column members subjected to monotonic and cyclic loading, and only in few cases the estimation of  $L_{pl}$  was based on numerical simulations only, e.g., [20], [43].

## 1 Concentrated plasticity modelling of RC frames in time-history analyses

---

In two independent studies, Bae and Bayrak [18] and Elmenhawawi et al. [19] compared experimental plastic hinge lengths, determined either as the measured length of an extensively damaged zone or as a mathematical expression relating the experimental curvature to the relevant chord displacement, with analytical models from the literature ([8]-[15]). The large scatter of results and the different performances of the models that were observed were ascribed to the fact that each formulation relies on particular assumptions, including the position of the actual hinge, i.e. of the center of rotation in the plastic hinge model, the definition of yielding and ultimate curvatures, the section geometry, the constitutive behavior of materials, the transverse reinforcement, the support conditions and the magnitude and type of loading [20], which are not the same for all the models. Moreover, the assessed models give different weight to the various anelastic mechanisms, which makes the dependence on a particular parameter predominant over the others.

Because the length of the zone affected by non-linear behavior tends to be greater for beams than for columns, dedicated theoretical expressions were proposed. The greater plastic hinge length observed for beams is attributed indeed to the low axial forces they are normally subjected to, which makes them more prone to shear-induced flexural deformations [19]. Further to this, beams are usually characterized by an asymmetric reinforcement layout. This feature affects the plastic hinge length too.

In the early models ([8]-[12]), expressions for  $L_{pl}$  accounted for bending deformations only. In a first improvement, Priestley and Park [13] proposed a two-component formulation, where the first term accounts for column bending, while the second term accounts for the fixed-end rotation due to bar slip and yield penetration of longitudinal bars into the column base. Paulay and Priestley [14] postulated the dependency of  $L_{pl}$  on the yield strength  $f_y$  of the longitudinal reinforcement, to more accurately account for different grades of flexural reinforcement, and later Priestley et al. [17] emphasized the importance of the ratio of ultimate tensile strength to yield strength of steel  $f_u/f_y$ ; for low  $f_u/f_y$  ratios plasticity is indeed activated close to the end section of the RC member, resulting in a short plastic hinge length, whereas high  $f_u/f_y$  ratios increase the length of spread of plasticity across the RC member.

Panagiotakos and Fardis [15] reviewed a large number of tests embracing both cantilevered columns and supported beams. The geometry of the tested specimens, the amount and layout of the reinforcement, the concrete strength, the type of steel, and the axial load covered a very large range of options. On such basis, the Authors proposed an expression where  $L_{pl}$  still depends on the shear span  $z$ , the diameter of the reinforcement  $d_b$  and the yield strength of steel  $f_y$ , but increased the weight of the flexural contribution and reduced the weight of the reinforcement.

Bae and Bayrak [18] formulated a new expression for  $L_{pl}$  that included the dependence on the amount of longitudinal reinforcement through the ratio  $\frac{A_s}{A_g}$  (where  $A_g$  is the gross area of concrete section and  $A_s$  is the area of tension reinforcement), because they observed that  $L_{pl}$  has a consistent tendency to increase proportionally to this quantity, independently of the axial load. This behavior was confirmed in later studies ([20], [43]). Furthermore, by testing column specimens subjected to a wide range of axial load, Bae and Bayrak [18] concluded that  $L_{pl}$  is nearly constant at low load levels but, beyond a certain threshold, namely

$P = 0.2 P_0$ , where  $P$  is the applied axial force, and  $P_0$  is the nominal axial load capacity, it increases significantly with increasing of the compression.

Elmenshawi et al. [19] introduced the contribution of the “shear spread” length  $l_s$ , which is more significant in beams than in columns because shear effects are normally more critical in flexural elements subjected to low axial force, where the contribution of the concrete in resisting shear stresses can be disregarded.

Ameli and Pantelides [44] proposed an iterative procedure to determine  $L_{pl}$  for either cast-in-place or precast columns, capable of simulating both the local and the global experimental response. The proposed expressions of  $L_{pl}$  accounted for both low-cycle fatigue and bond-slip and were in good agreement with empirical expressions available in literature, like e.g., in references [13] and [15].

Recently, Pereira and Romão [38] highlighted the need to consider all the local mechanisms that take place in the critical zone, in order to properly quantify the damage localization length; in fact, before the yielding of the reinforcement, the interface effects, along with flexure and shear deformations, mainly contribute to the deformation capacity, while, after yielding, the behavior is predominantly governed by flexure. For this reason, the authors suggested to decouple the interface effects from the material strain level in order to formulate these mechanisms in terms of the size-dependent behavior of the constitutive materials at their ultimate state, namely the strength and the stiffness deterioration of the concrete and reinforcing steel compressive and tensile responses.

It is worth mentioning that factors affecting the plastic hinge length in RC elements subjected to monotonic loadings could be different than those under reversed loading (either static or dynamic) [19], and therefore some expressions (e.g., references [15] and [16]) reported in Table 1-1 are valid under cyclic loading only.

Based on a wide experimental and numerical background, recommendations for concentrated plasticity modelling of flexural RC members in non-linear analyses were introduced in the Eurocode 8 (for brevity EC8) for design of seismic resistant structures. Part 2 of EC8 [45] gives provisions for modelling of RC piles of bridges, while Part 3 [24] addresses general modelling issues of RC members of framed buildings. Specifically, the Code [24] provides two formulas for the plastic hinge length

$$L_{pl} = 0.1z + 0.17h + 0.24 \left( \frac{d_b f_y}{\sqrt{f_c}} \right) \quad (1.2)$$

$$L_{pl} = \frac{z}{30} + 0.2h + 0.11 \left( \frac{d_b f_y}{\sqrt{f_c}} \right) \quad (1.3)$$

Both formulations are valid under the assumptions of the curvature profile across the member length given by Eq. (1.1), and the yield and ultimate rotations determined in accordance with Park and Paulay [40]. The Code recommends to use formula (1.2) in combination with a confinement model for concrete in accordance with Eurocode 2 [46], with the stress-strain relationship defined by a parabolic-rectangular curve according to the stress block theory; on the contrary, the formula (1.3) is valid when a more refined stress-strain model representing the improvement of  $\varphi_u$  with confinement under cyclic loading is assumed:

$$f_{cc} = f_c \left[ 1 + 3.7 \left( \frac{\alpha_c \rho_{sx} f_y}{f_c} \right)^{0.86} \right] \quad (1.4)$$

$$\varepsilon_{cc} = \varepsilon_{c2} \left[ 1 + 5 \left( \frac{f_{cc}}{f_c} - 1 \right) \right] \quad (1.5)$$

$$\varepsilon_{cu} = 0.004 + 0.5 \frac{\alpha_c \rho_{sx} f_y}{f_c} \quad (1.6)$$

where  $f_{cc}$  is the confined concrete strength and  $\varepsilon_{cc}$  is the associated strain,  $\varepsilon_{cu}$  is the ultimate strain of the extreme fiber of the compression zone,  $\rho_{sx}$  is the ratio of transverse steel parallel to the direction of loading and  $\alpha_c$  is the confinement effectiveness factor, which depends on the dimension of the confined core and the stirrup spacing.

Both expressions of Eq. (1.2) and Eq. (1.3) include the contributions of the shear span  $z$ , the overall depth  $h$  of beam or column cross-section, the diameter  $d_b$  and the yield strength  $f_y$  of the longitudinal reinforcement, and the concrete compressive strength  $f_c$ . It is noteworthy that only few equations, namely those defined in references [8], [18], [20] and [21], among those reported in Table 1-1 account for  $f_c$ , since experimental findings reported in literature seem to suggest that RC members made of high strength concrete (up to 175 MPa) have comparable extension of the plastic region with their normal strength concrete counterparts [19]. However, the concrete strength may have an indirect influence on  $L_{pl}$ , as shown, e.g., in reference [43], as it affects the curvature distribution and the flexural strength and, in turn, the shear demand on the element, which is considered (alongside the cross-section effective depth) the main factor influencing the plastic hinge length.

By referring to the Italian scenario, the Italian Building Code “Technical Norm for Constructions” (for brevity NTC) [37], in its Explanatory Circular [25] provides the same expression of  $L_{pl}$  as in Eq. (1.2), but differently from EC8 [24], it suggests to adopt the detailed stress-strain model for confined concrete according to Mander [47], instead of the parabolic-rectangular relationship defined in Eurocode 2 [46]. The effect of this combination will be investigated later.

In the concentrated plasticity formulation, the inelastic behavior is activated only within assigned regions of the structural member, while the remaining part is assumed to behave elastically. In order to account for the reduced flexural stiffness, an effective area moment of inertia  $I_{eq}$  of the elastic region intended to mimic (in a simplified manner) cracking-induced softening phenomena is frequently adopted ([28]-[30]). The simplest approach consists in taking the effective area moment of inertia as an assigned fraction of the area moment of inertia  $I_g$  of the gross cross-section, where 50% of  $I_g$  is a common figure ([28], [29]). In contrast, other authors suggest to adjust the effective stiffness on a mechanical model. Brason and Metz [48] proposed an expression for  $I_{eq}$  that accounts for the gradual change in stiffness with the progression of cracking

$$\text{If } M_b > M_{cr}, \text{ then } I_{eq} = \left(\frac{M_{cr}}{M_b}\right)^3 I_g + \left[1 - \left(\frac{M_{cr}}{M_b}\right)^3\right] I_{cr}, \text{ with } I_{eq} \leq I_g \quad (1.7a)$$

$$\text{If } M_b \leq M_{cr}, \quad \text{then } I_{eq} = I_g \quad (1.7b)$$

where  $M_b$  is the bending moment acting on the concrete section,  $M_{cr}$  is the bending moment at first cracking and  $I_{cr}$  is the area moment of inertia of the cracked section evaluated at the critical point of the moment-curvature relationship. Fardis [16] proposed both a *theoretical effective stiffness*, calculated directly from the yield moment  $M_y$  and the chord rotation at yielding  $\theta_y$ , and an *empirical effective stiffness*, fitted directly to test results. This latter expression depends on the structural member under consideration, the possible slippage of the longitudinal bars from their anchorage beyond the member end section, the shear span to depth ratio ( $\frac{z}{h}$ ) and the axial load ratio  $\nu = \frac{N}{A_g f_c}$  (here  $N$  is the axial load under gravity actions alone):

$$E_c I_{eq} = \alpha \left(0.8 + \log_{10} \frac{z}{h}\right) \left(1 + 0.048 \min\left(\frac{N}{A_g}, 50 \text{MPa}\right)\right) (1 - 0.25 a_{sl}) E_c I_g \quad (1.8)$$

where the value of  $\alpha$  depends on the member type (i.e., beams, columns, or walls) and  $a_{sl}$  counts either 1 or 0 depending on whether slippage of longitudinal steel is possible or not.

Another approach was proposed by Priestley [49], who recommended to calculate the effective flexural stiffness from the bilinear approximation to the moment – curvature relationship, according to the expression:

$$I_{eq} = \frac{M_N}{E_c \varphi_y} \quad (1.9)$$

where  $E_c$  is the concrete modulus of elasticity,  $M_N$  is the cross-section nominal flexural strength and  $\varphi_y$  is the yield curvature, which for rectangular columns can be evaluated as  $\varphi_y h = 2.12 \varepsilon_y \pm 10\%$ , being  $\varepsilon_y$  the yield strain of the longitudinal reinforcement and  $h$  the cross-section depth [49]. This formula has the merit to take into account the axial force, which increases the nominal flexural strength of the columns at the lower stories of a multistory building, and allows to differentiate between columns and beams. For ease of implementation, in design codes  $I_{eq}$  is generally assigned as a fixed fraction of  $I_g$ , with only few exceptions, like e.g. the North American code ACI 318 [23] where values of  $I_{eq}$  accounting for axial load, eccentricity, reinforcement ratio, and concrete compressive strength, similarly to the moment-dependent expression proposed by Branson and Metz [48], e.g., Equation (7), are adopted. Part 1 of EC8 [50] assigns the flexural and shear stiffnesses of the cracked concrete section as one-half of the stiffnesses of the uncracked section, thus defining the effective area moment of inertia as:

$$I_{eq} = 0.5I_g \quad (1.10)$$

and the same provision is given in the Italian Building Code [37]. A similar approach is followed also in e.g., the Greek and the New Zealand codes ([31], [32]), but the two norms prescribe different reduction factors, ranging from  $0.4I_g$  for beams to  $0.8I_g$  for the interior columns of a frame, depending on the expected axial load ratio of the RC member under consideration.

### 1.3. Numerical investigation

#### 1.3.1. RC case-study frames

The case-study structures examined in the study consist of four RC building frames from two to twelve stories in height. Each floor has three bays of 5 m in both horizontal directions (Figure 1-1) and a constant inter-story height of 3.5 m. The geometry of the four frames and the material properties are taken from reference [52].

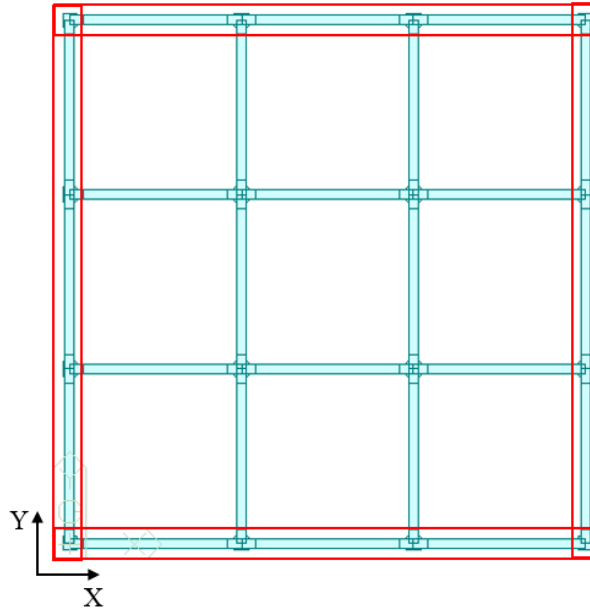


Figure 1-1: Typical plan of the case-study structures, with highlights of the peripheral seismic resistant frames [51]

The structures can be assumed as paradigmatic of low-rise (2 and 4 stories) and medium-rise (8 and 12 stories) buildings, designed in compliance with the Italian Building Code [37] for medium ductility class (CDB) with a behavioral factor  $q = 3.5$ , respecting the strong-column/weak-beam concept. The municipality of L'Aquila (Italy, latitude  $13.3944^\circ$ , longitude  $42.366^\circ$ ), a city in a high-seismic prone area ( $PGA = 4.062 \text{ m/s}^2$ ) belonging to seismic zone 1 (highest seismic hazard) of the Italian seismic classification [37], with soil Type C (medium-dense sand, gravel or stiff clay formation) and topographic category  $T_2$ , is assumed for the design. The buildings are designed as ordinary structures subjected to overcrowding, with functional class  $cu = \text{II}$ , and an anticipated design life  $V_n = 50$  years. Dead and live load contributions are given in Table 1-2, where the assumed live load  $Q = 4 \text{ kN/m}^2$  applies to use category D (shopping areas) of the Code [37]. The seismic combination, calculated according to the recommendations of NTC [37] and taking a combination factor of 0.6 for the live load  $Q$  as prescribed for use category D, controlled the design of the buildings.

## 1 Concentrated plasticity modelling of RC frames in time-history analyses

<i>Level</i>	<i>G<sub>1</sub></i> [kN/m <sup>2</sup> ]	<i>G<sub>2</sub></i> [kN/m <sup>2</sup> ]	<i>Q</i> [kN/m <sup>2</sup> ]
1 to n-1	3.5	4.5	4
n (roof)	3.5	3.5	2.18

Table 1-2: Dead and live loads (n: number of stories; G<sub>1</sub>: permanent structural loads; G<sub>2</sub>: permanent non-structural loads, Q: live loads) [51]

The peripheral frames are designed to provide horizontal resistance to seismic loads, while the internal columns are designed to carry only gravity loads (Figure 1-1). Two-way rigid floor slabs are assumed at each floor.

The frames are designed as ductile RC structures made from slender members, failing in flexure. For this reason, brittle mechanisms, such as shear failure of beams or columns or beam-column joints, are not taken into account in the numerical model. Also, other failure mechanisms like bond slip and low-cycle fatigue are not addressed in the study. In each building, the cross sections of beams and columns are kept constant for all floors (Table 1-3), in order to precisely control the locations where plastic hinges are triggered (namely, at the bases of the columns of the first floor and at the ends of the beams of each floor).

	<i>2 stories</i>	<i>4 stories</i>	<i>8 stories</i>	<i>12 stories</i>
Columns	40 x 40	70 x 70	70 x 70	90 x 90
Beams	30 x 40	50 x 60	50 x 70	50 x 90

Table 1-3: Cross-section dimensions for columns and beams, in [cm] [51]

In accordance with NTC [37], the total longitudinal reinforcement ratio  $\rho_l$  of the seismic resistant columns ranges from 1% to 4%, while in beams the ratio of the longitudinal reinforcement in tension,  $\rho_t$ , and the ratio of the longitudinal reinforcement in compression,  $\rho_c$ , fulfill the condition  $\frac{1.4}{f_y} < \rho_t < \rho_c + \frac{3.5}{f_y}$  (Table 1-4).

**1 Concentrated plasticity modelling of RC frames in time-history analyses**

<i>Floors</i>	<i>2 stories</i>		<i>4 stories</i>		<i>8 stories</i>		<i>12 stories</i>	
	$\rho_t$	$\rho_c$	$\rho_t$	$\rho_c$	$\rho_t$	$\rho_c$	$\rho_t$	$\rho_c$
11 <sup>th</sup> – 12 <sup>th</sup>							0.47	0.47
9 <sup>th</sup> – 10 <sup>th</sup>							0.59	0.59
7 <sup>th</sup> – 8 <sup>th</sup>					0.52	0.52	0.71	0.71
5 <sup>th</sup> – 6 <sup>th</sup>					0.77	0.77	0.82	0.82
3 <sup>rd</sup> – 4 <sup>th</sup>			1.01	0.76	1.03	1.03	0.94	0.94
1 <sup>st</sup> – 2 <sup>nd</sup>	1.6	1.26	1.26	1.3	1.03	1.03	1.18	1.18

Table 1-4: Longitudinal reinforcement ratios in tension and in compression in the critical zones of beams, in [%] [51]

The spacing of transverse reinforcement  $s$  in the critical zones of the structural members is determined as  $s = \min\left\{\frac{B_p}{2}; 17.5cm; 8d_b\right\}$  for seismic resistant pillars, and as  $s = \min\left\{\frac{\zeta}{4}; 225mm; 8 \cdot d_b; 24d_{st}\right\}$  for beams, where  $B_p$  is the section width of the pillars,  $\zeta$  is the lever arm of the beam cross-section and  $d_{st} \geq 6$  mm is the diameter of the stirrups. Table 1-5 and Table 1-6 provide the shear reinforcement ratio  $\rho_{sx}$  in the critical zones of beams and columns respectively, determined as the ratio  $\frac{A_{st}}{Bs}$ , where  $A_{st}$  is the area of the transverse reinforcement parallel to the direction of horizontal loading and  $B$  is the cross-section width of the structural element.

<i>Floors</i>	<i>2 stories</i>	<i>4 stories</i>	<i>8 stories</i>	<i>12 stories</i>
11 <sup>th</sup> – 12 <sup>th</sup>				0.35
9 <sup>th</sup> – 10 <sup>th</sup>				0.46
7 <sup>th</sup> – 8 <sup>th</sup>			0.35	0.46
5 <sup>th</sup> – 6 <sup>th</sup>			0.42	0.56
3 <sup>rd</sup> – 4 <sup>th</sup>		0.48	0.52	0.56
1 <sup>st</sup> – 2 <sup>nd</sup>	0.68	0.58	0.52	0.70

Table 1-5: Shear reinforcement ratio in the critical zones of beams, in [%] [51]

<i>Floors</i>	<i>2 stories</i>	<i>4 stories</i>	<i>8 stories</i>	<i>12 stories</i>
all	0.76	0.99	1.42	1.46

Table 1-6: Shear reinforcement ratio in the critical zones of columns, in [%] [51]

### 1.3.2. Numerical model of the RC case-study frames

Given the regularity in plan of the examined case-study frames and their symmetry along two horizontal axes, for each building a simplified 2D analysis is conducted on a single external peripheral seismic resistant frame in the X-direction and considering the tributary loads and masses pertaining to this frame, in line with accepted practice [29], [53]. This simplification allows to ease the interpretation of the results and to focus on the differences observed by using different modelling approaches [28], [29].

Seismic masses were evaluated by taking into account the combination of full permanent loads and live loads as recommended in the Code [37]. The periods of the first and second vibration modes of the frames, associated to more than 85% of the modal mass, are listed in Table 1-7. The apparently anomalous decrease of the fundamental period observed by switching from the two-story to the four-story frame is however justified by the huge increase of the cross-sections of beams and columns (Table 1-3), which results in an overall increase in stiffness for the taller building.

<i>Period [s]</i>	<i>2 stories</i>	<i>4 stories</i>	<i>8 stories</i>	<i>12 stories</i>
T <sub>1</sub>	0.490	0.433	0.815	0.916
T <sub>2</sub>	0.157	0.130	0.262	0.293

Table 1-7: Elastic periods of the case-study frames [51]

Finite element models of the structures are formulated within the OpenSees framework [1] according to two approaches: distributed plasticity and concentrated plasticity. In the first approach, beams and column members are modeled using the *forceBeamColumn* element object, which is based on the iterative force-based formulation [7]. This element object accounts for three distinct sub-elements, which represent the two external regions and the internal (middle) region of the member, respectively, and permits to assign a different material section model to every sub-element. A two-point Gauss-Radau integration scheme applied to each sub-element is used in the element state determination, for a total of six integration points across the whole element object [7], while geometrical consistency and equilibrium of internal forces between the sub-elements is provided by the object formulation. A variety of combinations of material models, either linear or non-linear, can be used for the external and the internal regions, encompassing both distributed plasticity and plastic hinge integration. The external regions correspond to the critical zones where non-linear behavior is supposed to be activated [37] and are characterized by closer stirrup spacing, as described in Section 3.1. In these regions, the confined concrete core presents higher compressive strength and ultimate strain than

the confined core of sections located in the middle region of the member. A material non-linear fiber section model is formulated in both the external and the middle sub-elements, allowing the spread of the plasticity also beyond the critical zones. Each steel bar is modeled as a single fiber using uniaxial Giuffre-Menegotto-Pinto constitutive law [54], corresponding to *Steel02* material model with isotropic strain hardening [55]. The yield strength  $f_y$ , the modulus of elasticity  $E_s$  and the strain-hardening ratio  $b$  are assumed equal to 390 MPa, 200,000 MPa and 0.01, respectively; the parameters that control the transition from the elastic to the plastic branch are assigned as  $R_0 = 18$ ,  $C_{R1} = 0.925$  and  $C_{R2} = 0.15$ , as recommended in reference [56]. The concrete part of the cross-section is discretized into 5 fibers in the cover patches and 20 fibers in the core patch. The Mander concrete model [47] is implemented with initial elastic modulus  $E_c = 29,584$  MPa, using the library uniaxial material *Concrete04*, which is based on the model proposed by Popovics [57]. Concrete class is C35/45; the compressive strength of the concrete cover is  $f_{cover} = 35$  MPa and strains  $\epsilon_c$  and  $\epsilon_{cu}$  are 0.002 and 0.004 mm/mm, respectively. Strength and strains of the confined concrete of the core patch are adjusted depending on the reinforcement details of the specific cross-section. The concrete tensile strength and corresponding strain are  $f_{ct} = 3.67$  MPa and  $\epsilon_t = 0.000124$  mm/mm.

In the concentrated plasticity approach, beams and column members are modelled again using the *forceBeamColumn* element [7]; a linear elastic material behavior is assigned to the internal sub-element, whereas the non-linear behavior can be activated only in the two external sub-elements. In these plastic regions, whose length is assigned by the user, the concrete non-linear behavior is modelled through a fiber section model with same material parameters used in the distributed inelasticity formulation, while an effective moment of inertia  $I_{eq}$  of the elastic element interior is considered to account for concrete cracking. In this version with elastic interior, the element object is also known as *beamWithHinges* element object [7], [56]. The same two-point Gauss-Radau integration scheme and the same number of integration points (six across each element object) is therefore used in the element state determination for both distributed and concentrated plasticity representations.

The six expressions of  $L_{pl}$  considered in the formulation of the concentrated plasticity models and the supporting hypotheses are listed in Table 1-8. Each expression for  $L_{pl}$  cannot be implemented independently of the paradigms introduced for the curvature profile, method to compute the yield and ultimate curvatures and moments, as well as for the adopted concrete confinement model and type of loading [16], [58]. For this reason, only expressions respectful of the hypotheses of Eq. (1.1) [40] and valid for both beam and column members have been considered. All the expressions in Table 1-8 were evaluated considering a well-detailed confinement model [47], and are valid for cycling loading, in line with the scope of the present work. The expressions P-P [14] and NTC (Eq.(1.2)) [25] can be implemented along with the classical Mander model for confined concrete, while CEN (Eq.(1.3)) [24], P-F [15] and FAR [16] expressions require the modified Mander formulation described by Eqs.(1.4) – (1.6). However, since the concrete strengths evaluated by the two formulations differ by less than 5% and the ultimate strains are nearly equivalent, the classical Mander concrete model has been adopted in the study whichever the plastic hinge model to be implemented. It must be mentioned that only the ELM expression [19] is not associated to any specific confinement model, but

## **1 Concentrated plasticity modelling of RC frames in time-history analyses**

---

the material and reinforcement properties of the case-study frames are within the range assessed in the experimental tests used for the development of the model [19] and therefore it is assumed that the Mander model can be adopted also for this formulation.

	NTC <sup>[25]</sup>	CEN <sup>[24]</sup>
$\theta_u$	$\frac{1}{\gamma_{el}} 0.016(0.3^v) \left[ \frac{\max(0.01; \omega')}{\max(0.01; \omega)} f_c \right]^{0.225} \left( \frac{z}{h} \right)^{0.35} 25^{\alpha \rho_{sx}} \frac{f_{yw}}{f_c} (1.25^{100 \rho_d})$ $\frac{1}{\gamma_{el}} \left( \theta_y + (\varphi_u - \varphi_y) L_{pl} \left( 1 - \frac{0.5 L_{pl}}{z} \right) \right)$	$\frac{1}{\gamma_{el}} 0.016(0.3^v) \left[ \frac{\max(0.01; \omega')}{\max(0.01; \omega)} f_c \right]^{0.225} \left( \frac{z}{h} \right)^{0.35} 25^{\alpha \rho_{sx}} \frac{f_{yw}}{f_c} (1.25^{100 \rho_d})$ $\frac{1}{\gamma_{el}} \left( \theta_y + (\varphi_u - \varphi_y) L_{pl} \left( 1 - \frac{0.5 L_{pl}}{z} \right) \right)$
$\theta_y$	$\frac{\varphi_y(z + a_v \zeta)}{3} + 0.0013 \left( 1 + \frac{1.5h}{z} \right) + 0.13 \varphi_y d_b f_y / \sqrt{f_c}$	$\frac{\varphi_y(z + a_v \zeta)}{3} + 0.00135 \left( 1 + \frac{1.5h}{z} \right) + \frac{\varepsilon_y}{d - d'} d_b f_y / 6 \sqrt{f_c}$
$f_{cc}$	$f_c \left( -1.254 + 2.254 \sqrt{1 + \frac{7.94 f'_l}{f_c}} - \frac{2 f'_l}{f_c} \right)$	$f_c \left( 1 + 3.7 \left( \frac{\alpha \rho_{sx} f_{yw}}{f_c} \right)^{0.86} \right)$
$\varepsilon_{cc}$	$\varepsilon_{c2} \left[ 1 + 5 \left( \frac{f_{cc}}{f_c} - 1 \right) \right]$	$\varepsilon_{c2} \left[ 1 + 5 \left( \frac{f_{cc}}{f_c} - 1 \right) \right]$
$\varepsilon_{cu}$	$\dagger$	$0.004 + 0.5 \left( \frac{\alpha \rho_{sx} f_{yw}}{f_{cc}} \right)$
$L_{pl}$	$0.1z + 0.17h + 0.24 d_b f_y / \sqrt{f_c}$	$\frac{z}{30} + 0.2h + 0.11 d_b f_y / \sqrt{f_c}$

Table 1-8: Plastic hinge length formulations investigated in the study [51]

## 1 Concentrated plasticity modelling of RC frames in time-history analyses

	<b>P-P<sup>[14]</sup></b>	<b>P-F<sup>[15]</sup></b>	<b>FAR<sup>[16]</sup></b>	<b>ELM<sup>[19]</sup></b>
$\theta_u$	$\left(\varphi_y \frac{z}{3} + (\varphi_u - \varphi_y)L_{pl} \left(1 - \frac{0.5L_{pl}}{z}\right)\right)$	$\left(\varphi_y \frac{z}{3} + (\varphi_u - \varphi_y)L_{pl} \left(1 - \frac{0.5L_{pl}}{z}\right)\right)$	$\theta_y + a_{sl}(\theta_{u,stip} - \theta_{y,stip}) + (\varphi_u - \varphi_y)L_{pl} \left(1 - \frac{0.5L_{pl}}{z}\right)$	$\left(\varphi_y \frac{z}{3} + (\varphi_u - \varphi_y)L_{pl} \left(1 - \frac{0.5L_{pl}}{z}\right)\right)$
$\theta_y$	$\left(\varphi_y \frac{z}{3}\right)$	$\varphi_y \frac{z}{3} + 0.0025 + \frac{a_{sl}(0.25\varepsilon_y d_b f_y)}{(d-d')\sqrt{f_c}}$	$\varphi_y \frac{(z + a_v \zeta)}{3} + 0.0013 \left(1 + \frac{1.5h}{z}\right) + \frac{a_{sl}(\varphi_y d_b f_y)}{8\sqrt{f_c}}$	$\left(\varphi_y \frac{z}{3}\right)$
$f_{cc}$	$f_c \left(-1.254 + 2.254 \sqrt{1 + \frac{7.94f'_l}{f_c}} - \frac{2f'_l}{f_c}\right)$	$f_c \left(1 + 3.7 \left(\frac{0.5\alpha\rho_s f_{yw}}{f_c}\right)^{0.87}\right)$	$f_c \left(1 + 3.7 \left(\frac{\alpha\rho_{sx} f_{yw}}{f_c}\right)^{0.86}\right)$	†
$\varepsilon_{cc}$	$0.002 \left[1 + 5 \left(\frac{f_{cc}}{f_c} - 1\right)\right]$	$0.004 + 0.6 \left(\frac{\varepsilon_{su}\rho_s f_{yw}}{f_{cc}}\right)$	†	†
$\varepsilon_{cu}$	$0.004 + 1.4 \left(\frac{\rho_s f_{yw} \varepsilon_{sm}}{f_{cc}}\right)$	†	$0.0035 + \left(\frac{10}{h_c}\right)^2 + 0.4 \left(\frac{\alpha\rho_{sx} f_{yw}}{f_{cc}}\right)$	†
$L_{pl}$	$0.08z + 0.022d_b f_y$	$0.12z + 0.014a_{sl}d_b f_y$	$0.09z + 0.2h$	$0.08z + 0.022d_b f_y + l_s$

† not specified in the reference

Table 1-8 continued: Plastic hinge length formulations investigated in the study [51]

The flexural area moment of inertia of the interior elastic sub-element was initially reduced by 50% with respect to that of the gross cross-section,  $I_g$ , as recommended in both NTC [37] and EC8 [50]. In order to assess the effect of the axial load, which increases the cross-section flexural strength of the columns at the lower stories, additional analyses were performed by considering the expression of the effective area moment of inertia proposed by Priestley [49] as per Eq.(1.9). The two expressions for  $I_{eq}$  will be labelled hereinafter as  $I_{0.5I_g}$  (Eq.(1.10)) and  $I_p$  (Eq.(1.9)), respectively. For each case-study frame a total of 12 analyses was therefore carried out considering the combinations of the six  $L_{pl}$ s and the two  $I_{eq}$ s.

In all models, the masses of the structural members (beams, columns, and slabs) are concentrated at the nodes, dead and live loads are uniformly distributed on each beam and have been calculated according to the tributary area concept; P-Delta effects are considered in the analysis, while bond slip and low-cycle fatigue effects have been disregarded. The columns at the ground floor have fixed base supports, simulating rigid foundations. The damping of the frame is defined according to the Rayleigh method. However, according to other studies ([17], [59]-[62]), the damping matrix is computed as a function of the tangent stiffness matrix only, assuming 5% damping ratio [63], [64]. In spite today it is well accepted that the values of damping of RC structures should range between 0.5% and 2% for NLTH analyses [65], [66], a 5% value has been chosen in order to take into account the energy dissipation coming from possible infill panels or other non-modelled non-structural components.

The floor slabs are modeled as rigid diaphragms, by constraining the nodes belonging to the same floor to have the same displacement. As highlighted e.g., in references [27], [53], the interaction between beam elements modeled with fiber sections and the rigid diaphragm may distort the response of the structure, overestimating the moment resistance of the beams. Under the effect of the seismic action, concrete elements tend to crack and because of that, the neutral axis of the RC cross-section undergoes a shift. The rigid diaphragm prevents the movement of the neutral axis, causing fictitious compressive axial forces in the beams, thus overestimating the actual bending moment resistance and modifying the overall collapse mechanism. To avoid this numerical issue, following Barbagallo et al. [53], an “axial buffer” has been introduced in the FE model. This element, which is assigned through a zeroLength element object [67] characterized by a virtually zero axial stiffness and very high stiffnesses in shear and bending, is placed between one end of each beam and the adjacent node belonging to the rigid diaphragm, and it works as an axial release to eliminate the fictitious axial force.

In accordance with NTC [37] and with established practice, non-linear dynamic analyses were performed considering a set of seven natural ground motions selected from the European Ground Motion Database [68] using the computer program REXEL [69]. The seismic inputs agree, in the interval of periods between 0.15 and 2.0 seconds, with the elastic spectrum at 5% equivalent viscous damping ratio defined by the Code [37] for the life-safety limit state (SLV) of an ordinary structure (functional class  $cu=II$ ) with a nominal life  $V_n = 50$  years, located in L'Aquila, soil type C, category  $T_2$ . The magnitude ( $M_w$ ) of the seven events was chosen within the interval [5.3 – 7.3], with an epicentral distance ( $R_{ep}$ ) in the range 0–30 km. Details of the input ground motions are provided in Table 1-9 and Figure 1-2.

## 1 Concentrated plasticity modelling of RC frames in time-history analyses

Waveform ID	PGA [m/s <sup>2</sup> ]	SF [-]	t [s]	Station ID	Earthquake Name	Magnitude Mw	R <sub>ep</sub> [km]
42ya	2.49	1.62	26.52	ST8	Ionian	5.8	15
133ya	0.93	4.35	26.42	ST33	Friuli	6.0	9
333xa	2.25	1.80	41.86	ST121	Alkion	6.6	20
599xa	0.97	4.15	47.17	ST223	Umbria Marche	5.7	25
772xa	0.56	7.16	15.16	ST223	Umbria Marche	5.3	20
1726ya	2.64	1.53	29.18	ST549	Adana	6.3	30
6975ya	0.51	7.93	34.85	ST327	Izmit	5.8	26

Table 1-9: Selected natural ground motions; PGA = Peak Ground Acceleration, SF = Scale Factor, t = duration of the earthquake [51]

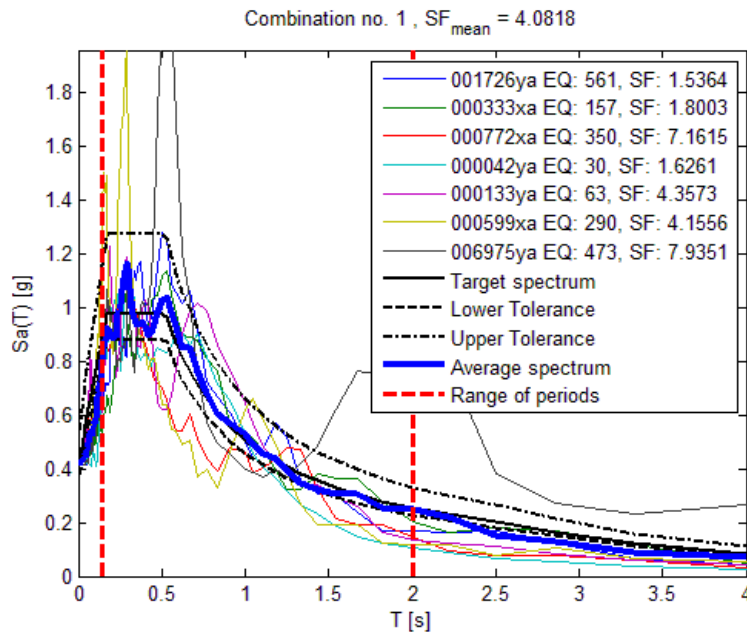


Figure 1-2: Scaled ground motion spectra and target spectrum according to NTC [37] [51]

Since one of the selected inputs shows an extremely high acceleration peak close to the first periods of the 2-story and the 4-story frames (i.e., 0.490 sec and 0.433 sec, respectively), it was preliminary checked that this record would not induce any irregular behavior of the structures that could bias the results. The maximum scatter from the mean estimates was found on the order of either 25% (2-story frame) or 35% (4-story frame) for the inter-story drift, and significantly smaller for the floor accelerations and the internal forces in the columns at the first floor.

## 1.4. Results

Since the structures are designed in compliance with the Italian code [37] and respectfully of the principles of the performance-based design, the distributed plasticity formulations (hereinafter referred to as FIBER models) of the four case-study frames are used as the benchmarks. Indeed, in the distributed plasticity model the non-linear behavior is not supposed/intended to be activated in assigned regions of the structural members, but can spread across their whole length, capturing in a more reliable way the overall flexural behavior of the frame ([34]-[36]). The concentrated plasticity models have been formulated as coherent and comparable to each other as possible, using expressions of the plastic hinge length  $L_{pl}$  respectful of the same fundamental hypotheses, applicable to both beam and column members and valid under cyclic loading. Moreover, these models are consistent with their distributed plasticity counterpart since all of them incorporate the same material properties and constitutive behaviors.

As a first consistency check, plastic deformations were verified to occur in the frames at the same locations independently of the adopted plasticity model. Figure 1-3 highlights the locations where activation of the plastic hinges has been predicted in time-history analyses. Only plastic hinges that are predicted both from the concentrated plasticity formulation of the frame and from the 12 distributed plasticity formulations (resulting from the six  $L_{pl}$  and the two  $I_{eq}$ ) have been reported. Filled spots indicate plastic hinges that are engaged in each model from all ground motions, and empty spots indicate hinges that are engaged in each model by at least two out of the seven ground motions, but not by all of them. The activation of plastic mechanisms at the ends of the beams and at the bases of the ground floor columns is in agreement with the capacity design principles, anticipated in the design of the case-study structures. It is apparent that in each frame, plastic hinges were triggered at the same locations, and the results were coherent regardless of the modelling choice. It is also worth noting that in the 8-story and the 12-story frames plastic hinges always formed in the external columns of the ground floor but not always in the internal columns, though these latter are subjected to greater moments, because the effective strength of the external columns can be significantly reduced with respect to the nominal value due to the variation of axial load during lateral swinging of the building.

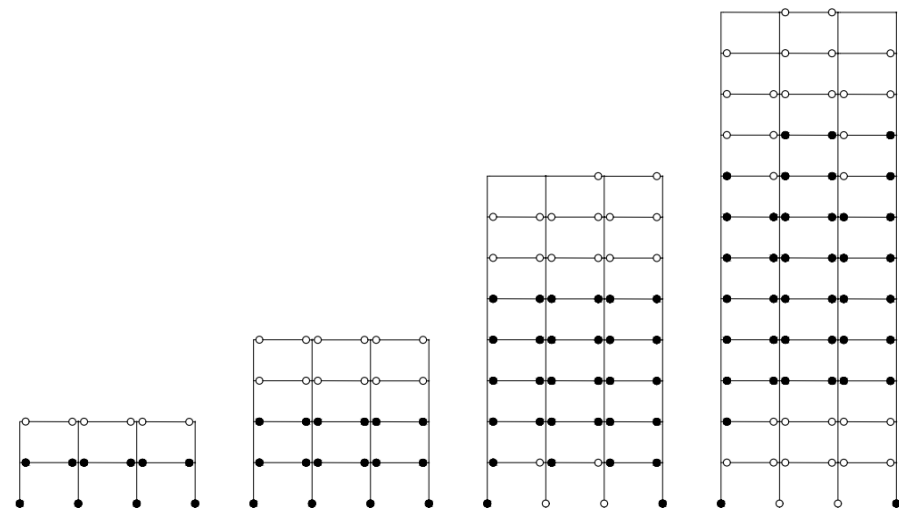


Figure 1-3: Locations of the plastic hinges triggered in the case-study frames [51]

## 1 Concentrated plasticity modelling of RC frames in time-history analyses

---

At the end of the time-history analyses, the response of the case-study structures has been evaluated considering engineering demand parameters such as inter-story drifts, absolute accelerations, and maximum forces and moments in the ground floor columns. During the post-processing of the analysis results relevant to each case-study frame, the maxima of each demand parameter have been identified for each time-history analysis (i.e. for each ground motion in Table 1-9); then, the mean value of these maxima has been computed for each plasticity formulation and evaluated. A detailed comparison among local-level response of the models is out of the scope of the present work.

Figure 1-4 to Figure 1-7 show the results obtained from the analyses performed considering the combination of the various plastic hinge lengths with a 50% reduction of the area moment of inertia ( $I_{0.5I_g}$ ) for the elastic interior of beam and column members, compared to the results provided by the distributed plasticity formulation (FIBER). The comparison is made in terms of maximum inter-story drift ratio  $\Delta_{max}$  and maximum Peak Floor Acceleration  $PFA_{max}$  evaluated over the whole structure, and maximum base shear  $V_{max}$  and base moment  $M_{max}$  in ground floor columns.

Regardless of the modelling approach, i.e. whether distributed or concentrated plasticity is implemented, and the adopted plastic hinge formulation, the 2-story and 4-story frames present the maximum inter-story drift ratio at the second floor, the 8-story frame at the third floor and the 12-story frame at the sixth floor; the maximum accelerations always occur at the last floor of each frame, while the most stressed elements across the frames are the internal columns at the ground floor, and for this reason, in the study the maximum base shear and the maximum base moment will always refer to these members.

Figure 1-4 shows the results for the maximum inter-story drift ratio  $\Delta_{max}$ : the panel on the left compares the estimates provided by the various  $L_{pl}$  formulations, while the panel on the right shows the relative deviation (in %) of each estimate from the benchmark value provided from the distributed inelasticity model. For the 2-story, 4-story and 8-story frames the concentrated plasticity models underestimate the benchmark response (Figure 1-4a); more precisely, the deviation is on the order of -10% for CEN, FAR, P-P and P-F formulations, whichever the frame, while the ELM and the NTC models provide a better agreement for the 4-story and the 8-story frames, with deviations on the other of -5% (Figure 1-4b). The opposite behavior is noticed for the 12-story frame: CEN, FAR, P-P and P-F formulations are in good agreement with the benchmark, while ELM and NTC overestimate it by about 5%. Only for the 2-story building the drift is not significantly affected by the assumed plastic hinge model.

Also for the maximum base moment  $M_{max}$  (Figure 1-5) the concentrated plasticity models underestimate the results of the distributed plasticity representation, though providing values comparable to each other. Relative deviations from the benchmark are on the order of -5% for the 2-story and 4-story frames, but rise to -10% for medium-rise buildings.

A fair agreement between the concentrated and the distributed plasticity formulations is found when the maximum base shear force and the maximum Peak Floor Acceleration are examined, with deviations in general smaller than 5% (Figure 1-6 and Figure 1-7). Regarding  $PFA_{max}$ , with P-P, P-F, FAR and CEN formulations the relative deviation (Figure 1-6b) is positive for low-rise frames, and negative for the 8-story

and the 12-story frames, but always less than 3%; the ELM and NTC models show a very fair agreement with the benchmark for all the buildings but for the 12-story frame, for which the deviation is on the order of 7 – 8%.

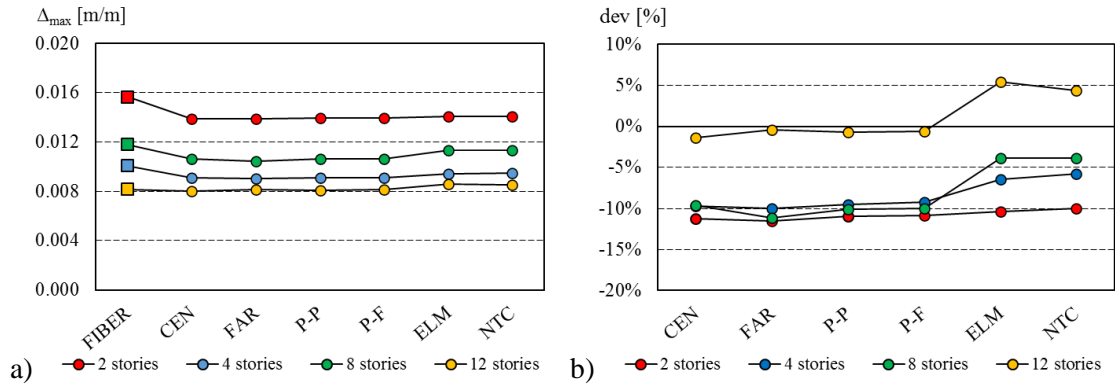


Figure 1-4: Maximum inter-story drift ratio  $\Delta_{max}$  (combination of  $L_{pl}$  with  $I_{0.5I_g}$ ) [51]

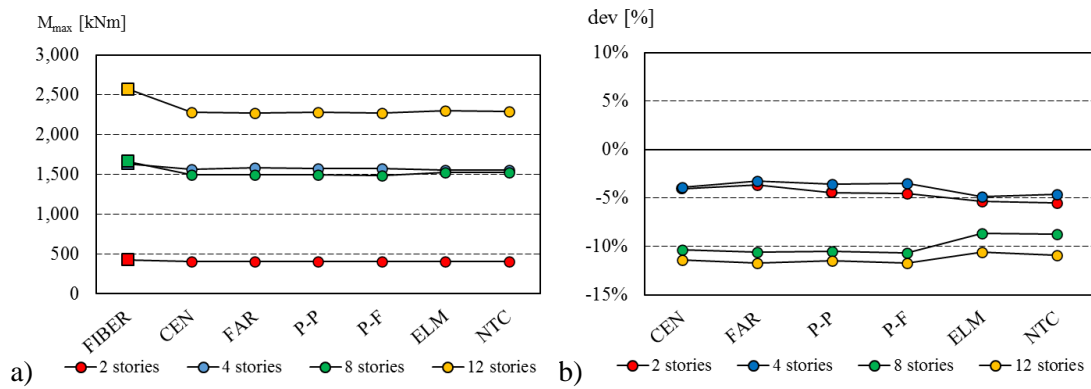


Figure 1-5: Maximum base moment  $M_{max}$  (combination of  $L_{pl}$  with  $I_{0.5I_g}$ ) [51]

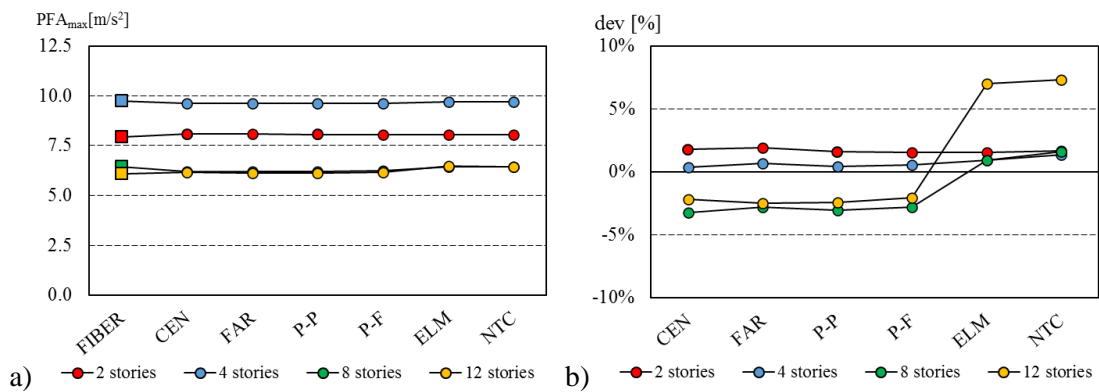


Figure 1-6: Maximum Peak Floor Acceleration  $PFA_{max}$  (combination of  $L_{pl}$  with  $I_{0.5I_g}$ ) [51]

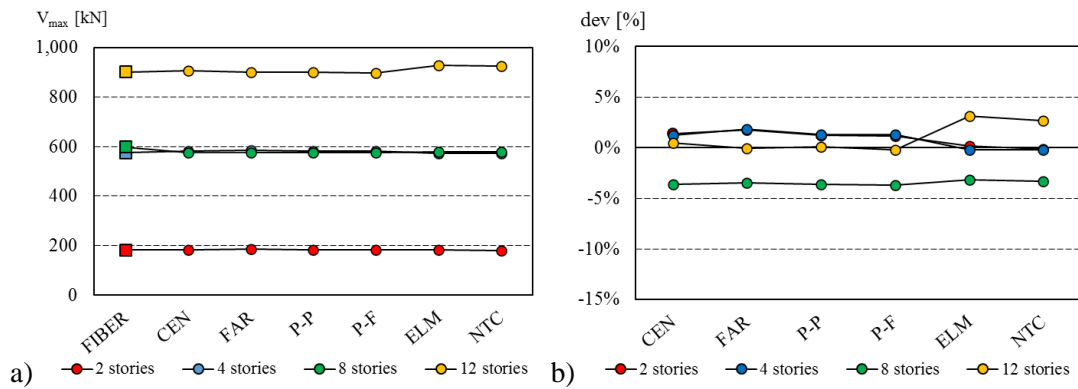


Figure 1-7: Maximum base shear  $V_{max}$  (combination of  $L_{pl}$  with  $I_{0.5I_g}$ ) [51]

Figure 1-8 to Figure 1-11 show the results obtained from the analyses performed combining the concentrated plasticity formulations with the effective area moment of inertia  $I_p$  according to Eq.(1.9).

In general, the lumped plasticity formulations keep underestimating the maximum inter-story drift ratio  $\Delta_{max}$  (Figure 1-8) predicted in the distributed plasticity approach (with only few exceptions, e.g., the 12-story frame with ELM or NTC models), but the agreement is significantly improved in comparison to Figure 1-4 for the 4-story and the 8-story frames: for the first structure, the deviations from the distributed plasticity benchmark become negligible, and for the second one, the deviation is on the order of 4% for ELM and CEN formulations, and of 6-7% for the other models. In contrast, there is no apparent benefits when the 12-story frame is considered: for ELM and NTC models the accord does not change, while for the others the deviation changes from a virtually zero value to about -5%. For the 2-story frame there is no substantial change with respect to Figure 1-4.

The maximum Peak Floor Acceleration  $PFA_{max}$  estimates (Figure 1-9) do not change significantly for the 2-story and the 4-story frames with respect to the results shown in Figure 1-6, while the agreement with the benchmark improves for the 8-story frame: notably, for these three frames the lumped plasticity formulations show a fair agreement with the distributed plasticity approach. For the 12-story frame the  $PFA_{max}$  is slightly overestimated by the plastic hinge formulations, with a deviation on the order of 5% for all models but for ELM and NTC models which have a deviation higher than 7%.

Also for the maximum base shear  $V_{max}$  (Figure 1-10), the results of the concentrated plasticity models are not significantly affected from the adopted expression for the effective area moment of inertia, and are comparable to those shown in Figure 1-7, confirming an acceptable agreement with the distributed plasticity approach (deviation less than 5%).

A remarkable improvement on the estimate of  $M_{max}$  is instead evident by comparing Figure 1-11 to Figure 1-5; the deviation between the lumped plasticity models and the benchmark is reduced to values below 10%, and for the 4-story frame, in some cases the deviation is even negligible. Anyway, the results confirm that the agreement is better for low-rise than for medium-rise frames, and the influence of the adopted plastic hinge formulation is generally low.

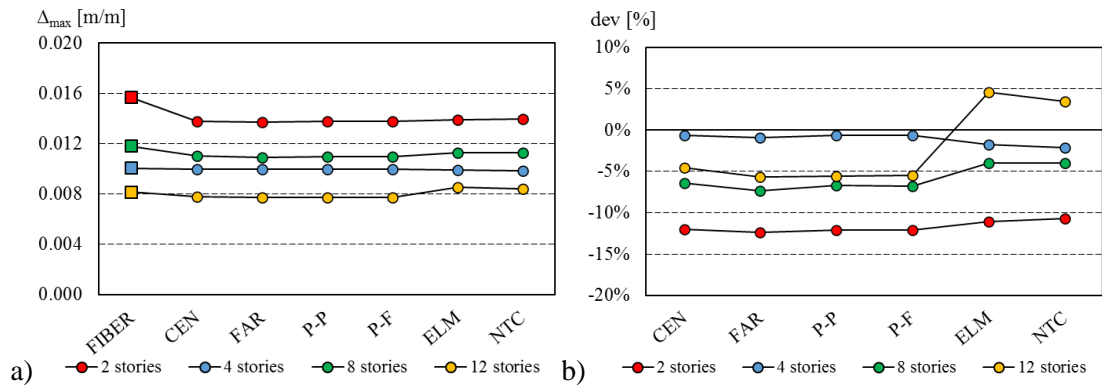


Figure 1-8:  $\Delta_{max}$  and % of deviation (combination of  $L_{pl}$  with  $I_p$ ) [51]

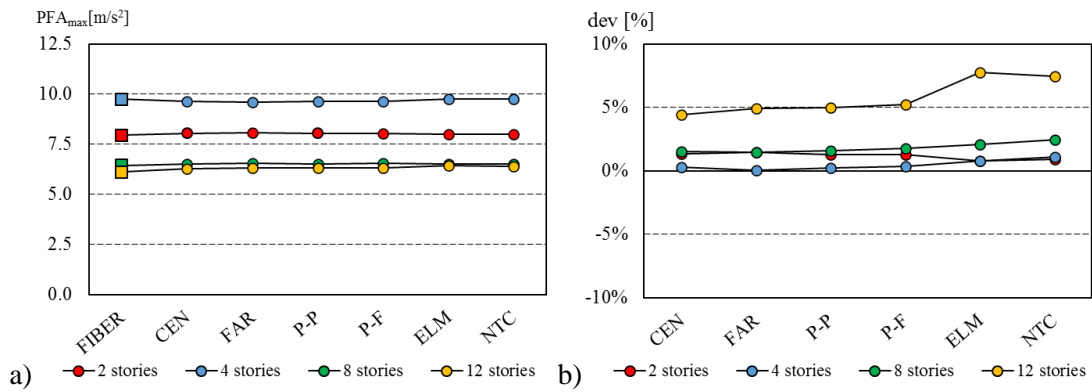


Figure 1-9:  $PFA_{max}$  and % of deviation (combination of  $L_{pl}$  with  $I_p$ ) [51]

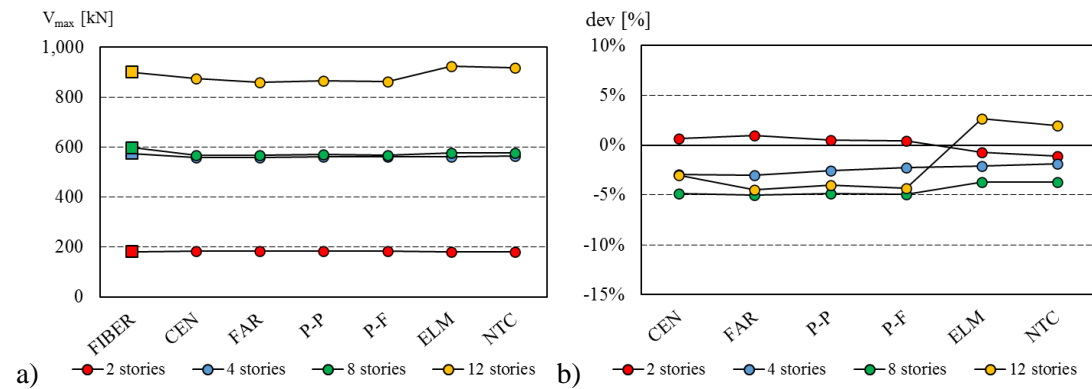


Figure 1-10:  $V_{max}$  and % of deviation (combination of  $L_{pl}$  with  $I_p$ ) [51]

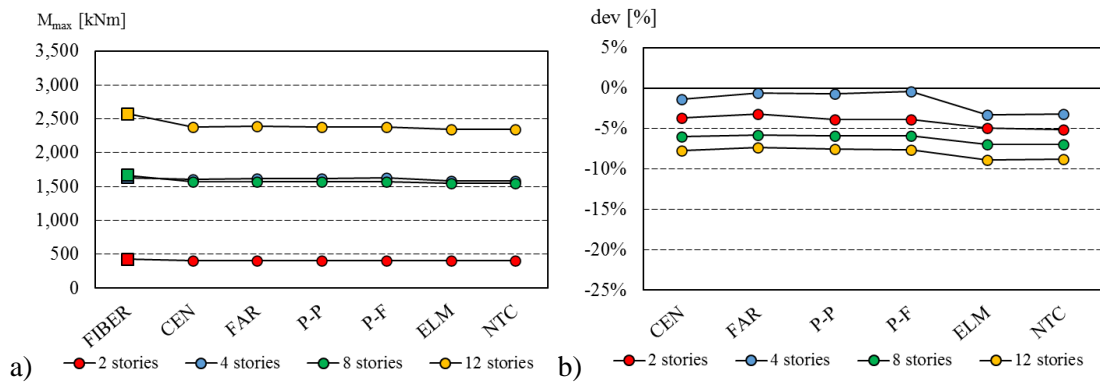


Figure 1-11:  $M_{max}$  and % of deviation (combination of  $L_{pl}$  with  $I_p$ ) [51]

Non-structural components, such as supply lines, plants and architectural elements, as well as technological content that may be present in the buildings, are sensitive to displacements and/or accelerations [70]; for this reason, a second comparison is made in terms of peak inter-story drift ratio  $\Delta$  and peak floor acceleration  $PFA$  at each floor. The results shown in Figure 1-12(a) to Figure 1-19(a) pertain to FIBER, P-P, CEN and ELM formulations combined with the effective area moment of inertia  $I_{0.5I_g}$  according to Eq. (1.10), and those shown in Figure 1-12(b) to Figure 1-19(b) pertain to P-P, CEN and ELM formulations combined with  $I_p$  according to Eq.(1.9). For sake of brevity, the results associated to P-F, FAR and NTC models have been omitted because very close to the ones relevant to P-P and ELM, respectively.

As apparent in Figure 1-12 to Figure 1-15, the lumped plasticity models generally provide a stiffer behavior than the distributed plasticity approach, underestimating the inter-story drift at each floor. However it is noted that for the 12-story frame the ELM model overestimates, in particular at floors 6 and 7 where the largest drifts occur, the response calculated by the FIBER model, consistently with the results presented in Figure 1-4 and Figure 1-8.

In contrast, the predicted Peak Floor Acceleration is not substantially affected by the modelling choice (Figure 1-16 to Figure 1-19), even though for the 12-story frame the concentrated plasticity models estimate slightly higher accelerations at the top floor than the benchmark. These results are consistent with those shown in Figure 1-6 and Figure 1-9.

Analyzing more in detail the effects of the modelling choices, the estimates of drift ratio and peak floor acceleration of the 2-story frame (Figure 1-12 and Figure 1-16) seem to be affected neither by the choice of  $L_{pl}$  nor by the effective area moment of inertia. However, while the differences from the distributed plasticity model in terms of  $PFA$  are negligible, the drifts are significantly underestimated.

For the 4-story frame the agreement on drift estimates is significantly improved by combining  $L_{pl}$  with  $I_p$ , and the diagrams of the various models practically overlap (Figure 1-13b). For the 8-story and 12-story frames, the differences among the models are more evident, in particular, when  $I_{eq}$  is taken as  $I_{0.5I_g}$ : the ELM curve is the closest to the benchmark at each floor, while CEN and P-P plots, though in good agreement

with each other, underestimate the FIBER values. The discrepancy between the lumped plasticity models and the benchmark are reduced when  $I_{eq}$  is assigned as  $I_P$ , Figure 1-14b and Figure 1-15b.

Little influence of the effective area moment of inertia is instead found on the estimate of floor acceleration. In general, the agreement on  $PFA$  is already very good among all models when  $I_{0.5I_g}$  is assigned, and switching to  $I_P$  does not lead to any practical improvement. Actually, only for the 12-story building (Figure 1-19) a certain mismatch is observed between P-P and CEN models on one side, and FIBER and ELM models on the other side, but the difference, which concerns only the intermediate floors, is within 10%, and does not affect  $PFA_{max}$  which is attained at the top floor.

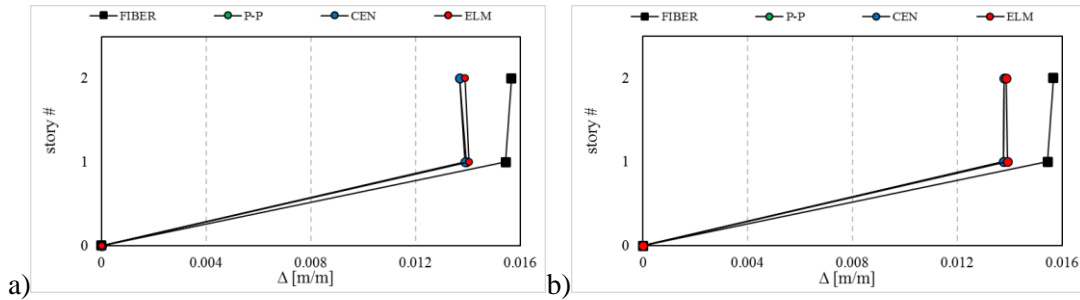


Figure 1-12: Inter-story drift ratio  $\Delta$  across the 2-story frame: a)  $I_{0.5I_g}$ ; b)  $I_P$  [51]

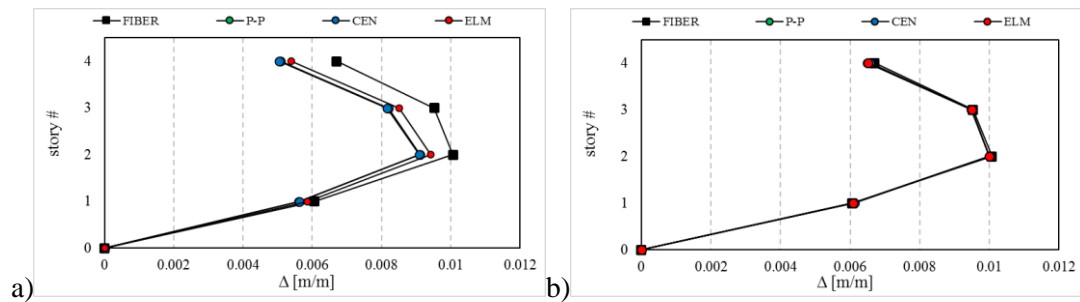


Figure 1-13: Inter-story drift ratio  $\Delta$  across the 4-story frame: a)  $I_{0.5I_g}$ ; b)  $I_P$  [51]

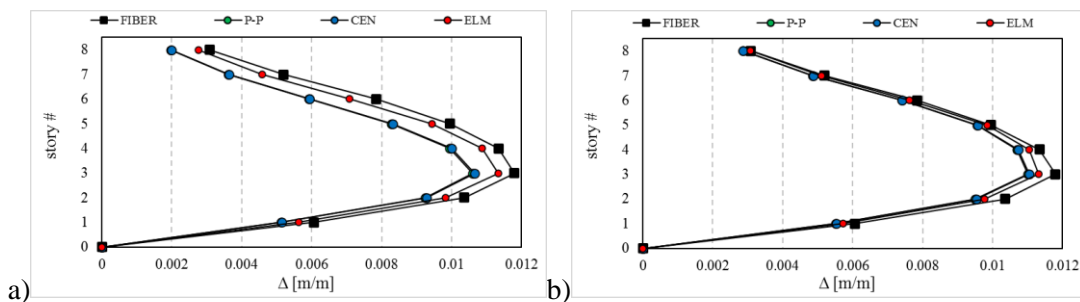


Figure 1-14: Inter-story drift ratio  $\Delta$  across the 8-story frame: a)  $I_{0.5I_g}$ ; b)  $I_P$  [51]

# 1 Concentrated plasticity modelling of RC frames in time-history analyses

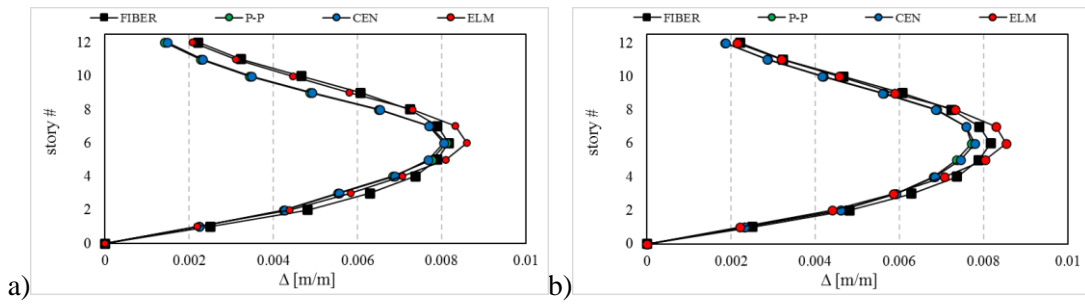


Figure 1-15: Inter-story drift ratio  $\Delta$  across the 12-story frame: a)  $I_{0.5I_g}$ ; b)  $I_P$  [51]

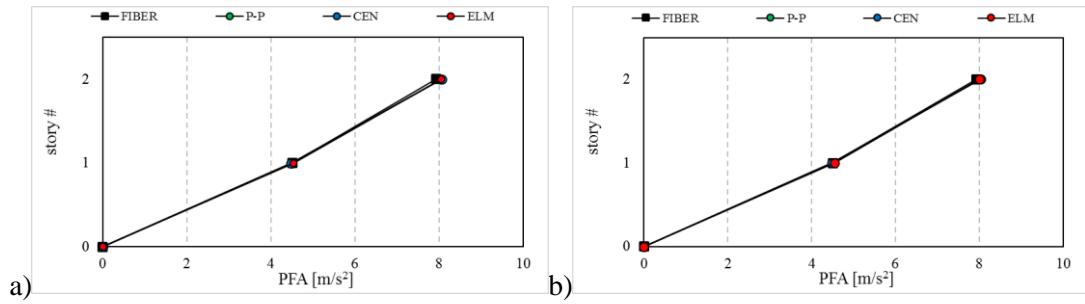


Figure 1-16: Peak Floor Acceleration  $PFA$  across the 2-story frame: a)  $I_{0.5I_g}$ ; b)  $I_P$  [51]

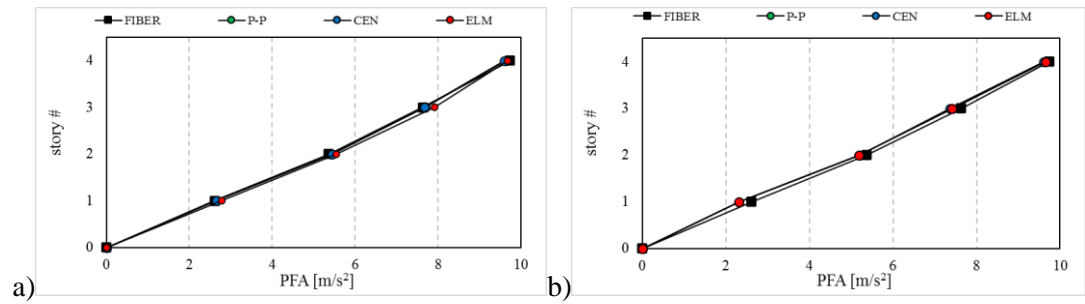


Figure 1-17: Peak Floor Acceleration  $PFA$  across the 4-story frame: a)  $I_{0.5I_g}$ ; b)  $I_P$  [51]

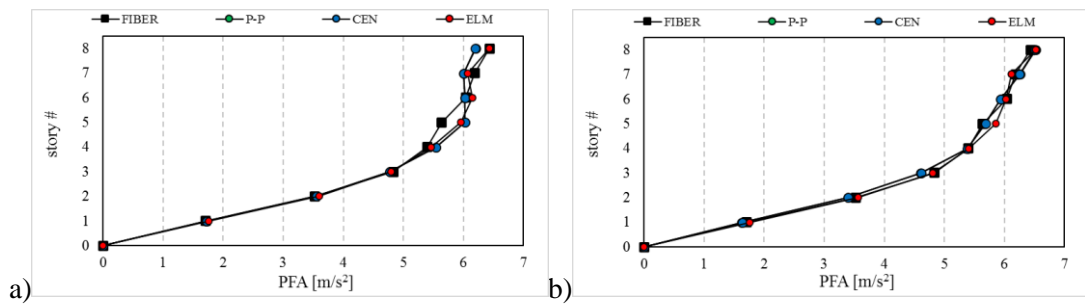


Figure 1-18: Peak Floor Acceleration  $PFA$  across the 8-story frame: a)  $I_{0.5I_g}$ ; b)  $I_P$  [51]

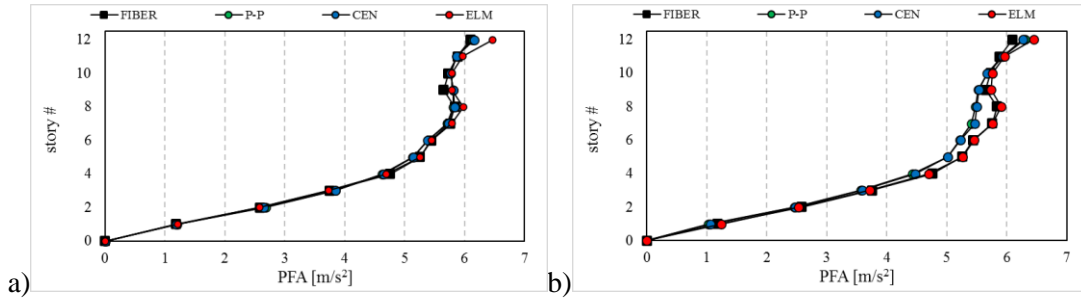


Figure 1-19: Peak Floor Acceleration  $PFA$  across the 12-story frame: a)  $I_{0.5I_0}$ ; b)  $I_p$  [51]

### 1.5. Discussion

---

The engineering demand parameters that appear to be mainly affected by the modelling decisions are the inter-story drift ratio  $\Delta$  and the maximum moment in the ground floor columns  $M_{max}$ , while the peak floor acceleration  $PFA$  and the maximum base shear  $V_{max}$  are less influenced. When a 50% reduction of the gross area moment of inertia  $I_{0.5I_0}$  of the cracked concrete section is assigned to every beam and column member, plastic hinge lengths according to the ELM and NTC formulations provide the estimates more in agreement with the distributed plasticity approach (Figure 1-4, Figure 1-12 - Figure 1-15). This especially occurs when the medium-rise (8-story and 12-story) frames are analyzed. In contrast, the results of the 2-story frame are practically unaffected by the modelling choices, and the inter-story drifts of the benchmark model are considerably underestimated regardless of the assumed plastic hinge length or the effective area moment of inertia, whereas the agreement on the internal forces in the most stressed columns at the ground floor is very fair.

The performances of the various formulations can be explained by considering the extension of the plastic hinge region associated to each model, as shown in Figure 1-20. P-P and P-F formulations provide very close values of  $L_{pl}$ , both for column members ( $L_{pl}$  from 0.30 to 0.33 m) and for beam members ( $L_{pl}$  from 0.35 to 0.38 m), whichever the analyzed frame, and indeed these two models yield similar results, as shown in Figure 1-12 to Figure 1-19. The two models account, in the expression of  $L_{pl}$ , for the contributions of the shear span  $z$  and of the longitudinal reinforcement (Table 1-1): indeed P-F assumes a 50% higher contribution of  $z$  than P-P, but this is counterbalanced by a lower influence of the reinforcement contribution  $d_b f_y$ . The FAR formulation anticipates shorter plastic hinge lengths than the previous two models, especially for the 2-story and the 4-story frames, but the difference disappears in taller structures. It is worth recalling that in the theory underlying the FAR formulation the dependence upon the reinforcement is not explicit in the formulation of  $L_{pl}$  but it is included in the expressions of the rotations at yielding and failure (Table 1-8).

The ELM formulation accounts, as an additional contribution, for the length of the shear spread, which is more important in beam than in column members. The predicted plastic hinge length is the largest among all the examined models, and ranges from 0.45 to 0.75 m for columns and from 0.50 to about 0.8 m for beams (Figure 1-20) depending on the considered frame.

The expressions of  $L_{pl}$  provided by the European and the Italian codes depend on the shear span, the section depth and the longitudinal reinforcement, but assign different weights to each contribution (Eq. (1.2) and Eq. (1.3)). Therefore, the plastic hinge lengths calculated according to NTC are about two times greater than their CEN counterparts, and close to ELM's. In this regard it is worth noting that in the 8-story and 12-story frames the plastic hinge lengths calculated according to NTC and ELM formulations stretch to about 1/6 of the total length of each structural member; in contrast, plastic hinge lengths according to P-P, P-F and FAR formulations are on the order of 10% of the member length for columns, and 8% for beams; intermediate values are provided by the CEN formulation. But for P-P and P-F models, the length of plastic hinge region

increases with the number of stories, which explains the poor agreement with the distributed plasticity model in terms of inter-story drift observed in the 2-story frame.

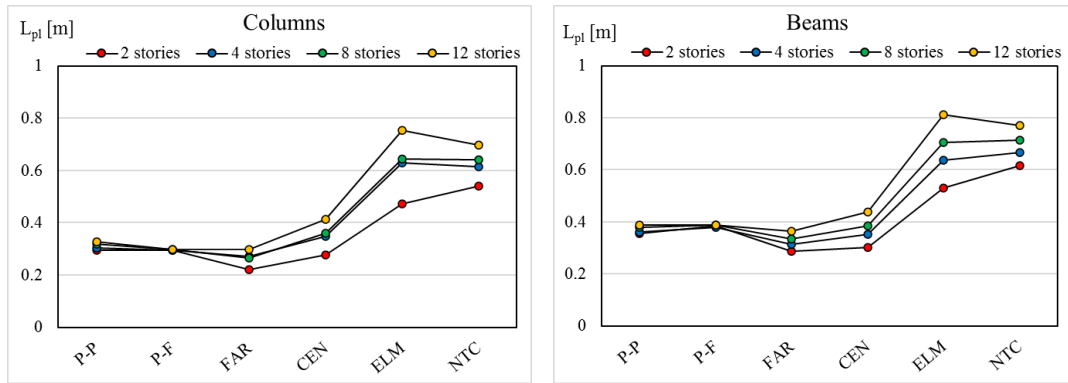


Figure 1-20: Plastic hinge length  $L_{pl}$  for column and beam members [51]

Disregarding the ELM and NTC models, for which the benefit is indeed negligible, the estimates of demand parameters provided by the concentrated plasticity formulations show an improved agreement with the distributed plasticity benchmark when the reduction of the gross area moment of inertia is assigned according to Eq. (1.9), i.e.  $I_{eq} = I_p$ . This formula indeed, which accounts for the contribution of the axial load, differentiates between column and beam members, and among columns at different floors. The ranges of the coefficients of reduction of  $I_p$  with respect to the area moment of inertia of the gross cross-section  $I_g$  calculated by Eq. (1.9) for the examined case-study frames are reported in Table 1-10. Beams, characterized by negligible axial force, have coefficients of reduction considerably lower than columns subjected to high axial load, which has a beneficial effect in increasing the cross-section nominal flexural strength. It is worth noting that the reduction coefficients shown in Table 1-10 are comparable to the ones prescribed in the New Zealand norm [31].

<i>Member</i>	<i>2 stories</i>	<i>4 stories</i>	<i>8 stories</i>	<i>12 stories</i>
Beam	0.37	0.25 – 0.3	0.24 – 0.28	0.22 – 0.34
Column, internal	0.57 – 0.6	0.53 – 0.46	0.56 – 0.58	0.52 – 0.58
Column, perimetral	0.56 – 0.57	0.53 – 0.54	0.55 – 0.59	0.54 – 0.59

Table 1-10: Reduction coefficients of the gross area moment of inertia of the case-study frames according to Eq. (1.9) [51]

As highlighted in Figure 1-8, for the 4-story, 8-story and 12-story frames the concentrated plasticity models combined with the reduced area moment of inertia  $I_p$  yield estimates of  $\Delta_{max}$  which deviate less than 10% from the benchmark; these results are also confirmed from the plots reported in Figure 1-13 to Figure 1-15 which show that the global deformation of the distributed plasticity model is well captured, especially for the 4-story frame. Good agreement is obtained also in terms of  $PFA$ ,  $PFA_{max}$  and  $V_{max}$  (Figure 1-9, Figure 1-10, and Figure 1-16 to Figure 1-19) with scatter less than 5%, even if these response parameters are less

## 1 Concentrated plasticity modelling of RC frames in time-history analyses

---

affected by the choice on  $I_{eq}$ . Also for  $M_{max}$  assigning  $I_{eq} = I_P$  leads to an improved agreement for P-P, P-F, FAR and CEN models (Figure 1-11). Generally speaking, the adoption of the area moment of inertia  $I_P$  dependent upon the axial load benefits more those lumped plasticity models which are characterized by a “short” plastic hinge length than those anticipating a “long”  $L_{pl}$  (e.g., ELM and NTC models), which indeed stretches across a significant part of the total length of the structural member and consequently is likely to envelop the actual cracked region.

The effective area moment of inertia  $I_P$  does not carry any substantial improvement in the analyses of the 2-story frame. Therefore, regarding the accuracy of the results, the lumped plasticity approach does not seem a viable alternative to distributed plasticity modelling for very short-rise buildings.

The results presented in this study highlight that for non-linear analyses of framed RC buildings adopting a lumped plasticity formulation in accordance with Eurocode 8 [24] or with the Italian Building Code [25], the agreement with the results of a full distributed plasticity formulation can be substantially improved, in terms of inter-story drifts and maximum base moments, when the effective area moment of inertia  $I_{eq}$  of the elastic region of each member is assigned according to the formula given in Eq.(1.9) accounting for the effect of the axial load, rather than according to the formula  $I_{eq} = 0.5I_g$  provided in the Codes themselves. This suggests that a more realistic approach is to differentiate the value of  $I_{eq}$  between either beam or column members, as well as among columns subjected to different levels of axial load, in line with other norms (references [31] and [32]).

## 1.6. Conclusions

The study investigates the performance of concentrated plasticity models used to represent the non-linear response of RC frames with flexural behavior in the context of time-history analyses. The models were formulated in the OpenSees framework using the *forceBeamColumn* element object [7] coded in the software libraries, considering different modelling choices pertaining to the length of the plastic hinge region  $L_{pl}$  and the effective area moment of inertia  $I_{eq}$  of the cracked concrete section. Four reinforced concrete frames with 2, 4, 8 and 12 stories were taken as case-study structures. The frames were designed in compliance with the current code recommendations and according with the principles of the capacity design, avoiding brittle collapse; other failure mechanisms, such as bond slip or low-cycle fatigue, were not considered as well. Non-linear dynamic analyses were performed, and the response of the frames evaluated under a set of seven spectrum-compatible earthquakes according to the Italian Building Code [37]. Only plastic hinge formulations valid for cyclic loading and applicable to both column and beam members were taken into account.

The main outcomes of the research are summarized in the next points:

- (1) depending on the modelling decision, the plastic hinge length  $L_{pl}$  varied between 10% and 20% of the member length for columns, and between 8% and 16% of the member length for beams, and, in the examined frames, was also affected from the height of the building, with greater lengths anticipated for taller structures; these differences were reflected in the analyses, with closer results provided by the models yielding comparable values of  $L_{pl}$ ;
- (2) all the concentrated plasticity models were able to capture the global mechanical response of the case-study buildings predicted according to a distributed plasticity formulation, and to identify the locations where plastic hinges were triggered;
- (3) regardless the choice of the plastic hinge length  $L_{pl}$  and the effective area moment of inertia  $I_{eq}$  of cracked concrete sections, estimates of absolute acceleration and maximum base shear provided by the concentrated plasticity models were in acceptable agreement with the distributed plasticity benchmark; in contrast, lumped plasticity models tended to underestimate the inter-story drift ratio and the maximum base moment in all frames, with the only exceptions of the 12-story frame, where the drifts were overestimated by the ELM and NTC models; better agreement on the maximum base moment was consistently achieved in low-rise than in medium-rise buildings;
- (4) regarding the modelling choice used to account for the reduced flexural strength of the cracked concrete section, a closer agreement with the results provided from the distributed plasticity approach was achieved by assigning an area moment of inertia dependent upon the axial load (Eq.(1.9) in the Chapter), rather than a fixed 50% reduction of gross area moment of inertia as recommended in the European [50] and the Italian [37] codes. The improvement was more evident for lumped plasticity formulations anticipating a “short” plastic hinge length than a “long”  $L_{pl}$ ; in the latter case, the assigned region, where plastic deformation is

## **1 Concentrated plasticity modelling of RC frames in time-history analyses**

---

allowed to occur, indeed extends over a significant part of the total length of the structural member and consequently is likely to envelop the actual cracked region;

The results of the study therefore suggest that, but for very low-rise frames like, e.g., the 2-story frame examined in the study, a better agreement with the results of distributed plasticity analyses, especially in terms of maximum inter-story drift ratio and maximum base moment, can be achieved by adopting different values of  $I_{eq}$  for either beams or columns, as well as for columns subjected to different levels of axial load, in line with the provisions of other norms [31], [32].

It should be noted that these conclusions might only apply to buildings exhibiting a strong-column/weak-beam behavior in line with the capacity design. The results were obtained examining four frames, from two to twelve stories in height, characterized by a regular distribution in plan and elevation, and considering only a set of seven ground motions. Though the number of ground acceleration histories is in accordance with the prescriptions of the Italian Building Code [37], bias-related issues due to the low number of ground motions may be a concern. In a future development the investigation will be extended to buildings with irregular plan and will consider a larger number of ground motions, representing different site characteristics and comprising both near-fault and far-field events, in order to confirm the validity of the present conclusions over a large variety of practical conditions. Nevertheless, despite these current limitations, the Authors believe that the study has some merit in providing, for the first time, a comprehensive comparison between the effects of the modelling decisions in the formulation of concentrated plasticity models for non-linear dynamic analyses of ductile RC frames.

## 1.7. Symbols

---

$a_v$  zero-one coefficient related to the cracking phenomena due to shear or flexure

$A_g$  gross area of concrete section

$A_s$  area of tension reinforcement

$A_{st}$  area of transverse reinforcement

$b$  strain-hardening ratio

$B$  section width of the structural element

$B_p$  section width of the pillars

$CR_1$  curvature degradation parameter

$CR_2$  curvature degradation parameter

$d$  section depth of tension reinforcement

$d'$  section depth of compression reinforcement

$d_b$  diameter of longitudinal reinforcement

$d_{st}$  diameter of transverse reinforcement

$E_c$  modulus of elasticity of concrete

$E_s$  modulus of elasticity of steel

$f_c$  compressive strength of concrete

$f_{cc}$  compressive strength of confined concrete

$f_{cover}$  compressive strength of the concrete cover

$f_{ct}$  tensile strength of the concrete section

$f'_l$  effective lateral confining stress on concrete

$f_y$  yielding stress of longitudinal reinforcement

$f_{yw}$  yielding stress of transverse reinforcement

$f_u$  ultimate tensile strength of reinforcement

$G_1$  permanent structural loads

$G_2$  non-permanent structural loads

$h$  overall depth of beam or column

$h_c$  section height of the confined core

$I_{0.5I_g}$  effective area moment of inertia evaluated according to Eq.(1.10)

## 1 Concentrated plasticity modelling of RC frames in time-history analyses

---

$I_{cr}$  area moment of inertia of the cracked section

$I_{eq}$  effective area moment of inertia

$I_g$  gross area moment of inertia

$I_p$  effective area moment of inertia evaluated according to Eq.(1.9)  $k_1 = 0.7$  for mild steel, 0.9 for cold worked steel in [8]

$k_2 = 1 + 0.5P/P_0$  used in [8]

$k_3 = 0.9 - \left(\frac{0.3}{23.5}\right)(f_c - 11.7)$  ( $f_c$  in MPa) in [8]

$L_{pl}$  plastic hinge length

$l_s$  length of shear spread

$M_b$  bending moment acting on the section

$M_{cr}$  bending moment at the first cracking

$M_{max}$  maximum base moment (in the most stressed column at the ground floor)

$M_N$  nominal flexural moment

$M_y$  yield flexural moment

$M_w$  magnitude

$N$  axial load under gravity actions alone

$P$  applied axial force in [18],[20],[21]

$P_0 = 0.85f_c(A_g - A_s) + f_yA_s$  nominal axial load capacity as per ACI 318 [23] in [18],[20],[21]

$PFA$  peak floor acceleration

$PFA_{max}$  maximum peak floor acceleration across the frame

$PGA$  peak ground acceleration

$q$  tension reinforcement index  $\left(= \frac{A_s}{bd} \cdot \frac{f_y}{f_c}\right)$  in [9]

$Q$  live loads

$q'$  compressive reinforcement index  $\left(= \frac{A'_s}{bd} \cdot \frac{f_y}{f_c}\right)$  in [9]

$q_b$  balanced tension reinforcement index  $\left(= \frac{A_b}{bd} \cdot \frac{f_y}{f_c}\right)$  in [9]

$R_{ep}$  epicentral distance

$R_0$  initial value of the curvature parameter

$s$  spacing of the transverse reinforcement

$SF$  scale factor

$t$  duration of the earthquake

$T_1$  period of the first vibration mode of the frames

$T_2$  period of the second vibration mode of the frames

$V_{max}$  maximum base shear (in the most stressed columns at the ground floor)

$z$  distance from critical section of maximum curvature and the element point of contraflexure

$\alpha$  coefficient depending on the type of structural element (0.108 for columns, 0.133 for beams, 0.152 for rectangular walls)

$\alpha_c$  confinement effectiveness factor

$\gamma_{el} = 1.5$  for primary seismic elements,  $= 1$  for secondary seismic elements

$\Delta$  inter-story drift ratio

$\Delta_{max}$  maximum inter-story drift ratio across the frame

$\delta$  ultimate top displacement of an RC cantilever column

$\varepsilon_c$  floating point value defining concrete strain at maximum strength

$\varepsilon_{c2}$  strain at which  $f_{cc}$  is attained in accordance with the model of Eurocode 2 [46]

$\varepsilon_{cc}$  strain at which  $f_{cc}$  is attained in accordance with the model of Eurocode 8 [24]

$\varepsilon_{cu}$  floating point value defining concrete strain at crushing strength

$\varepsilon_{sm}$  steel strain at maximum tensile stress

$\varepsilon_{su}$  ultimate elongation of steel

$\varepsilon_t$  tensile strain of the concrete section

$\varepsilon_y$  yield strain of the longitudinal reinforcement

$\zeta$  level arm equal to  $d - d'$  in rectangular sections

$\theta_y$  chord rotation at yielding

$\theta_{y,slip}$  yielding rotation due to slippage of longitudinal bars from the anchorage zone

$\theta_{u,slip}$  ultimate rotation due to slippage of longitudinal bars from the anchorage zone

$\nu$  axial load ratio  $\frac{N}{A_g f_c}$

$\varphi_y$  yield curvature

$\varphi_u$  ultimate curvature at failure

$\rho_c$  ratio of longitudinal reinforcement in compression

## **1 Concentrated plasticity modelling of RC frames in time-history analyses**

---

$\rho_d$  ratio of diagonal reinforcement (if present)

$\rho_l$  total longitudinal reinforcement ratio

$\rho_s$  volumetric ratio of confining steel

$\rho_{sx}$  ratio of transverse steel parallel to the direction x of loading

$\rho_t$  ratio of longitudinal reinforcement in tension

$\omega$  mechanical ratio of the tension longitudinal reinforcement

$\omega'$  mechanical ratio of the compression longitudinal reinforcement

---

## 1.8. References

---

- [1] McKenna F, Fenves GI, Scott MH. Open System for Earthquake Engineering Simulation, PEER Report, Berkeley, CA; 2000.
- [2] Dassault Systemes Simulia Corp. Abaqus/CAE user's guide, Providence, RI, USA; 2017.
- [3] CSPFEA. Midas Gen FX Manual, CSPFEA Engineering solutions. [http://www.cspfea.net/portfolio\\_page/midas-gen-fx/](http://www.cspfea.net/portfolio_page/midas-gen-fx/); 2018.
- [4] Brunetta M, Bandini L, De Lorenzi M. SAP2000, analisi lineare/nonlineare integrata con verifiche per strutture tridimensionali. CSI Computer and Structures Inc; 2006.
- [5] Calabrese A, Almeida JP, Pinho R. Numerical issues in distributed inelasticity modeling of RC frame elements for seismic analysis, *Journal of Earthquake Engineering* 2010;14: S1:38-68; DOI:10.1080/13632469.2010.495681.
- [6] Wu RY, Pantelides CP. Concentrated and distributed plasticity models for seismic repair of damaged RC bridge columns. *Journal of Composites for Construction* 2018, 10.1061/(ASCE)CC.1943-5614.0000879, 04018044.
- [7] Scott MH, Fenves GL. Plastic hinge integration methods for force-based beam-column elements, *Journal of Structural Engineering* 2006; 132(2):244-252; DOI:10.1061/(ASCE)0733-9445(2006)132:2(244).
- [8] Baker ALL. Ultimate load theory applied to the design of reinforced and prestressed concrete frames, Concrete Publications Ltd, London, UK; 1956, 91 pp.
- [9] Mattock AH. Rotational capacity of hinging regions in reinforced concrete beams, *Flexural Mechanics of Reinforced Concrete*, SP-12, American Concrete Institute: Farmington Hills, MI; 1964, p. 143-181.
- [10] Sawyer HA. Design of concrete frames for two failure stages. In *Proceedings of international symposium on the flexural mechanics of reinforced concrete*, Miami; 1964, ACI SP-12:405-431.
- [11] Corley WG. Rotational capacity of reinforced concrete beams, *Journal of the Structural Division*, ASCE 1966;92: ST5:121-146.
- [12] Mattock AH. Discussion of rotational capacity of hinging regions in reinforced concrete beams, *Journal of the Structural Division*, ASCE 1967;93: ST2:519-522.
- [13] Priestley MJN, Park R. Strength and ductility of concrete bridge columns under seismic loading, *ACI Structural Journal* 1987;84(1):61-76.
- [14] Paulay T, Priestley MJN. *Seismic design of reinforced concrete and masonry buildings*, John Wiley and Sons, New York; 1992, 767 pp.
- [15] Panagiotakos TB, Fardis MN. Deformation of reinforced concrete members at yielding and ultimate, *ACI Structural Journal* 2001;98(2):135-148.
- [16] Fardis MN. LESSLOSS – Risk mitigation for earthquakes and landslides, *Guidelines for displacement – based design of buildings and bridges*, Report n. 5/2007, IUSS Press, Pavia, Italy; 2007.
- [17] Priestley MJN, Calvi GM, Kowalsky MJ. *Displacement-based seismic design of structures*. IUSS Press, Pavia 2007.

- [18] Bae S, Bayrak O. Plastic hinge length of reinforced concrete columns, *ACI Structural Journal* 2008;105(3):290-300; retrieved from <https://search.proquest.com/docview/198338935?accountid=28385>.
- [19] Elmenshawi A, Brown T, El-Metwally S. Plastic hinge length considering shear reversal in reinforced concrete elements, *Journal of Earthquake Engineering* 2012;16(2):188-210; DOI:10.1080/13632469.2011.597485.
- [20] Mortezaei A, Ronagh HR. Plastic hinge length of reinforced concrete columns subjected to both far-fault and near-fault ground motions having forward directivity, *Structural Design of Tall and Special Buildings* 2013;22(12):903-926; DOI:10.1002/tal.729.
- [21] Ning CL, Bing L. Probabilistic approach for estimating plastic hinge length of reinforced concrete columns, *Journal of Structural Engineering* 2016;142(3): Article number 04015164; [https://doi.org/10.1061/\(ASCE\)ST.1943-541X.0001436](https://doi.org/10.1061/(ASCE)ST.1943-541X.0001436).
- [22] FEMA (Federal Emergency Management Agency). FEMA 356. Prestandard and commentary for the seismic rehabilitation of buildings, Applied Technology Council for the Federal Emergency Management Agency, Washington, DC, 2000.
- [23] ACI Committee 318. Building code requirements for structural concrete (ACI 318-19) and commentary (ACI 318R-19), American Concrete Institute, Farmington Hills, MI, USA, 2019.
- [24] CEN (European Committee for Standardization). Design of structures for earthquake resistance - Part 3: Assessment and retrofitting of buildings. EN 1998-3 Eurocode 8; 2005.
- [25] CSLLPP (Consiglio Superiore dei Lavori Pubblici). Circolare 21 gennaio 2019, n. 7 C.S.LL.PP. Istruzioni per l'applicazione dell'«Aggiornamento delle «Norme tecniche per le costruzioni» di cui al decreto ministeriale 17 gennaio 2018, Roma; 2019, in Italian.
- [26] Teruna DR, Wijaya H. Seismic responses comparison of RC building in consideration of plastic hinge models and properties, *IOP Conference Series: Material Science and Engineering* 2018;383: Article number 012025; DOI:10.1088/1757-899X/383/1/012025.
- [27] Lima C, Angiolilli M, Barbagallo F, Belletti B, Bergami AV, Camata G, Cantagallo C, Di Domenica M, Fiorentino G, Ghersi A, Gregori A, Lavorato D, Luciano R, Marino EM, Martinelli E, Nuti C, Ricci P, Rosati L, Ruggieri S, Sessa S, Spacone E, Terrenzi M, Uva G, Vecchi F, Verderame GM. Nonlinear modeling approaches for existing reinforced concrete buildings: the case study of De Gasperi-Battaglia school building in Norcia, *Lecture Notes in Civil Engineering* 2020;42:82-95; DOI:10.1007/978-3-030-23748-6\_7.
- [28] Inel M., Ozmen HB. Effects of plastic hinge properties in nonlinear analysis of reinforced concrete buildings, *Engineering Structures* 2006;28(11):1494-1502; DOI:10.1016/j.engstruct.2006.01.017.
- [29] Lopez AL, Tomas A, Olivares, G. Influence of adjusted models of plastic hinges in nonlinear behavior of reinforced concrete buildings, *Engineering Structures* 2016;124:245-57; DOI:10.1016/j.engstruct.2016.06.021.
- [30] Petrini L, Maggi C, Priestley MJN, Calvi GM. Experimental verification of viscous damping modeling for inelastic time history analyzes, *Journal of Earthquake Engineering* 2008, 12:S1, 125-145, DOI:10.1080/13632460801925822.

- [31] NZS (Standards Council of New Zealand). Concrete buildings. Part C – The design of concrete structures. NZS 2017.
- [32] KANEPE, Hellenic Code of Retrofitting of Reinforced Concrete Buildings. Organization of Seismic Design & Protection (OASP). Gov. Gaz. 2984/B/30-8-2017. Hellenic Ministry of Infrastructure, Transport and Network, 2012. (in Greek).
- [33] Lemes IJM, Barros RC, Silveira RAM, Silva ARD, Rocha PAS. Numerical analysis of RC plane structures: a concentrated nonlinear effect approach, *Latin American Journal of Solids and Structures* 2018;15(2) Article number e20; DOI:10.1590/1679-78254681.
- [34] Spacone E, Filippou F, and Taucer F. Fibre beam-column model for non-linear analysis of r/c frames: part I. formulation, *Earthquake Engineering and Structural Dynamics* 1996a, 25, 711–726; DOI:10.1002/(SICI)1096-9845(199607)25:7<711:AID-EQE576>3.0.CO;2-9.
- [35] Spacone E, Filippou F, and Taucer F. Fibre beam-column model for non-linear analysis of r/c frames: part II. Applications, *Earthquake Engineering and Structural Dynamics* 1996b, 25, 727–742; DOI:10.1002/(SICI)1096-9845(199607)25:7<727:AID-EQE577>3.0.CO;2-O.
- [36] Terrenzi M, Spacone E, Camata G. Comparison between phenomenological and fiber-section non-linear models, *Frontiers in Built Environment* 2020, 6:38; DOI:10.3389/fbuil.2020.00038.
- [37] CSLLPP (Consiglio Superiore dei Lavori Pubblici). D.M. 17 gennaio 2018 in materia di “norme tecniche per le costruzioni”. *Gazzetta ufficiale* n.42 del 20 febbraio 2018, Supplemento ordinario n.8, Ministero delle Infrastrutture e dei trasporti, Roma; 2018, in Italian.
- [38] Pereira N, Romao X. Damage localization length in RC frame components: Mechanical analysis and experimental observations, *Engineering Structures* 221 (2020) 111026; DOI:10.1016/j.engstruct.2020.111026.
- [39] Elmenshawi A, Brown T. Deformation capacity of ultra-high strength concrete flexural elements subjected to inelastic load reversals, *The Structural Design of Tall and Special Buildings* 2010; DOI:10.1002/tal.633.
- [40] Park R, Paulay T. *Reinforced Concrete Structures*, John Wiley and Sons, New York, 1975, 769 pp.
- [41] Verderame G, Ricci P, Manfredi G, Cosenza E. Ultimate chord rotation of RC columns with smooth bars: some considerations about EC8 prescriptions, *Bulletin of Earthquake Engineering* 2010;8(6):1351-1373; DOI:10.1007/s10518-010-9190-x.
- [42] Zhao X, Wu YF, Leung AYt, Lam HF. Plastic hinge length in reinforced concrete flexural members, *Procedia Engineering* 2011;14:1266-1274; DOI:10.1016/j.proeng.2011.07.159.
- [43] Yuan F, Yu-Fei W. Effect of load cycling on plastic hinge length in RC columns, *Engineering Structures* 2017;147:90-102; DOI:10.1016/j.engstruct.2017.05.046.
- [44] Ameli MJ, Pantelides CP. Seismic analysis of precast concrete bridge columns connected with grouted splice sleeve connectors, *Journal of Structural Engineering* 2017, ASCE, 10.1061/(ASCE)ST.1943-541X.0001678, 04016176.
- [45] CEN (European Committee for Standardization). Design of structures for earthquake resistance – Part 2: Bridges. EN 1998–2 Eurocode 8; 2005.

- [46] CEN (European Committee for Standardization). Design of concrete structures - Part 1-1: General rules and rules for buildings. EN 1992-1-1 Eurocode 2; 2005.
- [47] Mander JB, Priestley MJN, Park R. Theoretical stress-strain model for confined concrete, *Journal of Structural Engineering ASCE* 1988; 114(8), 1804-1825.
- [48] Branson DE, Metz GA. Instantaneous and time-dependent deflections of simple and continuous reinforced concrete beams, Auburn: Department of Civil Engineering and Auburn Research Foundation, Auburn University; 1963.
- [49] Priestley, MJN. Brief comments on elastic flexibility of reinforced concrete frames and significance to seismic design, *Bulletin NZ National Society for Earthquake Engineering* 1998;31(4):246-259.
- [50] CEN (European Committee for Standardization). Design of structures for earthquake resistance - Part 1: General rules, seismic actions and rules for building. EN 1998-1 Eurocode 8; 2005.
- [51] Bruschi E, Calvi PM, Quaglini V. Concentrated plasticity modelling of RC frames in time-history analyses, *Engineering Structures* 2021; 243: 112716; DOI: 10.1016/j.engstruct.2021.112716.
- [52] Pettinga JD, Priestley MJN. Dynamic behavior of reinforced concrete frames designed with direct displacement – based design, *Journal of Earthquake Engineering* 2005;9:309-330.
- [53] Barbagallo F, Bosco M, Marino E, Rossi P. On the fibre modelling of beams in RC framed buildings with rigid diaphragm, *Bulletin of Earthquake Engineering* 2020;18:189-210; DOI:10.1007/s10518-019-00723-z.
- [54] Menegotto M, Pinto PE. Method of analysis for cyclically loaded RC plane frames including changes in geometry and non-elastic behaviour of elements under combined normal force and bending, IABSE: Symposium on resistance and ultimate deformability of structures acted on by well defined repeated loads 1973 – Final Report.
- [55] Filippou FC, Popov EP, Bertero VV. Effects of bond deterioration on hysteretic behavior of reinforced concrete joints, Report EERC 83-19 (1983), Earthquake Engineering Research Center, University of California, Berkeley.
- [56] OpenSeesWiki, online manual. Available online at: [https://opensees.berkeley.edu/wiki/index.php/Main\\_Page](https://opensees.berkeley.edu/wiki/index.php/Main_Page) [last access: April 2021].
- [57] Popovics S. A numerical approach to the complete stress-strain curve of concrete, *Cement and Concrete Research* 1973; 3(5): 583-599.
- [58] Almeida JP, Tarquini D, Beyer K. Modelling approaches for inelastic behaviour of RC walls: multi-level assessment and dependability of results. *Archives of Computational Methods in Engineering* 23, no. 1 (2016): 69-100; DOI:10.1007/s11831-014-9131-y.
- [59] Mpampatsikos V, Nascimbene R, Petrini L. A critical review of the R.C. frame existing building assessment procedure according to Eurocode 8 and Italian Seismic Code. *Journal of Earthquake Engineering* 2008; 12(S1), 52-82; DOI:10.1080/13632460801925020 .
- [60] Wijesundara KK, Bolognin D, Nascimbene R, Calvi GM. Review of design parameters of concentrically braced frames with RHS shape braces. *Journal of Earthquake Engineering* 2009; 13(S1), 109 – 131; DOI:10.1080/13632460902813331.

- [61] Wijesundara KK, Rassati GA, Nascimbene R, Bolognini D. Seismic performance of brace-beam-column connections in concentrically braced frames. *Structures Congress 2010*; 930-942.
- [62] Fagà E, Ceresa P, Nascimbene R, Moratti M, Pavese A. Modelling curved surface sliding bearings with bilinear constitutive law: effects on the response of seismically isolated buildings. *Materials and Structures 2016*; 49: 2179 – 2196, DOI:10.1617/s11527-015-0642-2.
- [63] Priestley MNJ, Grant DN. Viscous damping in seismic design and analysis, *Journal of Earthquake Engineering 2005*; 9:sup2, 229-255, DOI:10.1142/S1363246905002365.
- [64] Petrini L, Maggi C, Priestley MJN, Calvi GM. Experimental verification of viscous damping modeling for inelastic time history analyzes, *Journal of Earthquake Engineering 2008*; 12:S1, 125-145, DOI:10.1080/13632460801925822.
- [65] Sousa R, Almeida JP, Correia AA, Pinho R. Shake table blind prediction tests: Contributions for improved fiber-based frame modelling, *Journal of Earthquake Engineering 2020*, 24:9, 1435-1476, DOI:10.1080/13632469.2018.1466743.
- [66] Correia AA, Almeida JP, Pinho R. Seismic energy dissipation in inelastic frames: understanding state-of-the-practice damping models, *Structural Engineering International 2013*, 23:2, 148-158, DOI:10.2749/101686613X13439149157001.
- [67] Mazzoni S, McKenna F, Scott MH, Fenves GL, Jeremic B. *OpenSEES command language manual*. Pacific Earthquake Engineering Research Center, University of California, Berkeley, 2003.
- [68] Ambraseys N, Smit P, Sigbjornsson R, Suhadolc P, Margaris B. *Internet-Site for European Strong-Motion Data*, European Commission, Research-Directorate General, Environment and Climate Programme, 2002.
- [69] Iervolino I, Galasso C, Cosenza E. REXEL: computer aided record selection for code-based seismic structural analysis, *Bulletin of Earthquake Engineering 2010*;8:339-362; DOI:10.1007/s10518-009-9146-1.
- [70] Gandelli E, Quaglini V, Dubini P, Limongelli MP, Capolongo S. Seismic isolation retrofit of hospital buildings with focus on non-structural components. *International Journal of Earthquake Engineering 2018*, 35(4), 20-56.



## 2. Characterization and numerical assessment of Lead Damper

---

This Chapter includes a first paragraph presenting the evolution of energy dissipation devices, with a focus on devices of hysteretic type. Due to the increasingly large number of available devices, the work does not attempt to present a state-of-the art on the subject, but to focus on discussing the main original research efforts as well as the most relevant drawbacks.

Then, the study presents an experimental assessment of an emerging energy dissipation device, namely Lead Damper (LED), which provides a resistive force by the friction created between a lead core and a shaft. Tests are performed according to the European standard EN 15129. The damper shows a rigid-plastic behavior without strength degradation regardless of the imposed deflection; the shape of the hysteresis loops is essentially rectangular, resulting in an effective damping of 0.55; the device is able to sustain multiple cycles of motion at the basic design earthquake displacement, providing maintenance-free operation even in presence of repeated ground shakes.

The Chapter includes also an investigation about the modelling alternatives to describe the constitutive law of the LED in OpenSees.

### 2.1. State of art of energy dissipation devices

---

#### 2.1.1. General introduction: principles of energy dissipation

In accordance with the Principle of Energy Conservation, a structure hit by an earthquake is defined by the relationship

$$E_I = E_S + E_D \quad (2.1)$$

where  $E_I$  represents the input energy from the ground shaking,  $E_S$  and  $E_D$  are the energies respectively stored and dissipated by the structure.

In order to protect a structure from the damaging effects of an earthquake, it is necessary to modify one of these terms.

A possibility may be the reduction of the input energy by isolating the structure, which consists of dividing the movement of the structure itself from the movement of the ground (Figure 2-1 – right). In this way, also the right-hand side of the equation is reduced for equilibrium, and integrity of the structure is preserved. Base isolation has proved as a viable approach to protect bridges, buildings and industrial plants from earthquakes [1] but in general it is not suitable for structures resting on soft soils [2]-[5] and for high-rise buildings [6]-[8]. The use of base isolation systems is widely adopted in new structures built in high seismicity regions to reduce the geometry and reinforcement of the structural members [9], [10] and also in such buildings where the critical parameter is the protection of the contents or the operation of the structure

## 2 Characterization and numerical assessment of Lead Damper

during the seismic event and in the aftermath of an earthquake, such as hospitals or other structures of strategic importance [11]-[13]. However, the high initial costs of installation of this retrofit solution could limit the widespread of this technique in the seismic retrofit of existing buildings [14].

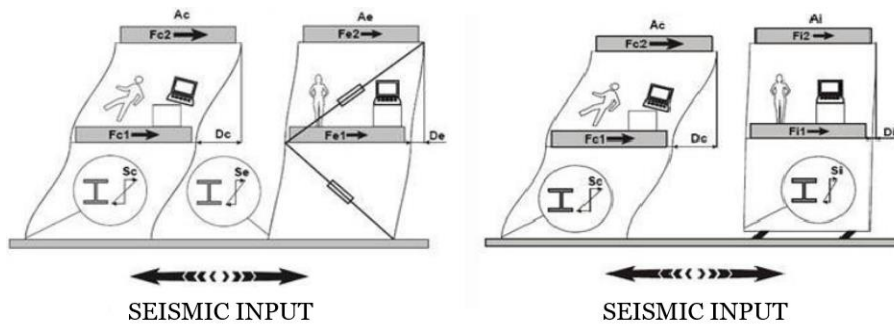


Figure 2-1: Left: comparison between a simple 2 floors building and the same building retrofitted with energy dissipation devices; right: comparison between the 2 floors building and the same building retrofitted with base isolation devices

Another option consists in increasing the dissipated energy, by inserting a special device system inside the structure (Figure 2-1 – left); this approach is aimed at achieving two effects, namely increase the structural stiffness, with consequent reduction of displacements, and dissipate much of the seismic energy, leading to a reduction of the accelerations [15] (Figure 2-2).

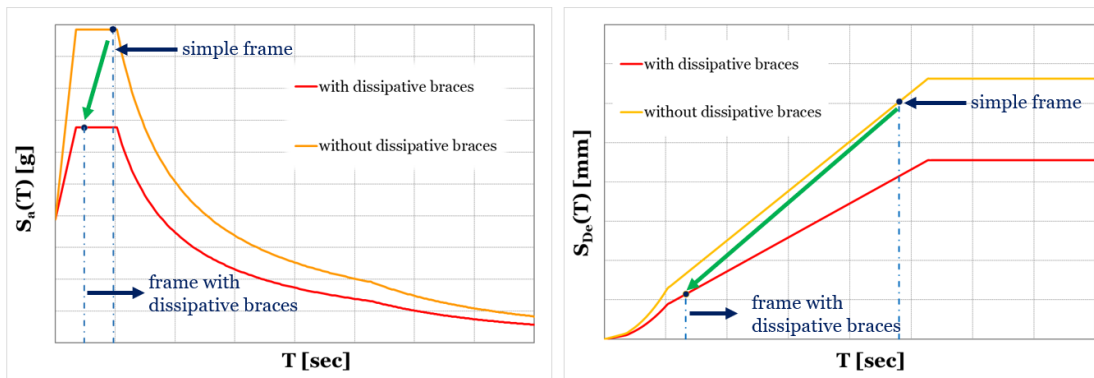


Figure 2-2: Comparison between a simple frame and a frame equipped with energy dissipation devices

Supplementary energy dissipation is employed both in new and retrofitted constructions in order to prevent structural damage, increase life-safety and achieve a desired level of performance [16], [17] appearing an appropriate and economically affordable solution to reduce the vulnerability of ordinary structures, such as residential, school and industrial buildings [18]-[21].

The hardware used to implement such strategies must fulfill strict performance requirements and its assessment is regulated by standards, like e.g., the European standard EN 15129 [22] which forms the basis for CE Marking of anti-seismic devices, compulsory within the European market.

2.1.2. Energy dissipation hardware: critical review of past studies

The concept of using separate elements to increase the damping in a structure was first postulated in the late sixties in Japan [23] and specific research on passive energy dissipation systems started less than 50 years ago in New Zealand [23], [24]. Its philosophy consists in eliminating or limiting damage to the structure by concentrating the dissipation of much of the seismic energy in elements out of the gravity framing system. Nowadays supplementary energy dissipation or damping systems are worldwide employed both in new and retrofitted constructions in order to prevent structural damage, increase life-safety and achieve a desired level of performance [16], [17].

Current energy dissipation devices can be classified in two main categories [25]. The first one includes the so-called fluid viscous dampers, where the dissipation is achieved through the lamination of a viscous fluid forced by a piston to pass through an orificing or valving system. The behavior of these devices strictly depends on the fluid velocity. Viscous fluid dampers are very versatile and can be designed to allow unconstrained slow motions (like e.g., thermal motions) as well as provide controlled damping of a structure to protect from wind load or earthquakes. The second category is represented by hysteretic dampers, which are further classified in hysteretic steel dampers, friction dampers and metal extrusion dampers, depending on the mechanism actually used to dissipate the seismic energy. The output force of these devices is essentially dependent on the deflection and independent (or only slightly dependent on velocity), and they are named as Displacement Dependent Devices (DDD). Most of the dampers used in residential, school and industrial buildings belong to the hysteretic damper's category ([17], [19], [21], [26] and [27]). The theoretical force-displacement curves of hysteretic dampers are shown in Figure 2-3, where  $N_D$  is the axial force and  $\Delta_D$  is the axial displacement of the damper, and  $N_y$  is the yield strength of the device; the area included in the curves corresponds to the energy dissipated by the device during a cycle.

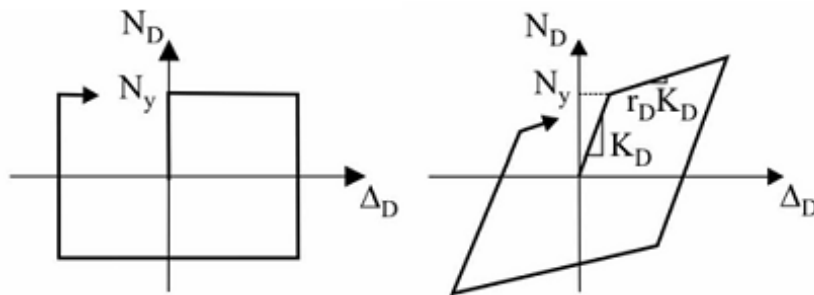


Figure 2-3: Typical constitutive law of hysteretic dampers: left, friction dampers; right, metal dampers [22]

The metallic dampers dissipate energy through the yielding of a metal, the friction dampers instead through the friction between two solid bodies sliding relative to one another, while the metal extrusion dampers through the extrusion of a metallic material.

A pioneering work on friction devices was developed in Canada in the early 1980s by Pall et al. [28], [29]. The pioneering idea of Pall consisted in protecting the main members of a structure introducing an anti-seismic system made of materials (for example steel) easily reachable and assembled in a simple geometry (Figure 2-4). Experimental results showed that the hysteretic behavior of the slipping friction joint was

## 2 Characterization and numerical assessment of Lead Damper

reliable and repeatable; for this reason, Pall carried out further research and introduced his friction device in the intersection of steel bracing, solving the drawbacks related to the performance of steel bracings. In fact, the braced frames are stiffer in order to control the lateral deflections due to wind and moderate earthquakes, but this stiffness attracts higher lateral inertial forces, and the energy dissipation capacity of the brace is very limited. Moreover, a brace in tension stretches during severe shock and buckles in compression during reversal of load. The introduction of a friction device in the intersection of the two braces guarantees that during a severe earthquake, the friction device slips, dissipating the seismic energy and preventing the buckling in compression of the bracing systems. The Pall friction bracing system has immediately found several applications for both steel and concrete buildings in new construction and retrofit of existing buildings [30]-[32], examples are the Concordia University Library in Montreal and the Canadian Space Agency Headquarters in Longueuil, Quebec.

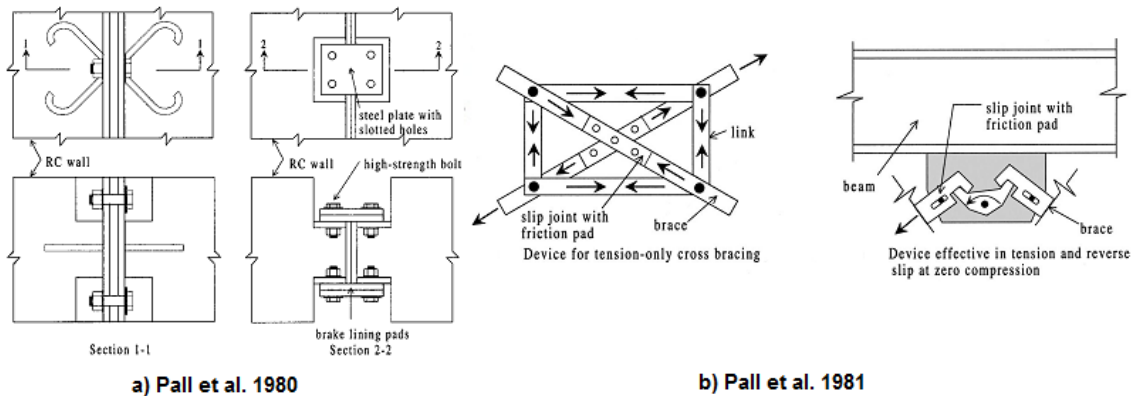


Figure 2-4: a) first friction devices introduced by Pall in 1980 [28]; b) first dissipative friction bracing system presented by Pall in 1981 [29]

Few years later, Anagnostides et al. ([33]-[35]) introduced a modification in the Pall dissipative bracing system, making a simpler design and adopting rotational friction as opposed to translational friction used by Pall. Anagnostides et al. had the merit to design a device able to guarantee a more consistent hysteretic friction behavior and easier to construct, which made the device cheaper.

The search for a simple and cost-effective device was followed by Grigorian et al. [36] who developed an improved and simpler type of friction device referred to as slotted bolted connection (SBC), which consists of a bolted connection where the elongated holes in the main connecting plate are parallel to the line of loading (Figure 2-5).

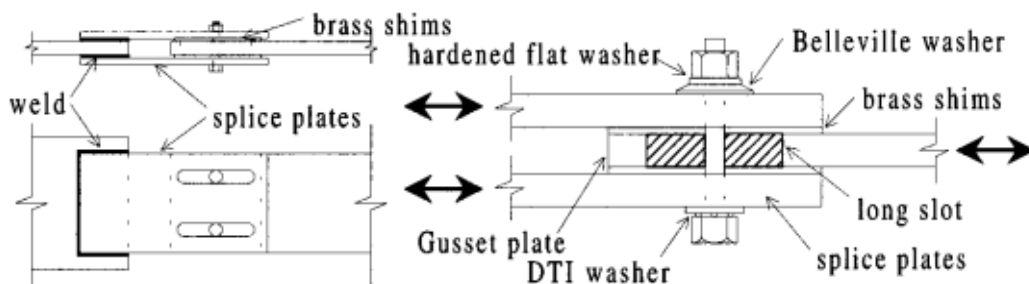


Figure 2-5: SBC, Slotted Bolted Connection [36]

This latter device pinpoints the significance of adapting and exploring the use of simpler materials and manufacture techniques for the fabrication of energy dissipation device, with the goal of producing dampers more attractive in seismic design and retrofit applications.

However, no one of these techniques has overcome the use of the brace systems, which are structurally invasive and give rise to undesired “side effects” such as significant amount of construction work, resulting in significant disturbance to the occupants, large increments in buildings weight and base shear and critical alterations to building layout [37]. For this reason, these devices have been used mainly in new constructions, where their introduction was already planned during the design stage, and rarely for the retrofit especially of the residential buildings, because of their excessive dimensions that ruin the aesthetic and architecture of the buildings [37].

In 1995, Martinez [38] highlighted the necessity of new upgrading schemes which reduce as much as possible the problems created by the structural intervention needed for retrofitting. He introduced a simple and small friction device to incorporate in the structure as a beam-column link or as a link between the base column and the ground (Figure 2-6).

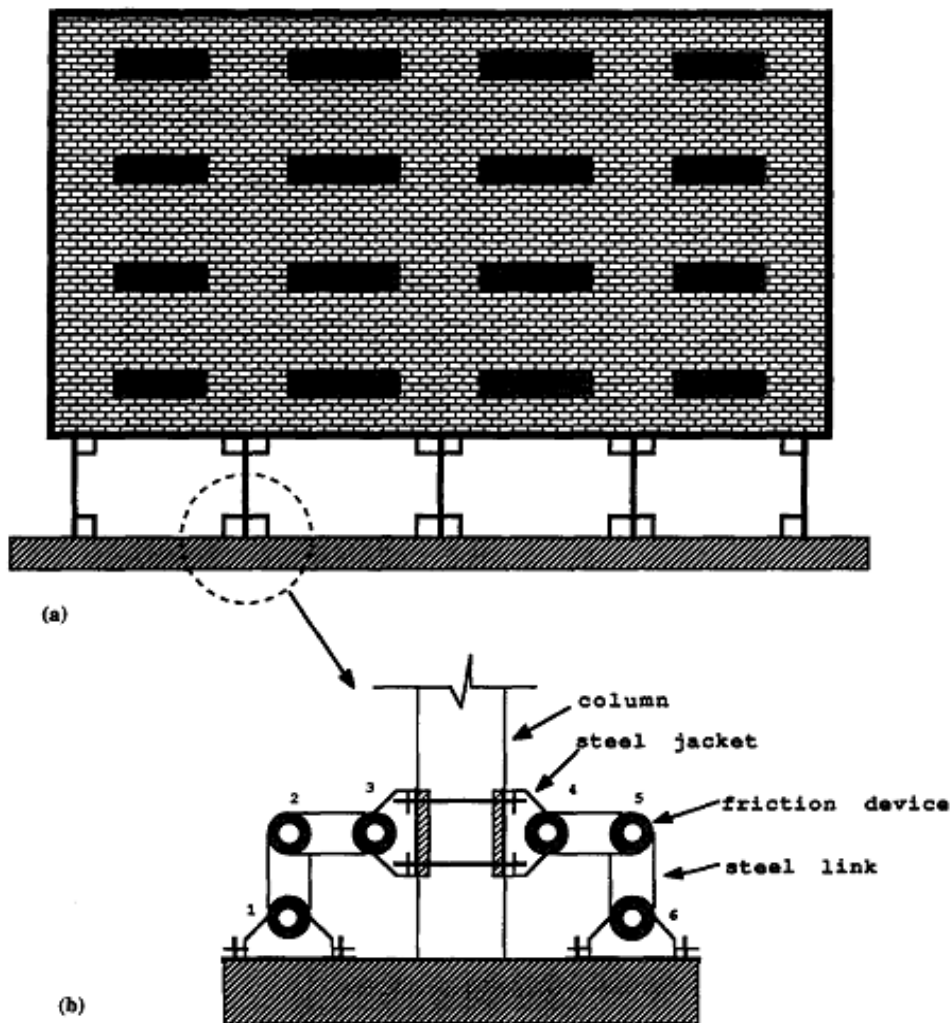


Figure 2-6: Introduction of the innovative friction dampers in the soft story building as a beam-column link and base column-ground link [39]

## 2 Characterization and numerical assessment of Lead Damper

This system was inspired by the device proposed earlier by Filiatrault [40] to incorporate in the corners of timber-sheathed wall structures. This technique showed great improvement in the hysteretic behavior of timber wall structures, without interfering with architectural or construction requirements (Figure 2-7).

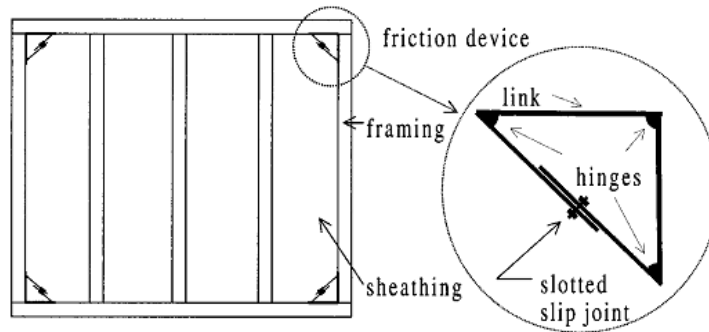


Figure 2-7: Friction device for wooden panels [40]

Martinez had the merit to extend this concept to all kind of frame structure (reinforced concrete and steel structures). He also proposed an innovative bracing system, adopting a geometry that partially solve the loss of space associated with the installation of traditional braces and favors the activation of rotational hysteretic devices at discrete locations of the braces (Figure 2-8).

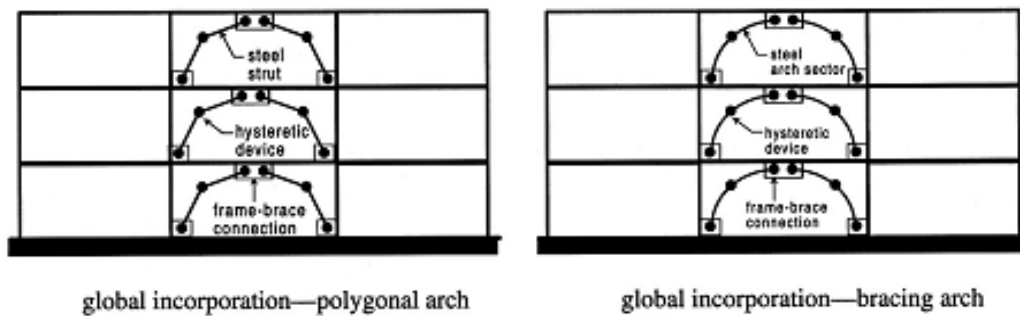


Figure 2-8: Alternative dissipative bracing systems [37]

Recently in 2010, Martinelli and Mulas [41] presented an exhaustive study of the application of this passive control technique as beam-column link and base column-ground link to reinforced concrete precast industrial buildings, followed later, in 2017, by Belleri et al.(Figure 2-9) [42]. However, these studies have not found practical application and are intended exclusively for precast industrial structures, which are just a portion of the Italian building stock, without considering a possible application also to the residential or school structures.

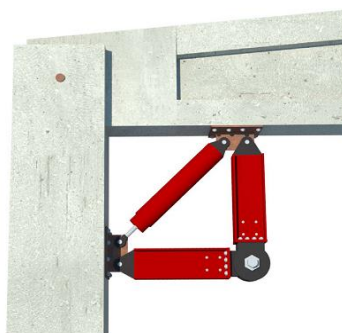


Figure 2-9: Dissipative and re-centering device [42]

Even if these more recent friction devices are low invasive anti-seismic solutions, they do not solve the problems already highlighted in their ancestor Pall friction device. Specifically, every device dissipates energy after its activation, but in case of friction devices, the activation starts when the dynamic force becomes greater than the static force acting in the contact area between the two bodies. In other words, the friction devices are designed not to move if the structure is invested by a windstorm or by weak vibrations from the ground and to dissipate a great amount of energy during strong earthquakes [37]. If a relatively weak earthquake occurs and the static force is greater than the seismic one, the dissipative system does not work, and this has detrimental consequences to the structure, especially to acceleration-sensitive non-structural components [20], [43]. In fact, after the insertion of the anti-seismic systems, the structure is stiffer than the original one, so it is invested by higher lateral forces, possibly causing damages to the main structural elements. Moreover, even in the case of activation, the dissipation is due to the slippage or the rotation of two bodies, causing wear phenomena. The wear may change the characteristics of friction of the sliding interface, modifying also the constitutive law of the device. After a strong shock, the device is compromised and needs repair or replacement, which are invasive actions especially in the cases of dissipative devices inserted in a bracing system. In addition, the metal surfaces are influenced by corrosion and contaminants that cause an increase in surface roughness; as a consequence, the static force increases and may cause a late activation of the devices under a strong earthquake. Finally, another non negligible problem is the relaxation of the bolt load that provides the adequate pressure contact among the two sliding bodies. Kulak et al. [44] intensively studied the behavior of preload bolts, showing an exponential decrease in time of the rate of change in bolt load.

The portfolios of the main European productors (such as FIP, Maurer, Mageba) include hysteretic dampers based on yielding of mild steel cores, while friction dampers are disregarded. Steel dampers are indeed the most popular system adopted for retrofitting residential, school and industrial buildings all around the world [18]-[21], and especially in Italy.

The development of hysteretic yielding devices started in New Zealand in the early 1970s to introduce additional damping to the base isolation systems (an example is in Figure 2-10).

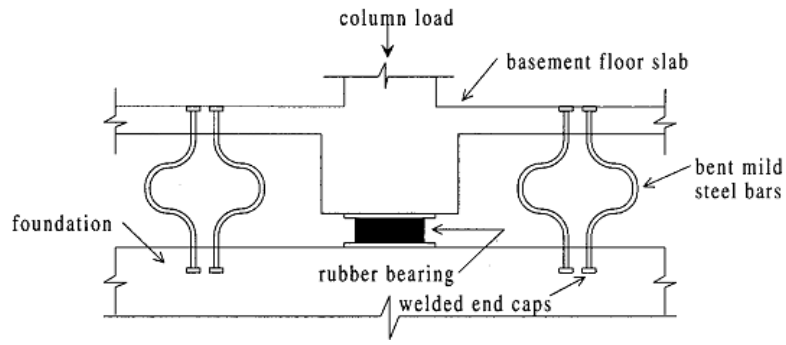


Figure 2-10: Bent mild steel bars as energy dissipation device in base isolation [2]

In Japan, Wakabayashi et al. [45], [46] conducted the first pioneering researches on the BRB, Buckling Restrained Brace, consisting of a steel core encased in a steel tube filled with concrete (Figure 2-11).

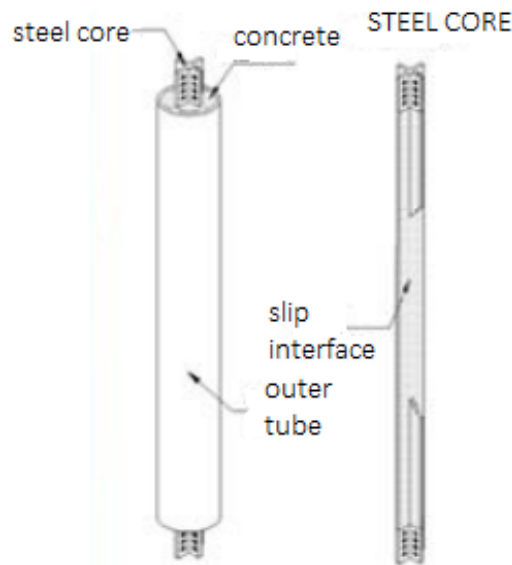


Figure 2-11: Buckling Restrained Brace - BRB

The valuable improvement of BRB over conventional braces is in their ability to carry load, yield and thus dissipate a great amount of energy when loaded in both tension and compression (Figure 2-12), whereas conventional braces achieve their full displacement capacity accompanied by yielding when they are loaded in tension, but buckle without dissipating substantial amount of energy when loaded in compression.

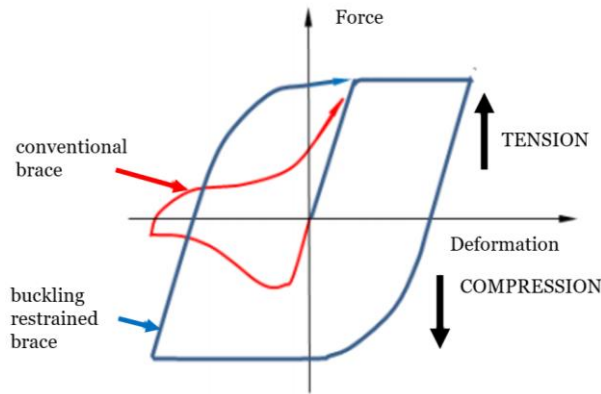


Figure 2-12: Behavior of Conventional Brace versus Buckling-Restrained Brace under tension/compression loads

The stable energy dissipation capacity of BRBs makes them very attractive for seismic protection applications; Figure 2-13 shows some examples of commercial BRBs currently available and implemented.



Figure 2-13: Commercial BRBs [47]-[49]

The advantage of BRBs over friction dampers is in their independence on the environmental factors and ageing components; in fact, the steel core is protected and does not need specific treatments or periodical maintenance. Moreover, differently from the friction dampers, BRBs guarantee a good energy dissipation capacity even for moderate seismic events.

Unfortunately, they are characterized by invasive structural dimensions and even if several solutions with reduced geometry have been studied [50] and commercially implemented (Figure 2-13), no one has eliminated the necessity of insertion in a bracing system, so also BRBs dramatically alter the architecture of a structure, Figure 2-14.

In addition, because of low-cycle fatigue and residual stresses of steel dampers, or large permanent deformations of friction and extrusion dampers, after severe earthquake, both hysteretic dampers need to be replaced or restated, with consequent costs (due also to the eventual interruption of the building function, painful for industrial and school buildings) but also with a potential threat to the safety of the structure, which is left exposed to aftershocks which may occur in the aftermath of the main event.



Figure 2-14: Examples of retrofit of school buildings with BRBs: a) Giacomo Leopardi school, Ancona; b) Liceo Capialdi, Vibo Valentia

It is worth mentioning that neither friction dampers nor yielding dampers have re-centering capacity: they do not guarantee that the structure will return to its original configuration after a shocking event and excessive residual deformations can even result in the total loss of a structure.

Nowadays, the current design approaches aim to resilient communities, where not only the life safety is guaranteed but also the buildings survive with no disturbance to business operation; it is clear that both friction and steel dampers (such as BRBs) do not satisfy this requirement.

The Shape Memory Alloys (SMA) are characterized by a flag-shaped hysteresis curve (Figure 2-15). The amount of energy dissipation is reduced compared to that of the other hysteretic systems, but the system returns to the zero-force, zero-displacement point at every cycle, and more importantly, at the end of the seismic loading.



Figure 2-15: Re-centering devices, [22]

The SMA are particularly sensitive to the temperature and frequency variations (Figure 2-16), for this reason, they need to be used in a controlled environment.

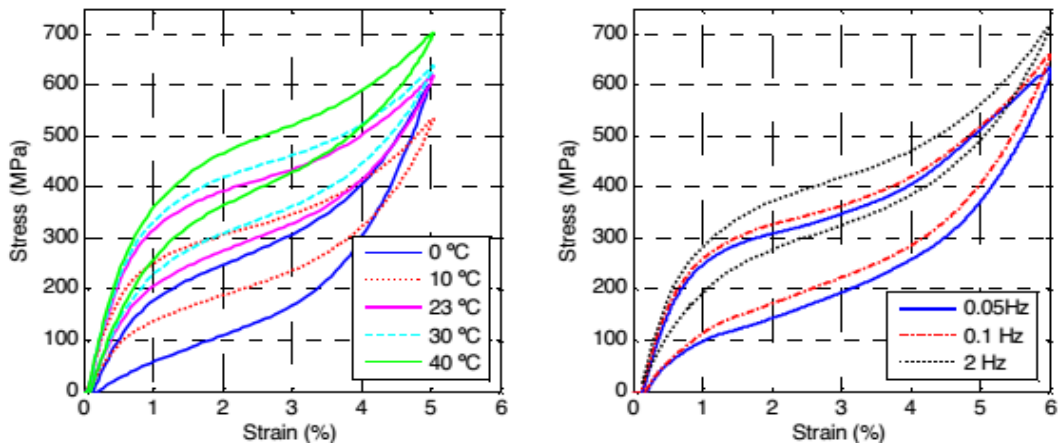


Figure 2-16: Effect of temperature and loading rate on superelastic behavior of SMA [51]

Currently, among the European manufacturers, only FIP has a SMA device in its portfolio, which was employed, to the knowledge of the Writer, only in Basilica di San Francesco in Assisi after the 1997 earthquake (Figure 2-17); the low spread of SMA-based dampers is caused by the high cost of the raw material, which justifies its use only for applications to high value buildings, such as the retrofit heritage buildings. Few studies ([52], [53]) have been recently developed about the use of SMA as anti-seismic system in civil structures, but they include the SMA within a bracing system, facing the problems already presented.



Figure 2-17: Retrofit of Basilica di San Francesco di Assisi with SMA devices

It is important to mention another issue that concerns the current hysteretic dampers: the design of dissipative bracing systems is performed respecting the “structural safety requirement” at the Ultimate Limit State only [17], [54]-[57]; indeed, the devices are designed not to be engaged under normal service loads and weak seismic excitations [37], since the dynamic force does not reach the yield force  $N_y$  (Figure 2-3), associated to e.g., yielding of a steel core or static friction between sliding surfaces. Consequently, under small earthquakes, a structure equipped with dissipative braces is subjected to greater accelerations than the bare configuration [20]. Moreover, tests carried out at the University of Basilicata (Italy)[58] have shown that the significant reduction of the frame lateral deformation, brought by the introduction of the hysteretic braces, is counteracted by a huge increase of Peak Floor Accelerations [20]. Similar results were obtained also from the numerical analyses performed by Gandelli et al. [43] on a hospital building equipped with dissipative bracing systems. This phenomenon has detrimental consequences especially to acceleration-sensitive non-

## 2 Characterization and numerical assessment of Lead Damper

structural components [20], [43]. In recent years, some researchers suggested using new kind of systems to control multi-levels of earthquake energy [21], to achieve stable deformation, increase structural ductility, and increase energy dissipation capacity with different stiffnesses [59], [60]. For example, Balendra et al. [61] suggested a two-level damper to control both severe earthquakes and wind and moderate earthquakes, Gandelli et al. [20] proposed an Adaptive Hysteretic Damper (AHD), capable to modulate its effective damping and stiffness based on the intensity level of the ongoing earthquake, while Palermo et al. [62] presented a Crescent Shaped Brace (CSB), which is characterized by a geometrical configuration defined in order to provide the structure with prescribed multiple seismic performances, within the performance based seismic design framework.

In conclusion, a more robust form of energy dissipation is needed that satisfies several objectives [63]: (i) more compact and architecturally less invasive design in order to be ideally located within the beam-column joint region; (ii) should not require maintenance after a major earthquake, in order to guarantee a high safety level and maintain an economical appeal, especially for the retrofitting of conventional buildings; (iii) should not be at risk of low-cycle fatigue bar fracture; (iv) should ensure the re-centering of the structure; residual forces in the energy dissipator should either re-center or creep back towards zero over time; and (iv) the cost of devices should be economical compared with conventional design solutions.

A hysteretic dissipation system that deserves a deeper analysis is the lead extrusion device ([64]-[66]), whose basic mechanism is depicted in Figure 2-18. A lead volume is confined into a tube where an orifice is created by an annular restriction, which is provided either from a constriction of the tube (a), or a bulged shaft (b). As the shaft is displaced, the lead is forced to flow through the annular restriction. This plastic flow adsorbs a large amount of energy, due to the shearing and plastic deformation of the material [67], providing high resistive forces. A part of the energy required to produce the plastic deformation of lead is immediately dissipated as heat, while some of the energy is stored in the deformed lead which quickly recrystallizes and regains its original properties [68], [69], resulting in consistent force across multiple cycles of response without any strain hardening or loss of strength or stiffness [65].

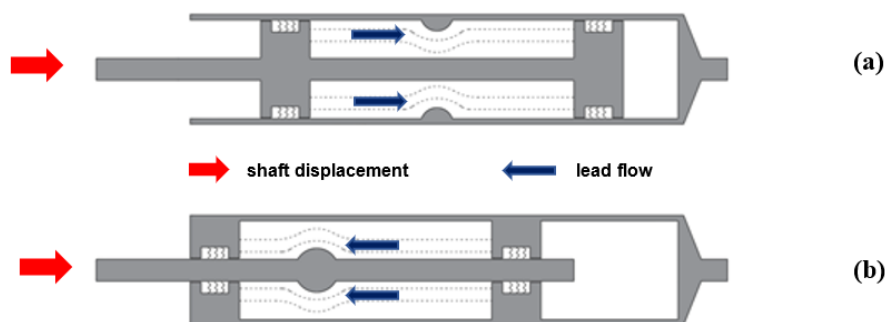


Figure 2-18: Longitudinal sections of lead extrusion damper: (a) constricted tube type; (b) bulged shaft type. Adapted from [70]

Lead extrusion dampers have been reported to present an essentially rectangular hysteretic curve, which maximizes the amount of energy dissipation for a given applied force and displacement [71], Figure 2-19.

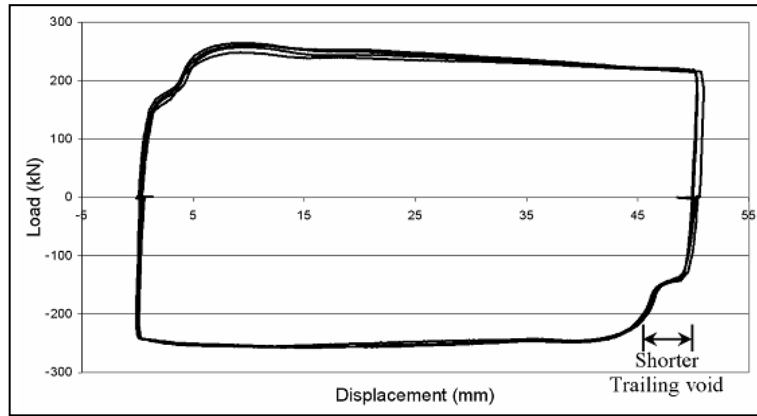


Figure 2-19: Hysteresis loop of lead extrusion damper [71]

### 2.2. Lead extrusion dampers

Lead extrusion dampers were first introduced as a passive energy dissipation device in the mid '70s in New Zealand [65]. These devices were volumetrically very large (Figure 2-20) and consequently, relatively expensive to produce; for this reason, their use was mainly limited as part of base isolation systems.

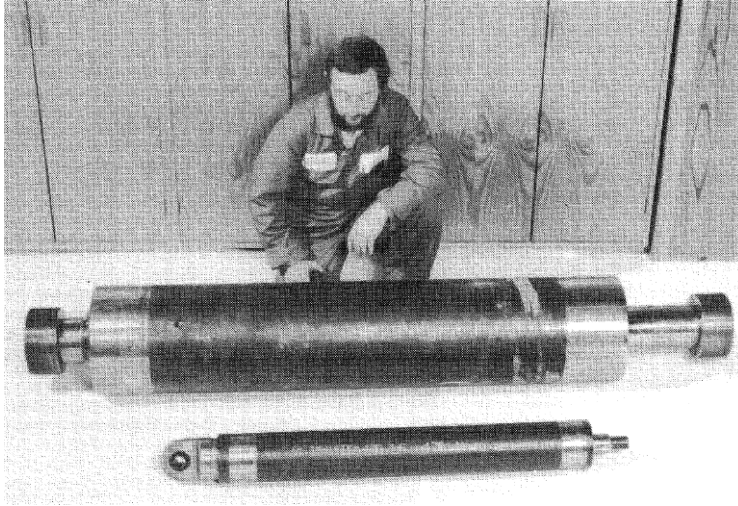


Figure 2-20: Lead extrusion devices with 100kN and 700kN force capacity [70]

After Robinson and Greenbank, the researcher that mostly worked on this topic was Rodgers, starting from 2006 [71]. Rodgers and his research group picked the bulged-shaft design because of its simplicity of manufacture and consequent low-cost and proposed a damper able to fit into confined spaces (Figure 2-21) within and around structural connections [72]. This device was called HF2V, lead-extrusion-based high force-to-volume device.

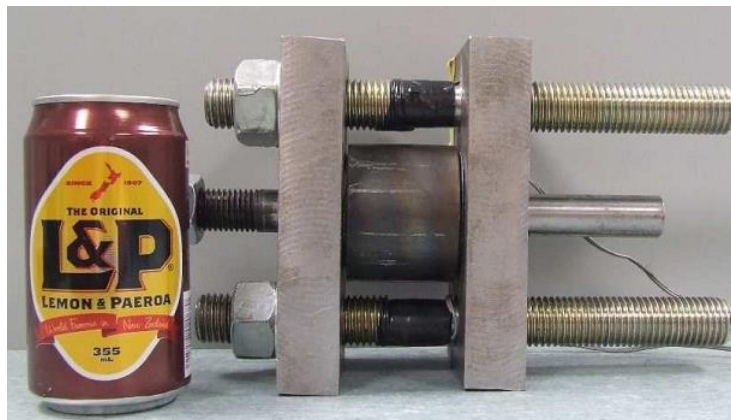


Figure 2-21: Damper photograph with 355ml soft drink for scale [72]

To forces of 100-350 kN corresponded compact dimensions, considerably smaller than other devices of similar capacities (Figure 2-21 and Figure 2-22), that made possible its inclusion within the beam-column joints of both steel and concrete structures [72]-[81]. This solution was proposed as a valid alternative to other retrofitting strategies used at that time, for example the mild steel rods proposed for the first time by Stanton et al. [82]. Rodgers studied both analytically and experimentally the application of this device within

the structural connection of precast structures ([63], [73], [83] and [84]) and steel structures ([72], [85] and [86]), showing that it could provide a level of energy dissipation comparable to, or in excess of, mild steel devices designed for the same yield force, without encountering any fatigue problem experienced by the alternative solutions. Moreover, because of low-cycle fatigue and residual stresses, mild steel energy dissipation systems needed replacement after an earthquake, while the lead damper did not need any maintenance and thanks to its ability of creeping out over time, ensured self-centering of any structure.

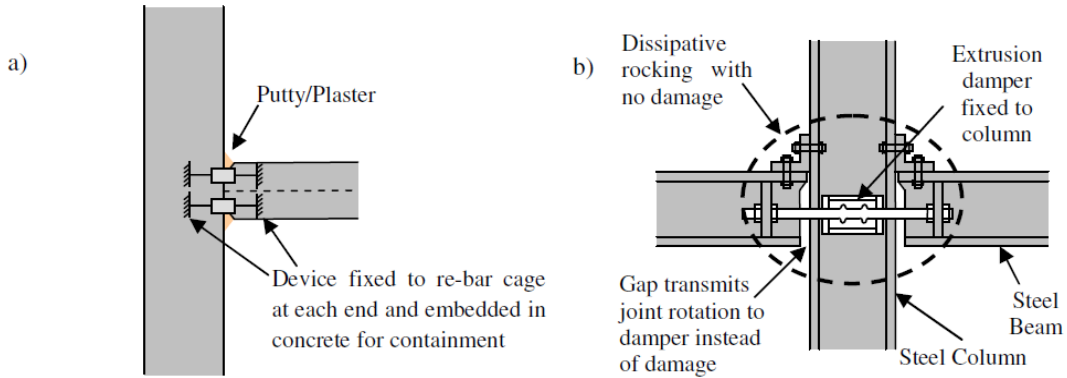


Figure 2-22: Schematic representation of lead extrusion damper placement into (a) reinforced beam-column connection and (b) steel beam-column connection [87]

Referring to the case of steel structures, Figure 2-23 shows the improvements in terms of energy dissipation between a standard purely bolted connection and the same connection equipped with the lead extrusion damper; even better performance can be achieved where the connection is equipped with the damper and made stiffer by welding the angles to the beam and column.

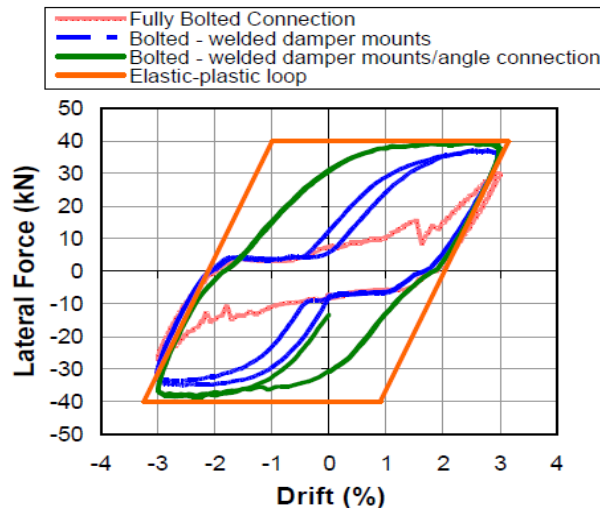


Figure 2-23: Effect of different types of connections on the hysteresis response of the beam-column joint connection with HF2V device [75]

Similar conclusions were obtained from the studies on precast concrete systems ([63], [73], [83] and [84]). Compact devices capable of being fitted directly into a structural connection were mounted across a beam-column joint (Figure 2-24); the tests showed that the dampers were able to provide consistent force on every

## 2 Characterization and numerical assessment of Lead Damper

(repeated) cycle and far greater energy dissipation than the bare connection: Figure 2-25 shows that the joint hysteresis loops are substantially larger when the dampers are present.



Figure 2-24: Left: lead extrusion damper externally mounted to the seismic beam; right: photograph of test specimen [73]

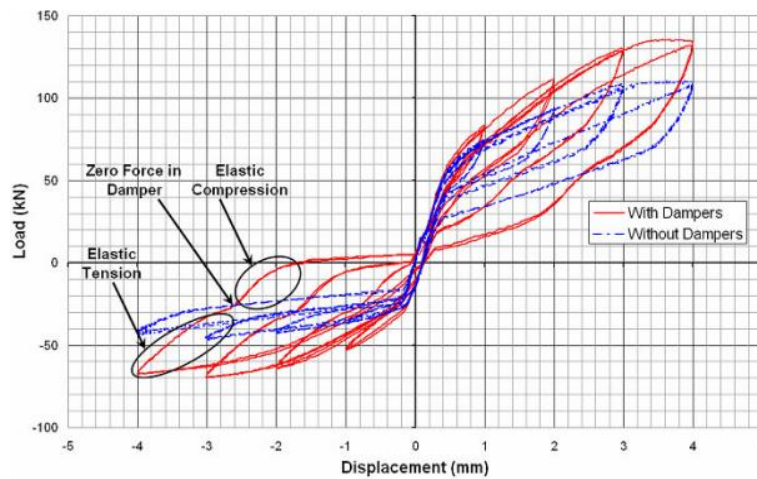


Figure 2-25: Comparison of joint hysteresis with and without dampers for corner joint set-up with increased damping for loading at 1, 2, 3 and 4% drift [63]

Two issues were reported to affect the performance of the lead extrusion damper [74]. The first is the heat build-up promoted by energy dissipation, which induces softening of the working material and reduces its strength; thus, the reaction force and the energy absorption decrease as the cycles proceed and the damper warms up. However, the effect is temporary, because when the device is allowed to cool down, the original value of resistive force is recovered. A second issue is the formation of voids within the working material during extrusion, which is attributed to compression of the lead: as the shaft moves, the material is compressed into a smaller volume leading to the formation of a trailing void. As the bulge passes through this void, the damper experiences less resistance and dissipates less energy. Lead extrusion dampers used in the first structural applications were therefore quite large, in order to provide sufficient reaction force.

In 2007, Rodgers et al. [74] performed a parametric study considering different sizes of bulges on a device with a 66 mm internal cylinder diameter, in order to determine the best combination of bulge and cylinder diameters. Moreover, a 400 kN force was applied to some devices after the solidification of the as-cast lead within the cylinder, in order to put a residual compressive stress on the material and examine the effect of

prestressing on the lead and the corresponding effect on the peak force achieved. The results showed the prestress made the hysteresis loop more optimally “square” and the resistive forces higher, leading to a general increase of the energy dissipated (Figure 2-26).

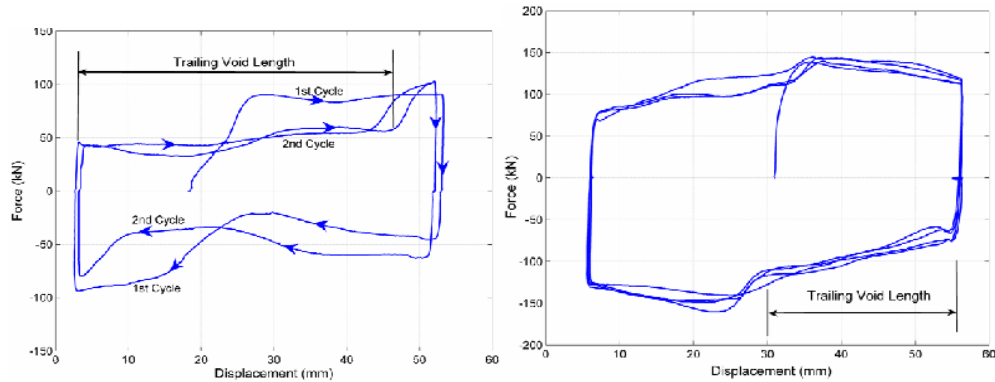


Figure 2-26: Hysteresis loops for 40 mm diameter bulge device: left, without prestressing of the lead; right, with 400kN compression force applied to the device [74]

Regarding the degradation of the hysteresis caused by the heating of the working material, cyclic experiments showed that any notable effects would be produced for the 3-4 large cycles that are likely to occur during an earthquake [74]; moreover, these effects are temporary, since the strength capacity would be restored once the device cools down [88].

### 2.2.1. Design modelling of lead extrusion dampers

A controversial aspect is associated to the equation used to describe the constitutive law of the lead extrusion damper. The device has always showed a weak velocity dependence [89], that has been confirmed also in more recent studies ([88], [90]) and a strong dependence on displacement. However, the equation usually presented to characterize the constitutive behavior of this device is the classical force-velocity relationship defined for fluid viscous devices:

$$F = C_{\alpha} \dot{x}^{\alpha} \quad (2.2)$$

where

$F$  is the extrusion damper force;

$\dot{x}$  is the velocity of the shaft;

$\alpha$  is the velocity coefficient which is a constant value;

$C_{\alpha}$  is the damper constant determined by physical prototype testing.

Golodrino et al. [90] tested different devices with straight, bulged and constricted shaft configurations subjected to velocities of 0.15-5.0 mm/s and concluded that the velocity dependence was relevant for velocity's range of 0.15-1.0 mm/s; after 1.0 mm/s the behavior was almost insensitive to the variation of the

## 2 Characterization and numerical assessment of Lead Damper

velocity (Figure 2-27). For this reason, an exponential bilinear model was suggested, characterized by a velocity exponent of 0.12 for velocities less than 1.0 mm/s and between 0.065 - 0.07 mm/s for velocities in the range 1.0-5.0 mm/s, depending on the shape of the shaft (straight, bulged or constricted).

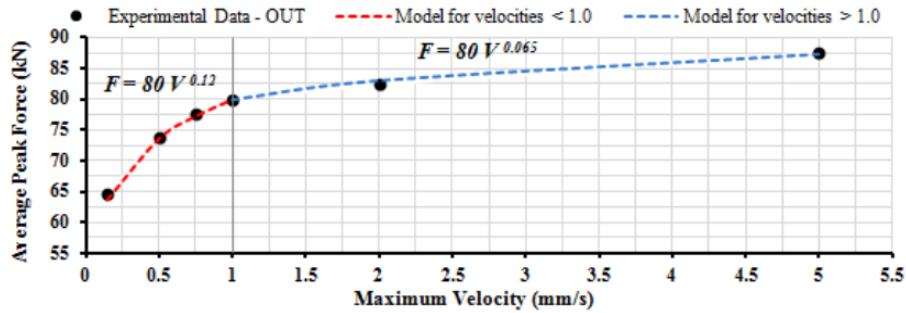


Figure 2-27: Lead extrusion device with 12 mm bulged shaft [90]

Another difficult point is the definition of a design model capable to characterize the damper. The first attempt came from Pearsons et al. [91] who gave a relationship between the force and associated cylinder and orifice areas during an extrusion process:

$$F = \left\{ Y \ln \left( \frac{A}{a} \right) + Y \right\} \exp(m) - Y (A - a) \quad (2.3)$$

where

$F$  is the extrusion force;

$Y$  is the yield strength for the working material;

$A$  is the annular area around the shaft (Figure 2-28)

$a$  is the annular area of orifice (Figure 2-28)

$(A - a)$  represents the projected face area of the bulge over which direct stress is applied to the shaft;

$m$  is a constant specific to the extrusion process, equal to  $\frac{4\mu L}{D}$ , where  $\mu$  is the coefficient of friction between the working material and the steel shaft,  $L$  is the length of the shaft in sliding contact with the working material and device end caps and  $D$  is the effective diameter corresponding to annular lead area  $A$ .

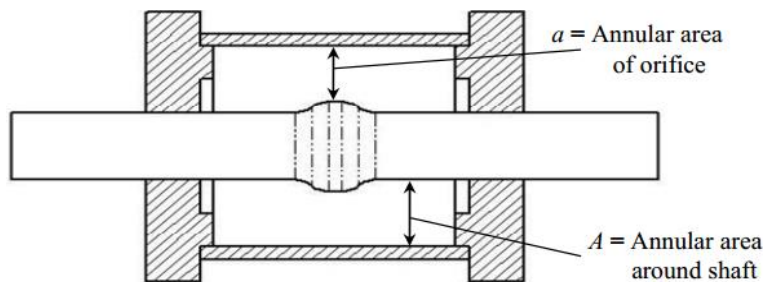


Figure 2-28: Schematic representation of the first device, showing the annular area of orifice and the annular area around shaft [74]

This model was valid for a classic extrusion process and the model parameters did not translate directly to the parameters of the lead extrusion dampers. Rodgers started from the Pearson's equation and studied an experimental relationship independent of the device scale, finding a relatively strong linear relationship for all experimental results (Figure 2-29).

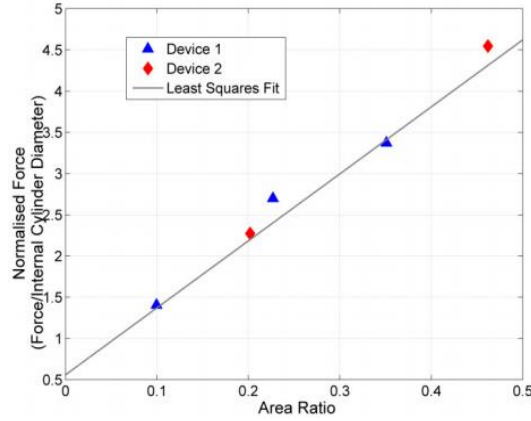


Figure 2-29: Normalized Force vs Area Ratio for all devices [74]

As an alternative to the extrusion theory, he also proposed a more straightforward stress-based model, implementing the Mohr-Coulomb failure criteria for a quasi-brittle material:

$$D_D = \tau_D A_{shaft} + \sigma_0 A_{bulge} \quad (2.4)$$

where

$D_D$  is the resistive force of the device;

$\tau_D$  is the shear stress due to the load between the shaft and the lead;

$\sigma_0$  is the direct stress imposed on the bulge face area;

$A_{shaft}$  is the surface area of the shaft;

$A_{bulge}$  is the annular area of the bulge.

Later, Vishnupriya et al. [92], deeply studied design models based on the sum of friction and extrusion forces modelled as a function of device dimensions (area ratio AR, surface area SA and bulge area AB), analyzing 14 linear and linear-quadratic models using regression analysis on data from 18 experimental devices with and without bulges on the central shaft (Table 2-1).

## 2 Characterization and numerical assessment of Lead Damper

$F =$	$\alpha_0 AR$	$\alpha_1 SA$	–	–	–
$F =$	$\alpha_0 AR D_{cyl}$	$\alpha_1 SA$	–	–	–
$F =$	$\alpha_0 AR$	$\alpha_1 SA$	$\alpha_2 AB$	–	–
$F =$	$\alpha_0 AR D_{cyl}$	$\alpha_1 SA$	$\alpha_2 AB$	–	–
$F =$	$\alpha_0 AR D_{blg}$	$\alpha_1 SA$	–	–	–
$F =$	$\alpha_0 AR D_{cyl}^2$	$\alpha_1 SA$	–	–	–
$F =$	$\alpha_0 AR D_{cyl}^2$	$\alpha_1 SA$	$\alpha_2 AB$	–	–
$F =$	$\alpha_0 AR$	$\alpha_1 SA$	–	$\alpha_3 AR^2$	–
$F =$	$\alpha_0 AR D_{cyl}$	$\alpha_1 SA$	–	$\alpha_3 AR^2$	–
$F =$	$\alpha_0 AR D_{cyl}^2$	$\alpha_1 SA$	–	$\alpha_3 AR^2$	–
$F =$	$\alpha_0 AR D_{cyl}^2$	$\alpha_1 SA$	–	$\alpha_3 AR^2 D_{cyl}^2$	–
$F =$	$\alpha_0 AR$	$\alpha_1 SA$	$\alpha_2 AB$	$\alpha_3 AR^2$	–
$F =$	$\alpha_0 AR$	$\alpha_1 SA$	–	$\alpha_3 AR^2$	$\alpha_4 SA^2$
$F =$	$\alpha_0 AR$	$\alpha_1 SA$	–	–	–

Note:  $AR$  area ratio;  $SA$  surface area;  $AB$  bulge area;  $D_{cyl}$  cylinder diameter;  $D_{blg}$  bulge diameter;  $L_{cyl}$  cylinder length;  $\alpha_0, \alpha_1, \alpha_2, \alpha_3$  weighting coefficients identified by fitting the models to experimental device data

Table 2-1: Potential model investigated [92]

He identified two very good models, from which one ( $F = \alpha_0 AR D_{cyl} + \alpha_1 SA + \alpha_2 AB$ ) was slightly better, since it produced the highest  $R^2 = 0.91$ .

2.2.2. Applications of lead extrusion dampers in real structures

To the Writer’s knowledge, there is just one published application of the Rodgers’s HF2V technology in the Kilmore Street Medical Center (now named Forte ‘Health) in New Zealand. It is predominantly a steel structure where the suspended composite floors slabs are supported by eight sets of coupled steel posttensioned braced frames around the perimeter to provide lateral load resistance (Figure 2-30).

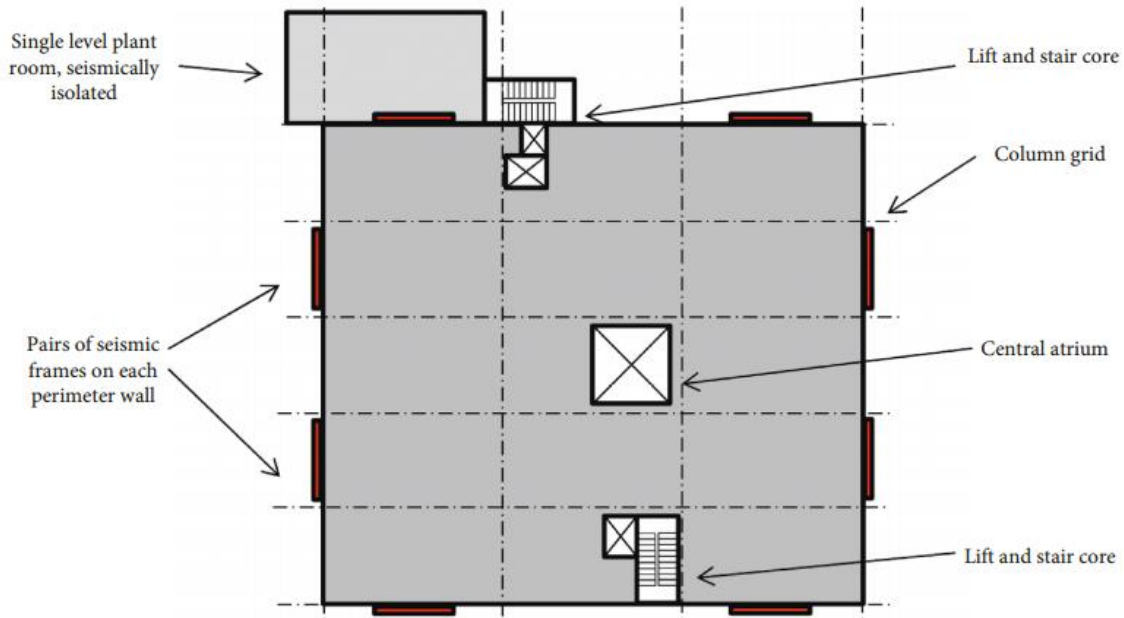


Figure 2-30: Plan view of Kilmore Street Medical Center showing 8 pairs of rocking frames [88]



Figure 2-31: Left: pair of steel braced frames assembled in the workshop with dampers; right: pair of steel braced frames erected on-site [93]

The HF2V devices are included within an “Advanced-Flag Shape” system, which is a hybrid system (Figure 2-32) that allow controlled rocking of the structure in order to reduce damage to the primary structural elements themselves. The energy dissipation occurs at the rocking interface thanks to the HF2V dampers, while un-bonded post-tensioned tendons or bars provide a restoring and self-centering force; the braced frames and post-tensioned bars are designed to remain elastic [93].

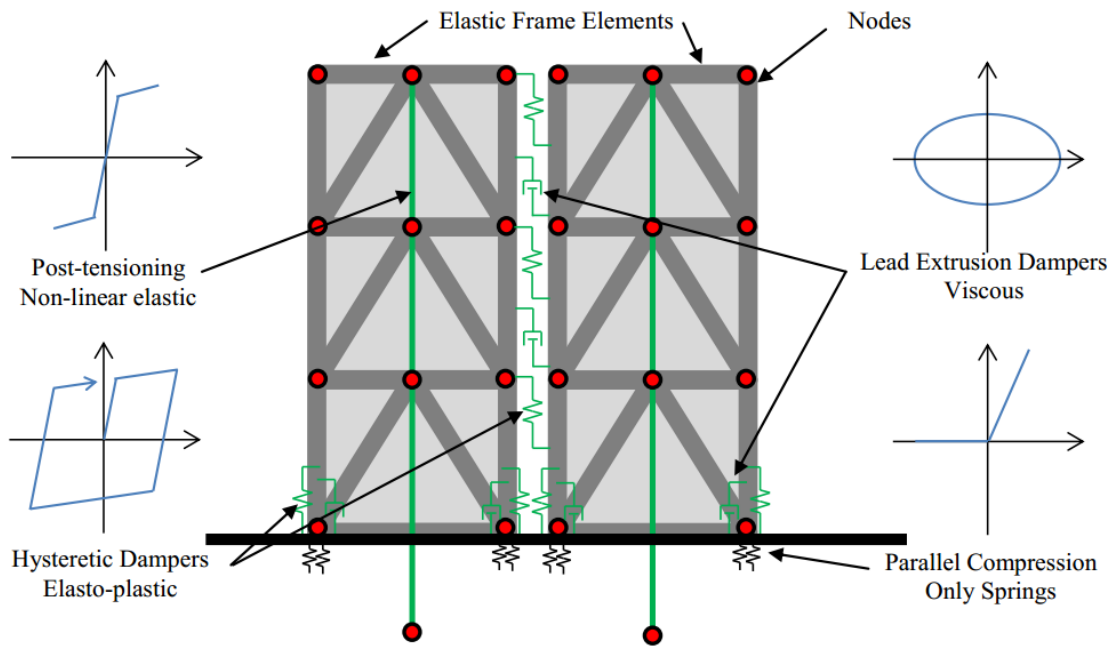


Figure 2-32: Idealized analysis model of coupled frame system [93]

The use of rocking systems equipped with HF2V damping devices was investigated also by Wrzesniak et al. [94], who were the first studying the applicability of these dampers in rocking timber structures, indicating that the devices represent a structurally feasible and cost-effective solution also for rocking timber structures.

Other authors studied the application of the lead extrusion device within both steel and RC structures. Mander et al. [86], for example, studied the application of an HF2V device within the beam-column joints of new steel structures. Two locations for mounting the dampers were investigated: one damper below the bottom flange and two concealed dampers mounted above the bottom beam flange. The research showed that in both cases no damage was experienced by the main structural beam and column elements, since the dissipation was concentrated on the devices, which achieved a far greater dissipative efficiency compared to conventional steel frame connections.

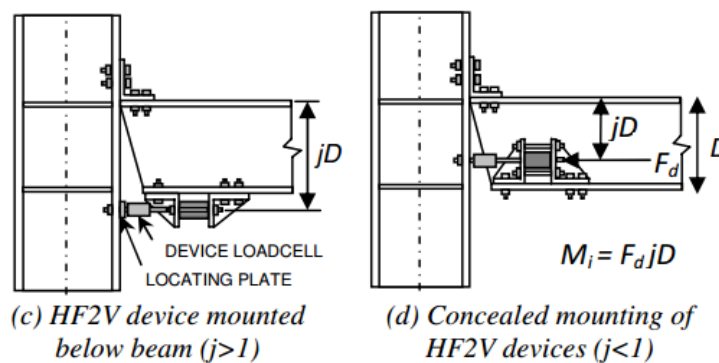


Figure 2-33: Two possible configurations of steel beam-column joint equipped with HF2V [86]

The interest to include lead extrusion dampers within new steel structures in order to achieve damage-free connections and reduced repairs was addressed also by Bacht et al. [95] and Desombre et al. [85]. Both works analyzed steel moment resisting frames designed within the SAC Steel Project, with the goal to present a

new design approach to minimize damage to steel moment frame buildings in future earthquakes. The SAC Project was primarily concerned with the impact of connection fractures of steel moment resisting frames in nine buildings, with three, nine and twenty stories designed for Los Angeles, Seattle and Boston locations [95].

In Bacht et al. [95], the three-story steel frame extracted from the building designed for Los Angeles (also called SAC-3 or LA-3) was analyzed by means of different models representing the structure as designed and the structure equipped with HF2V devices within the beam-column connections. The results confirmed the conclusions of the previous works of Rodgers et al. ([63], [72], [77], [79] and [80]) and Mander et al. [86]: the combination of HF2V dissipators with gravity frames and well-designed non-structural elements creates a system superior to conventional construction methods, able to experience almost no structural damage and low residual displacements after a seismic event. The work of Desombre et al. [85] aimed to model the behavior of HF2V devices included in steel connections, using a simple finite element (FE) model in ABAQUS [96]. The research produced two models: one simpler model that allows computationally efficient non-linear analysis of large structures with many degrees of freedom, and a more complex and physically accurate axial model, which allows detailed analysis of joint connection architecture.

The improvement in the seismic response of existing structures with lead extrusion dampers was investigated by Soydan and co-workers ([97]-[100]). Their research demonstrated that the retrofitting of existing steel and precast RC structures through the inclusion of the system within beam-column connections resulted in a significant increase of the lateral stiffness of the construction, a substantial reduction of the displacement and a notable increase of the dissipated energy. Moreover, thanks to the small dimensions of the damper, the inclusion at the beam-column connections allowed to overcome the architectural issues posed by the braces, like interference with the design of the façade and position of the openings [37].

Other studies considered the application of the lead extrusion dampers as a connection between two parallel structures [101] or a retrofitting strategy for large-span reticulated shell [102], exploring the viability of the damper to control the structural responses to a seismic shock of different structures from conventional precast RC and steel frames and with a method of installation different from the inclusion within a steel brace and a beam-column joint, already studied by other authors (e.g. [72], [85] and [95]).

The interest to the lead extrusion device brought other research groups to develop this technology and implement a new kind of energy dissipation devices, whose mechanism was based on the lead extrusion. Examples are the dampers presented by Zhang et al. [103] and by Yan et al. [104]. Zhang et al. [103] introduced the CLEMR damper, a new kind of combined lead extrusion magnetorheological damper, that was applied on a RC frame structure subjected to time-history analysis, showing significant beneficial effects. Yan et al. [104] introduced a new lead extrusion and friction composite damper (LEFCD), which is an assembly of components that are changeable and can provide specific performances (Figure 2-34): in particular, for strong earthquakes the LEFCD uses both the lead extrusion and friction dampers simultaneously.

## 2 Characterization and numerical assessment of Lead Damper

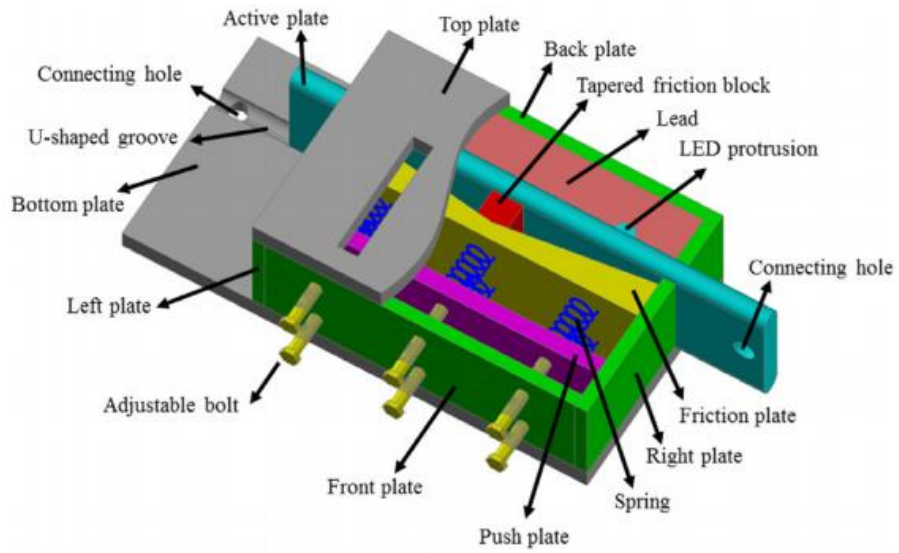


Figure 2-34: 3D view of the LEFCD [104]

## 2.3. Experimental investigation

### 2.3.1. Description of the LED prototype

A prototype of the prestressed Lead Damper has been experimentally investigated in the study. The prototype has four main components, namely the shaft, the tube, the cap and the working material (Figure 2-35).

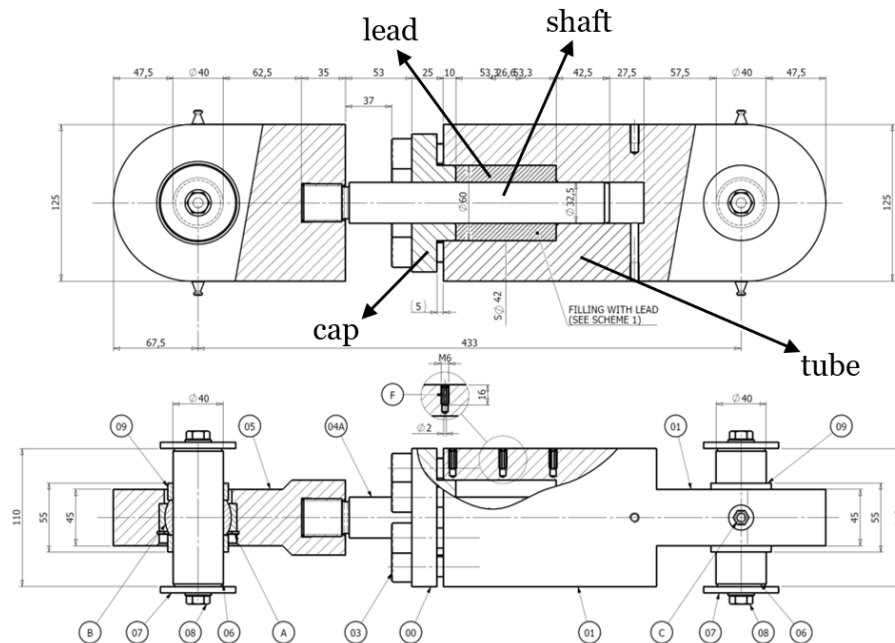


Figure 2-35: Cross-section of the LED prototype

Tube, shaft and cap are made of structural steel, while the working material is 99.99% pure lead. The shaft is plated with hard chromium ( $70 \mu\text{m}$  thickness) in order to minimize friction and wear during sliding through the bushing provided in the cap. The cap is fixed to the tube wall by means of eight screws.

The prototype features a shaft diameter  $D_s = 32.5 \text{ mm}$ , an inner diameter of the tube  $D_{cyl} = 60 \text{ mm}$ , and a length of shaft in contact with the working material  $L_s = 80 \text{ mm}$ . The design deflection is  $d_{bd} = 10 \text{ mm}$  in either direction (i.e.,  $20 \text{ mm}$  total stroke). The prototype was designed for a nominal force of  $220 \text{ kN}$ . In order to avoid off-axis loads, self-lubricating spherical hinges with a minimum rotation capacity of  $\pm 2^\circ$  are provided at both ends of the damper, namely at one end of the shaft and on the bottom of the tube.

During the assembling process, the working material was prestressed by tightening the screws connecting the cap to the tube wall to a torque of  $212 \text{ Nm}$ . The assembling process is sketched in Figure 2-36.

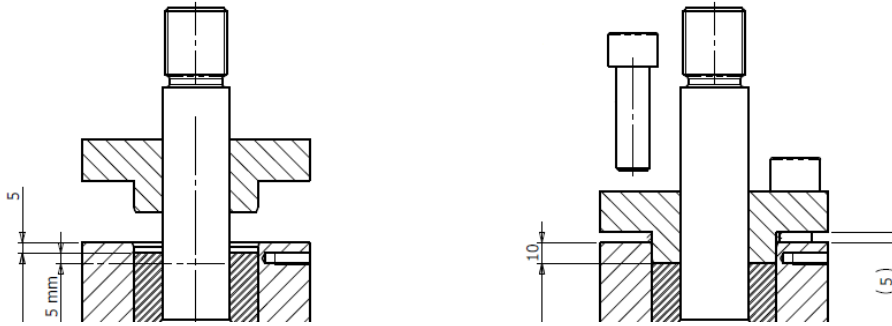


Figure 2-36: Prestressing of the working material

Three thermocouples were inserted into  $\varnothing 5 \text{ mm}$  blind holes drilled in the lateral wall of the containing tube, about 5 mm away from the chamber filled with the working material, in order to measure the temperature rise during the extrusion process.

### 2.3.2. Experimental protocol

The experiments were performed at the Materials Testing Laboratory of Politecnico di Milano, using a 500 kN servohydraulic testing machine (MTS Systems, Eden Prairie, MN), Figure 2-37.



Figure 2-37: Prototype installed on the testing machine

The specimen was subjected to the type testing protocol prescribed in the European standard EN 15129 [22] for assessment of Displacement Dependent Devices. The hysteretic force-deflection response was evaluated by imposing harmonic cycles of increasing amplitude at 25%, 50% and 100% of the design deflection  $d_{bd} = 10 \text{ mm}$ , at a loading frequency of 0.5 Hz. Five cycles for each intermediate amplitude and ten cycles for the maximum amplitude were applied. Eventually, a ramp test at 0.1 mm/s rate was performed to the amplified design displacement  $\gamma_b \gamma_x d_{bd} = 13.2 \text{ mm}$  (where  $\gamma_b = 1.1$  and  $\gamma_x = 1.2$  are the amplification factor and the reliability factor given in the standard, respectively), to assess the failure condition under quasi-static condition.

<i>Test</i>	<i>Amplitude</i> [mm]	<i>Frequency</i> [Hz]	<i>n° of cycles</i> [-]
	$0.25d_{bd}$	0.5	5
cyclic	$0.50d_{bd}$	0.5	5
	$1.00d_{bd}$	0.5	10
ramp	$1.32d_{bd}$	0.1 mm/s	1

Table 2-2: Testing protocol according to [22]

In order to investigate the dependence upon the velocity, three additional tests were performed at the design deflection  $d_{bd} = 10 \text{ mm}$  with different frequencies, Table 2-3.

<i>Test</i>	<i>Amplitude</i> [mm]	<i>Frequency</i> [Hz]	<i>n° of cycles</i> [-]
	$1.00d_{bd}$	0.25	5
rate	$1.00d_{bd}$	0.5	5
	$1.00d_{bd}$	0.75	5

Table 2-3: Testing protocol to investigate the dependence upon the velocity

Finally, the dedicated test prescribed by the Italian Building Code [105] for Displacement Dependent Devices and consisting in the application of 5 cycles at 0.5 Hz to the Collapse Limit State displacement  $d_2 = \gamma_x d_{bd}$  was performed.

2.4. Results

The force–displacement behavior of the tested prototype observed in a preliminary cycle to check the axial displacement capacity is shown in Figure 2-38. The prototype shows an initial elastic deformation, followed by a plastic behavior (i.e., constant force independent of the accommodated displacement) after the breakaway friction resistance of the working material has been overcome and sliding of the shaft has been engaged. It is also worth noting that due to the high elastic stiffness of the steel shaft the hysteresis loop has an almost perfectly rectangular shape, and the reaction provided from the damper either in extension ( $N > 0$ , shaft moving outwards) or in compression ( $N < 0$ , shaft moving inwards) resembles the design force. The behavior of the device is essentially symmetric in tension and compression. The small changes in the output force close to motion reversals suggest that the friction between the shaft and the working material has a shallow dependence on the velocity, though this dependency does not affect too much the overall response. The idle displacement observed after the motion reversal and highlighted in the figure by red arrows is due to the clearance of the spherical hinges.

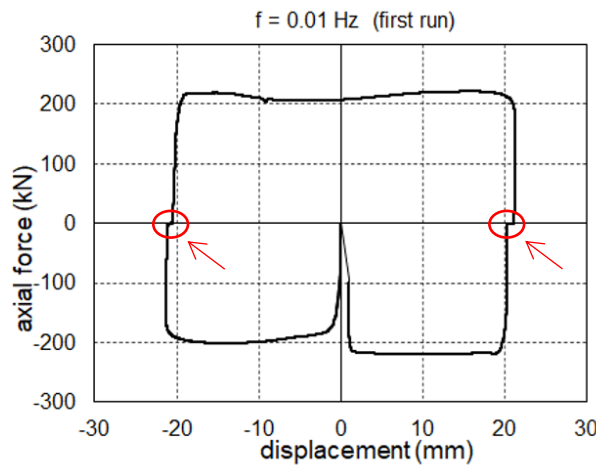


Figure 2-38: Hysteresis loop of the LED prototype

Figure 2-39 shows the hysteresis loops of the cyclic test according to EN 15129 [22], Table 2-2; the results of the additional tests of Table 2-3 are reported in Figure 2-40, while the test prescribed by the Italian Building Code [105] is presented in Figure 2-41.

A decrease in the output force occurs in the tests at  $0.5d_{bd}$  and  $1.0d_{bd}$  when the damper switches from compression ( $N < 0$ , shaft moving inwards) to extension ( $N > 0$ , shaft moving outwards). This behavior is possibly due to the leakage of the working material during the outwards movement of the shaft due to an excessive clearance between shaft and bore. Another possible reason is the progressive loosening of the screws caused by the movement of the shaft. Therefore, the asymmetric behavior observed in the cyclic test and absent in the preliminary loop shown in Figure 2-38 is ascribed to manufacturing faults of the tested prototype, and not inherent to the LED design.

Similar comments are valid also for the tests shown in Figure 2-39 and Figure 2-40.

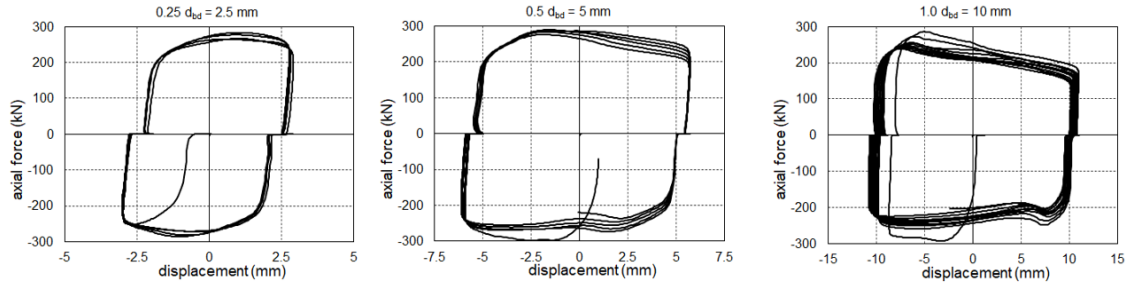


Figure 2-39: Hysteresis loops of the LED prototype at the cyclic tests according to [22]

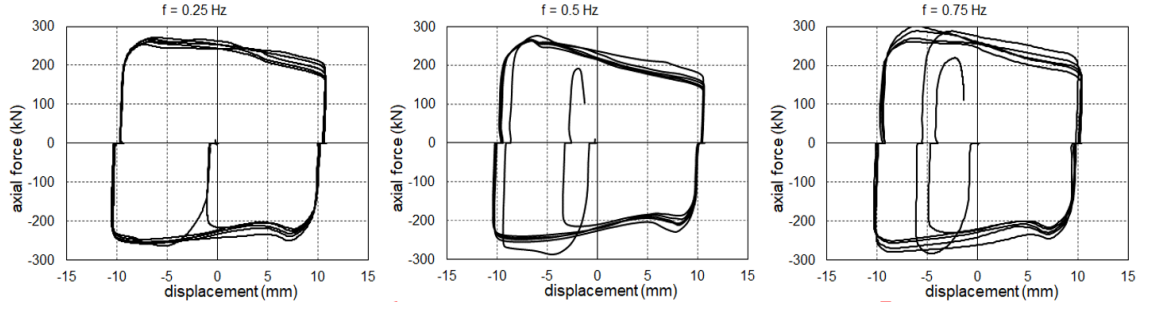


Figure 2-40: Hysteresis loops of the LED prototype at different frequencies

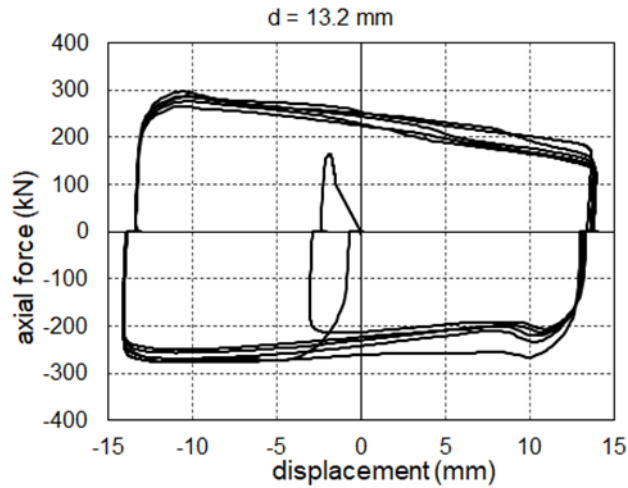


Figure 2-41: Hysteresis loops of the LED prototype at the cyclic test according to [105]

Two quantities are calculated at each cycle and used to characterize the response of the LED, namely the effective stiffness and the effective damping, determined through the expressions Eq. (2.5) and Eq. (2.6):

$$K_{eff} = \frac{N_b}{d_b} \quad (2.5)$$

$$\xi_{eff} = \frac{2}{\pi} \frac{A_{cycle}}{4K_{eff} \cdot d_b^2} \quad (2.6)$$

where  $N_b$  is the output force of the prototype,  $d_b$  is the maximum cyclic deflection, and  $A_{cycle}$  is the area of the hysteresis loop, i.e., the amount of energy dissipated in the cycle.

## 2 Characterization and numerical assessment of Lead Damper

---

The European norm prescribes that both quantities  $K_{eff}$  and  $\xi_{eff}$  remain essentially constant as the cycles proceed, as shown in Table 2-4, where  $i$  is the cycle number ( $i \geq 2$ ) and  $K_{eff,3}$  and  $\xi_{eff,3}$  are the effective stiffness and the effective damping at the third cycle respectively.

### *Requirements*

$$\frac{|K_{eff,i} - K_{eff,3}|}{K_{eff,3}} \leq 0.10$$

$$\frac{|\xi_{eff,i} - \xi_{eff,3}|}{\xi_{eff,3}} \leq 0.10$$

Table 2-4: Requirements of the European norm EN 15129 [22]

Figure 2-42 shows the cyclic variation of the effective stiffness and the effective damping assessed in the tests of Table 2-2, highlighting a robust and stable behavior. Both  $K_{eff}$  and  $\xi_{eff}$  essentially fulfill the stability requirements of Table 2-4, with a maximum change in the effective damping of 2.4% in the test sequence at  $d_b = 10mm$ . The average value of  $\xi_{eff}$  over 10 cycles performed at the design deflection is 0.55, i.e., 86% of the effective damping of an ideally rectangular loop, confirming the good dissipation capacity of the LED. After each sequence of tests, the prototype was left at ambient temperature for some time (45 min ÷ 90 min) and then subjected to the next sequence of cycles; the stiffness and damping were practically unchanged from the previous sequence. After cooling lead recrystallizes and recovers its original properties, thereby providing a reliable and consistent response even in case of multiple loading sequences occurring within short time

Eventually, in the monotonic ramp test the prototype was able to sustain the amplified design deflection  $\gamma_b \gamma_x d_{bd}$  and the force–deflection curves present a stable behavior, demonstrating the ability of the device to accommodate the prescribed displacement without any mechanical damage or deterioration of its stiffness.

Figure 2-43 shows the cyclic variation of the effective stiffness and the effective damping assessed in the additional tests performed to check the velocity dependence and the respect of the requirement of the Italian Building Code [105]: the response of the device shows a light dependence upon the velocity, already observed in Figure 2-38, and both stiffness and damping confirm their substantial stability over repeated cycles.

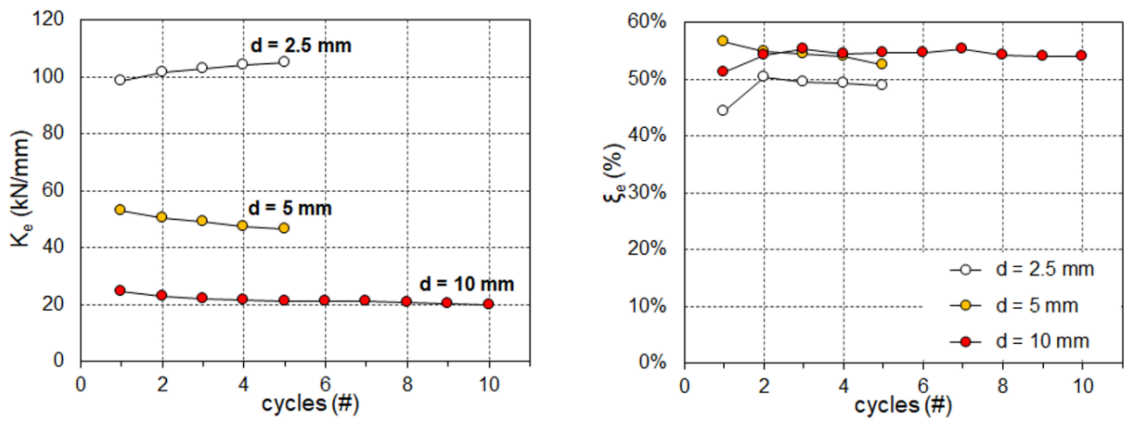


Figure 2-42: Plots of (a) effective stiffness  $K_{eff}$ , and (b) effective damping  $\xi_{eff}$  of the LED vs. number of cycles at different deflection amplitudes  $d_{bd}$

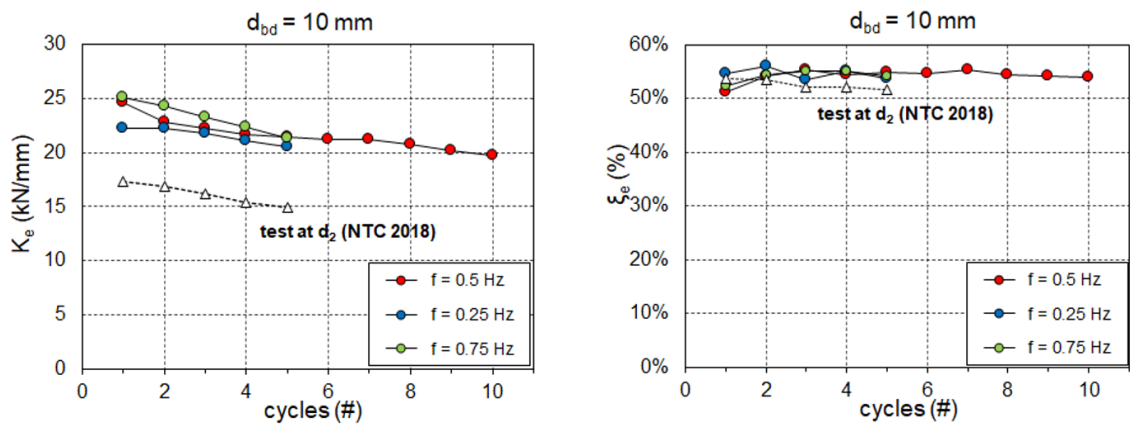


Figure 2-43: Plots of (a) effective stiffness  $K_{eff}$ , and (b) effective damping  $\xi_{eff}$  of the LED vs. number of cycles at different frequencies

2.5. Modelling of LED in OpenSees

The shape of the hysteresis loops of the LED is essentially rectangular, and the behavior of the device is robust and stable under multiple cycles of motion at the basic design earthquake displacement.

In order to leave out some irregular behavior observed in the tests due to manufacturing inaccuracies, the formulation of constitutive models of the LED is performed by referring to the regular behavior of the device shown in Figure 2-38.

For this reason, the simplest modelling option to represent the constitutive behavior of LED in OpenSees [106] is the elastic-perfectly plastic *uniaxialMaterial ElasticPP* object material [107]. The model is described by four parameters, namely the tangent  $E$ , the strain or deformation thresholds  $epsP$  and  $epsN$  at which the material reaches the plastic state in either tension or compression, respectively, and the initial strain  $eps0$ , Figure 2-44. For the LED, based on the test results presented in Section 2.3,  $eps0 = 0$  and  $epsP = -epsN$ , i.e., symmetric behavior in tension and compression is assumed.

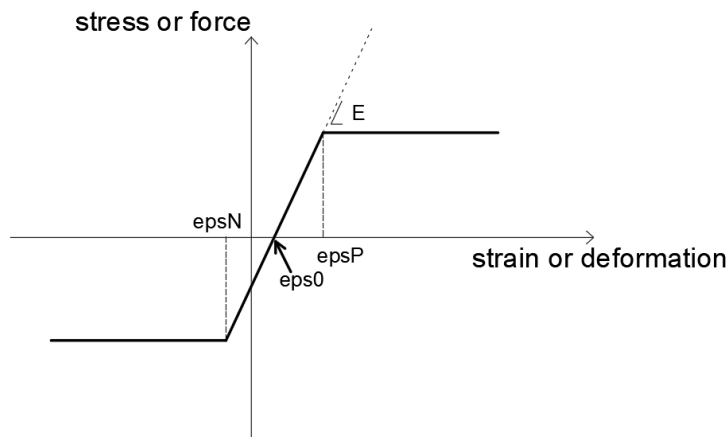


Figure 2-44: *uniaxialMaterial ElasticPP* law in OpenSees [107]

The strength of this element stands on its simplicity and on the fact that it is implemented in every software program for structural calculation. However, this representation does not take into account some additional features that were observed in the tests, e.g., a light dependence of the reaction force on velocity and its decrease at the reversal of the motion. For this reason, other *uniaxialMaterial* element objects in OpenSees that can be more suitable to represent the constitutive behavior of the LED are investigated.

By referring again to Figure 2-38, beyond a very stiff initial elastic response, the reaction force keeps almost constant and independent on the displacement. To represent this behavior, the model needs to incorporate a force contribution ( $F_1$ ) typical of an elastic-perfectly plastic material with a very high initial stiffness.

A minor contribution of velocity is also disclosed, as observed e.g., close to motion reversals. This behavior, which was already highlighted in other studies [90], can be modelled by a simple exponential relation like  $F_2 = C_d \cdot v^{\alpha_d}$ , typical of viscous solids, which are usually represented by a Maxwell model.

The model proposed hereinafter (referred as EPPV) and depicted in Figure 2-45, aims at describing the two aforesaid mechanisms by means of a simple rheological model comprising a parallel of two systems, namely

(i) a non-linear spring, with associated the *uniaxialMaterial ElasticPP* object material to represent an elastic perfectly plastic behavior with force  $F_1$ , and (ii) a Maxwell model with associated the *uniaxialMaterial Viscous Damper* object material, that provides the velocity-dependent response  $F_2$ . Such model can be formulated in the OpenSees framework by using a *truss element* with associated a *Parallel* material made of the two uniaxial object materials *ElasticPP* and *ViscousDamper*.

The EPPV model is described by 5 parameters, namely: the yield displacement  $d_y$  and the plastic force  $V_{EPP}$  of the *uniaxialMaterial ElasticPP* material object, and the stiffness  $K_d$  of the internal linear spring, the damping coefficient  $C_d$  and the velocity exponent  $\alpha_d$  of the *uniaxialMaterial ViscousDamper* object material (Figure 2-45).

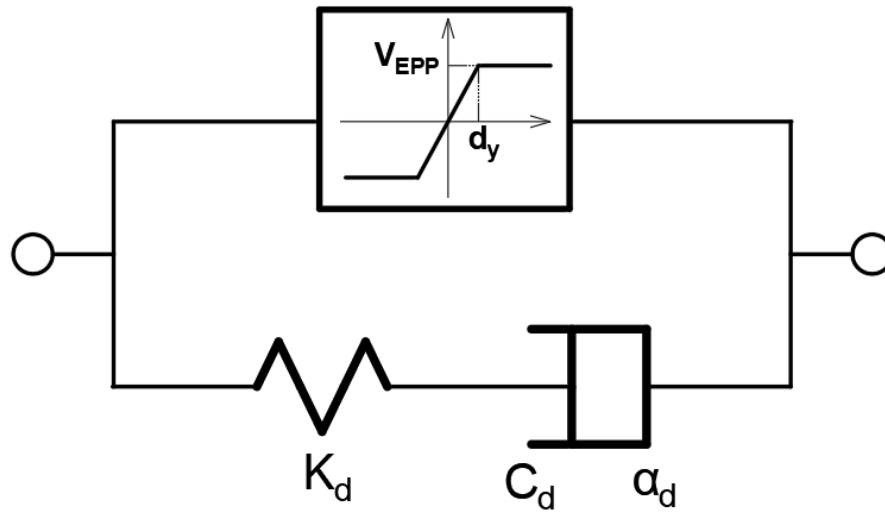


Figure 2-45: Model EPPV formulated in OpenSees

A simple procedure for tuning the EPPV system based on an experimental force – displacement plot is established. The procedure consists of five steps:

- (a) the plastic force  $V_{EPP}$  of the *uniaxialMaterial ElasticPP* material is set as a fixed part  $\beta$  (typically 80%) of the total output force of the parallel EPPV system; after sliding of the shaft onto the working material has been engaged, the plastic force  $V_{EPP}$  coincides with the output force  $F_1$  of the EPP system;
- (b) the yield displacement  $d_y$  of the *ElasticPP* material is identified from the initial branch of the experimental force – displacement curve as the deflection corresponding to an axial force equal to  $V_{EPP}$ ;
- (c) the stiffness of the internal spring of the *uniaxialMaterial ViscousDamper* material is set as  $K_d = 100 \cdot (\frac{V_{EPP}}{d_y})$ , where  $V_{EPP}/d_y$  is the initial stiffness of the *ElasticPP* material; this choice is motivated by the need to avoid deformation of the internal spring of the *ViscousDamper* material, and to concentrate the whole deflection in the dashpot portion;
- (d) the damping coefficient  $C_d$  of the *ViscousDamper* material is formulated as a function of the velocity exponent  $\alpha_d$  through the relation  $C_d = F_2/(v_{max})^{\alpha_d}$ , where  $F_2 = F_{max} - F_1 = (1 - \beta)F_{max}$  is the

## 2 Characterization and numerical assessment of Lead Damper

output force of the *ViscousDamper* material, and  $v_{max}$  is the maximum velocity developed by the damper through the cycle;

(e) eventually the velocity exponent  $\alpha_d$  of the *ViscousDamper* material is determined by minimizing the deviation between the areas enclosed in the experimental and numerical force – displacement loops.

The tuning strategy aims at matching the maximum experimental force of the LED (but for the negligible contribution of the internal damper spring with stiffness  $K_d$ ) and minimizing the deviation between the analytical and the experimental values of the Energy Dissipated per Cycle.

Figure 2-46 shows the fit of the EPPV analytical model to the experimental curve of Figure 2-38, after removing the idle displacements at zero force due to joint clearances.

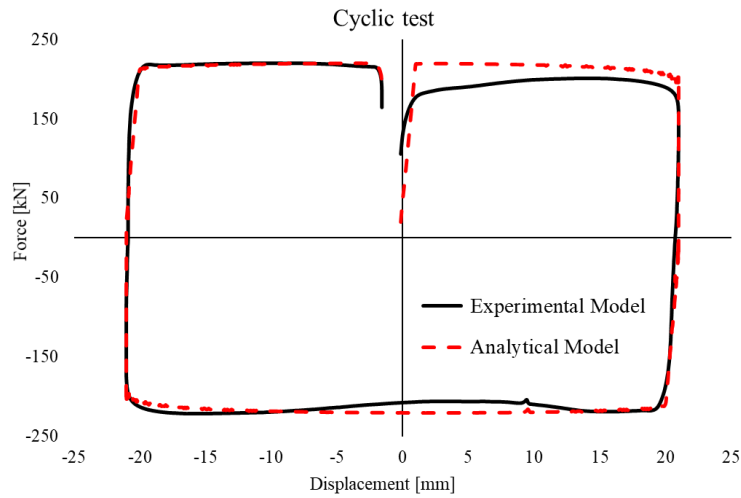


Figure 2-46: Fit of analytical model to experimental curve

The EPP system is supposed to provide a fraction  $\beta = 80\%$  of  $F_{max} = 220 \text{ kN}$ , corresponding to  $V_{EPP} = 176 \text{ kN}$ , and  $d_y = 1.0 \text{ mm}$  is the corresponding displacement in the experimental curve. The ductility of the device is then  $\mu_{DB} = \frac{d_{max}}{d_y} = 21$ , and the stiffness associated to  $F_1$  counts  $\frac{V_{EPP}}{d_y} = 176 \text{ kN/mm}$ .

The *ViscousDamper* material provides the remaining 20% of  $F_{max}$ . The stiffness value  $K_d$  is set to  $17600 \text{ kN/mm}$ , while the parameters  $a_d$  and  $C_d$  are estimated from the fitting procedure as  $\alpha_d = 0.3$  and  $C_d = 39.77 \text{ kN}(s/mm)^{0.3}$ .

The fair performance of the EPPV model is highlighted in Table 2-5 where the response of the prototype and the model are compared.

Parameters	Experimental	Analytical	Deviation
$F_{compression} [kN]$	220.27	220.28	0.005%
$F_{tension} [kN]$	-221.76	-220.28	-0.667%
$K_{eff} [\frac{kN}{mm}]$	10.51	10.48	-0.28%
$EDC [kJ]$	17.103	17.635	3.11%

Table 2-5: Comparison between the experimental response and the analytical model in terms of maximum compression ( $F_{compression}$ ) and maximum tension forces ( $F_{tension}$ ), effective stiffness ( $K_{eff}$ ) and Energy Dissipated in the Cycle ( $EDC$ )

The EPPV model is able to reproduce the essential behavior of the damper, including the light dependency of the axial force on the velocity that is apparent at motion reversals, providing accurate estimates of maximum force, effective stiffness and dissipated energy. The maximum discrepancy between the experimental and the analytical curves occurs in the first quadrant, where the actual force of the prototype is about 10% less than in the other quadrants, probably due to the inertial forces of the testing machine at the beginning of the test, that reduce the test velocity applied to the device. It is worth to highlight that if the first quadrant were ignored, the difference between the areas of the experimental and analytical model in the second, third and fourth quadrants would be as lower as 1.1%.

Finally, it must be mentioned that when the LED is encased in a brace, an additional spring should be added in series to reproduce the behavior of the latter component. The stiffness of the driver brace is an important design feature, because it needs to be higher than the stiffness of the damper in order to allow the device to be effective in dissipating energy [108].

### 2.6. Conclusions

---

The Lead Damper (LED), an emerging energy dissipation device, has been experimentally investigated. The device provides energy dissipation through the friction created between the lead core and a shaft and achieves high specific output force through preloading of the working material during the assembly.

A prototype of the LED was experimentally assessed according to the provisions of the European standard EN 15129 for Displacement Dependent Devices. The damper exhibits a consistent rigid-plastic behavior, with an equivalent damping ratio of 0.55, close to the maximum theoretical value of 0.63.

Cyclic tests were used to evaluate the response of the damper at different displacement amplitudes and showed a strength degradation when the damper switches from compression ( $N < 0$ , shaft moving inwards) to extension ( $N > 0$ , shaft moving outwards), especially for larger amplitudes. The difference among the two phases is primarily due to the leakage of the working material when the shaft moves outwards, due to an excessive clearance between shaft and bore, and to the lengthening of the screws in the cap, rather than being not an inherent feature of the LED device.

The tested specimen is able to sustain multiple sequences of motion at the basic design earthquake displacement, demonstrating its ability to provide maintenance-free operation even in presence of repeated ground shakes. Though a certain softening of the working material is observed due to heating, the changes in damping capacity over 10 cycles at the design deflection lie within the  $\pm 10\%$  bound. The effect of heating is only temporary, and when the damper is cooled down to ambient temperature, the stiffness and damping characteristics return to their original value.

Two constitutive models of the LED have been formulated in the OpenSees framework to perform non-linear dynamic analyses. The first model is an elastic-perfectly plastic material model (named EPP) with symmetric behavior in tension and compression (*uniaxialMaterial ElasticPP* object material), which is a simple formulation available in every software program for structural calculation. The second model is more refined and consists in a parallel set of two systems (named EPPV), namely an elastic-perfectly plastic material (*uniaxialMaterial ElasticPP* object material) and a Maxwell model (*uniaxialMaterial Viscous Damper* object material). This latter representation is able to reproduce the essential behavior of the damper, including the light dependency of the axial force on the velocity that is apparent at motion reversals, providing accurate estimates of maximum force, effective stiffness and dissipated energy. The EPPV model is described by 5 parameters, namely: the yield displacement  $d_y$  and the plastic force  $V_{EPP}$  of the *uniaxialMaterial ElasticPP* material object, and the stiffness  $K_d$  of the internal linear spring, the damping coefficient  $C_d$  and the velocity exponent  $\alpha_d$  of the *uniaxialMaterial ViscousDamper* material object. A simple procedure has been applied for tuning the EPPV system based on an experimental force – displacement. The model EPPV will be implemented in the non-linear analyses performed in Chapter 4.

## 2.7. Symbols

---

$a$  annular area of orifice

$A$  annular area around the shaft

$A_{bulge}$  annular area of the bulge

$A_{cycle}$  area of the hysteresis loop, equal to the amount of energy dissipated in the cycle

$A_{shaft}$  surface area of the shaft

$AB$  bulge area

$AR$  area ratio

$C_d$  damping coefficient of the *uniaxialMaterial ViscousDamper* object material in OpenSees [107] associated to the EPPV model

$D$  effective diameter corresponding to annular lead area  $A$

$d_2$  amplified displacement prescribed by [105] =  $\gamma_x d_{bd}$

$d_b$  maximum cyclic deflection of the LED prototype

$d_{bd}$  design displacement

$d_y$  yield displacement of the *uniaxialMaterial ElasticPP* object material in OpenSees [107] associated to the EPPV model

$D_{blg}$  bulge diameter

$D_{cyl}$  cylinder diameter

$D_D$  resistive force of the device

$D_s$  shaft diameter

$E$  tangent in the model *uniaxialMaterial ElasticPP* in OpenSees [107]

$E_D$  energy dissipated by the structure

$E_I$  input energy from the ground shaking

$F_1$  force contribution to the EPPV model with associated the *uniaxialMaterial ElasticPP* object material in OpenSees [107]

$F_2$  force contribution to the EPPV model with associated the *uniaxialMaterial ViscousDamper* object material in OpenSees [107]

$eps0$  initial strain in the model *uniaxialMaterial ElasticPP* in OpenSees [107]

$epsN$  deformation in compression in the model *UniaxialMaterial ElasticPP* in OpenSees [107]

## 2 Characterization and numerical assessment of Lead Damper

---

$\epsilon_{SP}$  deformation in tension in the model *uniaxialMaterial ElasticPP* in OpenSees [107]

$E_S$  energy stored by the structures

$f$  frequency

$F$  extrusion damper force

$F_{max}$  maximum output force of the LED

$K_d$  elastic stiffness of the internal spring of the *uniaxialMaterial ViscousDamper* object material in OpenSees [107] associated to the EPPV model

$K_{eff}$  effective stiffness

$L$  length of the shaft in sliding contact with the working material and device end caps

$L_{cyl}$  cylinder length

$L_s$  length of shaft in contact with the working material in the LED prototype

$m$  constant specific to the extrusion process  $= \frac{4\mu L}{D}$

$N$  axial force in the LED prototype

$N_b$  output force of the LED prototype

$N_D$  axial force in the hysteretic damper

$N_y$  yield strength in the hysteretic damper

$r_D$  stiffness hardening ratio of the damper

$SA$  surface area

$S_a$  spectral acceleration

$S_{De}$  spectral displacement

$V_{EPP}$  plastic force of the *uniaxialMaterial ElasticPP* object material in OpenSees [107] associated to the EPPV model

$\dot{x}$  velocity of the shaft

$Y$  yield strength for the lead

$\alpha$  velocity coefficient (constant value)

$\alpha_0, \alpha_1, \alpha_2, \alpha_3$  weighting coefficients identified by fitting the models to experimental device data

$\alpha_d$  velocity exponent of the *uniaxialMaterial ViscousDamper* object material in OpenSees [107] associated to the EPPV model

$\beta$  fraction of the total output force  $F$  of the LED assigned to the plastic force  $V_{EPP}$  of the *uniaxialMaterial ElasticPP* object material in OpenSees [107]

$\Delta_D$  axial displacement of the hysteretic damper

$\Delta_m$  maximum displacement of the cycle

$\gamma_b$  amplification factor = 1.1 [22]

$\gamma_x$  reliability factor = 1.2 [22]

$\xi_{eff}$  effective damping

$\mu$  coefficient of friction between the working material and the steel shaft

$\mu_{DB}$  ductility of the device

$\sigma_0$  direct stress imposed on the bulge face area

$\tau_D$  shear stress due to the load between the shaft and the lead

### 2.8. References

---

- [1] Calvi PM, Calvi GM. Historical development of friction-based seismic isolation systems, *Soil Dynamics and Earthquake Engineering* 2018, 106: 14-30, DOI:10.1016/j.soildyn.2017.12.003.
- [2] Kelly JM, Skinner RI, Heine AJ. Mechanisms of energy absorption in special devices for use in earthquake resistant structures, *Bulletin of the New Zealand Society for Earthquake Engineering* 1972, 5(3): 53-68.
- [3] Constantinou M, Kneifati M. Dynamics of soil-base-isolated-structure systems, *Journal of Structural Engineering* 1988, ASCE, 114: 211–221; DOI:10.1061/(ASCE)0733-9445(1988)114:1(211).
- [4] Spyrakos CC, Koutromanos IA, Maniatakis CA. Seismic response of base-isolated buildings including soil–structure interaction, *Soil Dynamics and Earthquake Engineering* 2009a, 29: 658–668; DOI:10.1016/j.soildyn.2008.07.002.
- [5] Spyrakos CC, Maniatakis CA, Koutromanos IA. Soil-structure interaction effects on base-isolated buildings founded on soil stratum, *Engineering Structures* 2009b, 31: 729–737; DOI:10.1016/j.engstruct.2008.10.012.
- [6] Ariga T, Kanno Y, Takewaki I. Resonant behaviour of base-isolated high-rise buildings under long-period ground motions, *Structural Design of Tall and Special Buildings* 2006, 15(3): 325–338; DOI: 10.1002/tal.298.
- [7] Roussis PC, Constantinou MC. Uplift-restraining Friction Pendulum seismic isolation system, *Earthquake Engineering and Structural Dynamics* 2006, 35(5): 577–593, DOI:10.1002/eqe.545.
- [8] Takewaki I. Robustness of base-isolated high-rise buildings under code-specified ground motions, *The Structural Design of Tall and Special Buildings* 2008, 17(2): 257–271; DOI:10.1002/tal.350.
- [9] Zhou FL, Yang Z, Liu WG, Tan P. New seismic isolation system for irregular structure with the largest isolation building area in the world, *13th World Conference on Earthquake Engineering* 2004, 1–11.
- [10] Ragni L, Cardone D, Conte N, Dall’Asta A, Di Cesare A, Flora A, Leccese G, Micozzi F, Ponzo C. Modelling and seismic response analysis of Italian code-conforming base-isolated buildings. *Journal of Earthquake Engineering* 2018, 22: 198–230; DOI:10.1080/13632 469.2018.1527263.
- [11] Kelly JM. The influence of base isolation on the seismic response of light secondary equipment, Report No. UCB/EERC41/17. Earthquake Engineering Research Center, 1982, University of California, Berkeley, CA.
- [12] Gandelli E, Quaglini V, Dubini P, Limongelli MP, Capolongo S. Seismic isolation retrofit of hospital buildings with focus on non-structural components, *Ingegneria Sismica - International Journal of Earthquake Engineering* 2018, XXXV(4): 20–56.
- [13] Shi Y, Kurata M, Nakashima M. Disorder and damage of base-isolated medical facilities when subjected to near-fault and long-period ground motions, *Earthquake Engineering and Structural Dynamics* 2020: 1683–1701; DOI:10.1002/eqe.2417.
- [14] Natale A, Del Vecchi C, Di Ludovico M. Seismic retrofit solutions using base isolation for existing RC buildings: economic feasibility and pay-back time, *Bulletin of Earthquake Engineering* 2021, 19: 483–512; DOI:10.1007/s10518-020-00988-9.

- [15] Yang F, Wang G, Li M. Evaluation of the seismic retrofitting of mainshock-damaged reinforced concrete frame structure using steel braces with soft steel dampers, *Applied Science* 2021, 11, 841; DOI:10.3390/app11020841
- [16] Di Cesare A, Ponzo F C, Nigro D. Assessment of the performance of hysteretic energy dissipation bracing systems, *Bulletin of Earthquake Engineering* 2014, 12(6): 2777–2796; DOI: 10.1007/s10518-014-9623-z.
- [17] Di Cesare A, Ponzo FC. Seismic retrofit of reinforced concrete frame buildings with hysteretic bracing systems: design procedure and behaviour factor, *Hindawi, Shock and Vibration* 2017, 2017 (2639361); DOI: 10.1155/2017/2639361.
- [18] Aliakbari F, Garivani S, Aghakouchak, AA. An energy based method for seismic design of frame structures equipped with metallic yielding dampers considering uniform inter-story drift concept, *Engineering Structures* 2020, 205 (110114); DOI:10.1016/j.engstruct.2019.110114.
- [19] Garivani S, Askariani SS, Aghakouchak AA. Seismic design of structures with yielding dampers based on drift demands, *Structures* 2020, 28: 1885–1899; DOI:10.1016/j.istruc.2020.10.019.
- [20] Gandelli E, Chernyshov S, Distl J, Dubini P, Weberd F, Taras A. Novel adaptive hysteretic damper for enhanced seismic protection of braced buildings, *Soil Dynamics and Earthquake Engineering* 2021, 141 (106522); DOI:10.1016/j.soildyn.2020.106522.
- [21] Golmoghany M., Zahrai SM. Improving seismic behavior using a hybrid control system of friction damper and vertical shear panel in series, *Structures* 2021, 31: 369–379; DOI:10.1016/j.istruc.2021.02.007.
- [22] CEN (European Committee for Standardization). European Committee for Standardization (2009). EN 15129. Anti-seismic devices. Brussels.
- [23] Muto K. Earthquake resistant design of 36 – storied Kasumigaseki Building, 4th World Conference on Earthquake Engineering 1969, Santiago, Chile.
- [24] Skinner RI, Kelly JM, Heine AJ. Hysteretic dampers for earthquake – resistant structures, *Earthquake Engineering and Structural Dynamics* 1974, 3(3): 287 – 296.
- [25] Christopolous C, Filiatrault A. Principles of passive supplemental damping and seismic isolation, IUSS Press 2006, Pavia.
- [26] Durucan C, Dicleli M. Analytical study on seismic retrofitting of reinforced concrete buildings using steel braces with shear link, *Engineering Structures* 2010, 32 (2995-3010); DOI:10.1016/j.engstruct.2010.05.019.
- [27] Mazza F, Vulcano A. Equivalent viscous damping for displacement-based seismic design of hysteretic damped braces for retrofitting framed buildings, *Bulletin of Earthquake Engineering* 2014, 12: 2797–2819; DOI 10.1007/s10518-014-9601-5.
- [28] Pall AS, Marsh C, Fazio P. Friction joints for seismic control of large panel structures, *Journal of Prestressed Concrete Institute* 1980, 25(6): 38-61.
- [29] Pall AS, Marsh C. Response of friction damped braced frames, *Journal of the Structural Division* 1981, ASCE, 108(ST6): 1313-1323.

## 2 Characterization and numerical assessment of Lead Damper

---

- [30] Pall AS, Verganelaskis V, Marsh C. Friction dampers for seismic control of Concordia Library Building, 5th Canadian Conference on Earthquake Engineering 1987, Ottawa, Canada.
- [31] Pall AS, Pall R. Friction-dampers used for seismic control of new and existing buildings in Canada, Seminar on Seismic Isolation, Passive Energy Dissipation and Active Control, (ACT 17.1), Applied Technology Council 1993, San Francisco, 2: 675-686.
- [32] Pall AS, Pall R. Friction dampers for seismic control of buildings: a Canadian experience, 11th World Conference on Earthquake Engineering 1996, Acapulco, Mexico.
- [33] Anagnostides G, Hargreaves A., Wyatt TA. Development and applications of energy absorption devices based on friction, *Journal of Constructional Steel Research* 1989, 13(4): 317-336.
- [34] Anagnostides G, Hargreaves A, Wyatt TA. Friction load control devices for steel braced frame structures, Research Report ESEE-90/3, Imperial College, London, 1990.
- [35] Anagnostides G, Hargreaves AC. Shake table testing on an energy absorption device for steel braced frames, *Soil Dynamic Earthquake Engineering* 1990, 9(3): 120-140.
- [36] Grigorian CE, Tsong-Shuoh Y, Popov EP. Slotted bolted connection energy dissipators, Report UCB/EERC-92/10, University of California, Berkeley, 1992.
- [37] Martínez-Rueda JE. On the evolution of energy dissipation devices for seismic design, *Earthquake Spectra* 2002, 18(2): 309-346; DOI: 10.1193/1.1494434.
- [38] Martínez-Rueda JE, Elnashai AS. A novel technique for the retrofitting of reinforced concrete structures, *Engineering Structures* 1995, 17(5): 359-71.
- [39] Martínez-Rueda JE. Energy dissipation devices for seismic upgrading of RC structures, Ph.D. dissertation, London (UK): Engineering Seismology and Earthquake Engineering 1997, Civil Engineering Department, Imperial College.
- [40] Filiatrault A. Analytical predictions of the seismic response of friction damped timber shear walls, *Earthquake Engineering and Structural Dynamics* 1990, 19(2): 259-273.
- [41] Martinelli P, Mulas MG. An innovative passive control technique for industrial precast frames, *Engineering Structures* 2010, 32: 1123-1132; DOI:10.1016/j.engstruct.2009.12.038.
- [42] Belleri A, Marini A, Riva P, Nascimbene R. Dissipating and re-centering devices for portal-frame precast structures, *Engineering Structures* 2017, 150: 736-745; <http://hdl.handle.net/10446/93629>.
- [43] Gandelli E, Taras A., Disti J, Quaglini V. Seismic retrofit of hospitals by means of hysteretic braces: influence on acceleration-sensitive non-structural components, *Frontiers in Built Environment* 2019, 5(100); DOI: doi.org/10.3389/fbuil.2019.00100.
- [44] Kulak GL, Fisher JW, Struik JHA. Guide to design criteria for bolted and riveted joints, 2nd edition, AISC, Chicago, IL, 2001.
- [45] Wakabayashi M, Nakamura T, Katagihara A, Yogoyama H, Morisono T. Experimental study on the elastoplastic behavior of braces enclosed by precast concrete panels under horizontal cyclic loading—Parts 1 & 2. Summaries of technical papers of annual meeting, Architectural Institute of Japan, Structural Engineering Section 1973, 10: 1041-4.

- [46] Wakabayashi M, Nakamura T, Katagihara A, Yogoyama H, Morisono T. Experimental study on the elastoplastic behavior of braces enclosed by precast concrete panels under horizontal cyclic loading— Parts 1 & 2. Summaries of technical papers of annual meeting, Kinki Branch of the Architectural Institute of Japan, Structural Engineering Section 1973, 10: 121–8.
- [47] Catalogo FIPMEC: <https://www.fipmec.it/>
- [48] Catalogo MAURER: <https://www.maurer.eu/en/index.html>
- [49] Catalogo FPC ITALIA: [http://www.fpcitalia.it/freyssinet/fpc-italia\\_en.nsf](http://www.fpcitalia.it/freyssinet/fpc-italia_en.nsf)
- [50] Braun C, Medeot R. (2015). Energy dissipating device, EP 2 921 612 A1 (European Patent Office). Applicant: Maurer Söhne Engineering GmbH & Co. KG, 80807 München (DE).
- [51] Ozbulut OE, Hurlebaus S. Optimal design of superelastic friction base isolators for seismic protection of highway bridges against near – field earthquakes, *Earthquake Engineering and Structural Dynamics* 2011, 40: 273-291.
- [52] Dolce M, Cardone D, Marnetto R. Implementation and testing of passive control devices based on shape memory alloys, *Earthquake Engineering and Structural Dynamics* 2000, 29: 945-968.
- [53] Song G, Ma N, Li HN. Applications of shape memory alloys in civil structures, *Engineering Structures* 2006, 28: 1266-1274.
- [54] CSSLPP (Consiglio Superiore dei Lavori Pubblici). Circolare 21 gennaio 2019, n. 7 C.S.LL.PP. Istruzioni per l'applicazione dell'«Aggiornamento delle “Norme tecniche per le costruzioni”» di cui al decreto ministeriale 17 gennaio 2018, Roma; 2019, in Italian.
- [55] Lomiento G, Bonessio N, Braga,F. Design criteria for added dampers and supporting braces, *Seismic Isolation and Protection Systems* 2010, 1(1): 55–73.
- [56] Braga F, Buttarazzi F, Dell'Asta A, Salvatore W. Protezione sismica di edifici in c.a. con controventi dissipativi in acciaio, Dario Flaccovio Editore 2015; (in Italian).
- [57] Mazza F, Vulcano A. Displacement-based design procedure of damped braces for the seismic retrofitting of r.c. framed buildings, *Bulletin of Earthquake Engineering* 2015, 12: 2121-2143; DOI 10.1007/s10518-014-9709-7.
- [58] Ponzio FC, Di Cesare A, Lamarucciola N, Nigro D. Seismic design and testing of post-tensioned timber buildings with dissipative bracing systems, *Frontiers in Built Environment* 2019, 5(104); DOI:10.3389/fbuil.2019.00104.
- [59] Li Z, Dong H, Wang X, He M. Experimental and numerical investigations into seismic performance of timber-steel hybrid structure with supplemental dampers, *Engineering Structures* 2017, 151: 33-43; DOI:10.1016/j.engstruct.2017.08.011.
- [60] Naeem A, Kim J. Seismic performance evaluation of a multi-slit damper, *Engineering Structures* 2019, 189: 332-346; DOI:10.1016/j.engstruct.2019.03.107.
- [61] Balendra T, Yu CH, Lee FL. An economical structural system for wind and earthquake loads, *Engineering Structures* 2001, 23: 491–501; DOI:10.1016/S0141- 0296(00)00061-4.
- [62] Palermo M, Silvestri S, Gasparini G, Trombetti T. Crescent shaped braces for the seismic design of building structures, *Materials and Structures* 2015, 48: 1485-1502; DOI 10.1617/s11527-014-0249-z.

## 2 Characterization and numerical assessment of Lead Damper

---

- [63] Rodgers GW, Solberg KM, Chase JG, Mander JB, Bradley BA, Dhakal RP, Li L. Performance of a damage-protected beam-column subassembly utilizing external HF2V energy dissipation devices, *Earthquake Engineering and Structural Dynamics* 2008, 37(13): 1549-1564; DOI: 10.1002/eqe.830.
- [64] Robinson WH, Greenbank LR. Properties of an extrusion energy absorber, *Bulletin of the New Zealand National Society for Earthquake Engineering* 1975, 8(3): 187 – 191.
- [65] Robinson WH, Greenbank LR. Extrusion energy absorber suitable for the protection of structures during an earthquake, *Earthquake Engineering & Structural Dynamics* 1976, 4(3): 251-259.
- [66] Robinson WH, Cousins WJ. Recent developments in lead dampers for base isolation, *Proceedings of the Pacific Conference On Earthquake Engineering* 1987, 2: 279-283.
- [67] Sadek F., Mohraz B, Taylor AW, Chung RM. Passive energy dissipating devices for seismic applications. Report NISTIR 5923, Building and Fire Research Laboratory, National Institute of Standards and Technology, Gaithersburg, Maryland, 1996.
- [68] Wulf J, Taylor JF, Shaler AJ. *Metallurgy for Engineers*, John Wiley and Sons, New York, 1956.
- [69] Birchenall CE. *Physical Metallurgy*. McGraw-Hill, London, 1959.
- [70] Cousins WJ, Porrit TE. Improvements to lead-extrusion damper technology, *Bulletin of the New Zealand National Society for Earthquake Engineering* 1993, 26: 342-348.
- [71] Rodgers GW, Chase JG, Mander JB, Leach NC, Denmead CS, Cleeve L, Heaton D. High force-to-volume extrusion dampers and shock absorbers for civil infrastructures, 19th Australasian conference on the mechanics of structures and materials, 2006.
- [72] Rodgers GW. Next generation structural technologies: implementing high force-to-volume energy absorbers Ph.D. Thesis, University of Canterbury, Christchurch, New Zealand, 2009.
- [73] Rodgers GW, Mander JB, Chase JG, Dhakal RP, Solberg KM. DAD post-tensioned concrete connections with lead dampers: analytical models and experimental validation, 8th Pacific Conference on Earthquake Engineering, Singapore, 2007.
- [74] Rodgers GW, Chase JG, Mander JB, Leach NC, Denmead CS. Experimental development, tradeoff analysis and design implementation of high force-to-volume damping technology, *Bulletin of the New Zealand National Society for Earthquake Engineering* 2007, 40(2): 35-48.
- [75] Rodgers GW, Mander JB, Chase JG, Dhakal RP, Leach NC, Denmead CS. Spectral analysis and design approach for high force-to-volume extrusion damper-based structural energy dissipation, *Earthquake Engineering and Structural Dynamics* 2008, 37: 207 – 223.
- [76] Rodgers GW, Mander JB, Chase JG, Dhakal RP, MacRae GA. Steel beam-column connections designed for damage avoidance utilizing high force-to-volume dampers, *Australasian Conference on Mechanics of Structure and Materials (ACMSM20)*, Toowoomba, Queensland, 2008.
- [77] Rodgers GW, Chase JG, MacRae G, Bacht T, Desombre J, Dhakal RP. Analytical investigation of the effects of HF2V damping devices on the seismic performance of the SAC3 Building, 13th Asia Pacific Vibration Conference, University of Canterbury, New Zealand, 2009.
- [78] Rodgers GW, Mander JB, Chase JG. Full-scale experimental validation of a DAD post-tensioned concrete connection utilizing embedded High Force-to-Volume lead dampers, *New Zealand Society for Earthquake Engineering Annual Conference*, New Zealand, 2009a.

- [79] Rodgers GW, Mander JB, Chase JG. Experimental testing and analytical modelling of damage-avoidance steel connections using HF2V damping devices, New Zealand Society for Earthquake Engineering Annual Conference, New Zealand, 2009b.
- [80] Rodgers GW, Chase JG, MacRae GA, Bacht T, Dhakal RP, Desombre J. Influence of HF2V damping devices on the performance of the SAC3building subjected to the SAC ground motion suites, 9th US National and 10th Canadian Conference on Earthquake Engineering, 2010.
- [81] Rodgers GW, Solberg KM, Mander JB, Chase JG, Bradley BA, Dhakal RP. High-Force-to-Volume seismic dissipators embedded in a jointed precast concrete frame, *Journal of Structural Engineering* 2012, 138.
- [82] Stanton J, Stone WC, Cheok GS. Hybrid reinforced precast frame for seismic regions, *PCI Journal* 1997, 42(2): 20-32.
- [83] Solberg KM, Bradley BA, Rodgers GW, Mander JB, Dhakal RP, Chase JG. Quasi-static testing of a damage protected beam-column subassembly with internal lead damping devices, 2007.
- [84] Solberg KM, Bradley BA, Mander JB, Dhakal RP, Rodgers GW, Chase JG. Multi-level seismic performance assessment of a damage-protected beam-column joint with internal lead dampers, New Zealand Society for Earthquake Engineering Annual Conference, Palmerston North, New Zealand, 2007.
- [85] Desombre J, Rodgers GW, MacRae GA, Rabczuk T, Dhakal RP, Chase JG. Experimentally validated FEA models of HF2V damage free steel connections for use in full structural analysis, *Structural Engineering and Mechanics* 2011, 37(4); DOI:10.12989/sem.2011.37.4.38.
- [86] Mander TJ, Rodgers GW, Chase JG, Mander JB, MacRae GA. A damage avoidance design steel beam-column moment connection using High-Force-To-Volume dissipators, *Journal of Structural Engineering* 2009, 135(11): 1390-1397.
- [87] Rodgers GW, Denmead C, Leach N, Chase JG. Spectral evaluation of high force – volume lead dampers for structural response reduction, New Zealand Society for Earthquake Engineering Annual Conference, Napier, New Zealand, 2006.
- [88] Rodgers GW, Chase JG, Mander JB. Repeatability and high-speed validation of supplemental lead-extrusion energy dissipation devices, *Hindawi, Advances in Civil Engineering* 2019, 2019(7935026).
- [89] Rodgers GW, Chase JG. Testing of Lead Extrusion Damping devices undergoing representative earthquake velocities, New Zealand Society for Earthquake Engineering Annual Conference, Wellington, New Zealand, 2013.
- [90] Golodrino JC, Chase JG, Rodgers GW, MacRae GA, Clifton CG. Velocity dependence of HF2V devices using different shaft configurations, New Zealand Society for Earthquake Engineering Annual Conference, New Zealand, 2012.
- [91] Pearsons CE, Parkins RN. *The extrusion of metals*, 2nd Edition Revised, London: Chapman & Hall Ltd, 201-221, 1960.
- [92] Vishnupriya V, Rodgers GW, Mander JB, Chase JG. Precision Design Modelling of HF2V Devices, *Structures* 2018, 14: 243-250.

## 2 Characterization and numerical assessment of Lead Damper

---

- [93] Latham DA, Reay AM, Pampanin S. Kilmore Street Medical Centre: application of an advanced flag-shape steel rocking system, New Zealand Society for Earthquake Engineering Annual Conference, Wellington, New Zealand, 2013.
- [94] Wrzesniak D, Rodgers GW, Fragiacommo M, Chase JG. Experimental testing of damage-resistant rocking glulam walls with lead extrusion dampers, *Construction and Building Materials* 2016, 102: 1145-1153.
- [95] Bacht T, Chase JG, MacRae G, Rodgers GW, Rabczuk T, Dhakal RP, Desombre J. HF2V dissipator effects on the performance of a 3 story moment frame, *Journal of Constructional Steel Research* 2011, 67: 1843-1849.
- [96] Dassault Systemes Simulia Corp. Abaqus/CAE user's guide, Providence, RI, USA; 2017.
- [97] Soydan C, Yüksel E, İrttem E. Numerical modeling of single-storey precast frame's pinned connections with a special damper, *COMPADYN 2013, 4th ECCOMAS Thematic Conference on Computational Methods in Structural Dynamics and Earthquake Engineering*, Kos Island, Greece.
- [98] Soydan C, Yüksel E, İrttem E. The Behavior of a steel connection equipped with the Lead Extrusion Damper, *Advances in Structural Engineering* 2014, 17(1).
- [99] Soydan C, Yüksel E, İrttem E. Determination of the characteristics of a new prestressed Lead Extrusion Damper, *16th World Conference on Earthquake Engineering*, Santiago, Chile, 2017.
- [100] Soydan C, Yüksel E, İrttem E. Retrofitting of pinned beam–column connections in RC precast frames using lead extrusion dampers, *Bulletin of Earthquake Engineering* 2018, 16 (1273).
- [101] Patel CC. Seismic analysis of parallel structures coupled by lead extrusion dampers, *International Journal of Advanced Structural Engineering* 2017, 9: 177-190.
- [102] Yang MF, Xu ZD, Zhang XC. Experimental study on lead extrusion damper and its earthquake mitigation effects for large-span reticulated shell, *Steel and Composite Structures* 2015, 18(2): 481-496.
- [103] Zhang XC, Xu ZD. Testing and modelling of a CLEMR damper and its application in structural vibration reduction, *Nonlinear Dynamics* 2012, 70: 1575-1588; DOI:10. 1007/s11071-012-0557-1.
- [104] Yan X, Chen Z, Qi A, Wang X, Shi S. Experimental and theoretical study of a lead extrusion and friction composite damper, *Engineering Structures* 2018, 177(3). 306-317; DOI:10.1016/j.engstruct.2018.09.080.
- [105] CSLPP (Consiglio Superiore dei Lavori Pubblici). D.M. 17 gennaio 2018 in materia di “norme tecniche per le costruzioni”. *Gazzetta ufficiale* n.42 del 20 febbraio 2018, Supplemento ordinario n.8, Ministero delle Infrastrutture e dei trasporti, Roma; 2018, in Italian.
- [106] McKenna F, Fenves GI, Scott MH. *Open System for Earthquake Engineering Simulation*, PEER Report, Berkeley, CA, 2000.
- [107] OpenSeesWiki, online manual. Available online at: [https://opensees.berkeley.edu/wiki/index.php/Main\\_Page](https://opensees.berkeley.edu/wiki/index.php/Main_Page).
- [108] Scozzese F, Gioiella L, Dall'Asta A, Ragni L, Tubaldi E. Influence of viscous dampers ultimate capacity on the seismic reliability of building structures, *Structural Safety* 2021, 91 (102096); DOI:10.1016/j.strusafe.2021.102096.

# 3. Design procedure for the seismic retrofit of RC framed structures

---

This Chapter presents a simple and affordable design procedure for the seismic upgrade of frame structures equipped with hysteretic dampers. The proposed framework is aimed at leading the designer to proportion the damper device(s) in order to achieve a desired structural performance level. According to the method, the structural system composed by frame and dampers is replaced by an equivalent Single Degree of Freedom (SDOF) system, characterized through its secant stiffness and equivalent viscous damping, both defined in relation to a “performance point” which is assigned on the basis of the allowable damage of the frame and on the first mode deformation of the main structure. The global stiffness and strength of the equivalent SDOF system are then distributed along the height of the frame according to a stiffness-proportionality criterion, and the properties of the damper units are calculated depending on the chosen layout. Two case-studies relevant to as many reinforced concrete frames are provided to demonstrate the effectiveness of the suggested procedure, obtaining a satisfactory agreement between the design target and numerical capacity curves. Structural models are coded in the OpenSees framework adopting a concentrated plasticity approach, as studied in Chapter 1. Non-linear dynamic analyses are further performed to assess the reliability of the methodology

## 3.1. Introduction

---

Supplementary energy dissipation in structures is typically achieved by incorporating energy dissipation devices, commonly referred to as dampers, intended to absorb much of the earthquake input energy thus eliminating or limiting the damage to the structural frame. It is noteworthy that, if necessary, energy dissipation devices can be easily replaced at the end of the seismic event [1]. Current dampers can be classified in two categories [1]: (i) viscous dampers, which provide dissipation through the lamination of a viscous fluid forced to pass through an orifice or a valving system, and whose behavior mainly depends on the velocity; and (ii) hysteretic dampers, whose behavior mainly depends on the imposed displacement, and which are further classified into hysteretic steel dampers, friction dampers and metal extrusion dampers, depending on the energy dissipation mechanism.

A common practice for the seismic upgrade of existing structures using supplementary energy dissipation systems consists in determining the size and the suitable location of the dissipation units within the building starting from a trial configuration based on the engineer’s expertise and assessing the retrofitted structure through dynamic or static analyses [2]. The properties and/or the number of the added dissipation units are iteratively changed until the target performance is reached. It is evident that this trial-and-error approach can be a laborious task.

Several procedures have been proposed in recent years for the design of supplementary energy dissipation systems and some of them are based on the Direct Displacement-Based Design (DDBD) method [3]. In the DDBD approach [4], a target displacement demand is defined and related to a given inter-story drift that a

### 3 Design procedure for the seismic retrofit of RC framed structures

---

structure should achieve when subjected to the design earthquake. Based on the target displaced configuration, a “substitute” SDOF model is defined and used to replace the multi-degree of freedom (MDOF) structure. The substitute SDOF model consists of an equivalent linear system, characterized by an effective (secant) stiffness and an effective energy dissipated, represented through an equivalent damping ratio. The design displacement of the equivalent SDOF structure is used in combination with the design displacement response spectrum, to determine the effective period of the substitute structure and, in turn, its effective stiffness. The design base shear is then obtained as the product of the design displacement of the SDOF system and its secant stiffness [5]. Over the years, this approach has been implemented to design new structures and efforts have been made by several authors to adapt the DDBD method to the design and retrofit of structures equipped with dissipating devices [5]-[12], by incorporating an equivalent viscous damping term proportional to the energy dissipation provided by the dampers [3]. It is also worth mentioning the procedure described by Levy et al. [13] who use an equivalent SDOF system to obtain the optimal period of the braced structure by performing a full non-linear dynamic analysis for a set of recorded ground motions.

Kim and Choi [2] applied the general procedure of the DDBD documented in the SEAOC Blue Book [14] in reverse order for evaluating the seismic performance of an existing structure. In principle the procedure is similar to the Capacity Spectrum Method [15], in that the design performance point is determined as the point where the displacement demand of the earthquake equals the plastic deformation capacity of the structure. However, the displacement response spectrum instead of the acceleration-displacement response spectrum (ADRS) is used, and the required damping is calculated as the difference between the total effective damping needed to meet the target displacement and the equivalent damping provided by the structure at the target displacement. For viscous dampers the design process ends here, while for dampers with stiffness, such as viscoelastic or hysteretic dampers, iterations are required because the introduction of the devices increases the stiffness of the system as well. In that case, the capacity curve of the structure needs to be redrawn considering added dampers, and the process is repeated until convergence.

Mazza and Vulcano [16]-[18] developed a building retrofit procedure according to the Performance-Based Design in order to achieve, for a given seismic intensity level, a specified performance objective, for example an assigned level of damage of either the structural or non-structural elements. The procedure aims at controlling the inter-story drifts of the building and, in particular, a proportional stiffness criterion, which assumes the elastic lateral story-stiffness due to the dissipating braces ( $K_{DB}$ ) proportional to that of the unbraced frame ( $K_F$ ), is combined with the DDBD method, in which the design starts from the target deformation. In this iterative approach, the ratio  $K_{DB}/K_F$  is assigned depending on the strength of the unbraced frame and on the protection level expected for the building, and is kept constant at each story throughout the whole procedure. Though initially conceived for essentially regular structures, it has been extended to in-elevation irregular framed structures ([19], [20]) and unsymmetric-plan structures ([21], [22]).

Lin et al. [23] adapted their original method, initially formulated for the design of new and regular buildings equipped with generic energy dissipation systems [6], to retrofit existing buildings using non-linear viscous dampers based on the concept of equivalent linear system. In this method, the location and properties of the

dampers need to be established at the beginning of the process. Londono et al. [24] provided an additional tool, complementary to conventional damper design strategies, that can be used to calculate the stiffness required by the supporting brace to provide the specified effectiveness of the damping action. Raju and Iyer [25] developed a methodology useful for finding the capacity and the distribution of viscous fluid dampers fitted in different mechanisms (specifically in chevron, upper toggle and scissor jack mechanisms) located in buildings.

Bergami and Nuti [26] developed a general procedure, valid for any typology of dissipative brace, intended to achieve the following performance objectives: (i) protect the structure against structural damage or collapse; (ii) avoid non-structural damage; and (iii) avoid excessive base shear. This DDBD approach is based on the Capacity Spectrum Method [27] and consists of an iterative procedure where the capacity curve of the braced structure is evaluated at each iteration step considering the different contributions of the as-built structural frame and of the damped brace systems. The desired performance of the structure is selected as the target displacement corresponding to a selected limit state for a given seismic action, and the additional damping introduced from the dissipative brace system is estimated as the difference between the total damping required to achieve the performance point, and the hysteretic damping of the structure without braces.

Di Cesare and Ponzo [28] focused on steel hysteretic brace systems and proposed an iterative procedure intended to control the maximum inter-story drifts, by regularizing the stiffness and strength along the height of the braced building according to the regularity criteria provided by seismic codes (e.g. [29], [30]). This method has found applications in some recent publications ([31], [32]).

Barbagallo et al. [33] focused on the retrofit of existing reinforced concrete (RC) frame buildings using Buckling Restrained Braces (BRBs). The authors highlighted that all the procedures in the literature do not allow a direct control of drift demand; for this reason, they proposed an iterative method, consistent with the prescriptions of Eurocode 8 (EC8) [29], to determine the size of BRBs at each story. Differently from the previous methods, this approach operates on the MDOF system (not on the substitute SDOF) and the non-linear static analysis is performed only to evaluate the internal force of the frame members.

Ferraioli and Lavino [3] identified some critical aspects common to all the previous methods: (i) the frame-damped brace interaction is neglected, as no method considers the increase of the axial force in the frame columns and the consequent reduction of the deformation capacity; (ii) the proportional stiffness criterion commonly adopted to distribute the damper properties along the height of the frame may produce a non-uniform distribution of peak story drift under earthquake ground motions, not preventing soft-story mechanisms. Moreover, the existing methods generally include only the first mode contribution, neglecting the influence of higher modes in the response of MDOF elastoplastic systems, and in case of asymmetric-plan buildings the behavior of the RC bare frame is dominated by the torsional effects, which disappear when the damped braced structure is analyzed. For this reason, the authors divided their procedure in two phases: in the first phase, a preliminary design of the dissipative braces is conducted, and relevant properties and position are determined according to the method of Mazza and Vulcano [18]; in the second phase, the

### **3 Design procedure for the seismic retrofit of RC framed structures**

---

Displacement-based Adaptive Pushover (DAP) [34] is carried out and an adaptive version of the Capacity Spectrum Method is developed (starting from the classical version of Fajfar [27]), in order to overcome the assumptions that the structure vibrates predominantly in a single mode and that the dynamic properties of the structure remain unchanged after the insertion of the braces.

Recently, Nuzzo et al. [35], [36] proposed a procedure, similar to the one of Bergami and Nuti [26], valid for design and retrofit of frame structures equipped with hysteretic dampers, taking into account the flexibility of the supporting brace, usually provided to connect the device to the external frame. However, differently from reference [26], the pushover analysis is performed only at the beginning of the procedure in order to define the capacity curve of the bare frame, while in the following steps, the capacity curve of the braced frame is evaluated by means of simple analytical equations.

Some authors proposed simplified procedures to directly determine the characteristics of the supplementary energy dissipation systems avoiding iterations. Diotallevi et al. [37] focused on non-linear viscous dampers and based the retrofit procedure on a new dimensionless parameter, called damper index, which has been introduced in the equations of motion. This method was later extended by Landi et al. [38] to include the case of structures exceeding the elastic limit.

Other authors decided to adopt energy-based methods. Silvestri et al. [39] and Palermo et al. [40] proposed a 5-steps energy-based procedure for the dimensioning of viscous dampers, starting from the practical indications given by Christopoulos and Filiatrault [1]. The method is direct, no iterations are needed, and it does not require to introduce fictitious springs, since only the additional damping is considered; differently from the other procedures, this method requires the application of time-history analyses instead of pushover analyses.

Durucan and Dicleli [41] proposed an iterative energy-based approach to upgrade the performance of seismically vulnerable RC buildings. The methodology is based on the equal energy dissipation principle, whereby the energy dissipated by an elastic system can be assumed to be equal to that dissipated by an identical (non-linear) system that yields at a certain lateral force level. The difference between the areas under the elastic and inelastic base shear force vs. roof displacement curves is the required additional energy that needs to be absorbed by the retrofitting system.

Terenzi [42] improved the method originally proposed [43], focusing on the retrofit of RC structures upgraded with fluid viscous dampers. This approach does not require any preliminary evaluation of the input energy demand and is intended only for relatively stiff frame structures, where the seismic performance can be enhanced by incorporating a supplementary damping system with limited stiffness capacity.

Finally, De Domenico et al. [44] presented a deep review of different design strategies for the protection of buildings using fluid viscous dampers, concluding that energy-based design strategies provide the best method to define the optimal damper distribution in the building, and permits a global control of the seismic response including displacements, accelerations, forces and energy-specific quantities.

As a matter of fact, most of the methods presented above are not straightforward and nowadays many practitioners still have little confidence in supplementary energy dissipation strategies, especially for applications to ordinary constructions where simple and affordable methods may foster the adoption of seismic mitigation strategies based on damper technology. The present study proposes an effective and easy to use procedure for the seismic upgrade of existing frame structures by means of hysteretic damped braces. The procedure is suitable for professional applications and consists of two main parts: (i) a simple method to define the global properties of the damped brace system, described by means of an equivalent SDOF system; and (ii) a strategy to determine the distribution of the properties of the equivalent SDOF damped brace along the height and across each floor of the structure.

The procedure to calculate the global properties of the energy dissipation system is based on the Capacity Spectrum Method [15], [27]. Similarly to the method [35], the capacity curve of the main frame is determined at the beginning of the process via non-linear static analysis (NLSA), while the capacity curve of the braced frame is defined by simple analytical equations, thus providing an iterative procedure that converges in few steps and that can be implemented in a spreadsheet.

The second part of the procedure is focused on distributing the effective properties of the damped brace system along the height and across the stories of the building. A method, derived from the literature and based on the principle of distributing the stiffness and strength proportionally to the stiffness of each floor calculated via dynamic analysis is presented. Finally, the properties of the dissipation braces at each floor are determined accounting for the actual number and layout of the devices.

The ease and effectiveness of the method is illustrated analyzing two RC buildings. The first structure is an existing 4-story frame building located in a medium/high seismic area and designed according to outdated standards [28], which needs to be retrofitted to comply with the performance requirements of the most recent Italian norm [30]. The second structure is a residential 6-story building, designed according to the current Italian Building Code [30] for a low seismicity zone [45], which is upgraded to resist higher seismic excitations corresponding to a high seismicity area. Both structures are supposed to fail in flexure and specific issues, typical of existing buildings (namely, shear failure of beams, columns, or beam-column joints) are not taken into account in the numerical models.

The procedure is applied to the two case-studies and illustrated step by step, discussing the main results. The effects of the distribution of the damper properties at the various floors are also highlighted by examining, as an alternative to the method recommended in the procedure, a second procedure available in the literature. Non-linear static and dynamic analyses (NLSA and NLDA) are eventually performed.

It must be finally mentioned that, though the case-studies presented in the paper refer to RC structures, the procedure herein proposed has been formulated for conventional, flexible framed structures and is applicable to steel structures as well.

3.2. Design procedure of the damped brace system

This section presents a design methodology for the upgrade of an existing structure via hysteretic dampers, to achieve the specified performance level. The design procedure is based on the Capacity Spectrum Method [46]: the required performance is expressed in terms of a target displacement demand, associated to the acceptable damage to the main frame, and the structural response is obtained by reducing the demand response spectrum as a function of the additional damping introduced by the supplementary energy dissipation. Iterations are required since the addition of braces increases the stiffness of the system and the capacity curve has to be continuously updated as the characteristics of the damped braces are defined.

The procedure is applicable to frame buildings equipped with hysteretic dampers with behavior dependent solely on the axial deformation, and insensitive to velocity. The non-linear response of the bare structure is initially estimated by performing a pushover analysis on the multi-degree of freedom (MDOF) frame and then idealized as the bilinear curve of an equivalent single-degree of freedom (SDOF) system, as prescribed in Eurocode 8 – Part 1 [47]. The equivalent SDOF unbraced frame (F) and the damped brace (DB) systems are considered as bi-linear springs working in parallel, providing the equivalent response of the combined Frame + Damped Brace (F+DB) system, Figure 3-1.

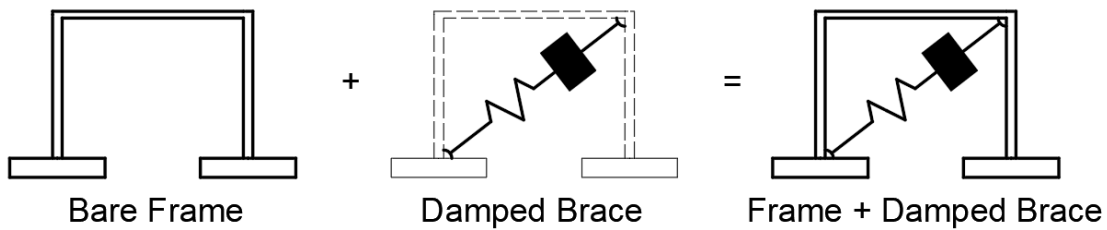


Figure 3-1: Rheological model of the unbraced frame, the damped brace and the combined braced frame systems [48]

The theoretical force–deflection curve of a hysteretic damper is shown in Figure 3-2, where  $N_D$  is the output force,  $d_D$  is the axial deflection,  $N_{yD}$  and  $d_{yD}$  are the yield force and yield deflection of the device,  $N_{uD}$  and  $d_{uD}$  are the ultimate force and deflection, and  $r \geq 0$  is the hardening parameter; the area enclosed in the hysteresis loop corresponds to the energy dissipated by the damper during a cycle.  $K_D = N_{yD}/d_{yD}$  is the initial or elastic stiffness and  $K_{2,D} = r K_D$  is the post-yield stiffness. Hysteretic dampers can have either a hardening behavior with positive post-yield stiffness ( $r > 0$ ), or an elastic-perfectly plastic behavior ( $r = 0$ ), which provides an output force independent on the accommodated deflection [49]. In the description of the procedure, hysteretic dampers with elastic-perfectly plastic behavior are assumed, but the method can be generalized to dampers with any  $r \geq 0$ .

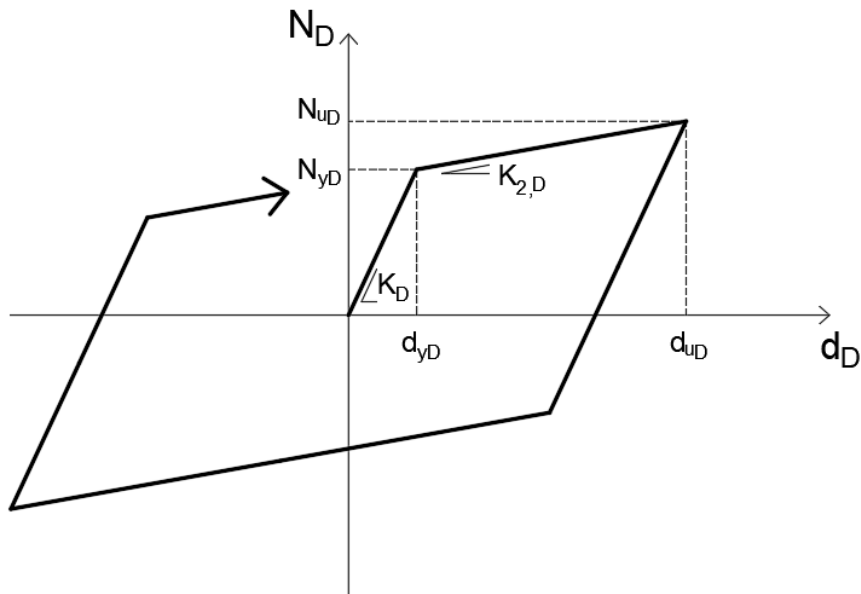


Figure 3-2: Theoretical force – deflection diagram of hysteretic dampers [48]

The method is developed in the acceleration-displacement response spectrum (ADRS) space and the DB capacity curve is obtained as the difference between the capacity curve of the F+DB system achieving the target displacement, and the capacity curve of the bare frame F. Then, the mechanical properties of the identified equivalent SDOF damped brace are distributed at each story according to a proportionality criterion with respect to the first mode properties of the unbraced frame.

The design procedure, which consists of 5 steps, is schematically shown in the flowchart in Figure 3-3 and detailed through the following sub-sections, each one corresponding to a single step of the framework. It is necessary to recall that a pre-requisite for the application of the procedure is that the behavior of the frame building is governed by the first mode, which legitimates the condensation of the MDOF structure to the equivalent SDOF system.

### 3 Design procedure for the seismic retrofit of RC framed structures

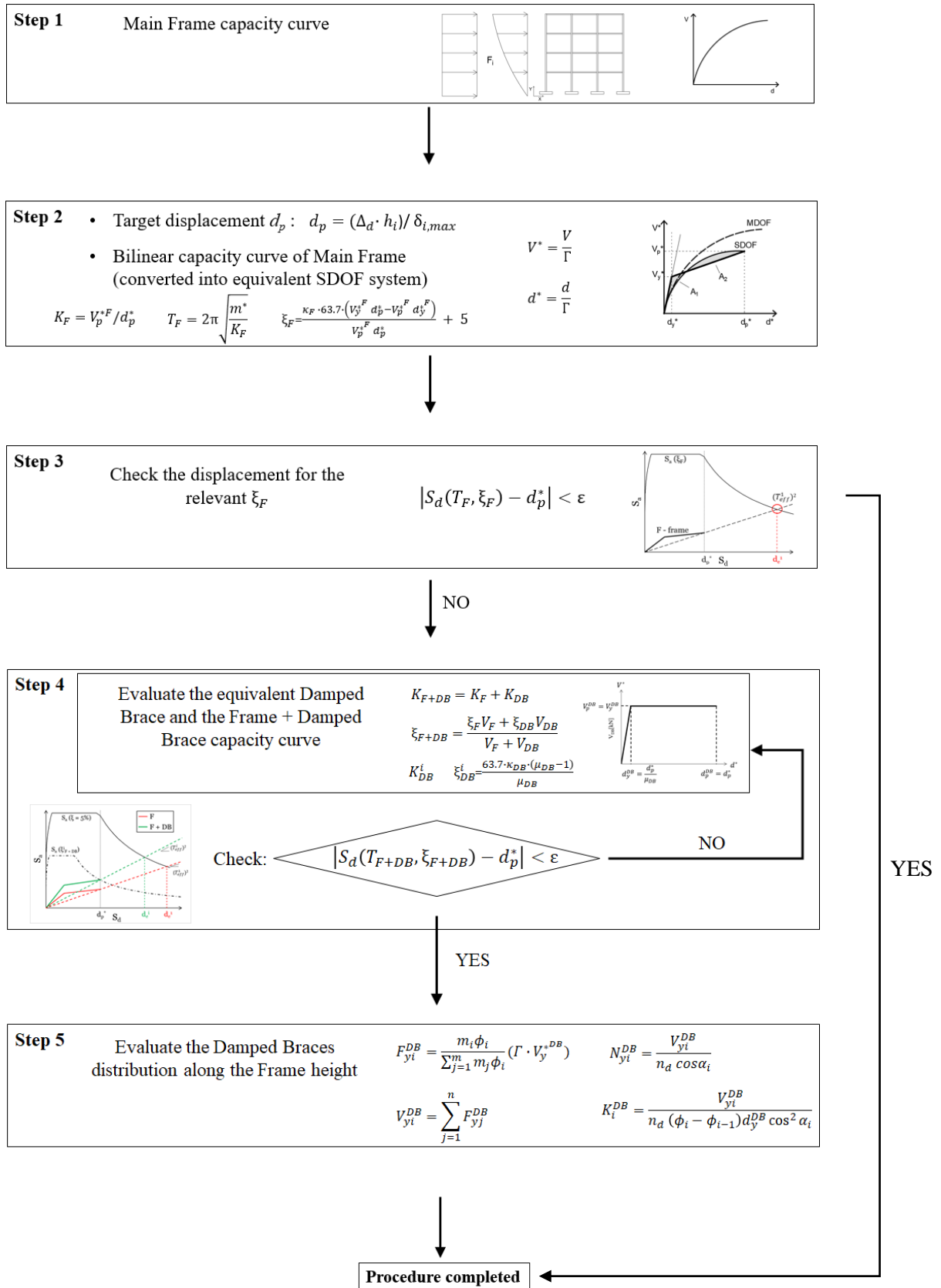


Figure 3-3: Flowchart of the proposed procedure [48]

*3.2.1 Define the capacity curve of the Main Frame*

In the first step of the procedure, the capacity curve of the as-built structure is evaluated via a non-linear static analysis: the structural frame is statically loaded with gravity loads combined with a set of lateral forces to calculate the relationship between the lateral force and the lateral displacement of a suitable point of the structure, e.g., the center of mass of the roof. According to the prescriptions of [47], two lateral load distributions are considered: a uniform pattern, proportional to the floor masses  $m_i$  (with  $i = 1 \div n$ , where  $n$  is the total number of floors) and a modal pattern, obtained multiplying the first mode eigenvector components  $\phi_i$  by the corresponding floor masses  $m_i$ . The load distributions are applied in both the positive and negative direction of each axis, considering 5% accidental eccentricity of the center of mass of each story [47]. For each load distribution the relevant base shear force vs. roof displacement ( $V_F - d_F$ ) curve is calculated, and the lowest curve is taken as the capacity curve of the main (unbraced) structure.

The  $V_F - d_F$  capacity curve of the MDOF structure is then converted to the  $V_F^* - d_F^*$  capacity curve of the equivalent SDOF system through the modal participation factor  $\Gamma$  (Eq. 3.1) [27], [47]. The displacement  $d_F^*$ , the force  $V_F^*$  and the mass  $m^*$  of the equivalent SDOF system are determined via equations (3.2) – (3.4):

$$\Gamma = \frac{\sum_{i=1}^n m_i \phi_i}{\sum_{i=1}^n m_i \phi_i^2} \quad (3.1)$$

$$d_F^* = \frac{d_F}{\Gamma} \quad (3.2)$$

$$V_F^* = \frac{V_F}{\Gamma} \quad (3.3)$$

$$m^* = \sum_{i=1}^n m_i \phi_i \quad (3.4)$$

*3.2.2 Identify the target displacement and define the equivalent bilinear capacity curve of the Main Frame*

The target displacement  $d_p$  of the structure is identified depending on the required level of performance in accordance with the assumed design code. By referring to, e.g., the Italian Building Code (NTC) [30], the target displacement  $d_p$  can be chosen in order to fulfill the limits recommended in Table 7.3.III of NTC for the protection of both structural and non-structural elements. For example, depending on the considered limit state, the target displacement limiting damage to non-structural elements corresponds to a maximum inter-story drift ratio  $\Delta_d$  ranging between 0.5% and 0.75% [35].

In order to fit the required performance at each story, the lateral displacement at the top of the frame is bound to match the target displacement

$$d_p = \min \frac{\Delta_d \cdot h_i}{\delta_i} \quad (3.5a)$$

where  $\Delta_d$  is the target inter-story drift ratio,  $h_i$  is the height of the  $i^{\text{th}}$  story, and  $\delta_i = (\phi_i - \phi_{i-1})$ . The product  $\Delta_d \cdot h_i$  represents the target drift of the  $i^{\text{th}}$  story, while  $\delta_i$  is the difference between the first mode eigenvector components of the adjacent stories. If the inter-story height is uniform, i.e.,  $h_i = h_0$  for  $i = 1, \dots, n$  ( $n = \text{number of stories}$ ), then Equation (3.5a) can be simplified as

$$d_p = \frac{\Delta_d \cdot h_0}{\delta_{max}} \quad (3.5b)$$

with  $\delta_{max} = \max(\phi_i - \phi_{i-1})$ .

By setting the ultimate displacement of the as-built structure equal to the identified target displacement  $d_u = d_p$ , the ductility of the main frame is defined as  $\mu_F = d_p/d_y$  where  $d_y$  is the yield displacement of the frame. Obviously, if the target is that the structure remains in the elastic range,  $\mu_F = 1$ .

Once the target displacement  $d_p$  (and the corresponding base shear force of the main frame  $V_p^F$ ) is assigned, the bilinear curve of the equivalent SDOF system is evaluated in accordance with reference [26] and clause C.7.3.4.2 of reference [51]. Such equivalent bilinear curve is defined by three conditions, namely: (i) same initial stiffness as the initial stiffness of the MDOF capacity curve, (ii) crossing of the performance point  $(d_p^*, V_p^{*F})$  where  $d_p^* = d_p/\Gamma$  and  $V_p^{*F} = V_p^F/\Gamma$ , and (iii) equivalence of areas A1 and A2 between the two curves, as shown in Figure 3-4.

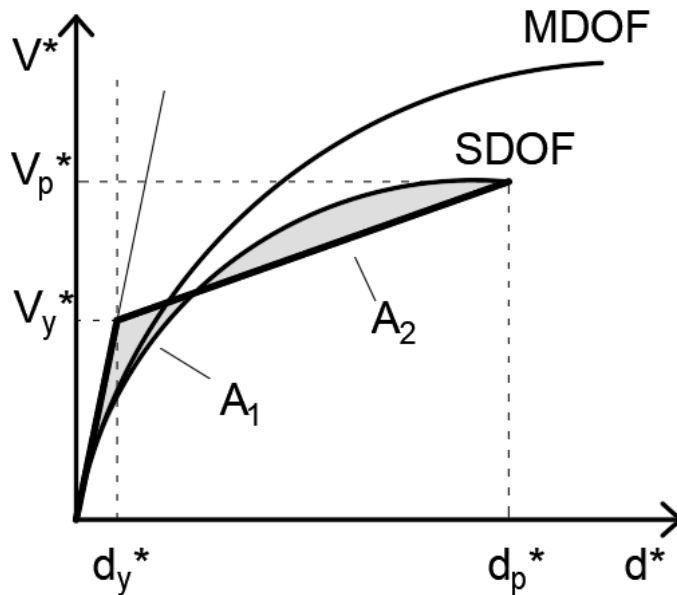


Figure 3-4: Definition of the equivalent bilinear curve according to [51], [48]

Through the equivalent bilinear curve, the SDOF system is characterized by an equivalent secant stiffness  $K_F^* = V_p^{*F} / d_p^*$  and an equivalent viscous damping ratio  $\xi_F$  (in percent) defined as in [50], [51]:

$$\xi_F = \frac{\kappa_F \cdot 63.7 \cdot (V_y^{*F} d_p^* - V_p^{*F} d_y^{*F})}{V_p^{*F} d_p^*} + 5 \quad (3.6)$$

where parameter  $\kappa_F$  accounts for the energy dissipation capacity of the bare structure and can be taken as 1.0 for structures with high damping capability (providing wide and stable hysteresis loops), 0.66 for structures with moderate damping capability (with moderate change of the hysteresis loops) and 0.33 for structures with low damping capability (with hysteresis loops affected by substantial pinching and decrease of area) [15]. On the right side of Eq. (3.6) the first term represents the contribution of the inelastic deformation of the frame to the total equivalent damping, and the second term is the 5% inherent viscous damping of the structure. Though in the current literature the damping ratio to be considered in NLTH analyses of both RC and steel structures is estimated in the range of 0.5% to 2% [52]-[55], a 5% value is chosen in order to take into account the energy dissipation coming from possible infill panels or other non modelled non-structural components.

### 3.2.3 Check the displacement for the relevant $\xi_F$

The equivalent bilinear capacity curve  $V_F^* - d_F^*$  is converted into the capacity spectrum in the acceleration-displacement response spectrum (ADRS) space, where the spectral coordinates are defined as  $S_a = V^{*F} / m^*$  (acceleration in  $m/s^2$ ) and  $S_d = d_F^*$  (displacement in m).

The seismic action for the considered performance level is defined in terms of acceleration – displacement response spectra corresponding to different damping levels. For example, a 2% to 5% damped response spectrum is generally used to represent the demand when the structure responds as linearly-elastic, while higher damped response spectra are used to account for the hysteretic non-linear structural response of the system. To develop damped demand spectra, Equations (3.7a) and (3.7b) [47] are used in the procedure

$$S_a(T; \xi) = S_a(T; \xi = 5\%) \sqrt{\frac{10}{5 + \xi}} \quad (3.7a)$$

$$S_d(T; \xi) = S_d(T; \xi = 5\%) \sqrt{\frac{10}{5 + \xi}} \quad (3.7b)$$

where T is the period of vibration in seconds. Response spectra are generally plotted in  $S_a$  vs T or  $S_d$  vs T coordinates, however in order to have a direct comparison to the capacity spectrum, the response spectra are plotted in the acceleration-displacement plane, with a set of coordinates defined by  $S_a$  and  $S_d$ . It should be noted that when the spectral values are plotted in ADRS format, the period is represented by lines radiating from the origin [56].

### 3 Design procedure for the seismic retrofit of RC framed structures

The spectral displacement of the main frame for the considered seismic action is determined analytically. The secant stiffness of the capacity spectrum to the target displacement  $K_F^* = V_p^{*F} / d_p^*$  is used to calculate the effective period of the main structure  $T_F^* = 2\pi \sqrt{\frac{m^*}{K_F^*}}$  and hence the corresponding spectral displacement  $S_d(T_F^*; \xi_F) = S_d(T_F^*; \xi = 5\%) \sqrt{\frac{10}{5+\xi_F}}$  where  $\xi_F$  is the equivalent viscous damping ratio of the unbraced structure defined by Eq. (3.6). If  $S_d(T_F^*; \xi_F) \leq d_p^*$  the unbraced structure meets the performance requirement and the procedure ends (no retrofit is required). If  $S_d(T_F^*; \xi_F) > d_p^*$  the main frame alone is unable to meet the performance level and the damped brace system must be introduced.

#### 3.2.4 Evaluate the equivalent damped brace and the frame + damped brace capacity curve

An iterative procedure is used to evaluate the damped brace. In the first iteration the undamped structure is considered with effective stiffness  $K_{eff}^1 = K_F^*$  and effective period  $T_{eff}^1 = T_F^*$ , with  $K_F^*$  and  $T_F^*$  defined above. The line radiating from the origin with slope  $(T_{eff}^1)^2$  identifies, where it crosses the 5% damped response spectrum, the spectral displacement  $d_e^1$  of an elastic oscillator with period  $T_{eff}^1$  corresponding to the effective period of the unbraced frame at maximum response  $d_p^*$ , i.e.  $d_e^1 = S_d(T_{eff}^1; \xi = 5\%)$  (Figure 3-5).

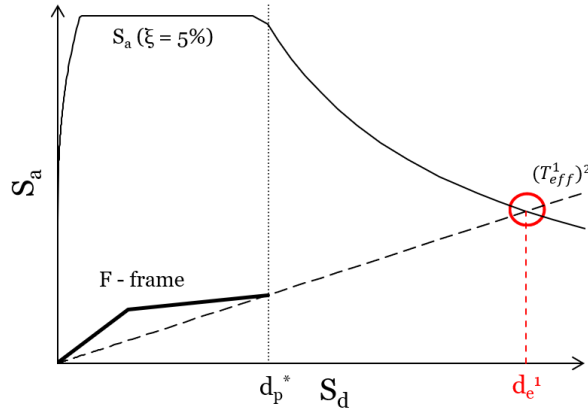


Figure 3-5: Evaluation of the spectral displacement  $d_e^1$  at first iteration [48]

In order to meet the target displacement  $d_p^*$ , additional damping must be supplied by the damped brace. According to Eq. (3.7b), the total damping  $\xi_{eff}^1$  required for the combined frame and damped brace (F+DB) system shall fulfill the displacement equality

$$S_d(T_{eff}^1; \xi_{eff}^1) = d_p^* \quad (3.8)$$

from which a first estimate of the effective viscous damping  $\xi_{eff}^1$  is determined as

$$\xi_{eff}^1 = 10 \cdot \left( \frac{S_d(T_{eff}^1; \xi = 5\%)}{d_p^*} \right)^2 - 5 = 10 \cdot \left( \frac{d_e^1}{d_p^*} \right)^2 - 5 \quad (3.9)$$

The properties of the equivalent SDOF damped brace are determined as a function of ductility  $\mu_{DB}$ , which is assigned as a design input depending on the employed damper technology. An optimal design ductility for hysteretic steel dampers is assumed in the range of  $4 \div 10$  [31], whereas for friction and extrusion dampers there is no technological limitation to the displacement capacity that can be achieved without strength degradation [49]. The damper yield strength  $V_y^{DB}$ , which coincides with  $V_p^{DB}$  for devices characterized by an elastic-perfectly plastic behavior (Figure 3-2), is instead the unknown of the procedure.

The equivalent viscous damping of the damped brace system  $\xi_{DB}$  is calculated according to expression [50]

$$\xi_{DB} = \frac{\kappa_{DB} \cdot 63.7 \cdot (V_y^{*DB} d_p^{*DB} - V_p^{*DB} d_y^{*DB})}{V_p^{*DB} d_p^{*DB}} \quad (3.10)$$

and by setting the ultimate displacement of the equivalent SDOF damped brace equal to the target displacement  $d_u^{*DB} = d_p^*$ , which yields  $d_y^{*DB} = d_p^*/\mu_{DB}$ , Eq. (3.10) simplifies to Eq. (3.11):

$$\xi_{DB} = \frac{63.7 \cdot \kappa_{DB} \cdot (\mu_{DB} - 1)}{\mu_{DB}} \quad (3.11)$$

In Eqs. (3.10) and (3.11) the value of  $\kappa_{DB}$  can be selected based on experience and past applications or calibrated from experimental evidence.

The yield strength of the damped bracing system at first iteration  $V_{y,1}^{*DB} = V_{p,1}^{*DB}$  is hence evaluated through the energetic equivalence of Eq. (3.12) [54]:

$$\xi_{eff}^1 \cdot V_p^{*F} = \xi_F \cdot V_p^{*F} + \xi_{DB} \cdot V_{p,1}^{*DB} \quad (3.12)$$

where  $\xi_F$  is defined through Eq. (3.6). The introduction of the damped brace in parallel with the main frame yields an increase of  $V_{p,1}^{*DB}$  of the total strength of the combined system F + DB at the target displacement  $d_p^*$ .

The bilinear curve of the equivalent SDOF model of the retrofitted structure is constructed and plotted in  $S_a - S_d$  coordinates to check if the identified damped brace is appropriate. The ultimate displacement of the upgraded capacity curve is equal again to the target displacement  $d_p^*$ , while the correspondent base shear force is  $V_{p,2}^{*F+DB} = V_p^{*F} + V_{p,1}^{*DB}$ . The new equivalent SDOF Frame + Damped brace (F + DB) system is characterized by an equivalent viscous damping

### 3 Design procedure for the seismic retrofit of RC framed structures

$\xi_{F+DB}^2 = \frac{\xi_F \cdot V_p^{*F} + \xi_{DB} \cdot V_{p,1}^{*DB}}{V_p^{*F} + V_{p,1}^{*DB}} + 5$  and by an effective stiffness and an effective period equal to

$K_{eff}^2 = \frac{V_{p,2}^{*F+DB}}{d_p^*}$  and  $T_{eff}^2 = 2\pi \sqrt{\frac{1}{K_{eff}^2}}$ , respectively. The spectral displacement for the considered damping

ratio is determined as  $S_d(T_{eff}^2; \xi_{F+DB}^2)$  and checked against the target displacement  $d_p^*$ . If  $|S_d(T_{eff}^2; \xi_{F+DB}^2) - d_p^*|/d_p^* \leq \varepsilon$  (with  $\varepsilon$  sufficiently small, e.g. 0.05), the process ends and the properties of the damped bracing systems at each floor are determined in the next step, otherwise the iteration continues until the difference between  $d_p^*$  and  $S_d(T_{eff}^i; \xi_{F+DB}^i)$  ( $i$  = number of iteration) is sufficiently small, Figure 3-6.

At the  $i^{\text{th}}$  iteration, the shear force at the target displacement  $d_p^*$  is updated as  $V_{p,i}^{*F+DB} = V_p^{*F} + V_{p,(i-1)}^{*DB}$ , and the equivalent viscous damping ratio of the equivalent SDOF Frame + Damped brace (F + DB) system is determined from Eq. (3.13):

$$\xi_{F+DB}^i = \frac{\xi_F \cdot V_p^{*F} + \xi_{DB} \cdot V_{p,(i-1)}^{*DB}}{V_p^{*F} + V_{p,(i-1)}^{*DB}} \quad (3.13)$$

The effective stiffness and the effective period are  $K_{eff}^i = \frac{V_{p,i}^{*F+DB}}{d_p^*}$  and  $T_{eff}^i = 2\pi \sqrt{\frac{1}{K_{eff}^i}}$ , respectively. The required effective viscous damping at the  $i^{\text{th}}$  iteration is calculated according to Eq. (3.8) and is equal to  $\xi_{eff}^i = 10 \cdot \left(\frac{d_e^i}{d_p^*}\right)^2 - 5$  (%), where  $d_e^i = S_d(T_{eff}^i; \xi = 5\%)$ . The strength of the equivalent SDOF damped brace is eventually calculated via Eq. (3.14), where the unknown quantity is  $V_{p,i}^{*DB} = V_{y,i}^{*DB}$

$$\xi_{eff}^i \cdot (V_p^{*F} + V_{p,(i-1)}^{*DB}) = \xi_F \cdot V_p^{*F} + \xi_{DB} \cdot V_{p,i}^{*DB} \quad (3.14)$$

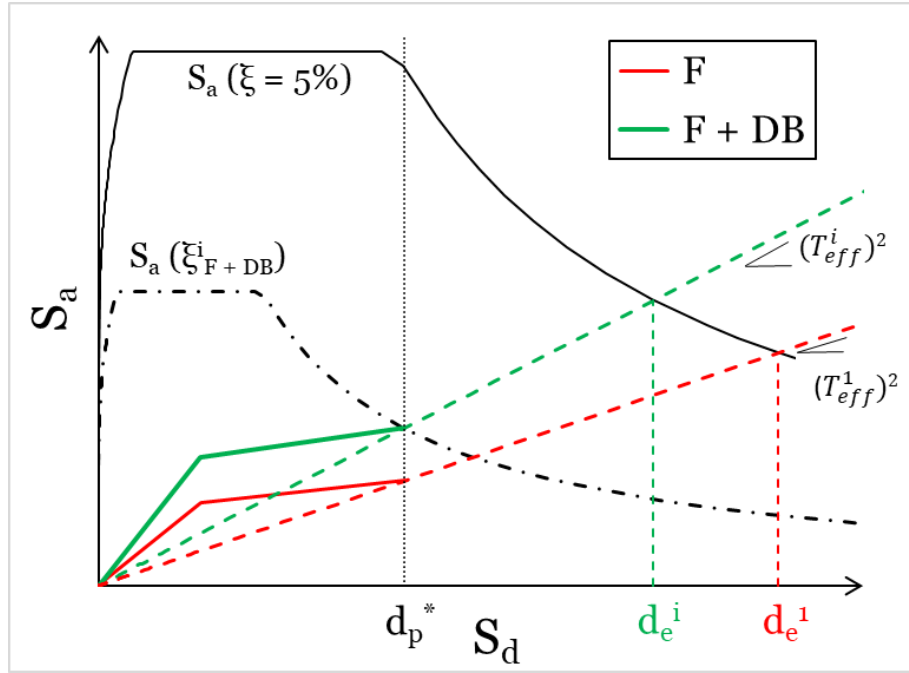


Figure 3-6: Graphical procedure for design of the damped braced structure [48]

### 3.2.5 Evaluate the Damped Brace distribution along the Frame height

Once the properties of the equivalent SDOF damped brace are determined, their distribution across the stories of the structure is performed on the basis of a proportionality criterion ([16]-[22]).

The method uses, as input parameters, the yield properties (strength  $V_y^{DB}$  and displacement  $d_y^{DB}$ ) of the equivalent SDOF damped brace and the components  $\phi_i$  of the eigenvector associated to the first mode of vibration of the main frame. At each floor the properties of the braces equipped with hysteretic dampers are determined via Eq. (3.15) – (3.18), see Figure 3-7.

$$F_{yi}^{DB} = \frac{m_i \phi_i}{\sum_{j=1}^m m_j \phi_j^2} (\Gamma \cdot V_y^{*DB}) \quad (3.15)$$

$$V_{yi}^{DB} = \sum_{j=1}^{n_d} F_{yj}^{DB} \quad (3.16)$$

$$N_{yi}^{DB} = \frac{V_{yi}^{DB}}{n_d \cos \alpha_i} \quad (3.17)$$

$$K_{yi}^{DB} = \frac{V_{yi}^{DB}}{n_d (\phi_i - \phi_{i-1}) d_y^{DB} \cos^2 \alpha_i} \quad (3.18)$$

here  $N_{yi}^{DB}$  and  $K_{yi}^{DB}$  represent the strength and stiffness of the single damped brace installed at the  $i^{\text{th}}$  floor, where  $n_d$  is the total number of dampers per floor chosen by the designer. At each floor, the damped braces are tuned in order to guarantee that the mode shape of the braced frame matches the first mode shape of the as-built structure [18], [19], [35]. If the frame remains elastic, the deformation remarks its fundamental

### 3 Design procedure for the seismic retrofit of RC framed structures

mode shape, ensuring the same inter-story drift distribution [35]. It must be noted that Equations (3.17) and (3.18) which are used to calculate the properties of the individual damped brace refer to the diagonal configuration shown in Figure 3-7, but can be easily modified to adapt to other configurations, such as chevron, upper toggle, etc.

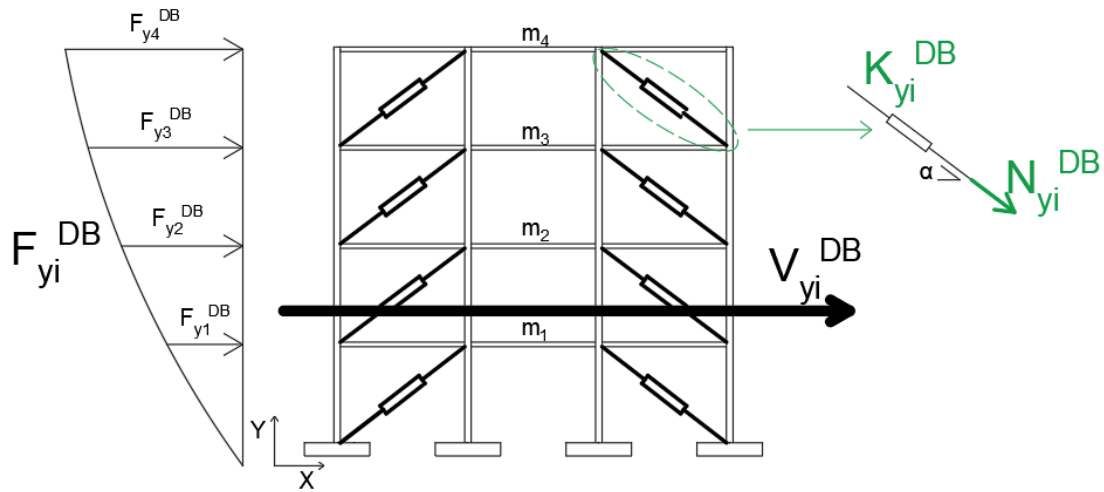


Figure 3-7: Quantities for design of diagonal braces with hysteretic dampers [48]

It is worth noting that the distribution method requires, as input variable, the number of damped braces at every story. This choice depends ultimately on the designer, who has to take both architectural demands related to, e.g., the invasiveness of braces in facades, and economic issues related to local strengthening of columns and beams subjected to increase in internal forces due to the actions transmitted by the braces [58].

### 3.3. Application of the design procedure

The design method presented in Section 2 is applied to two case-study structures. The first structure is an existing 4-story reinforced concrete (RC) building located in Potenza (Italy) [28], in a medium/high seismic area with PGA of  $2.45 \text{ m/s}^2$ , and it is assumed to be founded on soil type B with topographic factor  $T_1$ . This structure backs to the '80s of the last century, when seismic regulations were not yet developed and only gravity loads were considered for design; for this reason, it is assumed as paradigmatic of a large part of the Italian building stock, characterized by poor seismic details. The main dimensions of the building in plan and in elevation are sketched in Figure 3-8. Columns have a square section of  $30 \times 30 \text{ cm}$  and are reinforced with  $4\phi 16$  longitudinal steel bars plus  $2\phi 14$  skin bars at the ground floor, and with  $4\phi 16$  longitudinal bars at the other floors;  $\phi 6$  stirrups with  $15 \text{ cm}$  spacing are used at each floor. Beams have a rectangular section of  $30 \times 50 \text{ cm}$ ; the longitudinal reinforcement consists of  $4\phi 14$  steel bars on top and  $2\phi 14$  on bottom at end sections, while the rebar is reversed in the middle of the beam. The transverse reinforcement consists of  $\phi 6$  stirrups with spacing of  $15 \text{ cm}$  at end sections and  $20 \text{ cm}$  in the middle. The concrete compressive strength  $f_{ck}$  is  $20 \text{ MPa}$  and the steel yield strength  $f_{yk}$  is  $375 \text{ MPa}$ ; floor masses are  $86 \text{ ton}$  at the last floor and  $115 \text{ ton}$  at all the other stories. Additional information is reported in reference [28].

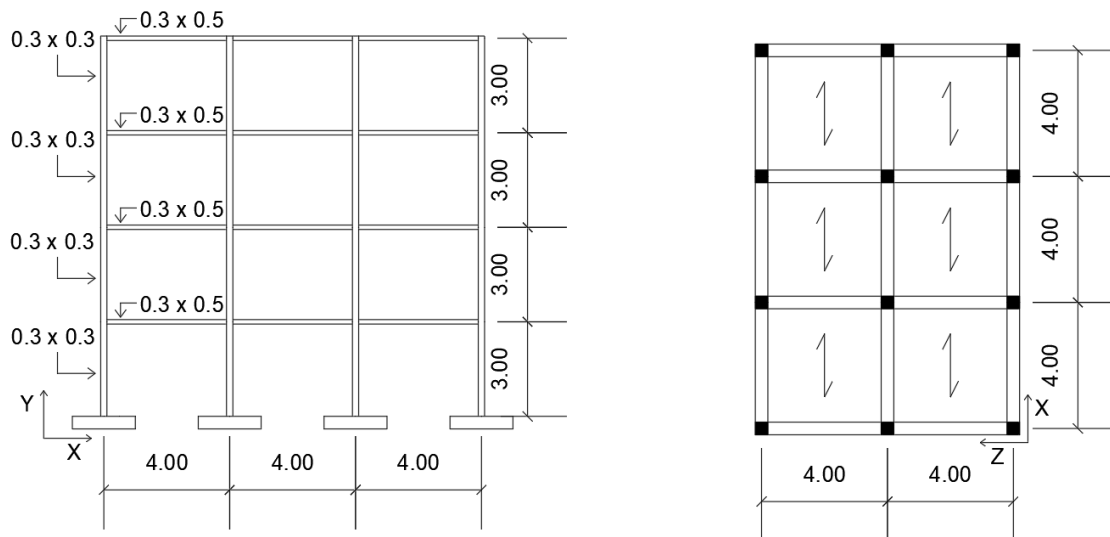


Figure 3-8: Existing RC frame building in Potenza: elevation and plan views [48]

The second structure is a residential 6-story RC building, designed according to the most recent Italian Building Code [30], which provides a similar approach to the Eurocode 8 [29]. Sketches of the building, with the main dimensions in plan and in elevation, are reported in Figure 3-9; structural loads and additional design information are reported in reference [45]. According to the assumed code, the structural frame was designed with seismic details for a low seismicity zone corresponding to the municipality of Pordenone, Italy [45], characterized by a  $\text{PGA} = 1.91 \text{ m/s}^2$  and soil type B. Geometry and reinforcement of columns and beams are illustrated in Figure 3-10 and floor masses are reported in Table 3-1; the concrete compressive strength  $f_{ck}$  is  $25 \text{ MPa}$  and the steel yield strength  $f_{yk}$  is  $450 \text{ MPa}$ .

### 3 Design procedure for the seismic retrofit of RC framed structures

In this study, the structure is upgraded to resist to higher seismic excitations corresponding to a high seismic area.

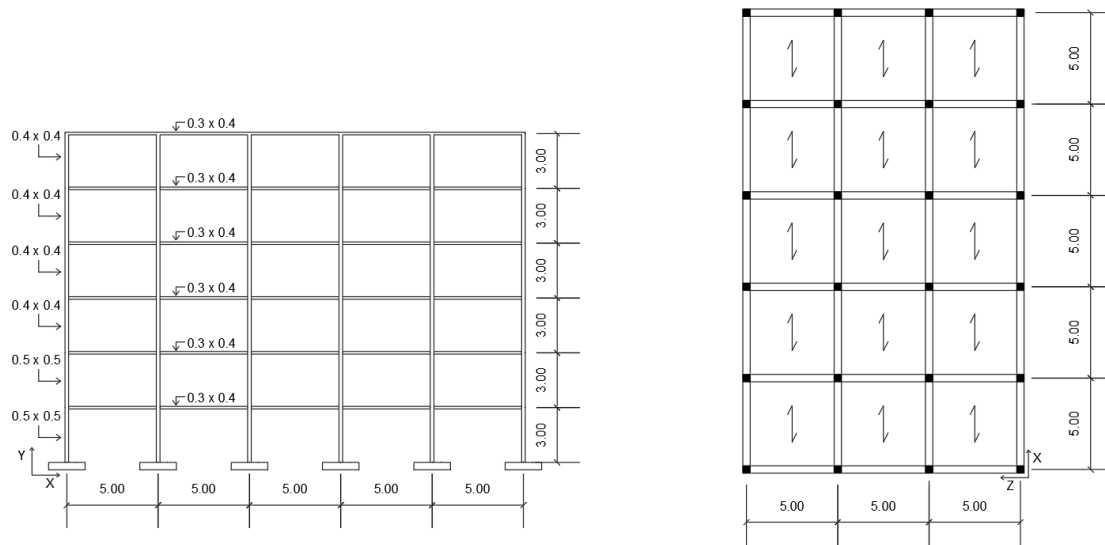


Figure 3-9: Existing RC framed building in Pordenone: elevation and plan views [48]

Floors	1 <sup>st</sup>	2 <sup>nd</sup>	3 <sup>rd</sup>	4 <sup>th</sup>	5 <sup>th</sup>	6 <sup>th</sup>
Masses [ton]	239.7	231.4	223.2	223.2	223.2	124.4

Table 3-1: Floor masses of the existing RC framed building in Pordenone

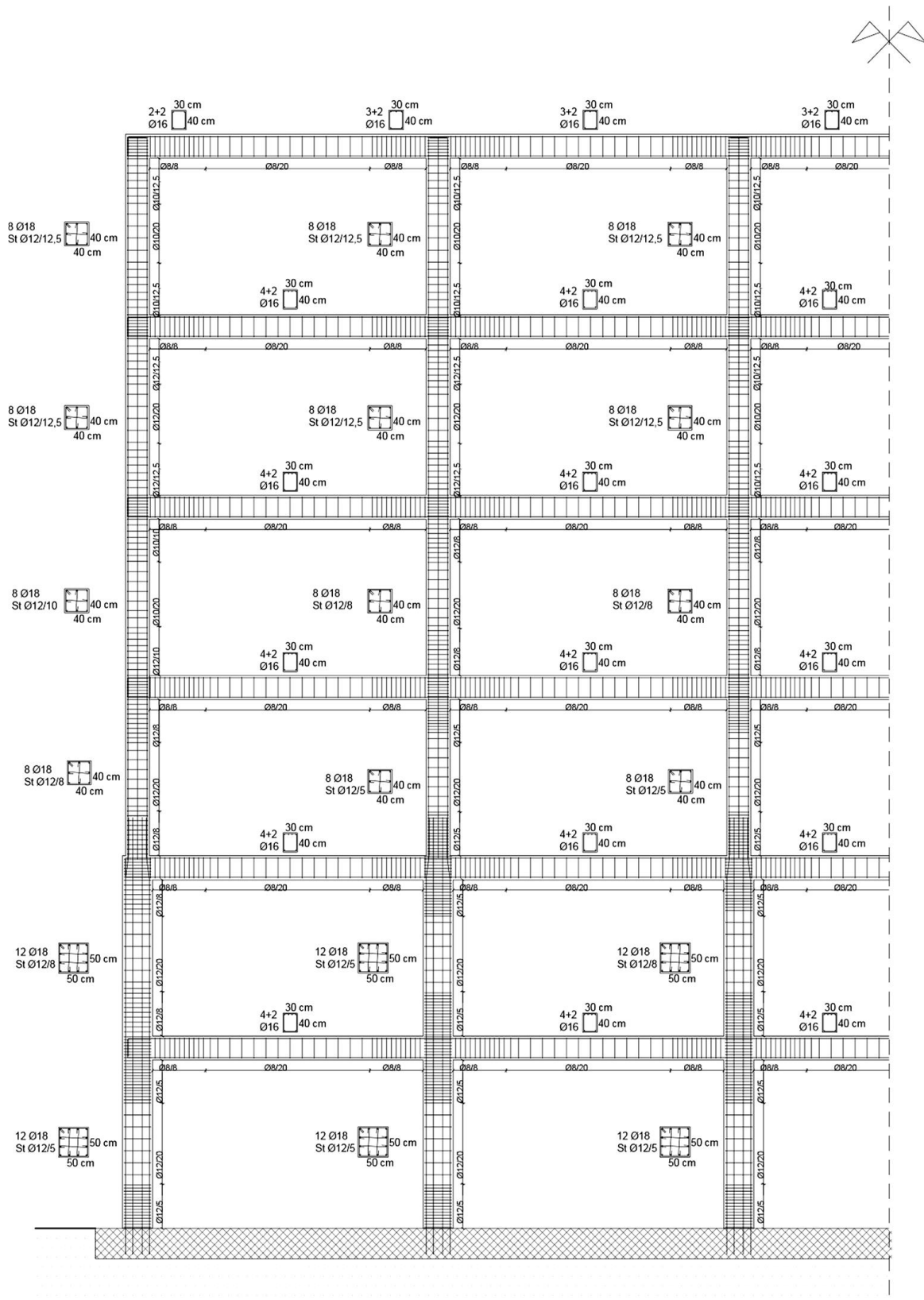


Figure 3-10: Structural details of the existing RC framed building in Pordenone [45]

Both structures are intended to fail in flexure, thus other failure mechanisms (such as shear failure of beams, columns or beam-column joints, bond slip and low-cycle fatigue, etc.) especially relevant to buildings designed according to outdated standards [57], are out of the scope of the present work.

### 3 Design procedure for the seismic retrofit of RC framed structures

---

For the seismic upgrade of both structures, steel braces equipped with hysteretic dampers characterized by an elastic-perfectly plastic behavior are used.

#### 3.3.1. Numerical model of the RC case-study framed buildings

Full 3-D numerical models of both buildings are formulated within the OpenSees framework [59]. Beams and columns are modeled using the *forceBeamColumn* element object [60], in the form of the *beamWithHinges* element [61], assigning a linear elastic material behavior to the internal sub-element, whereas non-linearities can be activated only in the two external sub-elements. The length of the plastic hinge  $L_{pl}$  is evaluated with Eq. (3.19) in accordance with the Eurocode 8 [29], valid when a well-detailed confinement model of concrete is assumed [62]:

$$L_{pl} = \frac{z}{30} + 0.2h + 0.11 \left( \frac{d_b f_y}{\sqrt{f_c}} \right) \quad (3.19)$$

In these plastic regions, the concrete non-linear behavior is modelled through a fiber section model, where each steel bar corresponds to a single fiber using uniaxial Giuffre-Menegotto-Pinto constitutive law [63], equivalent to *Steel02* material model with isotropic strain hardening [64]. The strain-hardening ratio  $b$  is assumed equal to 0.005 for the building in Pordenone, as specified in reference [45], and, in absence of any indication, equal to 0.01 for the building in Potenza [28], according to the modelling assumptions introduced in reference [62]. The parameters that control the transition from the elastic to the plastic branch are assigned as  $R_0 = 18$ ,  $C_{R1} = 0.925$  and  $C_{R2} = 0.15$  [61]. The concrete model is implemented using the library uniaxial material *Concrete04*, which is based on the model proposed by Popovics [65]; the properties of the core region of the sections are evaluated referring to Equations (A6 – A8) of the Eurocode 8 [29] and the tensile strength of concrete is neglected in both core and cover regions [66]. It is worth mentioning that the material properties of the building are evaluated disregarding the confidence factors [29], [30]. In order to account for concrete cracking, the interior elastic sub-element is characterized by an effective area moment of inertia  $I_{eq}$ , equal to 50% of the gross area moment of inertia  $I_g$ , according to the provisions of the Italian and the European norms [47], [30].

The chosen modelling approach is consistent with the design code adopted [29], [47] and has been demonstrated to reproduce, with enough accuracy, the seismic response of RC members characterized by flexural behavior [62].

In all models, the masses of the structural members (beams, columns, and slabs) are concentrated at the master nodes, dead and live loads are uniformly distributed on each beam and have been calculated according to the tributary area concept; P-Delta effects are considered in the analysis, while bond slip and low-cycle fatigue effects are disregarded. The columns at the ground floor have fixed base supports, simulating rigid foundations. The damping of the frame is defined according to the Rayleigh method, as a function of the tangent stiffness matrix only, assuming 5% viscous damping ratio, to take into account the energy dissipation coming from infill panels and other non modelled non-structural components [62].

The floor slabs are modelled as rigid diaphragms, by constraining the nodes belonging to the same floor to have the same displacement. An “axial buffer” [66] has been introduced in the FE model, through a *zeroLength* element object [67] characterized by a virtually zero axial stiffness and very high stiffnesses in shear and bending, placed between one end of each beam and the adjacent node belonging to the rigid diaphragm. This element works as an axial release to eliminate the fictitious axial force generated by the interaction between beam elements modelled with fiber sections and the rigid diaphragm [66].

The braces equipped with the hysteretic damper are modelled as truss elements [61] with an associated *uniaxialMaterial* model with elastic-perfectly plastic behavior [67].

### 3.3.2. Case-study 1: building in Potenza

The upgrade of the RC building in Potenza is carried out considering the seismic loads provided by NTC [30] for life-safety limit state (SLV), site of Potenza (Long 15° 48’ 20.1744’’, Lat 40° 38’ 25.4688’’), functional class  $c_u = II$ ,  $PGA = 2.45 \text{ m/s}^2$ , soil type B and topographic factor  $T_1$ . Diagonal steel braces equipped with hysteretic dampers are inserted in the perimetral frames of each story, according to the layout shown in Figure 3-11.

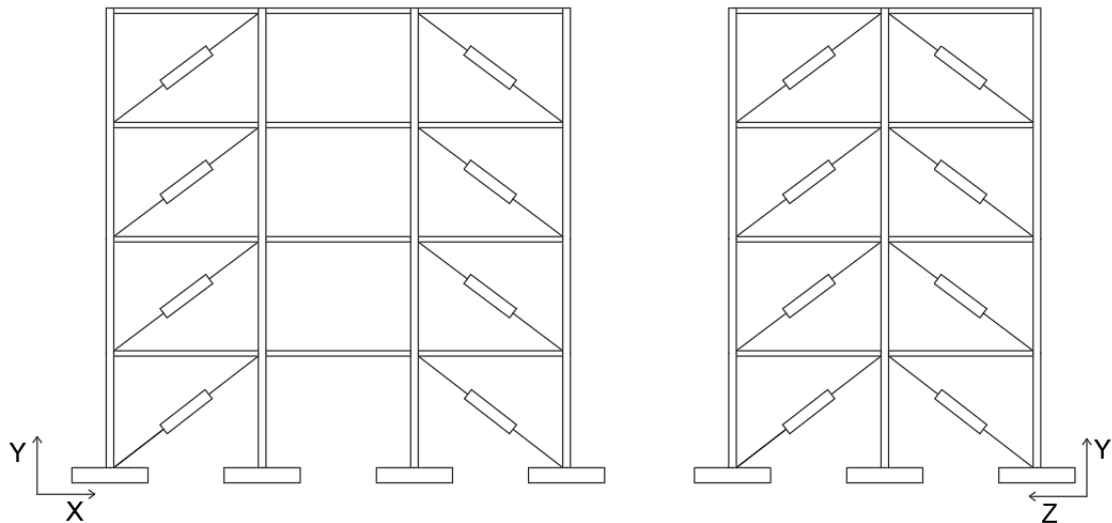


Figure 3-11: Diagonal layout of steel braces equipped with hysteretic dampers for case-study 1 building; the dissipative braces are installed in the perimetral frames [48]

NLSAs are performed in both positive and negative directions of the two horizontal (X and Z) axes, applying horizontal force distributions proportional to either mass (referred hereinafter as UNIFORM) or modal (MODAL) properties, and considering 5% accidental eccentricity of the center of mass of each story, as prescribed in [30] and [47]. The MODAL capacity curve is the lowest in both directions (Figure 3-12) and is used to evaluate the main parameters of the equivalent SDOF systems, Eqs.(3.1) – (3.6) .

Since the building, designed in accordance with updated codes, is missing of seismic details, the hysteretic damper system is designed with the aim of keeping the main frame in the elastic range, limiting as much as possible structural damage. The target inter-story drift ratio is set to  $\Delta_d = 0.005 \text{ m/m}$ , corresponding

### 3 Design procedure for the seismic retrofit of RC framed structures

through Eq. (3.5b) to the target displacement  $d_p = 0.045\text{ m}$  of the MDOF structure ( $h_0 = 3.0\text{ m}$ ,  $\delta_{i,max} = 0.3306$ ), and  $d_p^* = 0.036\text{ m}$  of the equivalent SDOF system, respectively (Figure 3-12). The equivalent bilinear capacity curves of the main frame in the two horizontal directions are then calculated according to Section 3.2.2 (Table 3-2). At the selected performance point the equivalent viscous damping ratio of the main frame is quite negligible (Table 3-2).

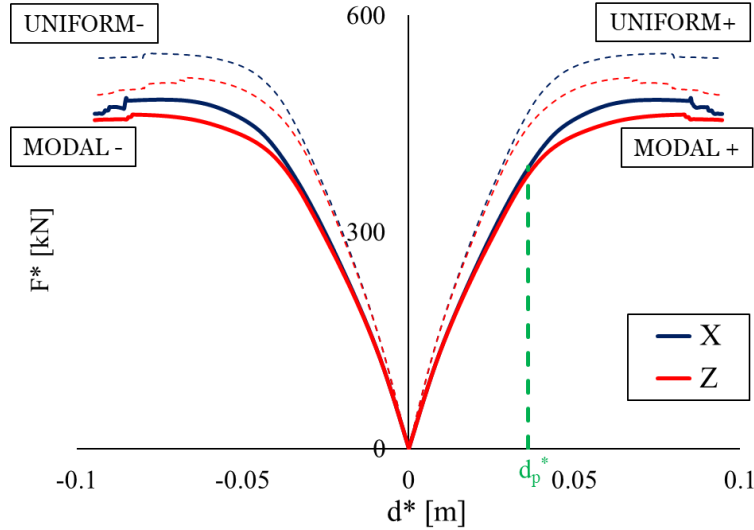


Figure 3-12: Determination of capacity curves in X- and Z- direction [48]

<i>Direction</i>	$\Gamma$	$d_y^*$	$V_y^{*F}$	$d_p^*$	$V_p^{*F}$	$\xi_F$	$m^*$
	[–]	[m]	[kN]	[m]	[kN]	[%]	[ton]
<b>X</b>	1.27	0.012	182	0.036	388	5.7	340
<b>Z</b>	1.27	0.012	186	0.036	385	6.4	339

Table 3-2: Properties of the equivalent SDOF system and bilinear capacity curves of case-1 structure in the two horizontal directions [48]

The design procedure described in Section 3.2 is separately applied to both X- and Z- directions: the bilinear capacity curve of the equivalent SDOF model is represented in ADRS format (Figure 3-2) and the effective viscous damping ratio at first iteration  $\xi_{eff}^1$  is determined by applying the Eq.(3.9).

The ductility of the equivalent damped brace system  $\mu_{DB}$  is the design input. As the ductility factor for hysteretic steel dampers typically ranges between 4 and 10 [31], the upper and lower boundaries of the range, namely  $\mu_{DB} = 4$  and  $\mu_{DB} = 10$ , are investigated. According to Eq.(3.11), the two ductility factors correspond to equivalent viscous damping ratios  $\xi_{DB} = 47.8\%$  and  $\xi_{DB} = 57.3\%$ , respectively.

The bilinear curve of the equivalent SDOF *Frame + Damped brace* system in either horizontal direction is plotted in the ADRS plane to check if the identified damper is appropriate for the RC case-study frame

(Figure 3-13). Step 4 of the procedure is iterated until the inelastic displacement of the equivalent SDOF braced structure converges to the target displacement  $d_p^*$  with  $\varepsilon < 0.05$ . As shown in Figure 3-14, convergence is always achieved within three iterations.

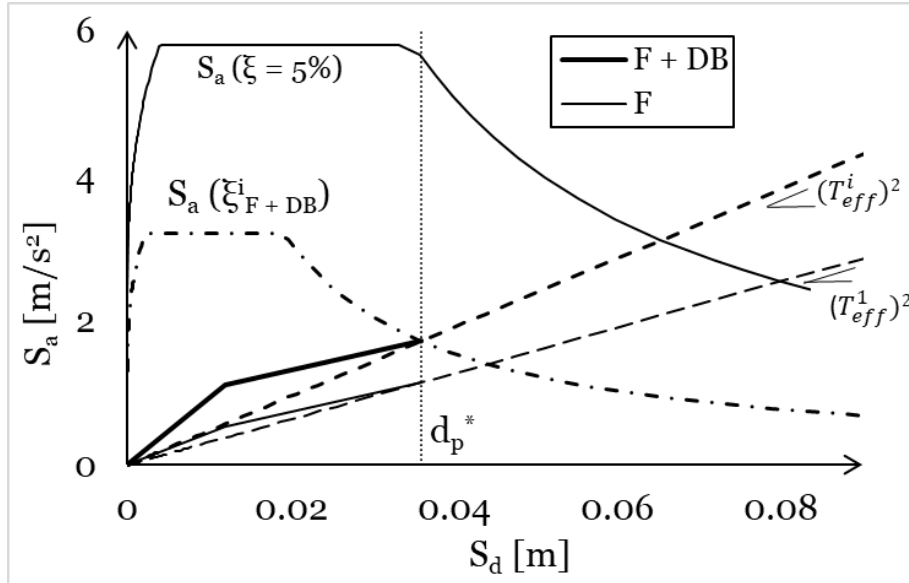


Figure 3-13: Equivalent capacity curves in X-direction of the main Frame (F) and Frame + Damped brace (F + DB) system with  $\mu_{DB} = 10$  and relevant demand response spectra [48]

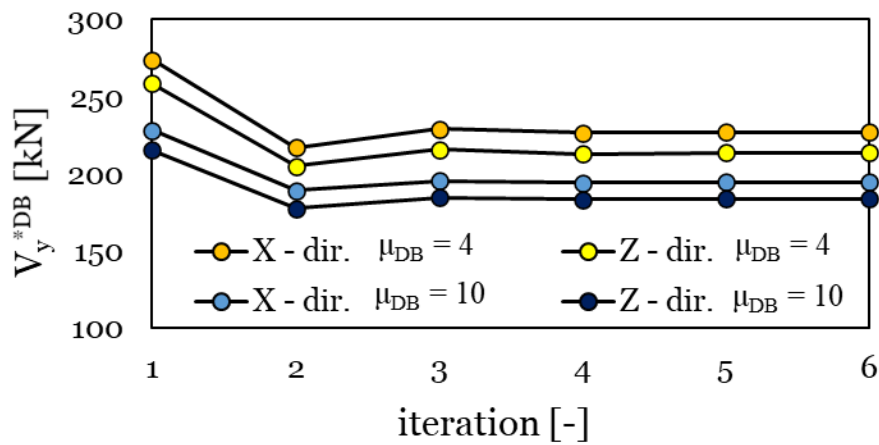


Figure 3-14: Iterative procedure for tuning the equivalent SDOF damped brace: damper yield strength vs. iteration number [48]

The damped brace system is distributed along the height of the frame in accordance with the method illustrated in Section 3.2.5 (hereinafter called Method A). However, in order to highlight the effects of the damper distribution on the frame response, a second method described in literature ([28], [31] and [32]), named Method B, has been investigated as well.

By referring to the layout shown in Figure 3-11, with 4 dampers per story in each direction, the resulting strength and stiffness of the dissipating braces calculated with either method are reported in Table 3-3.

### 3 Design procedure for the seismic retrofit of RC framed structures

		$\mu_{DB} = 4$				$\mu_{DB} = 10$			
		<i>Method A</i>		<i>Method B</i>		<i>Method A</i>		<i>Method B</i>	
<i>Direction</i>	<i>story</i>	$K_i^{DB}$	$N_{yi}^{DB}$	$K_i^{DB}$	$N_{yi}^{DB}$	$K_i^{DB}$	$N_{yi}^{DB}$	$K_i^{DB}$	$N_{yi}^{DB}$
		$\left[\frac{kN}{mm}\right]$	$[kN]$	$\left[\frac{kN}{mm}\right]$	$[kN]$	$\left[\frac{kN}{mm}\right]$	$[kN]$	$\left[\frac{kN}{mm}\right]$	$[kN]$
<b>X</b>	1 <sup>st</sup>	31.5	90	29.2	54.6	67.4	77	62.5	46.7
	2 <sup>nd</sup>	26.2	79	20.5	48.5	56.1	68	44	41.6
	3 <sup>rd</sup>	26	56.7	19.3	36.2	55.5	48.6	41.4	31
	4 <sup>th</sup>	24.4	26	17.7	19.2	52.3	22.3	38	16.5
<b>Z</b>	1 <sup>st</sup>	29.1	84.7	26.5	51.5	62.6	73	57	44.3
	2 <sup>nd</sup>	24	74.6	19	46	51.5	64.1	41	39.5
	3 <sup>rd</sup>	23.6	53.5	18	34.2	51	46	38.5	29.4
	4 <sup>th</sup>	22.12	24.5	16	18.2	47.6	21.1	34.3	15.6

Table 3-3: Case-study 1: properties of the damped braces for two assigned ductility factors [48]

For both  $\mu_{DB}$ s, the recommended Method A provides the highest values of strength and stiffness of the damping braces. By considering, e.g., the X-direction, the ratio between the stiffnesses determined according to either Method A or B varies from 1.08 at the first floor to about 1.40 at the fourth floor, and the ratio between the strengths varies from 1.65 at the first floor to 1.35 at the fourth floor. These figures do not change regardless of the damper ductility. Higher strengths are associated to  $\mu_{DB} = 4$  than to  $\mu_{DB} = 10$  in order to counteract the lower dissipation capacity.

Figure 3-15 compares in the ADRS plane the capacity curves of the upgraded building for  $\mu_{DB} = 4$  (Figure 3-15 (a)) and  $\mu_{DB} = 10$  (Figure 3-15 (b)); similar results are obtained along the Z-direction and not reported for conciseness.

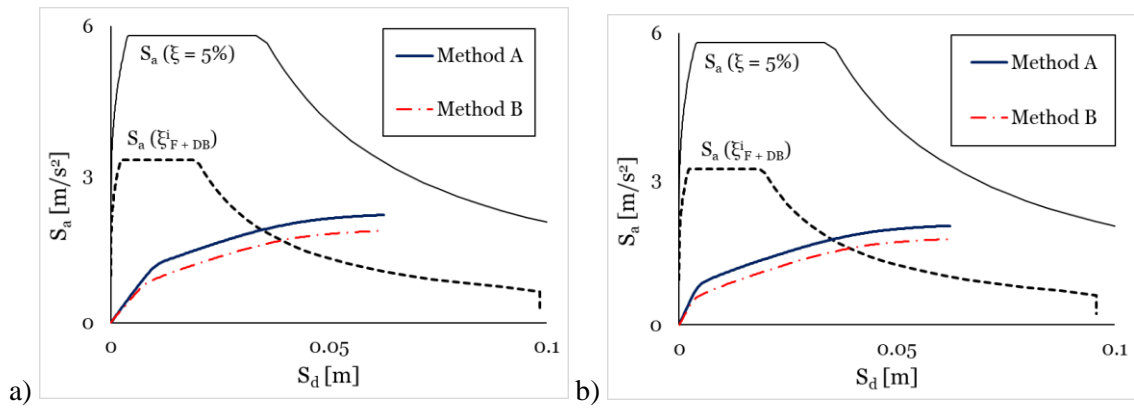


Figure 3-15: Comparison of capacity curves in X-direction for different damped brace ductility: a)  $\mu_{DB} = 4$  ; b)  $\mu_{DB} = 10$  [48]

The design target is met by the upgraded frame for either value of  $\mu_{DB}$ . However, regardless of  $\mu_{DB}$ , the capacity curve of the structure upgraded according to Method A shows a stiffer response, and the performance point is characterized by a higher force at a smaller displacement, than its Method B counterpart.

NLSAs evaluate the response of the retrofitted structure in terms of global quantities only, such as the total base shear force and the displacement of the reference point, but do not provide any check on local quantities, like, e.g., drifts and forces at each story, and the damping capacity of the dissipating brace system inserted in the structure. To have a deeper insight, bidirectional non-linear dynamic analyses (BNLDAs) are performed in compliance with the NTC [30] and EC8 [47] considering two sets of seven artificial ground motions generated using the computer code SIMQKE [68]. The artificial accelerograms are characterized by a pseudo-stationary part of 10 sec and a total duration of 25 seconds as prescribed in [30], and are compatible on average with the elastic spectrum defined by the code [30] in the range of periods between 0.15 and 2 sec.

At the end of the BNLDAs, the response of the case-study structure has been evaluated considering engineering demand parameters such as absolute accelerations and inter-story drifts, which are commonly considered the main parameters to appraise the performance of frame structures and the effectiveness of the retrofitting technique. During the post-processing of the analysis, the mean value of the maxima of the parameters calculated for the seven pairs of bidirectional accelerograms has been evaluated for each direction. Figure 3-16 - Figure 3-19 show the numerical results in terms of maximum inter-story drift ratio  $\Delta$  and maximum Peak Floor Acceleration *PFA* at each story, comparing the as-built configuration to the retrofitted configurations with dissipating braces distributed according to either Method A or Method B, and considering either  $\mu_{DB} = 4$  or  $\mu_{DB} = 10$ . The maximum values of  $\Delta$  and *PFA* may not occur at the same time step of the analysis.

Figure 3-16 and Figure 3-18 show that inter-story drift ratios  $\Delta$  drastically decrease when the damped braces are introduced. The damper distribution according to Method A produces at each floor, in either direction and for both values of  $\mu_{DB}$ , maximum  $\Delta$  values smaller than 0.5%, which is the design target drift ratio. In contrast, if Method B is adopted,  $\Delta$  exceeds the specified limit at the second floor in the Z-direction for both

### 3 Design procedure for the seismic retrofit of RC framed structures

$\mu_{DB}S$  ( $\Delta = 0.0056$  for  $\mu_{DB} = 4$  and  $\Delta = 0.0052$  for  $\mu_{DB} = 10$ , Figure 3-16 and Figure 3-18). As expected [35], *PFA* increases in the braced structure (Figure 3-17 and Figure 3-19), and the increase is higher for the stiffer distribution following Method A: e.g., at the fourth floor *PFA* in X-direction grows by either 12.6% with Method B or 28.4% with Method A, considering  $\mu_{DB} = 4$ , while the increase is either 7.4% or 9.16%, respectively, with  $\mu_{DB} = 10$ . The amplification of ground acceleration decreases by increasing the damping capacity of the dissipation system.

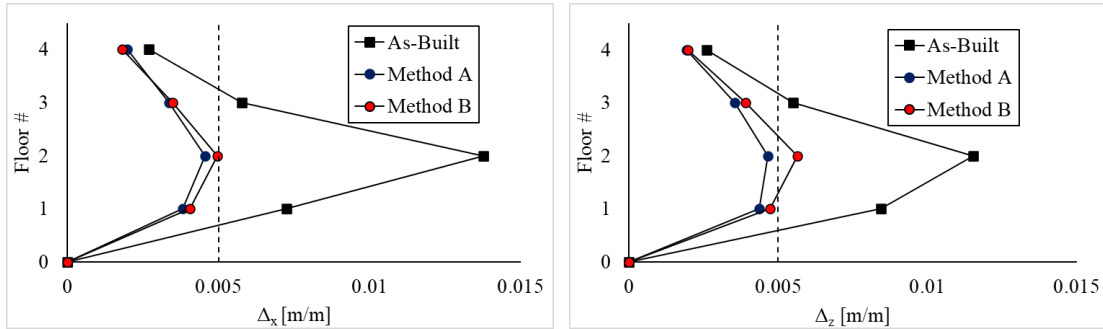


Figure 3-16: Comparison of maximum inter-story drift ratio  $\Delta$  obtained by BNLDA with and w/o damped braces with  $\mu_{DB} = 4$  [48]

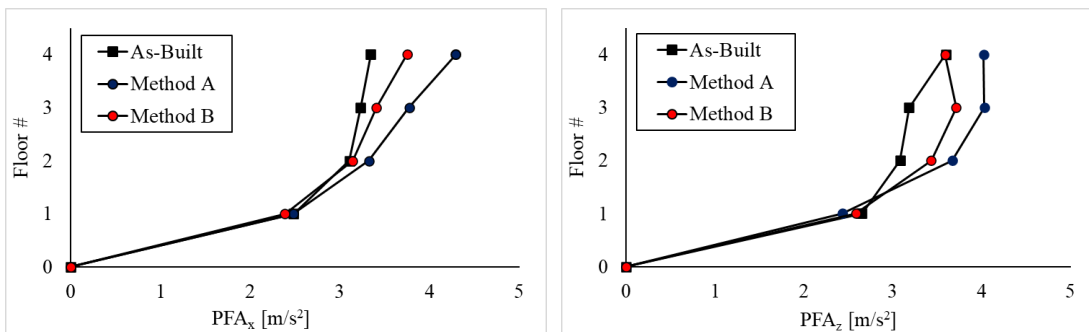


Figure 3-17: Comparison of maximum Peak Floor Acceleration *PFA* obtained by BNLDA with and w/o damped braces with  $\mu_{DB} = 4$  [48]

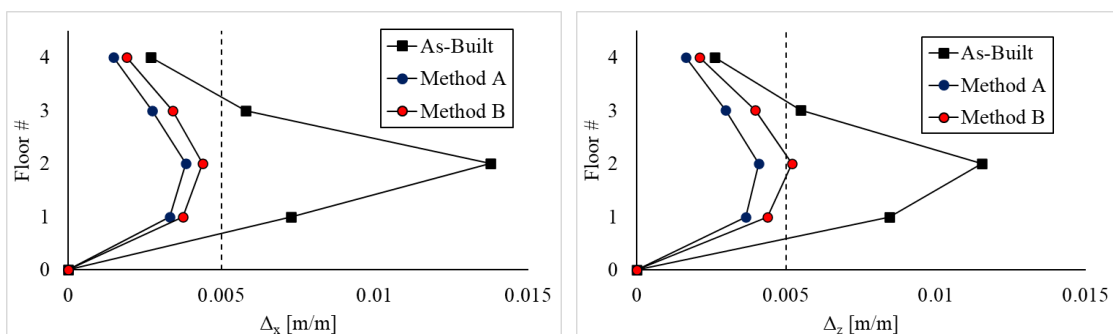


Figure 3-18: Comparison of maximum inter-story drift ratio  $\Delta$  obtained by BNLDA with and w/o damped braces with  $\mu_{DB} = 10$  [48]

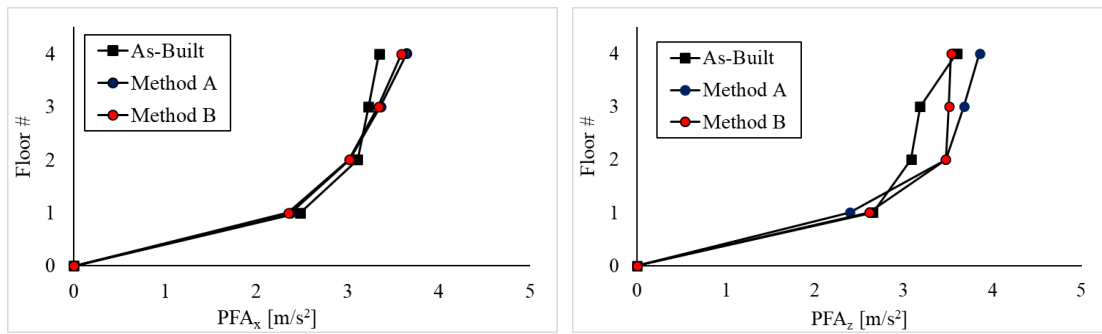


Figure 3-19: Comparison of maximum Peak Floor Acceleration  $PFA$  obtained by BNLDA with and w/o damped braces with  $\mu_{DB} = 10$  [48]

Figure 3-20 and Figure 3-21 compare the capacity curves of the as-built and the upgraded structures with the results of the BNLDA, expressed in terms of average maximum top displacement and maximum base shear force. The comparison confirms that Method A is more conservative than Method B, as already shown by NLSAs. In both directions and for both values of  $\mu_{DB}$ , the average maximum displacement of Method B ( $d_{p,B}$ ) is closer to the target displacement. In the Z-direction the values of  $d_{p,B}$  are almost coincident with  $d_p$  with a maximum deviation of -4.3%, while the average maximum displacement of Method A ( $d_{p,A}$ ) deviates by more than -15% (Table 3-4); in the X-direction the deviation is about -20% for Method B, while for Method A ranges from -20% to -32% depending on  $\mu_{DB}$ . The introduction of dissipative braces produces an increase in the maximum base shear  $V_{max}$ , as shown in Figure 3-22. Consistently with the observed increase in  $PFA$ , Method A produces the largest increase on  $V_{max}$  (up to 41.5% more than in the as-built configuration), while Method B leads to a maximum increase of 20.5%.

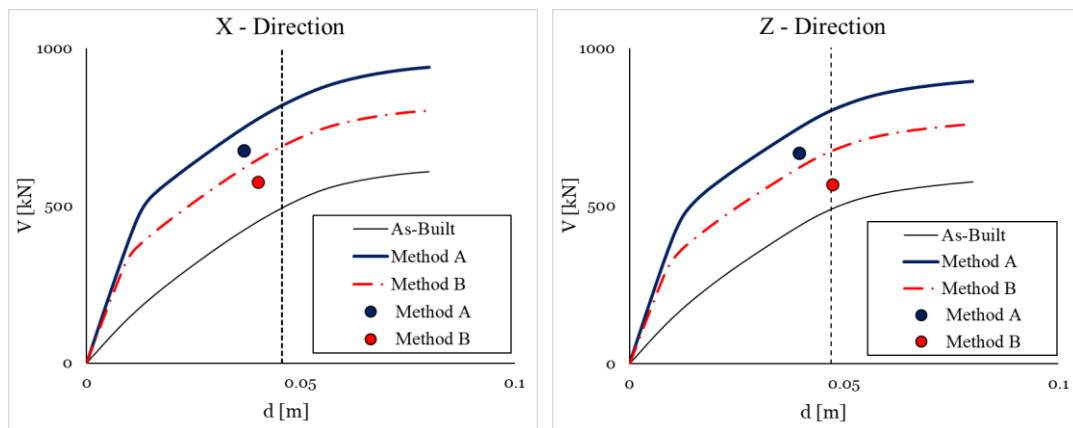


Figure 3-20: Comparison between capacity curves calculated by NLSA (solid lines) and maximum top displacement versus base shear force by BNLDA (dots), damped brace ductility  $\mu_{DB} = 4$  [48]

### 3 Design procedure for the seismic retrofit of RC framed structures

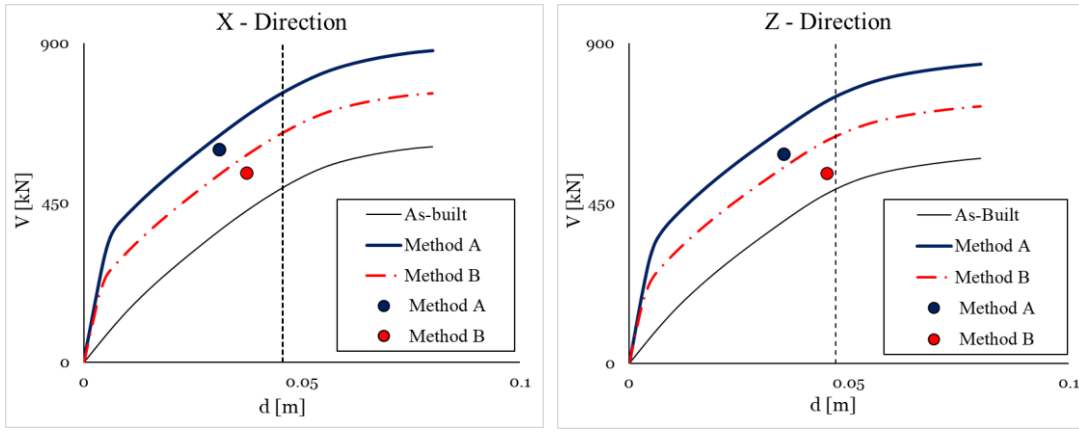


Figure 3-21: Comparison between capacity curves calculated by NLSA (solid lines) and maximum top displacement versus base shear force by BNLDA (dots), damped brace ductility  $\mu_{DB} = 10$  [48]

<i>Direction</i>	$\mu_{DB} = 4$					$\mu_{DB} = 10$			
	$d_p$	$d_{p,A}$	$dev$	$d_{p,B}$	$dev$	$d_{p,A}$	$dev$	$d_{p,B}$	$dev$
	[m]	[m]	[%]	[m]	[%]	[m]	[%]	[m]	[%]
<b>X</b>	0.046	0.037	<b>-19.5</b>	0.040	<b>-12.5</b>	0.031	<b>-32</b>	0.037	<b>-18.5</b>
<b>Z</b>	0.047	0.040	<b>-15.6</b>	0.047	<b>0.6</b>	0.035	<b>-25</b>	0.045	<b>-4.3</b>

Table 3-4: Comparison between the target displacement  $d_p$  and the average maximum top displacement of the damped braced frame with  $\mu_{DB} = 4$  or  $\mu_{DB} = 10$ , and different distribution Method (A or B) [48]

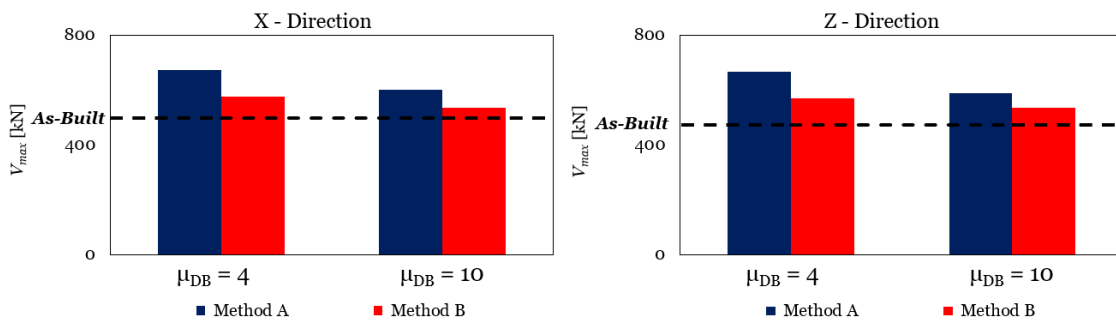


Figure 3-22: Comparison between the average maximum base shear force of the damped braced frame with  $\mu_{DB} = 4$  or  $\mu_{DB} = 10$ , and different distribution Method (A or B); maximum base shear force of the as-built structure reported as broken line [48]

In conclusion, the damped brace system designed according to proposed procedure in combination with the recommended distribution method (Method A) allows to fulfill the performance requirements for the upgraded frame. Alternative distribution methods, such as Method B, may look more effective by considering the global performance of the upgraded structure in terms of maximum top displacement and maximum base shear forces, as they provide floor drifts closer to the target performance without an excessive

increase of the shear force at the base columns. However, as highlighted in Figure 3-16 and Figure 3-18, Method A provides a more effective control of the lateral deformation along the height of the building, ensuring that the maximum inter-story drift ratio is less than 0.5% at each floor, which is the goal of the retrofit design. In contrast, for Method B the target performance is found not satisfied at the second floor, whichever the assumed ductility factor. A further conclusion that is apparent from Figure 3-22 is that low-ductility damped braces turn out to be less effective for the control of both lateral drifts and shear forces of the main building.

### 3.3.3. Case-study 2: building in Pordenone

The second case-study is a residential 6-story building, designed in compliance with NTC [30] for a low seismicity zone corresponding to the municipality of Pordenone, Italy [45] ( $PGA = 1.91m/s^2$ , soil type B). This building is characterized by square 50x50cm columns at the ground level and at the first floor, and by square 40x40cm columns from the second to the last floor, Figure 3-9. This arrangement results in a variation of stiffness along the height of the building and different floor masses at each story. The building is upgraded for a high seismicity area, considering the seismic loads provided by the code [30] for life-safety limit state (SLV), site of L'Aquila (Long  $13^\circ 23.9724'$ , Lat  $42^\circ 21.033'$ ), functional class  $c_u = II$ ,  $PGA = 4.062 m/s^2$ , soil type C and topographic factor  $T_2$ . Diagonal steel braces equipped with hysteretic devices are inserted in the facades, according to the layout shown in Figure 3-23 (4 units at each floor in both X- and Z- directions). In this case too, two ductility levels  $\mu_{DB} = 4$  and  $\mu_{DB} = 10$  are considered. Since the results are similar to those found for case-study 1, for brevity, only those relevant to the lateral deformation of the building are presented and discussed.

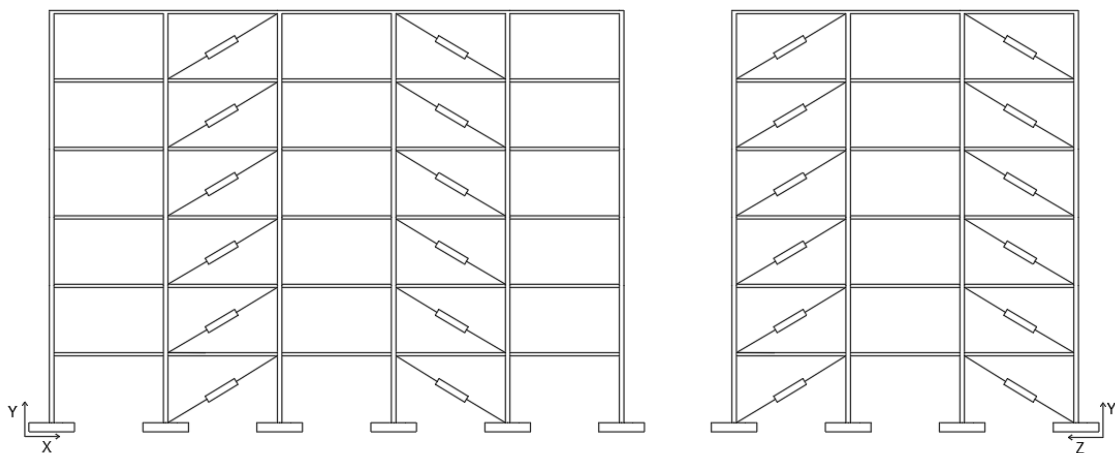


Figure 3-23: Diagonal layout of steel braces equipped with hysteretic dampers for case-study 2 building [48]

As in case-study 1, the bilinear curve of the equivalent SDOF system of the as-built structure in either horizontal direction (X and Z) is determined from the MODAL capacity curve, Figure 3-24. The target displacement is calculated considering a maximum inter-story drift of the braced structure equal to  $\Delta_d = 0,005 m/m$ , to satisfy the stability requirement (STA) for non-structural elements at the ultimate limit state as recommended in [30]. Being  $h_0 = 3.0 m$  and  $\delta_{i,max} = 0.2257$ , values of  $d_p = 0.059 m$  for the MDOF

### 3 Design procedure for the seismic retrofit of RC framed structures

frame and  $d_p^* = 0.044$  m for the equivalent SDOF system result. The parameters of the equivalent bilinear capacity curves of the main frame in the two horizontal directions are reported in Table 3-5.

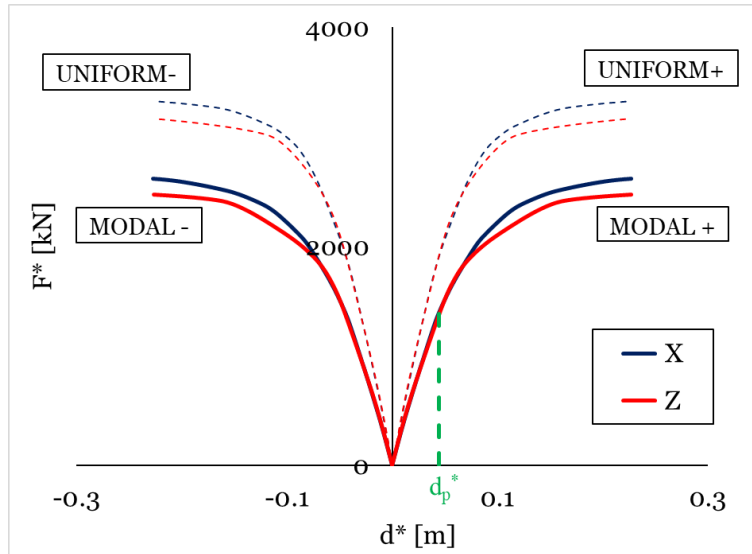


Figure 3-24: Capacity curves in X- and Z- direction [48]

<i>Direction</i>	$\Gamma$ [-]	$d_y^*$ [m]	$V_y^{*F}$ [kN]	$d_p^*$ [m]	$V_p^{*F}$ [kN]	$\xi_F$ [%]	$m^*$ [ton]
<b>X</b>	1.32	0.017	602.6	0.044	1387	2.2	958
<b>Z</b>	1.32	0.014	510	0.044	1368	2.4	956

Table 3-5: Properties of the equivalent SDOF system and bilinear capacity curves of case-study 2 structure in the two horizontal directions [48]

The bilinear capacity curves in the X- and Z- directions are separately reported in the acceleration-displacement plane and the procedure described in Section 3.2.4 is iterated until the performance point of the equivalent SDOF braced structure converges to the target displacement  $d_p^*$  with  $\varepsilon \leq 0.05$ . Figure 3-25 show the ADRS representation of the equivalent SDOF capacity curves along the X-direction of the main frame (F) and the upgraded frame (F + DB). Convergence to values reported in Table 3-6 is obtained at the third iteration. It is to be noted that for the building under consideration, the properties of the equivalent SDOF damped brace along the two horizontal directions are practically the same.

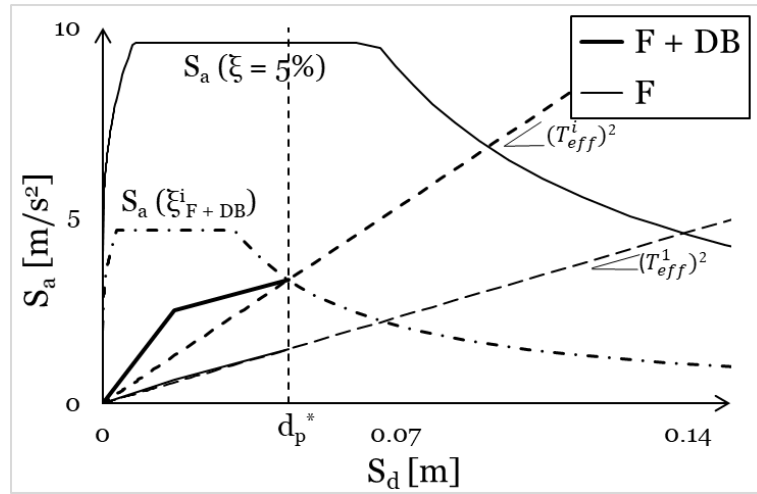


Figure 3-25: Equivalent capacity curves in X-direction of main Frame (F) and Frame + Damped brace (F + DB) with  $\mu_{DB} = 10$  [48]

$\mu_{DB}$	X-direction			Z-direction		
	$V_y^{*DB}$ [kN]	$d_p^*$ [m]	$\xi_{DB}$ [%]	$V_y^{*DB}$ [kN]	$d_p^*$ [m]	$\xi_{DB}$ [%]
4	2056	0.044	47.78	2045.5	0.044	47.78
10	1764.5	0.044	57.33	1756	0.044	57.33

Table 3-6: Properties of the SDOF damped brace for case-study 2 [48]

After the strength of the equivalent SDOF damped brace has been determined, the properties of the dissipative braces at each story are distributed in agreement with either Method A or Method B.

NLSAs are performed on both upgraded configurations and the relevant capacity curves are plotted in ADRS format to verify the effectiveness of the design, Figure 3-26. As expected, the distribution of stiffnesses and strengths according to Method A produces a stiffer global response.

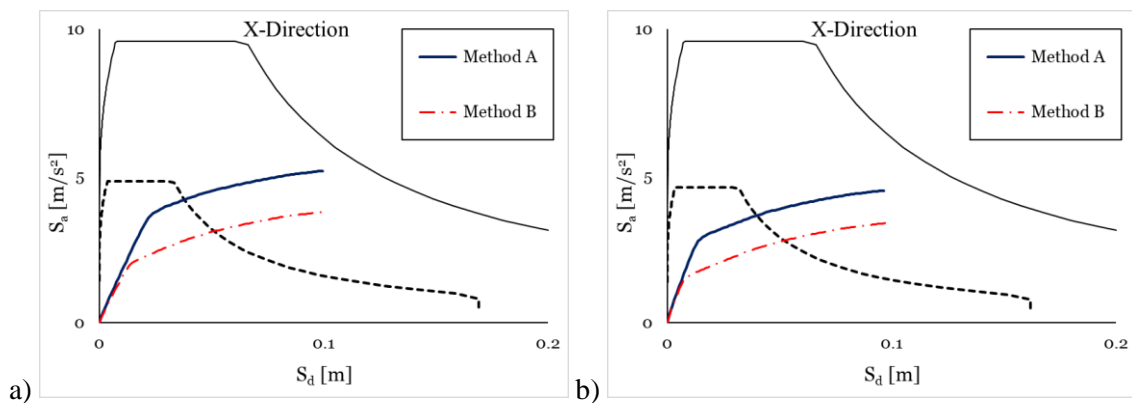


Figure 3-26: Comparison of capacity curves in X-direction for damper brace ductility: a)  $\mu_{DB} = 4$ ; b)  $\mu_{DB} = 10$  [48]

### 3 Design procedure for the seismic retrofit of RC framed structures

BNLDAs are performed in conformity with NTC [30] and EC8 [47] considering two sets of seven artificial ground motions [68], compatible with the response spectrum defined by NTC [30].

Figure 3-27 and Figure 3-28 compare the capacity curves of the as-built and the upgraded structures with the results of the BNLDAs (average maximum top displacement and base shear force). Method B provides indeed an excellent agreement between structural displacement and the target value  $d_p^*$  for both ductility factors; with Method A the average BNLDA displacement coincides with the target value when the low ductility damper is considered, while for  $\mu_{DB} = 10$  the method appears to be conservative, as already observed for case-1 building.

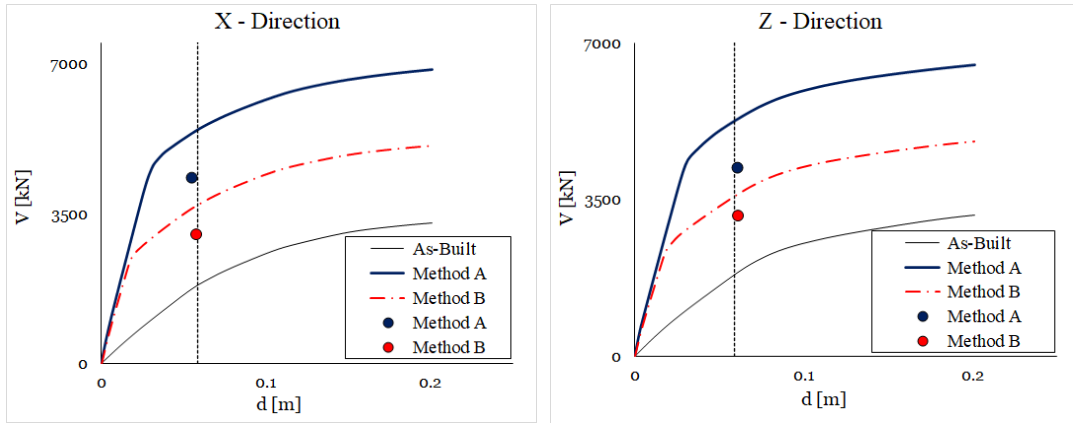


Figure 3-27: Comparison between capacity curves calculated by NLSA (solid lines) and maximum top displacement versus base shear force by BNLDA (dots), damped brace ductility  $\mu_{DB} = 4$  [48]

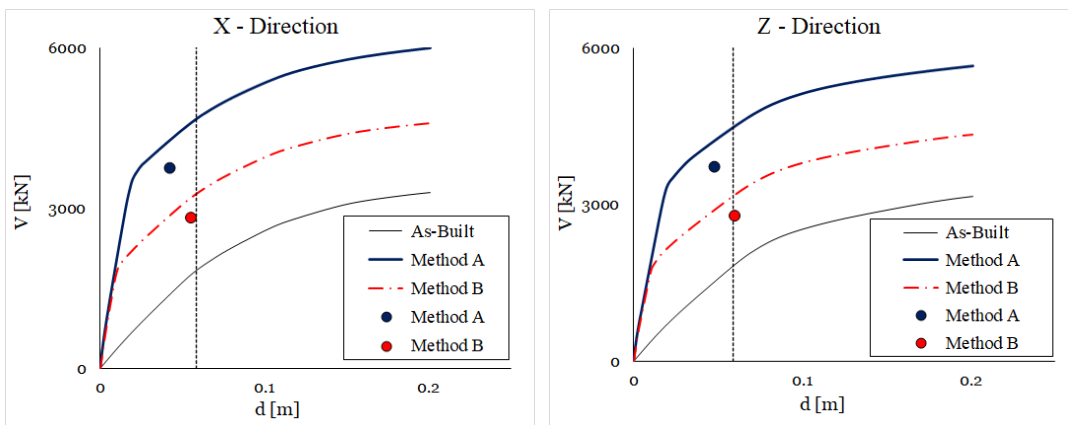


Figure 3-28: Comparison between capacity curves calculated by NLSA (solid lines) and maximum top displacement versus base shear force by BNLDA (dots), damped brace ductility  $\mu_{DB} = 10$  [48]

However, the global response needs to be analyzed in conjunction with the local behavior. Figure 3-29 and Figure 3-30 show the maximum inter-story drift ratio  $\Delta$  at each floor, comparing the as-built configuration with the upgraded configurations according to Method A and Method B.

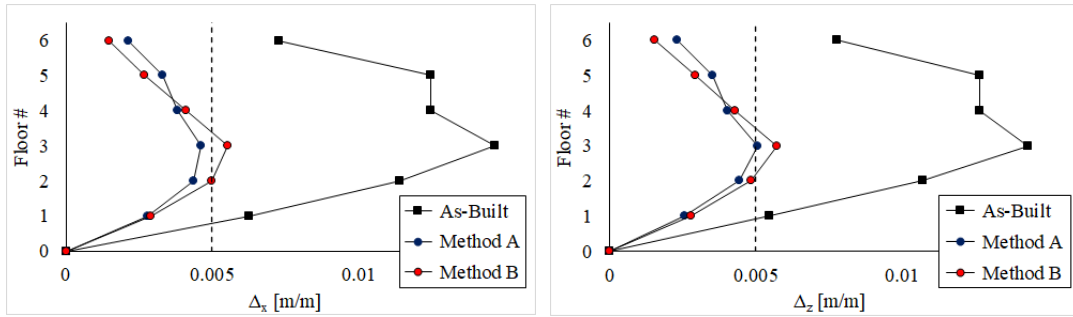


Figure 3-29: Maximum inter-story drift ratio  $\Delta$  in X and Z directions obtained by BNLDAs with  $\mu_{DB} = 4$  [48]

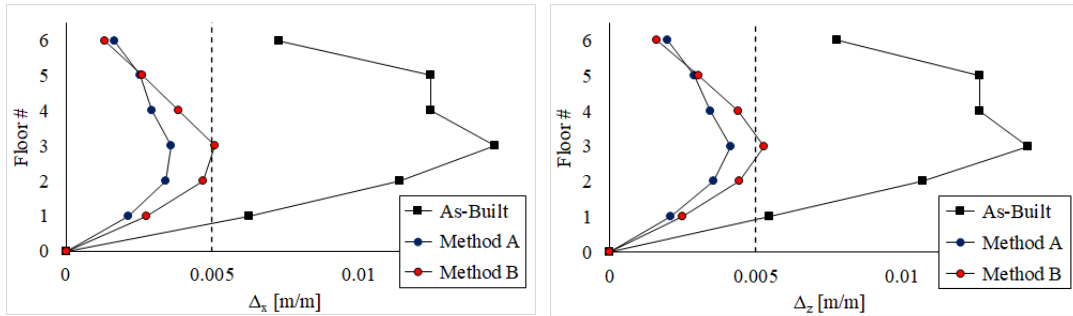


Figure 3-30: Maximum inter-story drift ratio  $\Delta$  in X and Z directions obtained by BNLDAs with  $\mu_{DB} = 10$  [48]

For  $\mu_{DB} = 10$  (Figure 3-30) the target drift ratio is substantially met at each floor with either damper distribution (only in Z-direction,  $\Delta = 0.0053$  m/m with Method B). In contrast, for  $\mu_{DB} = 4$  (Figure 3-29) only the distribution according to Method A meets the target, while with Method B at the third floor the drift ratio exceeds the limit in both X- ( $\Delta = 0.0055$  m/m) and Z- ( $\Delta = 0.0057$  m/m) directions.

#### 3.4. Discussion and conclusions

---

A displacement-based design procedure based on the Capacity Spectrum Method [46] has been developed for the seismic upgrade of frame structures via addition of hysteretic damped braces. A substitute structure consisting of an equivalent SDOF braced frame is introduced to represent the overall behavior of the existing frame and the damped brace system acting in parallel. The performance point for the upgraded structure is assigned in order to control the maximum inter-story drift, by assuming that the lateral deformation of the damped braced frame matches the first mode deformation of the main frame. The secant stiffness and the equivalent viscous damping ratio are used to characterize the non-linear behavior of the upgraded frame, which allows the direct calculation of the global properties of the hysteretic damper system.

The global stiffness and strength of the equivalent SDOF damped brace identified by the procedure are distributed along the height of the building according to a proportionality criterion which constrains the drifts of the braced frame to follow the first mode deformation of the main frame. The adopted distribution of the damped brace properties in elevation is expected to promote the simultaneous engagement of the dampers at each floor during the earthquake. Since the design methodology is based on the condensation of the MDOF structure to an equivalent SDOF system, the simultaneous engagement of the dampers along the height of the building is essential for the condensation to be accurate [13]. Moreover, ensuring that the first mode of the braced and unbraced frame is the same, it is also required for dimensioning the target displacement  $d_p$  according to Eqs. (3.5a) and (3.5b), which assume the proportionality of inter-story drifts of the upgraded and the main structure. Once the global stiffness and strength of the damped braces at each floor are determined, the properties of the single units are eventually calculated, depending on the selected brace configuration.

Even if some analogies exist with other approaches based on the response spectrum and utilizing either the initial stiffness ([18], [28]), or the secant stiffness to the maximum response level ([26], [35]), the strength of the proposed method relies on its simplicity: only one NLSA of the as-built structure is performed at the beginning of the process, to determine the capacity curve of the main frame, and at each iteration the capacity curve of the upgraded frame is calculated by means of analytical equations accounting for the stiffness and the strength of the damped brace system. The iterative procedure can be implemented in a spreadsheet, and convergence is usually reached in few steps; in addition, the graphical representation of both curves in the ADRS plane has the added advantage of giving the engineer the opportunity to visualize at any iteration the relationship between demand and capacity.

Global approaches based on the definition of a capacity spectrum via an equivalent SDOF system have the merit to provide a simple, direct, and fast design procedure. However, as observed for similar approaches ([16]-[22], [28], [35], [54], [57]), in general they do not allow for a direct control of the drift demand at each floor. To overcome this limit, a criterion based on the proportionality between the inter-story drift distribution of the upgraded and the modal properties of the main frame has been presented in the study. Though the distribution method is not intended to make the inter-story drift distribution more uniform, it allows to limit

the lateral deformation of the weak story of the building to an assigned threshold associated to the design level of performance.

The effectiveness of the proposed distribution method (Method A) is assessed in comparison to a second method (Method B) which distributes the global properties based on a proportionality criterion with respect to floor stiffnesses calculated from NLSA ([28], [57]).

The two methods lead to differences in strengths and stiffnesses of the damped braces at each floor; this difference has a relatively low influence on the top displacement but has large effect on the distribution of the inter-story drifts. Namely, Method B was effective when dissipative braces with high ductility factor were considered, but it was unable to control the drift of the weak story of the frame when a damper with low ductility was selected. In contrast, the effectiveness of Method A was proved for both high and low  $\mu_{DB}$  values. Another effect of the adopted distribution method regards the increase in floor accelerations and in the internal forces of the structural elements of the main frame where the forces developed by the dampers are transferred (typically, the elements where the braces are connected). In this regard, the Method B examined in the case-studies seems to be more suitable, because of the lower strength and stiffness of the devices. However, in the proposed design method, the performance requirement is expressed in terms of target displacement and inter-story drift ratio, and in this respect the effectiveness of the recommended Method A is superior. Nevertheless, for different design requirements, e.g., when a main target is to control floor accelerations to protect acceleration-sensitive elements [31] or to limit the increase in axial load in weak elements, alternative distribution methods can be considered.

The presented procedure is directly applicable to low-rise and mid-rise buildings with in-plan and in-elevation regular distribution, for which the lateral deformation is essentially governed by the first mode. Two RC frame structures, characterized by different seismic design, are investigated to demonstrate the effectiveness of the method. The first structure is a 4-story building, and it is selected as paradigmatic of a large part of the Italian building stock, designed according to old standards and with inappropriate seismic details. The second structure is a 6-story building designed with seismic details for a low seismicity zone according to the latest codes and it is upgraded to resist to higher seismic excitations corresponding to a high seismic area.

The presented method is not suitable for structures where the contribution of higher modes is not negligible, but this does not represent a critical limitation from a practical point, given that in many countries, (e.g., Italy), the largest part of the existing building stock designed according to outdated codes, consists of low-rise and medium-rise buildings. Examples include residential buildings, schools, industrial sheds etc. [69].

The procedure, conceived for regular buildings, will be extended in a future study to in-elevation irregular frames and unsymmetric-plan structures.

Analogously, while only tested on RC structures in this study, the proposed procedure is applicable to steel structures as well. The extension of the approach to steel systems is the object of an ongoing investigation.

### 3 Design procedure for the seismic retrofit of RC framed structures

---

Owing to its ease, the procedure is aimed at enhancing the confidence of practitioners in using supplementary energy dissipation systems by providing a simple, fast, and handy procedure to tune the effective parameters of the damped braces. However, some limitations of the method exist, which are highlighted in the following points.

The case-studies have also highlighted that the global structural response estimated via BNLDAs is typically lower, in terms of base shear force and top displacement, than the one calculated via NLSAs of the MDOF braced frame system; this can be explained considering that the results of NLSAs depend on the considered lateral load distribution and in general neglect dynamic effects. Moreover, damped braces can provide an equivalent structural damping  $\xi_{F+DB}$  greater than 28% (as indeed occurred in the two case-studies examined in the study) which represents the limit over which the simplified shapes of pseudo-acceleration and displacement response spectra are no longer valid [29]. Therefore, the evaluation of  $d = d_p$  carried out by referring to the displacement spectrum for  $\xi = \xi_{F+DB}$  can provide only an approximate value of the displacement of the frame retrofitted with damped braces. These are inherent limits of all procedures for dimensioning of damped braces based on Direct-Displacement-Based Design (DDBD) method which exploit the capacity curves of the bare and retrofitted frame and the response demand spectra to evaluate the performance point.

The number and location of damping units to be installed in the structure, and their distribution along the height of the building, remain a design input which is to be decided by the user based on past experience or via trial and error. Evidently, the brace configuration cannot be standardized in a general procedure as it actually depends on specific constraints posed by e.g., architectural requirements, modification of the building layout, ability of structural members to resist the increased internal forces due to the braces and cost of strengthening procedures, etc.

The non-linear analyses presented in the study were performed considering artificial ground motions, because artificial accelerograms with smooth spectrum allow a more accurate control of the frame response than real accelerograms, usually characterized by a large scatter of spectral accelerations, thereby making the interpretation / comparison with NLSA simpler and more focused on the specific aspects that are analyzed in the work. In future developments the verification will be extended to include natural ground motions as well.

### 3.5. Symbols

- $b$  strain-hardening ratio
- $CR_1$  curvature degradation parameter
- $CR_2$  curvature degradation parameter
- $d_b$  diameter of longitudinal reinforcement
- $d_F$  roof displacement of the unbraced Multi Degree Of Freedom (MDOF) structure
- $d_F^*$  roof displacement of the unbraced Single Degree Of Freedom (SDOF) structure
- $d_D$  axial deflection of a hysteretic damper
- $d_e$  spectral displacement of an elastic oscillator with period  $T_{eff}$
- $d_p$  target displacement of MDOF structure
- $d_{p,A}$  averaged max. displacement of damped braced frame according to distribution Method A
- $d_{p,B}$  averaged max. displacement of damped braced frame according to distribution Method B
- $d_p$  target displacement of MDOF structure
- $d_p^*$  target displacement of SDOF structure
- $d_u$  ultimate displacement of the unbraced MDOF structure
- $d_{uD}$  ultimate deflection of a hysteretic damper
- $d_u^{*DB}$  ultimate displacement of the equivalent SDOF damped brace
- $d_y$  yield displacement of the MDOF main structure
- $d_{y,i}$  yield displacement of the  $i^{\text{th}}$  story of the main structure (with  $i = 1 \div n$ , where  $n$  is the total number of stories)
- $d_y^*$  yield displacement of the SDOF main structure
- $d_{yD}$  yield deflection of a hysteretic damper
- $d_y^{*DB}$  yield displacement of the equivalent SDOF damped brace
- $d_y^{*F}$  roof displacement at yielding of the unbraced SDOF structure
- $f_c$  compressive strength of concrete
- $F_i$  horizontal seismic force (with  $i = 1 \div n$ , where  $n$  is the total number of stories)
- $f_y$  yield stress of longitudinal steel reinforcement

### 3 Design procedure for the seismic retrofit of RC framed structures

---

$F_{yi}^{DB}$  seismic lateral loads at yielding point of damped braces at the  $i^{\text{th}}$  floor (with  $i = 1 \div n$ , where  $n$  is the total number of stories)

$h$  overall depth of beam or column

$h_i$  inter-story height

$h_0$  uniform inter-story height

$I_{eq}$  effective area moment of inertia of beam or column

$I_g$  gross area moment of inertia of beam or column

$K_D$  initial stiffness of the theoretical force–deflection curve of a hysteretic damper

$K_{2,D}$  post-yield stiffness of the theoretical force–deflection curve of a hysteretic damper

$K_{eff}$  effective stiffness of the equivalent SDOF frame + damped brace system

$K_F^*$  secant stiffness of the bilinear capacity curve to the target displacement

$K_i^{DB}$  stiffness of the damped braces at the  $i^{\text{th}}$  story (with  $i = 1 \div n$ , where  $n$  is the total number of stories)

$K_i^F$  stiffness of the  $i^{\text{th}}$  story of the as-built main structure (with  $i = 1 \div n$ , where  $n$  is the total number of stories)

$L_{pl}$  plastic hinge length

$m_i$  floor masses (with  $i = 1 \div n$ , where  $n$  is the total number of stories)

$m^*$  equivalent mass of the SDOF structure

$n_d$  total number of dampers per floor

$N_D$  output force of a hysteretic damper

$N_{yD}$  yield force of a hysteretic damper

$N_{yi}^{DB}$  strength of the damped brace at the  $i^{\text{th}}$  story (with  $i = 1 \div n$ , where  $n$  is the total number of stories)

$N_{uD}$  ultimate force of a hysteretic damper

$PGA$  peak ground acceleration

$PFA$  maximum peak floor acceleration across the frame

$r$  hardening parameter of the theoretical force–deflection curve of a hysteretic damper

$R_0$  initial value of the curvature parameter

$S_a$  acceleration spectrum

$S_d$  displacement spectrum

$T$  fundamental period

- $T_{eff}$  effective period of the equivalent SDOF frame + damped brace system
- $T_F^*$  effective period of the SDOF main structure
- $V_F$  base shear force of the MDOF main structure
- $V_F^*$  base shear force of the SDOF main structure
- $V_{max}$  averaged maximum base shear
- $V_p^{DB}$  ultimate strength of the MDOF damped brace
- $V_p^{*DB}$  ultimate strength of the SDOF damped brace
- $V_p^F$  ultimate strength of the SDOF damped brace
- $V_y^{DB}$  yield strength of the MDOF damped brace
- $V_{yi}^{DB}$  yield shear force of damped brace at the  $i^{\text{th}}$  story (with  $i = 1 \div n$ , where  $n$  is the total number of stories)
- $V_y^{*DB}$  yield strength of the SDOF damped brace
- $V_y^F$  base shear force at yielding of the MDOF main structure
- $V_y^{*F}$  base shear force at yielding of the SDOF main structure
- $V_{yi}^F$  yield force of the  $i^{\text{th}}$  story of the main structure (with  $i = 1 \div n$ , where  $n$  is the total number of stories)
- $z$  distance from critical section of maximum curvature and the element point of contraflexure
- $\Gamma$  participation factor
- $\delta_i$  difference between two consecutive first mode eigenvector components =  $(\phi_i - \phi_{i-1})$
- $\Delta_d$  target inter-story drift ratio
- $\Delta_i$  maximum inter-story drift ratio at the  $i^{\text{th}}$  story
- $\xi$  structural viscous damping ratio
- $\xi_{DB}$  equivalent viscous damping ratio of the damped brace system
- $\xi_{eff}$  required equivalent viscous damping ratio
- $\xi_F$  equivalent viscous damping ratio of the main structure (unbraced)
- $\xi_{F+DB}$  equivalent viscous damping ratio of the equivalent SDOF frame + damped brace
- $\kappa_{DB}$  coefficient accounting for the energy dissipation capacity of the damped brace
- $\kappa_F$  coefficient accounting for the energy dissipation capacity of the main structure
- $\mu_{DB}$  ductility of the damped brace
- $\mu_F$  ductility of the main structure

### **3 Design procedure for the seismic retrofit of RC framed structures**

---

$\phi_i$  first mode eigenvector component (with  $i = 1 \div n$ , where  $n$  is the total number of stories)

### 3.6. References

---

- [1] Christopolous C, Filiatrault A. Principles of passive supplemental damping and seismic isolation. IUSS Press 2006, Pavia.
- [2] Kim J, Choi H. Displacement-Based Design of supplemental dampers for seismic retrofit of a framed structure, *Journal of Structural Engineering* 2006; 132(6): 873-883; DOI:10.1061.
- [3] Ferraioli M, Lavino A. A Displacement-Based Design Method for seismic retrofit of RC buildings using dissipative braces, *Hindawi, Mathematical Problems in Engineering* 2018; Volume 2018, Article ID 5364564, 28 pages; DOI: 10.1155/2018/5364564.
- [4] Priestley MJN. Myths and fallacies in earthquake engineering-conflicts between design and reality, *Bulletin of New Zealand Society for Earthquake Engineering* 1993; 26(3): 329-341; DOI: 10.5459/bnzsee.26.3.329-341.
- [5] Noruzvand M, Mohebbi M, Shakeri K. Modified direct displacement-based design approach for structures equipped with fluid viscous damper, *Structural Control and Health Monitoring* 2020; 27: e2465; DOI: 10.1002/stc.2465.
- [6] Lin YY, Tsai MH, Hwang JS, Chang KC. Direct Displacement-Based Design for buildings with passive energy dissipation systems, *Engineering Structures* 2003; 25(1): 25-37; DOI: 10.1016/S0141-0296(02)00099-8.
- [7] Pennuci D, Calvi GM, Sullivan TJ. Displacement-Based Design of precast walls with additional dampers, *Journal of Earthquake Engineering* 2009; 13(1): 40–65; DOI: 10.1080/13632460902813265.
- [8] Wijesundara KK, Nascimbene R, Sullivan TJ. Equivalent viscous damping for steel concentrically braced frame structures, *Bulletin of Earthquake Engineering* 2011; (9): 1535-1558; DOI 10.1007/s10518-011-9272-4.
- [9] Sullivan TJ, Lago A. Towards a simplified Direct DBD procedure for the seismic design of moment resisting frames with viscous dampers, *Engineering Structures* 2012; (35): 140-148; DOI: 10.1016/j.engstruct.2011.11.010.
- [10] O'Reilly GJ, Sullivan TJ. Direct Displacement-Based seismic design of eccentrically braced steel frames, *Journal of Earthquake Engineering* 2016; 20(2): 243-278; DOI: 10.1080/13632469.2015.1061465.
- [11] Segovia VA, Ruiz SE. Direct Displacement-Based Design for buildings with hysteretic dampers, using best combinations of stiffness and strength ratios; *Journal of Earthquake Engineering* 2017; 21(5): 752-775; DOI: 10.1080/13632469.2016.1185054.
- [12] Sahoo DR, Prakash A. Seismic behavior of concentrically braced frames designed using direct displacement-based method, *International Journal of Steel Structures* 2019; 19(1): 96-109; DOI: 10.1007/s13296-018-0092-0.
- [13] Levy R, Lavan O, Rutenberg A. Seismic design of friction damped braced frames based on historical records, *Earthquake Spectra* 2005; 21(3): 761-778.
- [14] Seismology (1999). Recommended Lateral Force Requirements and Commentary, Seismology Committee, Structural Engineers Association of California, SEAOC.

### **3 Design procedure for the seismic retrofit of RC framed structures**

---

- [15] ATC (1996) Seismic evaluation and retrofit of concrete buildings. ATC-40, Applied Technology Council, Redwood City, California.
- [16] Mazza F, Vulcano A. Displacement-Based Seismic Design procedure for framed buildings with dissipative braces Part I: Theoretical formulation, Seismic Engineering Conference Commemorating the 1908 Messina and Reggio Calabria Earthquake (MERCEA08), Reggio Calabria, Italy. American Institute of Physics Conference Proceedings 2008a, U.S.A, Vol. 1020 (part two), 1399-1406.
- [17] Mazza F, Vulcano A. Displacement-Based Seismic Design procedure for framed buildings with dissipative braces Part II: Numerical Results, Seismic Engineering Conference Commemorating the 1908 Messina and Reggio Calabria Earthquake (MERCEA08), Reggio Calabria, Italy. American Institute of Physics Conference Proceedings 2008b, U.S.A, Vol. 1020 (part two), 1407-1416.
- [18] Mazza F, Vulcano A. Displacement-Based Design procedure of damped braces for the seismic retrofitting of RC framed buildings, *Bulletin of Earthquake Engineering* 2015; (13): 2121-2143; DOI: 10.1007/s10518-014-9709-7.
- [19] Mazza F, Vulcano A. Displacement-Based seismic Design of hysteretic damped braces for retrofitting in-elevation irregular RC framed buildings, *Soil Dynamics and Earthquake Engineering* 2015; 69: 115-124; DOI: 10.1016/j.soildyn.2014.10.029.
- [20] Mazza F, Vulcano A. Nonlinear seismic analysis of r.c. framed buildings with setbacks retrofitted by damped braces, *Engineering Structures* 2016; 126: 559-570; DOI: 10.1016/j.engstruct.2016.07.055.
- [21] Mazza F. Nonlinear seismic analysis of unsymmetric-plan structures retrofitted by hysteretic damped braces, *Bulletin of Earthquake Engineering* 2016; 14: 1311-1331; DOI: 10.1007/s10518-016-9873-z.
- [22] Mazza F, Pedace E, Del Favero F. Effectiveness of damped braces to mitigate seismic torsional response of unsymmetric-plan buildings, *Mechanical Systems and Signal Processing* 2017; 85: 610-624; DOI: 10.1016/j.ymsp.2016.09.003.
- [23] Lin YY, Chang KC, Chen CY. Direct Displacement-Based Design for seismic retrofit of existing buildings using nonlinear viscous dampers, *Bulletin of Earthquake Engineering* 2008; 6: 535-552; DOI 10.1007/s10518-008-9062-9.
- [24] Londono JM, Wagg DJ, Neild SA. Supporting brace sizing in structures with added linear viscous fluid dampers: A filter design solution, *Earthquake Engineering & Structural Dynamics* 2014; 43: 1999-2013; DOI: 10.1002/eqe.
- [25] Raju KR, Ansu M, Iyer NR. A methodology of design for seismic performance enhancement of buildings using viscous fluid dampers, *Structural Control and Health Monitoring* 2014; 21: 342-355; DOI: 10.1002/stc.1568.
- [26] Bergami AV, Nuti C. A design procedure of dissipative braces for seismic upgrading structures, *Earthquakes and Structures* 2013; 4(1): 85-105; DOI: 10.12989/eas.2013.4.1.085.
- [27] Fajfar P. Capacity spectrum method based on inelastic demand spectra, *Earthquake Engineering & Structural Dynamics* 1999; 28(9): 979-993.
- [28] Di Cesare A, Ponzo FC. Seismic retrofit of reinforced concrete frame buildings with hysteretic bracing systems: design procedure and behaviour factor, *Hindawi, Shock and Vibration* 2017; Volume 2017, Article ID 2639361; DOI: 10.1155/2017/2639361.

- [29] CEN (European Committee for Standardization). Design of structures for earthquake resistance – Part 3: Assessment and retrofitting of buildings. EN 1998–3 Eurocode 8; 2005.
- [30] CSLLPP (Consiglio Superiore dei Lavori Pubblici). D.M. 17 gennaio 2018 in materia di “norme tecniche per le costruzioni”. Gazzetta ufficiale n.42 del 20 febbraio 2018, Supplemento ordinario n.8, Ministero delle Infrastrutture e dei trasporti, Roma; 2018, in Italian.
- [31] Gandelli E, Taras A, Disti J, Quaglini V. Seismic retrofit of hospitals by means of hysteretic braces: influence on acceleration-sensitive non-structural components. *Frontiers in Built Environment* 2019; 5(100); DOI: doi.org/10.3389/fbuil.2019.00100.
- [32] Carofilis W, Perrone D, O’Reilly GJ, Monteiro R, Filiatrault A. Seismic retrofit of existing school buildings in Italy: Performance evaluation and loss estimation, *Engineering Structures* 2020; 225; DOI: 10.1016/j.engstruct.2020.111243.
- [33] Barbagallo F, Bosco M, Marino EM, Rossi PP, Stramondo P. A multi-performance design method for seismic upgrading of existing RC frames by BRBs, *Earthquake Engineering & Structural Dynamics* 2017; 46: 1099-1119; DOI: 10.1002/eqe.
- [34] Antoniou S, Pinho R. Development and verification of a displacement-based adaptive pushover procedure, *Journal of Earthquake Engineering* 2004; (8)5: 643-661; DOI: 10.1080/13632460409350504.
- [35] Nuzzo I, Losanno D, Caterino N. Seismic design and retrofit of frames structures with hysteretic dampers: a simplified displacement-based procedure, *Bulletin of Earthquake Engineering* 2019; 17: 2787-2819; DOI: 10.1007/s10518-019-00558-8.
- [36] Nuzzo I, Losanno D, Caterino N. DIBRAST: A computer-aided seismic design procedure for frame structures equipped with hysteretic devices, *Frontiers in Built Environment* 2020; 6(13); DOI: 10.3389/fbuil.2020.00013.
- [37] Diotallevi PP, Landi L, Dellavalle A. A methodology for the direct assessment of the damping ratio of structures equipped with nonlinear viscous dampers, *Journal of Earthquake Engineering* 2012; 16(3): 350-373; DOI: 10.1080/13632469.2011.618521.
- [38] Landi L, Fabbri O, Diotallevi PP. A two-step direct method for estimating the seismic response of nonlinear structures equipped with nonlinear viscous dampers, *Earthquake Engineering & Structural Dynamics* 2014; 43(11): 1641-1659; DOI: 10.1002/eq.
- [39] Silvestri S, Gasparini G, Trombetti T. A five-step procedure for the dimensioning of viscous dampers to be inserted in building structures, *Journal of Earthquake Engineering* 2010; 14(3): 417-447; DOI: 10.1080/13632460903093891.
- [40] Palermo M, Muscio S, Silvestri S, Landi L, Trombetti T. On the dimensioning of viscous dampers for the mitigation of the earthquake-induced effects in moment-resisting frame structures, *Bulletin of Earthquake Engineering* 2013; 11(6): 2429-2446.
- [41] Durucan C, Dicleli M. Analytical study on seismic retrofitting of reinforced concrete buildings using steel braces with shear link. *Engineering Structures* 2010; 32(10): 2995-3010; DOI: 10.1016/j.engstruct.2010.05.019.

### 3 Design procedure for the seismic retrofit of RC framed structures

---

- [42] Terenzi G. Energy-Based Design criterion of dissipative bracing systems for the seismic retrofit of frame structures, *Applied Science* 2018; 8(2), 268; DOI :10.3390.
- [43] Sorace S, Terenzi G. Seismic protection of framed structures by fluid viscous damped braces, *Journal of Structural Engineering* 2008; 134(1): 45-55; DOI: 10.1061/(ASCE)0733-9445(2008)134:1(45).
- [44] De Domenico D, Ricciardi G, Takewaki I. Design strategies of viscous dampers for seismic protection of building structures: A review, *Soil Dynamics and Earthquake Engineering* 2019; 118: 144-165; DOI: 10.1016/j.soildyn.2018.12.024.
- [45] Faleschini F, Zanini MA, Toska K. Seismic reliability assessment of code-conforming reinforced concrete buildings made with electric arc furnace slag aggregates, *Engineering Structures* 2019; 195: 324-339; DOI: 10.1016/j.engstruct.2019.05.083.
- [46] Freeman SA. The Capacity Spectrum Method as a tool for seismic design, *Proceedings of the 11<sup>th</sup> European Conference on Earthquake Engineering* 1998, Sept 6-11, Paris.
- [47] CEN (European Committee for Standardization). Design of structures for earthquake resistance – Part 1: General rules, seismic actions and rules for building. EN 1998–1 Eurocode 8; 2005.
- [48] Bruschi E, Quaglini V, Calvi PM. A simplified design procedure for seismic upgrade of frame structures equipped with hysteretic dampers, *Engineering Structures* 2021; 251: 113504; DOI: 10.1016/j.engstruct.2021.113504.
- [49] Quaglini V, Pettoruso C, Bruschi E. Experimental and numerical assessment of prestressed lead extrusion dampers, *International Journal of Earthquake Engineering* 2021; 2.
- [50] Dwairi HM, Kowalsky MJ, Nau JM. Equivalent damping in support of Direct Displacement-Based Design, *Journal of Earthquake Engineering* 2007; 11(4): 512-530; DOI: 10.1080/13632460601033884.
- [51] CSLLPP (Consiglio Superiore dei Lavori Pubblici). Circolare 21 gennaio 2019, n. 7 C.S.LL.PP. Istruzioni per l'applicazione dell'«Aggiornamento delle “Norme tecniche per le costruzioni”» di cui al decreto ministeriale 17 gennaio 2018, Roma; 2019, in Italian.
- [52] Sousa R, Almeida JP, Correia AA, Pinho R. Shake table blind prediction tests: Contributions for improved fiber-based frame modelling, *Journal of Earthquake Engineering* 2020; 24(9): 1435-1476; DOI: 10.1080/13632469.2018.1466743.
- [53] Correia AA, Almeida JP, Pinho R. Seismic energy dissipation in inelastic frames: Understanding state-of-the-practice damping models, *Structural Engineering International* 2013; 23(2): 148-158; DOI: 10.2749/101686613X13439149157001.
- [54] Mazza F, Vulcano A. Design of hysteretic damped braces to improve the seismic performance of steel and R.C. framed structures, *International Journal of Earthquake Engineering* 2014; 31(1): 5-16.
- [55] Kudu FN, Uçak S, Osmancikli G, Türker T, Bayraktar A. Estimation of damping ratios of steel structures by Operational Modal Analysis Method, *Journal of Constructional Steel Research* 2015; 112: 61-68; DOI: 10.1016/j.jcsr.2015.04.019.
- [56] Mahaney JA, Paret TF, Kehoe BE, Freeman SA. The Capacity Spectrum Method for evaluating structural response during the Loma Prieta earthquake, 1993 National Earthquake Conference, Memphis, TN.

- [57] Ponzo FC, Di Cesare A, Arleo G, Totaro P. Protezione sismica di edifici esistenti con controventi dissipativi di tipo isteretico: aspetti progettuali ed esecutivi, *Progettazione Sismica* 2010; II(1): 19-42.
- [58] Martinez-Rueda JE. On the evolution of energy dissipation devices for seismic design, *Earthquake Spectra* 2002; 18(2): 309-346.
- [59] McKenna F, Fenves GI, Scott MH. Open System for Earthquake Engineering Simulation, PEER Report, Berkeley, CA; 2000.
- [60] Scott MH, Fenves GL. Plastic hinge integration methods for force-based beam-column elements, *Journal of Structural Engineering* 2006; 132(2): 244-252; DOI: 10.1061/(ASCE)0733-9445(2006)132:2(244).
- [61] OpenSeesWiki online manual. Available online at: [https://opensees.berkeley.edu/wiki/index.php/Main\\_Page](https://opensees.berkeley.edu/wiki/index.php/Main_Page) [last access: April 2021].
- [62] Bruschi E, Calvi PM, Quaglini V. Concentrated plasticity modelling of RC frames in time-history analyses, *Engineering Structures* 2021; 243: 112716; DOI: 10.1016/j.engstruct.2021.112716.
- [63] Menegotto M, Pinto PE. Method of analysis for cyclically loaded RC plane frames including changes in geometry and non-elastic behaviour of elements under combined normal force and bending, IABSE: Symposium on resistance and ultimate deformability of structures acted on by well defined repeated loads 1973 – Final Report.
- [64] Filippou FC, Popov EP, Bertero VV. Effects of bond deterioration on hysteretic behavior of reinforced concrete joints, Report EERC 83-19 (1983), Earthquake Engineering Research Center, University of California, Berkeley.
- [65] Popovics S. A numerical approach to the complete stress-strain curve of concrete, *Cement and Concrete Research* 1973; 3(5): 583-599.
- [66] Barbagallo F, Bosco M, Marino E, Rossi P. On the fibre modelling of beams in RC framed buildings with rigid diaphragm, *Bulletin of Earthquake Engineering* 2020; 18: 189-210; DOI: 10.1007/s10518-019-00723-z.
- [67] Mazzoni S, McKenna F, Scott MH, Fenves GL, Jeremic B. OpenSEES command language manual. Pacific Earthquake Engineering Research Center, University of California, Berkeley, 2003.
- [68] SIMQKE (SIMulation of earthQuAKE ground motions). Available online at: [https://gelfi.unibs.it/software/simqke/simqke\\_gr.htm](https://gelfi.unibs.it/software/simqke/simqke_gr.htm) (last accessed: July 2021).
- [69] CRESME Ricerche, Incentivi e riduzione del rischio sismico in Italia, *Ingegneria Sismica Italiana*, 2020, in Italian.



## 4. Assessment of the Lead Damper for the seismic rehabilitation of RC framed structures

---

This chapter aims at assessing the use of the Lead Damper (LED) for the seismic rehabilitation of RC framed buildings. The two RC structures presented in Chapter 3 are considered as case-studies and a supplementary energy dissipation system comprising LED units is designed according to the method previously proposed. In order to evaluate the suitability of the LED to achieve different performance levels, the design is performed considering two different damage targets for each structure. In the first case, the structure is retrofitted in order to remain in the elastic range under the design earthquake, while in the second case a partially dissipative behavior is allowed, with formation of plastic hinges, and limited repairable damage. The constitutive behavior of the LED has been investigated in Chapter 2, and the device is modelled in OpenSees framework through the customized material object already described. Non-linear dynamic analyses are carried out, considering a suite of artificial ground motions with response spectra matching on average the target spectrum according to the Italian Building Code [1] for the life-safety limit state. Eventually, a comparison between the retrofit configuration with Lead Dampers and conventional steel hysteretic dampers is presented. The results of the study demonstrate both the viability of the LED device and the effectiveness of the rehabilitation procedure.

### 4.1. Case-study 1: building in Potenza

---

The case-study structure located in Potenza [2] and presented in Section 3.3 is examined, designing the seismic retrofit for two distinct performance levels corresponding to as many behaviors of the upgraded structure, namely (i) an elastic behavior, avoiding any structural damage under the design earthquake, and (ii) a partially dissipative behavior, with formation of plastic hinges to a repairable level. Both the numerical model used in the non-linear analyses (static and dynamic) and the accelerograms adopted in the bidirectional time histories have been already introduced in Chapter 3, and for this reason, they are not presented hereinafter.

#### 4.1.1. Retrofit with elastic frame behavior

The performance displacement  $d_p$  is evaluated via Eq. (3.5b), assuming a target inter-story drift ratio  $\Delta_d$  equal to  $0.005 m/m$ , as suggested in Section 3.2.2, corresponding to a target displacement  $d_p = 0.045 m$  for the MDOF system, and  $d_p^* = 0.036 m$  for the equivalent SDOF system. The procedure described in Section 2 of Chapter 3 is applied separately to both X- and Z- directions, providing the equivalent bilinear capacity curves in ADRS format.

The seismic rehabilitation of the structure is performed by referring to a diagonal brace configuration (Figure 3-11), equipped with Lead Damper (LED) devices (hereinafter this system will be referred to as LED-DBS). The experimental characterization of the Lead Damper highlighted an elastic-perfectly plastic behavior of the device, with an equivalent damping ratio  $\xi_{DB} = 55.0\%$  and a ductility factor of 20 (Section 2.4).

#### 4 Assessment of the Lead Damper for the seismic rehabilitation of RC framed structures

Consistently, the properties of the equivalent damped brace system are assigned as  $\mu_{DB} = 20$  and  $\kappa_{DB} = 0.9$  (corresponding to high damping capability with wide and stable hysteresis loops). For simplicity, the stiffness of the damped brace has been assumed to coincide with the stiffness of the hysteretic damper, i.e., the steel brace rods used to link the damper to the structural frame are very stiff and, under the actions induced by the design earthquake, undergo negligible deflection in comparison to the damper's one. Otherwise, a simple approach to account for the flexibility of link elements can be found in references [2] and [3]. The design of the LED-DBS system is performed in accordance with the procedure described in Chapter 3. The bilinear curve of the equivalent SDOF *Frame + Damped brace* system is plotted in the ADRS plane; by implementing the recursive procedure introduced in Section 3.2; convergence is achieved at the 3<sup>rd</sup> iteration (Figure 4-1).

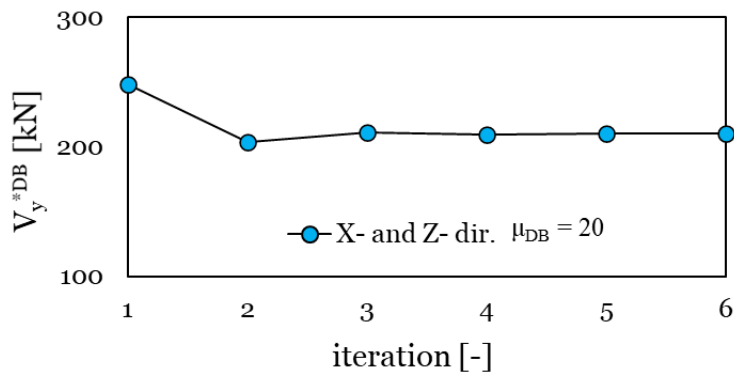


Figure 4-1: Iterative procedure for tuning the equivalent SDOF LED-DBS for elastic frame behavior: damper yield strength vs. iteration number

The distribution of the LED-DBS along the height of the frame is performed in accordance with the method illustrated in Section 3.2.5, referring to the layout shown in Figure 3-11, with 4 dampers at each story in either horizontal direction. The results are reported in Table 4-1 in terms of strength and stiffness of the damped brace units at each floor.

story	X-direction		Z-direction	
	$K_{yi}^{DB}$	$N_{yi}^{DB}$	$K_{yi}^{DB}$	$N_{yi}^{DB}$
	$\left[\frac{kN}{mm}\right]$	$[kN]$	$\left[\frac{kN}{mm}\right]$	$[kN]$
1 <sup>st</sup>	146.5	83.2	148.3	83.3
2 <sup>nd</sup>	121.9	73.2	122.1	73.3
3 <sup>rd</sup>	120.5	52.5	120.5	52.6
4 <sup>th</sup>	113.7	24.0	112.7	24.1

Table 4-1: Properties of LED-DBS units in case of retrofit for elastic frame behavior

The effectiveness of the design is validated by performing both NLSAs and NLDA in the OpenSees framework [4]. The LED-DBS is modelled as a *truss element* with associated either *uniaxialMaterial* object, depending on the type of analysis:

- *uniaxialMaterial* EPP [4] with properties according to Table 4-1 for NLSA;
- *uniaxialMaterial* EPPV, with properties according to Table 4-2 for NLDA, obtained by tuning the model parameters according to the procedure defined in Appendix A.

The different model choice is due to the fact that the *uniaxialMaterial* EPPV (Section 2.4) includes a velocity-dependent force contribution that is not engaged during the quasi-static application of load performed in NLSA, and therefore its use is reserved to NLDA, where it is expected to provide a more accurate representation of the hysteretic force – displacement loop (and therefore a more accurate estimate of the dissipated energy) in case of earthquake-induced large velocities.

#### 4 Assessment of the Lead Damper for the seismic rehabilitation of RC framed structures

<i>Direction</i>	<i>story</i>	$K_{EPP,i}$ [ $\frac{kN}{mm}$ ]	$V_{EPP,i}$ [kN]	$\alpha_{d,i}$ [-]	$K_{d,i}$ [ $\frac{kN}{mm}$ ]	$C_{d,i}$ [ $kN(s/mm)^{\alpha_d}$ ]
X	1 <sup>st</sup>	146.5	66.6	0.3	2500	3.7
	2 <sup>nd</sup>	121.9	58.5	0.3	2500	3.25
	3 <sup>rd</sup>	120.5	41.9	0.3	2500	2.33
	4 <sup>th</sup>	113.7	19.2	0.3	2500	1.07
Z	1 <sup>st</sup>	148.3	66.6	0.3	2500	3.7
	2 <sup>nd</sup>	122.1	58.6	0.3	2500	3.25
	3 <sup>rd</sup>	120.5	42.1	0.3	2500	2.33
	4 <sup>th</sup>	112.7	19.3	0.3	2500	1.07

Table 4-2: Properties of the EPPV for the case-1 building in Potenza retrofitted for elastic frame behavior

In Figure 4-2, the capacity curves in X- and Z- directions of the upgraded structure are plotted in the ADRS plane and compared with the response demand curve for the relevant damping. The design requirement is met by the upgraded frames since the displacement at the performance point, where capacity and demand curves cross each other, meets the target displacement selected at the beginning of the design process.

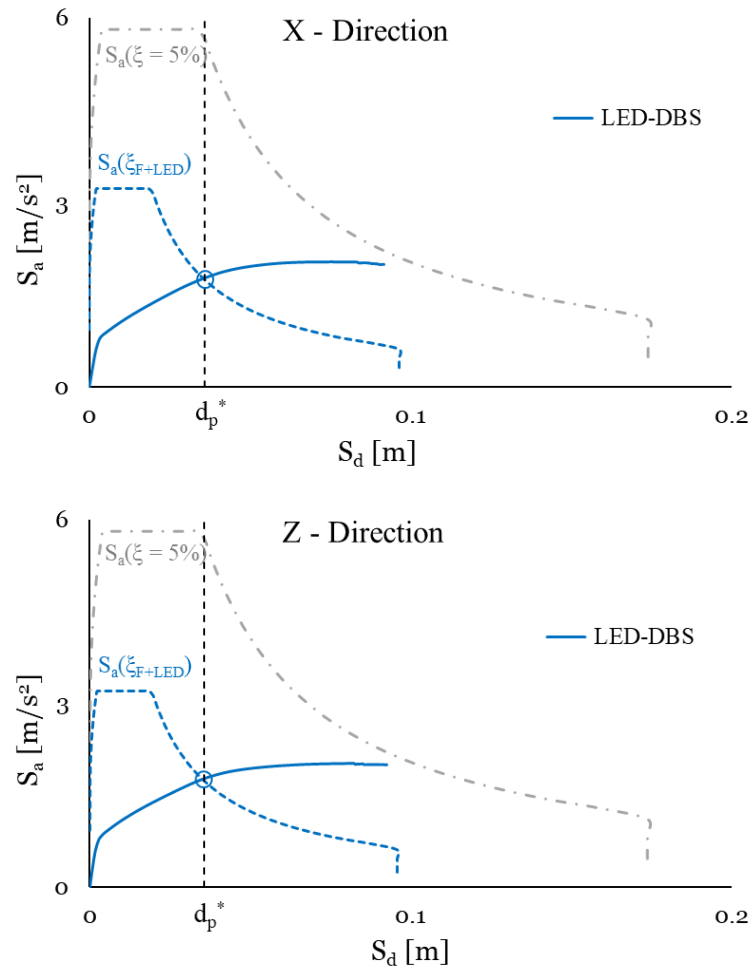


Figure 4-2: Capacity curves in X- and Z- direction of the case-1 structure retrofitted with the LED-DBS for elastic frame behavior

In order to evaluate the performance of the upgraded structure in terms of engineering response parameters, such as maximum inter-story drift ratio  $\Delta$  and maximum shear force  $V$  at each floor, BNLDA are performed using the ground motions of Chapter 3. Figure 4-3 and Figure 4-4 show the numerical results in terms of  $\Delta$  and  $V$  at each floor, comparing the as-built configuration to the retrofitted configuration with the LED-DBS. The inter-story drift ratio  $\Delta$  drastically decreases in amplitude and shows a regular shape, respecting at each floor the target value  $\Delta_d = 0.005 \text{ m/m}$ , Figure 4-3.

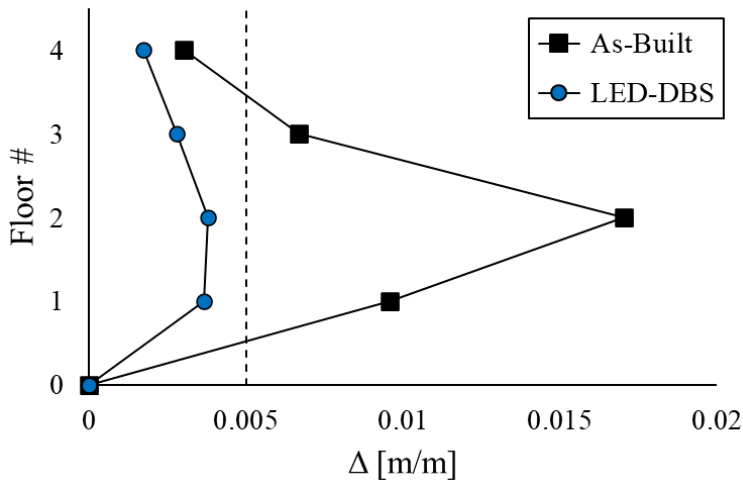


Figure 4-3: Maximum inter-story drift ratio  $\Delta$  in case-1 structure with and w/o LED-DBS for elastic frame behavior

Usually, buildings retrofitted with hysteretic devices exhibit smaller lateral deformation, but increased shear forces  $V$  at the floors with respect to the bare structure. However, in the present case, shear forces remain substantially unaffected from the upgrade, thanks to the high damping introduced in the structure by the LED-DBS which limits increase in floor accelerations. In particular, at the first two floors, the shear force of the retrofitted structure is even smaller (about 5% at the first floor) than that of the as-built one, and only a slight increase occurs at the last floor where  $V$  increases by 2.2%, from 348 kN to 355 kN, Figure 4-4.

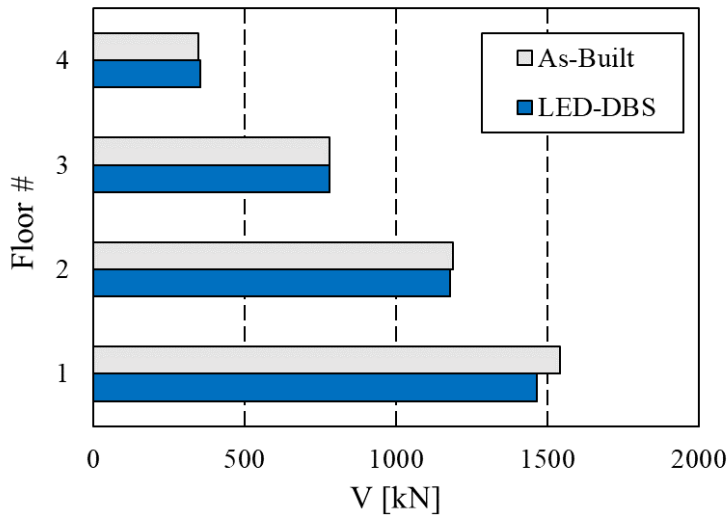


Figure 4-4: Maximum shear force  $V$  at each floor of case-1 with and w/o LED-DBS for elastic frame behavior

Figure 4-5 shows the force-displacement cyclic behavior of the LED-DBS units installed at the various floors along the X-direction, demonstrating the fair agreement between the actual stiffness and strength of the devices and the design values specified in Table 4-1.

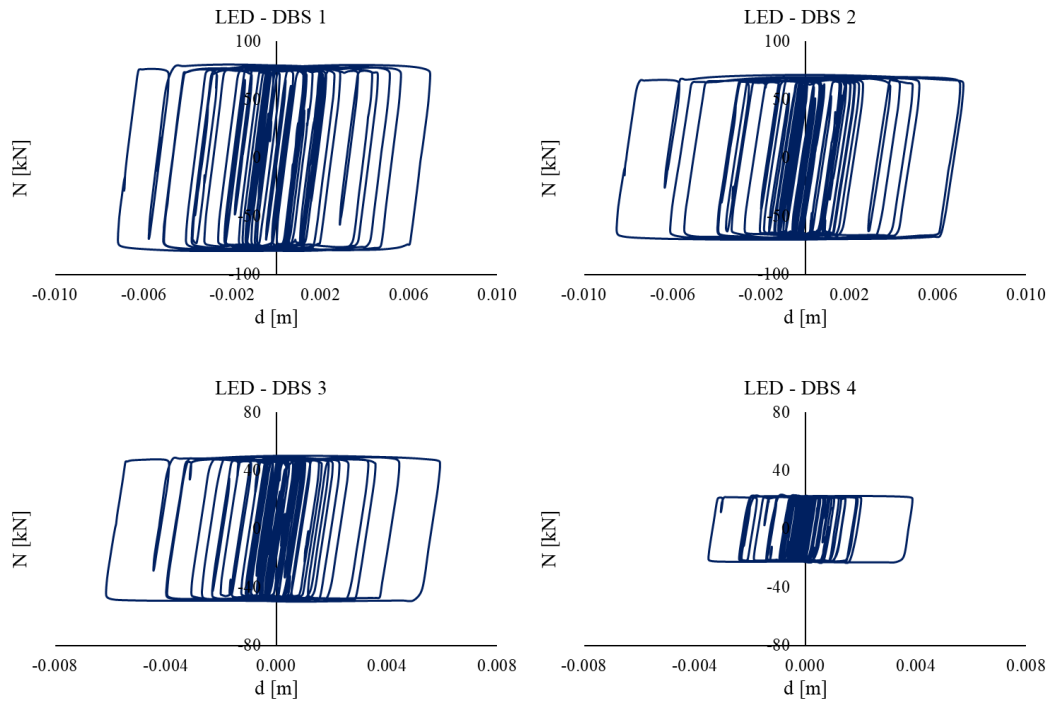


Figure 4-5: Force-displacement cyclic behavior of LED-DBS at each floor along X-direction

4.1.2. Retrofit with dissipative frame behavior

The target displacement  $d_p$  is evaluated with the Eq. (3.5b), for a target inter-story drift ratio  $\Delta_d$  equal to  $0.00625\text{ m/m}$ , resulting in  $d_p = 0.057\text{ m}$  and  $d_p^* = 0.045\text{ m}$ . By assuming an inter-story drift ratio  $\Delta = 0.5\%$  as the elastic limit, the target  $\Delta_d$  indeed corresponds to a ductility factor  $\mu_F = 1.25$  at the weak story of the main frame. The properties of the equivalent SDOF system corresponding to the assumed  $d_p^*$  are reported in Table 4-3.

<i>Direction</i>	$\Gamma$	$d_y^*$	$V_y^{*F}$	$d_p^*$	$V_p^{*F}$	$\xi_F$	$m^*$
	[–]	[m]	[kN]	[m]	[kN]	[%]	[ton]
<b>X</b>	1.27	0.013	200.2	0.045	438.0	6.8	339.8
<b>Z</b>	1.27	0.014	209.2	0.045	419.3	7.9	339.4

Table 4-3: Properties of the equivalent SDOF system of case-1 structure in either horizontal direction

Also in this case, the retrofit is designed assuming a LED-DBS characterized by  $\kappa_{DB} = 0.9$  and  $\mu_{DB} = 20$ , which correspond to  $\xi_{DB} = 55.0\%$ , Eq. (3.11). The tuning procedure converges at the 3<sup>rd</sup> iteration, Figure 4-6, and the properties of the LED-DBS units at each floor, for the configuration represented in Figure 3-11, are reported in Table 4-4.

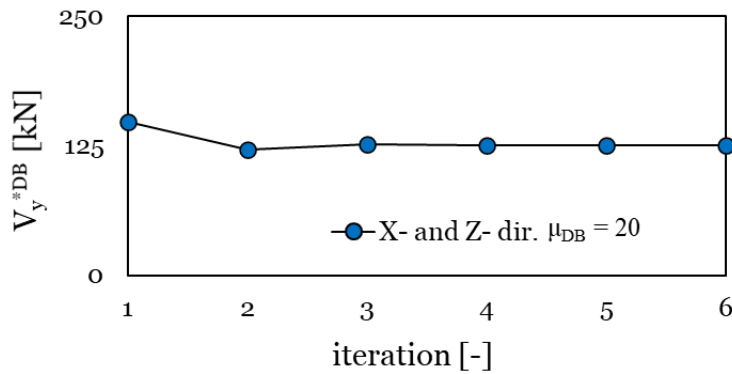


Figure 4-6: Iterative procedure for tuning the equivalent SDOF LED-DBS for dissipative frame behavior: damper yield strength vs. iteration number

story	X-direction		Z-direction	
	$K_{yi}^{DB}$	$N_{yi}^{DB}$	$K_{yi}^{DB}$	$N_{yi}^{DB}$
	$\left[\frac{kN}{mm}\right]$	[kN]	$\left[\frac{kN}{mm}\right]$	[kN]
1 <sup>st</sup>	70.1	49.8	69.6	48.8
2 <sup>nd</sup>	58.3	43.8	57.3	42.9
3 <sup>rd</sup>	57.7	31.4	56.5	30.8
4 <sup>th</sup>	54.4	14.4	52.9	14.2

Table 4-4: Properties of the LED-DBS in case of retrofit for dissipative frame behavior

The LED-DBS is modelled as a *truss element* with associated either *uniaxialMaterial* object:

- *uniaxialMaterial* EPP [4] with properties according to Table 4-4 for NLSA;
- *uniaxialMaterial* EPPV, with properties according to Table 4-5 for NLDA

Direction	story	$K_{EPP,i}$	$V_{EPP,i}$	$\alpha_d$	$K_d$	$C_{d,i}$
		$\left[\frac{kN}{mm}\right]$	[kN]	[-]	$\left[\frac{kN}{mm}\right]$	$[kN(s/mm)^{\alpha_d}]$
X	1 <sup>st</sup>	70.1	49.8	0.3	2500	2.21
	2 <sup>nd</sup>	58.3	43.8	0.3	2500	1.95
	3 <sup>rd</sup>	57.7	31.4	0.3	2500	1.39
	4 <sup>th</sup>	54.4	14.4	0.3	2500	0.64
Z	1 <sup>st</sup>	69.6	48.8	0.3	2500	2.17
	2 <sup>nd</sup>	57.3	42.9	0.3	2500	1.91
	3 <sup>rd</sup>	56.5	30.8	0.3	2500	1.37
	4 <sup>th</sup>	52.9	14.2	0.3	2500	0.63

Table 4-5: Properties of the EPPV for the case-1 building in Potenza retrofitted for dissipative frame behavior

As done in Section 4.1.1, to check the effectiveness of the LED-DBS, NLSAs and BNLDAs are performed and Figure 4-7 - Figure 4-9 show the relevant results. In Figure 4-7, the capacity curves along X- and Z-directions of the upgraded structure are reported in the ADRS plane, proving that the design requirement is achieved by the upgraded frames.

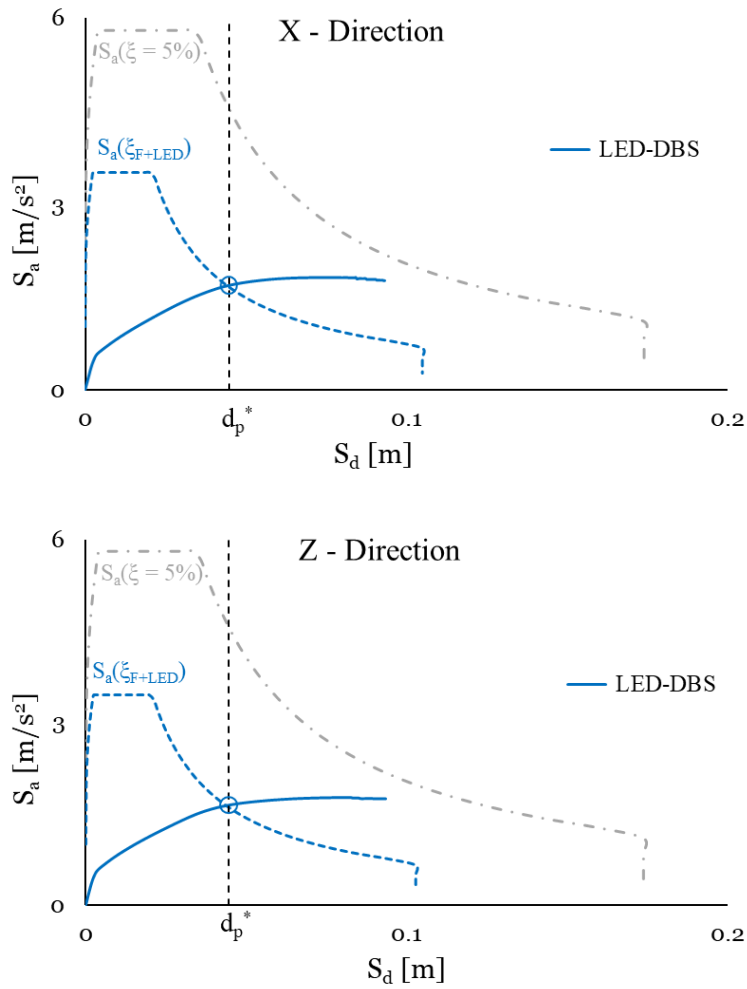


Figure 4-7: Capacity curves in X- and Z- directions of the case-1 structure retrofitted with the LED-DBS for dissipative frame behavior

In Figure 4-8, the inter-story drift ratio  $\Delta$  of the upgraded configuration shows a significant reduction with respect to the bare frame's one, with a peak value of  $0.0055 \text{ m/m}$  at the second floor, which corresponds to a ductility factor  $\mu_F = 1.1$ , thereby respecting the limit of  $\mu_F = 1.25$  selected at the beginning of the design procedure.

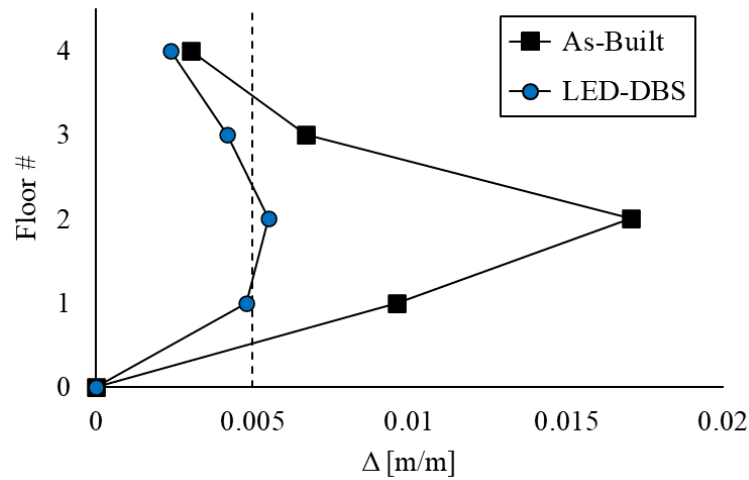


Figure 4-8: Maximum inter-story drift ratio  $\Delta$  in case-1 structure with and w/o LED-DBS for dissipative frame behavior

The shear forces  $V$  at each floor of the retrofitted configuration are not increased with respect to the as-built frame (Figure 4-9), confirming the low impact of the LED-DBS on the structural elements surrounding damped braces.

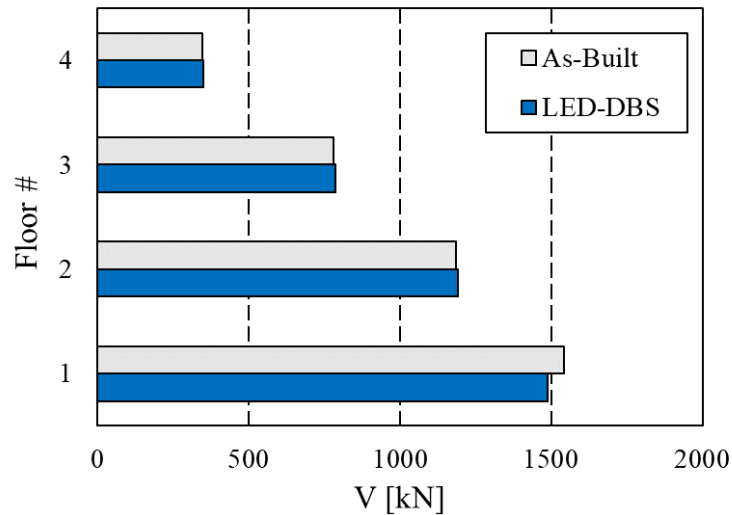


Figure 4-9: Maximum shear force  $V$  at each floor of case-1 structure with and w/o LED-DBS for dissipative frame behavior

To check the effectiveness of the LED-DBS for controlling the damage of the RC frame members, unidirectional NLDAs exploiting artificial ground motions 1-7 along X-direction and 8-14 along Z-direction (see Section 3.3.2) were performed, and the ductility demand  $\mu'_F$  of every beam and column were determined.  $\mu'_F$  corresponds to the ratio of the maximum curvature  $\varphi_{max}$  (averaged over the set of seven ground motions for each direction) at either end section of the structural member and the yield curvature  $\varphi_y$ , evaluated from a sectional analysis, considering the seismic load for the columns. The highest values of  $\mu'_F = \varphi_{max}/\varphi_y$  at each story of the retrofitted frame were attained at the column labelled as C8 and at the beams labelled as B6 and B7 in Figure 4-10.

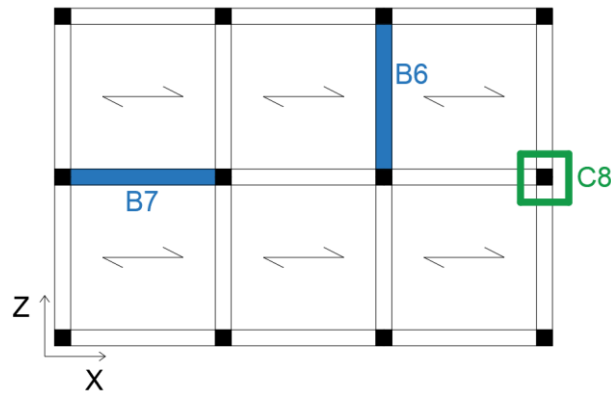


Figure 4-10: Most stressed element at each floor

By upgrading the structure with the LED-DBS, the ductility demand is substantially reduced in each element; in fact, while the bare frame exhibits huge plastic deformation of the columns at all stories but for the fourth one, the retrofitted structure seems to develop a controlled engagement of plastic hinges, which are triggered only in the beams of the first and second floor, thereby respecting the principle of strong column / weak beam assumed in performance-based design.

Figure 4-11 shows the results relevant to beams B7 and B6 for accelerograms directed along the X- and the Z- direction, respectively. Indeed, when subjected to unidirectional accelerograms along the direction perpendicular to their long axes, the beams have a negligible deformation. Here, the *F* tag refers to the as-built configuration, and the *F+DB* tag refers to the structure upgraded for partially dissipative frame behavior. The huge plastic deformation experienced by the as-built configuration is apparent; the maximum beam curvature is achieved at the first floor, with a maximum ductility demand  $\mu'_F = 6.29$  in beam B7. In the retrofitted configuration, beams B6 and B7 are again in the plastic regime at the first and second floor, where B6 reaches ductility demands  $\mu'_F = 1.48$  and  $\mu'_F = 1.19$  respectively, while B7 attains the values  $\mu'_F = 1.72$  at the first floor and  $\mu'_F = 1.13$  at the second floor.

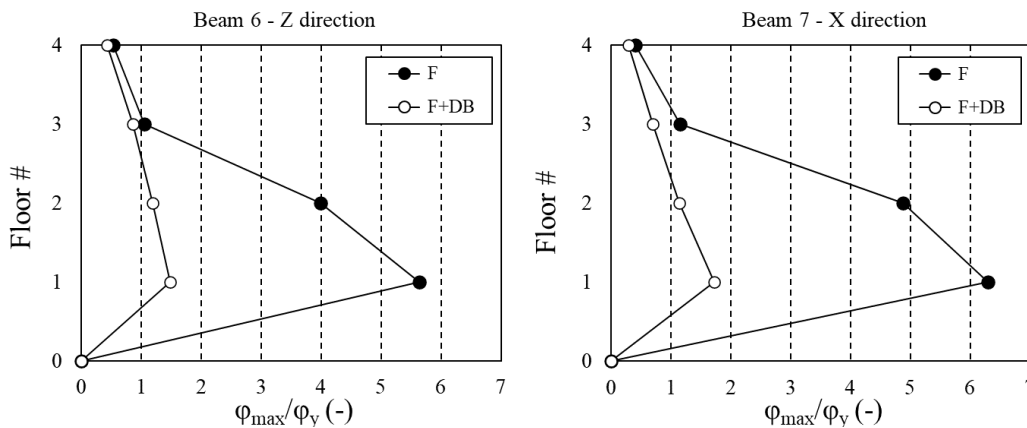


Figure 4-11: Maximum ductility demand  $\mu_F$  in beam B6 along Z-direction and beam B7 along X-direction at each floor

Figure 4-12 to Figure 4-15 focus more in detail on the response of the identified structural members under the set of the unidirectional accelerograms by reporting the maximum values of the ductility demand  $\mu'_F$  for each individual ground motion. Figure 4-12 and Figure 4-13 show the results for columns in position C8,

and Figure 4-14 and Figure 4-15 for beams in position B6 and B7, respectively. For sake of brevity, the results at the third and fourth floor are disregarded since, owing to the lower ductility demand, the effect of the introduction of the LED-DBS is less evident. It is worth noting that, as apparent especially from the distribution of drift ratios in elevation shown in Figure 4-8, the introduction of dampers at the two last floors is aimed at constraining the drifts of the braced frame to follow the first mode deformation of the as-built frame in order to promote the simultaneous engagement of the dampers at each floor during the earthquake. A second effect of the introduction of the LED-DBS, beyond the decrease of the ductility demand averaged over the seven accelerograms, is to reduce the sensitiveness of the response of the structural layout on the characteristics of the ground motion, and the ductility demand of the upgraded frame becomes little dependent on the individual input; this is especially evident for C8 along X-direction where the ratio  $\varphi_{max}/\varphi_y$  becomes practically constant (Figure 4-12).

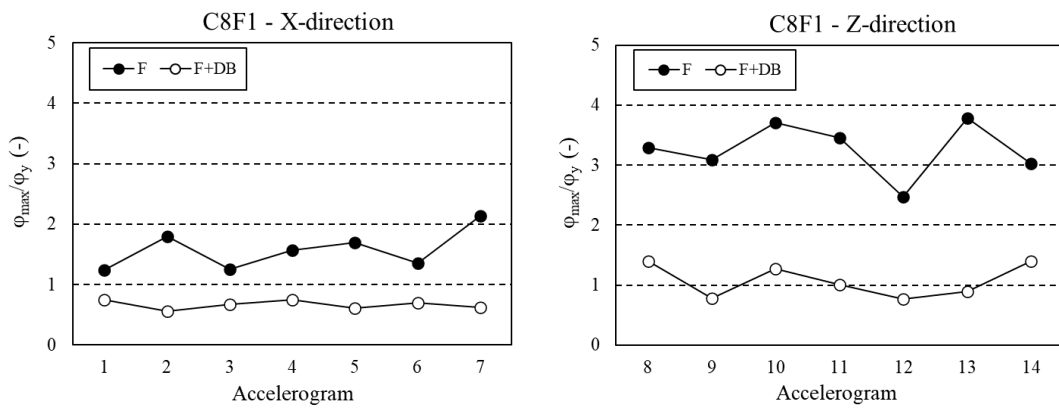


Figure 4-12: Maximum ductility demand of column C8 at first floor along X-direction (left) and Z-direction (right)

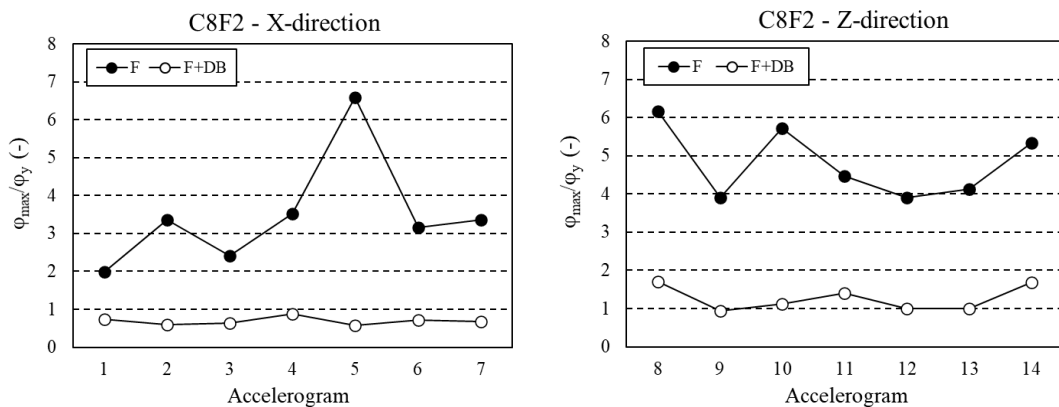


Figure 4-13: Maximum ductility demand of column C8 at second floor along X-direction (left) and Z-direction (right)

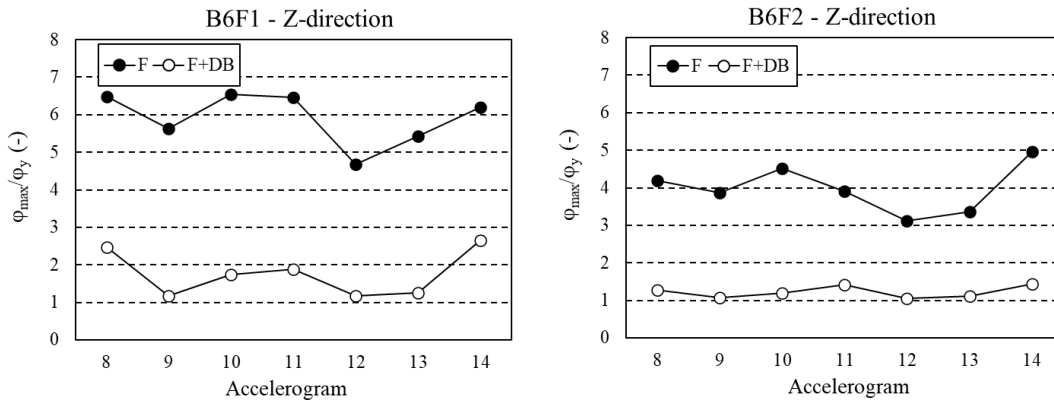


Figure 4-14: Ductility demand of beam B6 at first (left) and second (right) floor along Z-direction for the set of ground motions 8-

14

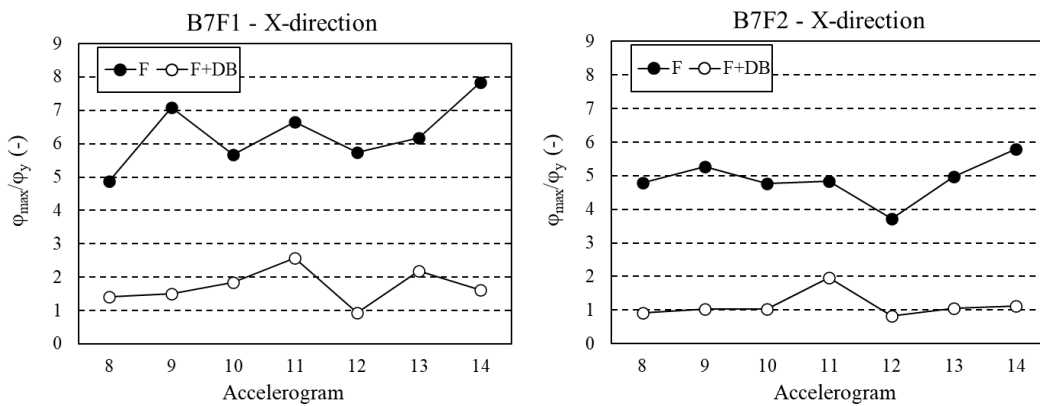


Figure 4-15: Ductility demand of beam B7 at first (left) and second (right) floor along Z-direction for the set of ground motions 1-

7

Figure 4-16 shows the curves representing the average and the maximum ductility demands of the beam members at the first and second stories. The third and fourth story are again disregarded since their beams have an elastic behavior. In these graphs, the  $F+DB(AVG)$  plot refers to the ductility demand  $\phi_{max}/\phi_y$  averaged over all the beams at the floor, and the  $F+DB(max)$  to the ductility demand of the most stressed beams at the floor. For comparison, also the ductility demand for the unbraced structure is reported and labeled as  $F(AVG)$  and  $F(max)$  respectively. It is worth noting that when the frame is subjected to unidirectional ground motions along the Z-direction, all beams at the first floor are subjected to almost equivalent anelastic deformations; in contrast, in case of ground motions along the X-direction the plastic engagement of the beams is less uniform, with a ratio between maximum and average ductility demand of 1.26.

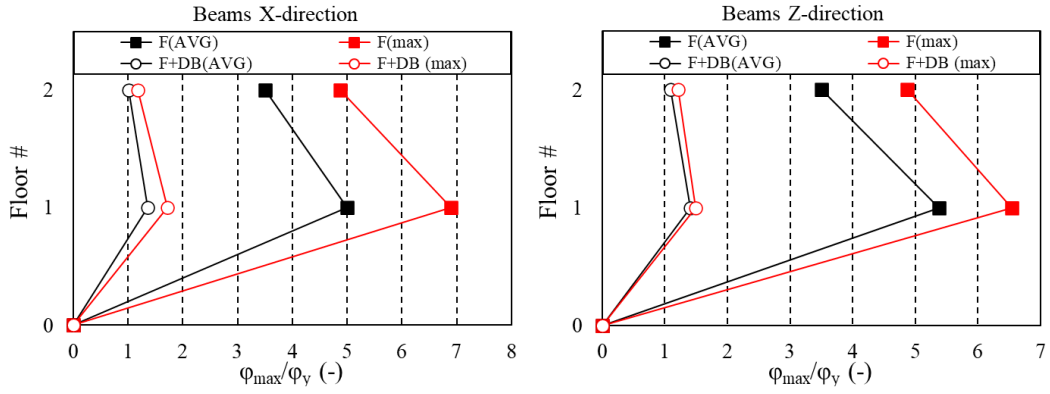


Figure 4-16: Average and maximum ductility demand  $\mu'_F$  of beams along X-direction (left) and Z-direction (right) at first and second floor

### 4.1.3. Comparison between LED- and SHD-DBS

In this paragraph, the case-study 1 structure is retrofitted by using a steel hysteretic damped brace system (SHD-DBS) for both elastic and partially dissipative frame behavior. According to reference [5], the SHD-DBS selected for this investigation is characterized by  $\kappa_{DB} = 0.425$  and  $\mu_{DB} = 10$ , yielding an equivalent viscous damping ratio  $\xi_{DB} = 24.4\%$ , which is less than half of the equivalent viscous damping ratio of the LED-DBS, assumed based on experimental data. A direct comparison between the strength and stiffness of the SHD-DBS and the LED-DBS solution is reported. Moreover, NLSAs are performed in order to show the effectiveness of the LED-DBS and its advantages over the conventional SHD-DBS.

#### 4.1.3.1. Elastic frame behavior

In analogy to Section 4.1.1, in order to keep the response of the retrofitted configuration in the elastic range, the target displacement is set to  $d_p^* = 0.036$  m in either horizontal direction. By applying the iterative procedure introduced in Chapter 2, the properties of the SHD-DBS are defined at the 4<sup>th</sup> iteration; Figure 4-17 shows a comparison between the tuning of the equivalent LED-DBS and of the equivalent SHD-DBS SDOF systems.

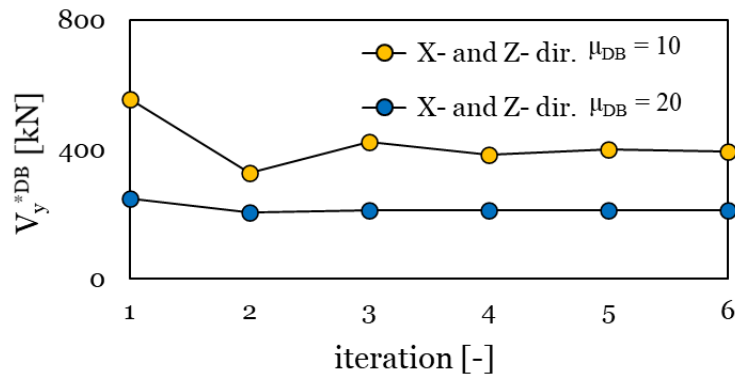


Figure 4-17: Comparison between the tuning of the equivalent LED-DBS and the equivalent SHD-DBS SDOF systems for elastic frame behavior: damper yield strength vs. iteration number

#### 4 Assessment of the Lead Damper for the seismic rehabilitation of RC framed structures

The diagonal brace layout shown in Figure 3-11 is assumed for both LED-DBS and SHD-DBS retrofits. Table 4-6 performs a direct comparison, in terms of strength and stiffness of the damped brace units at each story, between the SHD- and the LED-DBS, distributed along the height of the frame according to the method of Section 3.2.5. At each floor the ratio between the initial stiffnesses  $K_{yi}^{DB}$  of the LED-DBS and the SHD-DBS counts 1.066, i.e., the stiffness of the LED-DBS unit is only 6.6% higher than that of the SHD-DBS unit. Noteworthy, the ratio between the axial forces  $N_{yi}^{DB}$ , of the LED-DBS and the SHD-DBS is 0.533: owing to its superior energy dissipation capability, about 55% higher than that of the SHD-DBS, the LED-DBS halves the strength demand.

Directions	story	SHD - DBS		LED - DBS	
		$K_{yi}^{DB}$	$N_{yi}^{DB}$	$K_{yi}^{DB}$	$N_{yi}^{DB}$
		$\frac{kN}{mm}$	[kN]	$\frac{kN}{mm}$	[kN]
X	1 <sup>st</sup>	137.5	156.2	146.6	83.2
	2 <sup>nd</sup>	114.4	137.3	122	73.2
	3 <sup>rd</sup>	113.1	98.4	120.5	52.5
	4 <sup>th</sup>	106.7	45.1	113.7	24
Z	1 <sup>st</sup>	139.2	156.4	148.3	83.3
	2 <sup>nd</sup>	114.7	137.6	122.1	73.3
	3 <sup>rd</sup>	113.1	98.8	120.5	52.6
	4 <sup>th</sup>	105.8	45.3	112.7	24.1

Table 4-6: Comparison between design properties of the SHD-DBS and the LED-DBS at each story for elastic behavior

Figure 4-18 and Figure 4-19 compare the capacity curves of the upgraded structure with either DBS solution. In both directions, the design requirement is met by the upgraded frames, which attain the target displacement  $d_p$  at their performance point (this is a further confirmation of the effectiveness of the design procedure even for damper with different ductility). However, as an effect of the different dissipation capacity, dissimilar values of base shear force are achieved. As shown in Figure 4-20, the increase in shear force in case of SHD-DBS with respect to the LED-DBS is on the order of 34% in X-direction, and of 35% in Z-direction. This result highlights a valuable advantage of the LED-DBS over the SHD-DBS. In fact, structures strengthened with dissipative braces are usually affected from stress concentrations in the structural elements surrounding the braces, as well as at foundation level [6], implying the necessity of combining the DBS with local strengthening to increase the capacity of the structural members. Such stress concentrations can be mitigated or even avoided by using the LED-DBS, resulting in an overall reduction of the cost of the retrofit intervention.

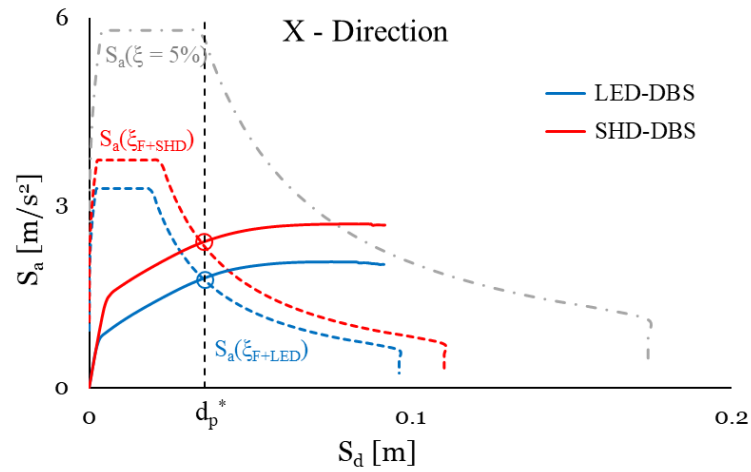


Figure 4-18: Comparison of the capacity curves in X-direction of the case-1 structure retrofitted with the LED-DBS and the SHD-DBS for elastic frame behavior

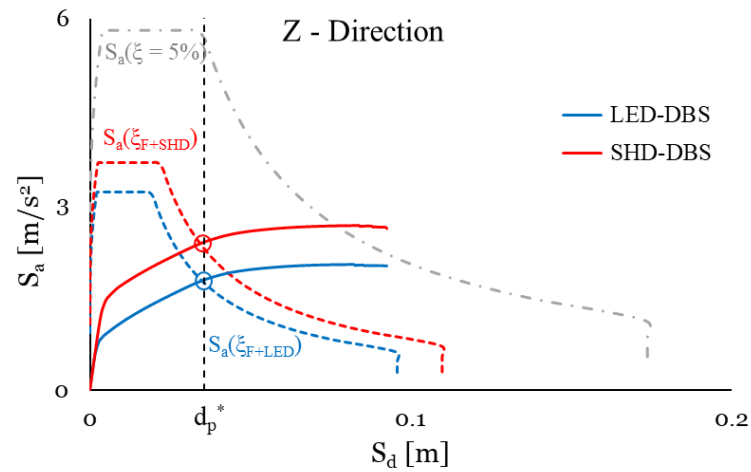


Figure 4-19: Comparison of the capacity curves in Z-direction of the case-1 structure retrofitted with the LED-DBS and the SHD-DBS for elastic frame behavior

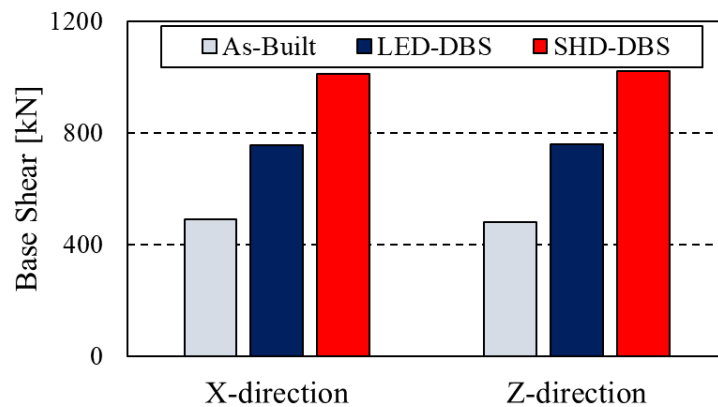


Figure 4-20: Comparison of the base shear force of the case-1 structure retrofitted with either LED-DBS or SHD-DBS for elastic frame behavior

4.1.3.2. Dissipative frame behavior

The seismic rehabilitation of the building assuming partially dissipative frame behavior is repeated with the SHD-DBS system by assuming again a target displacement  $d_p^* = 0.045$  m. Figure 4-21 compares the progress of the tuning procedure of the equivalent SDOF LED-DBS and SHD-DBS, and Table 4-7 reports the strength and stiffness of the individual damped brace unit at each floor for either DBS configuration.

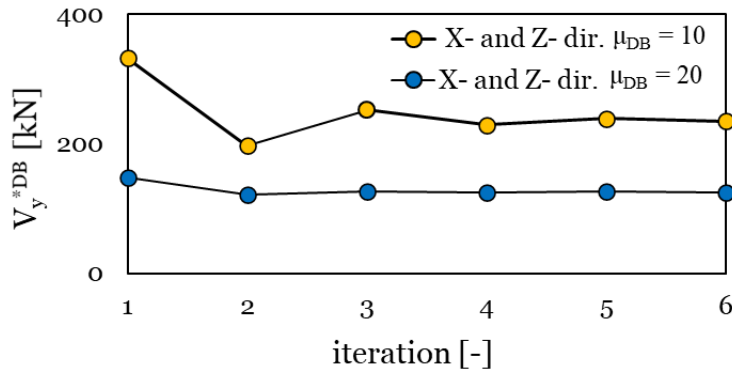


Figure 4-21: Comparison between the tuning of the equivalent SDOF LED-DBS and SHD-DBS for dissipative frame behavior: damper yield strength vs. iteration number

Directions	story	SHD - DBS		LED - DBS	
		$K_{yi}^{DB}$ [ $\frac{kN}{mm}$ ]	$N_{yi}^{DB}$ [kN]	$K_{yi}^{DB}$ [ $\frac{kN}{mm}$ ]	$N_{yi}^{DB}$ [kN]
<b>X</b>	1 <sup>st</sup>	66	93.6	70.1	49.8
	2 <sup>nd</sup>	54.9	82.3	58.3	43.8
	3 <sup>rd</sup>	54.2	59	57.7	31.4
	4 <sup>th</sup>	51.2	27	54.4	14.4
<b>Z</b>	1 <sup>st</sup>	65.5	92	69.6	48.8
	2 <sup>nd</sup>	54	81	57.3	42.9
	3 <sup>rd</sup>	53.3	58.1	56.5	30.8
	4 <sup>th</sup>	49.8	26.7	52.9	14.2

Table 4-7: Comparison between design properties of the SHD-DBS and the LED-DBS at each story for dissipative behavior

By comparing these results to the ones obtained for the retrofit with elastic frame behavior, it is apparent that the damper strength is almost halved, thanks to the contribution of energy dissipation introduced by plastic deformation of the frame, Figure 4-21. Consequently, also the properties of the SHD-DBS and LED-DBS units at each floor (Table 4-7) are drastically reduced (almost halved) in comparison the ones reported in Table 4-6 for elastic frame behavior. It is worth mentioning that along either direction the ratios between

the stiffnesses and the strengths of the LED-DBS and the SHD-DBS match those obtained for retrofit with elastic frame behavior ( $1.06$  for stiffness  $K_{yi}^{DB}$ , and  $0.53$  for strength  $N_{yi}^{DB}$ ).

The capacity curves reported in Figure 4-22 and Figure 4-23, and the values of base shear shown in Figure 4-24 confirm that the upgraded structure meets the design requirement whichever the adopted damped brace system, but the SHD-DBS induces again higher base shear forces, due to the smaller energy dissipation capability in comparison to the LED-DBS. In contrast, by comparing Figure 4-22 and Figure 4-23 to Figure 4-18 and Figure 4-19, as well as Table 4-7 to Table 4-6, it comes out that the capacity curves of the structure retrofitted for partially dissipative frame behavior with either SHD- and LED-DBS are closer to each other, with lower differences between the strength  $N_{yi}^{DB}$  of the damped brace; this is ascribed to the dissipation capability of the main structure which reduces the damping demand to the energy dissipation devices. This is evident by comparing Figure 4-24 to Figure 4-20: in this case, the increase in base shear force of SHD-DBS with respect to the LED-DBS is on the order of 22% in X-direction, and of 23% in Z-direction.

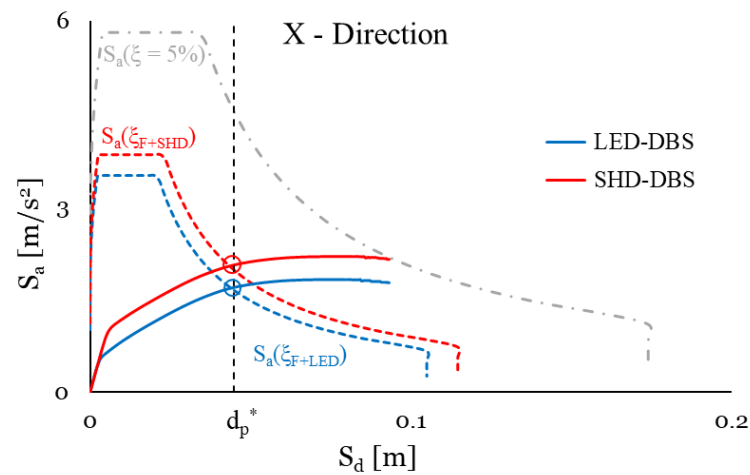


Figure 4-22: Comparison of the capacity curves in X-direction of the case-study structure retrofitted with the LED-DBS and the SHD-DBS for dissipative frame behavior

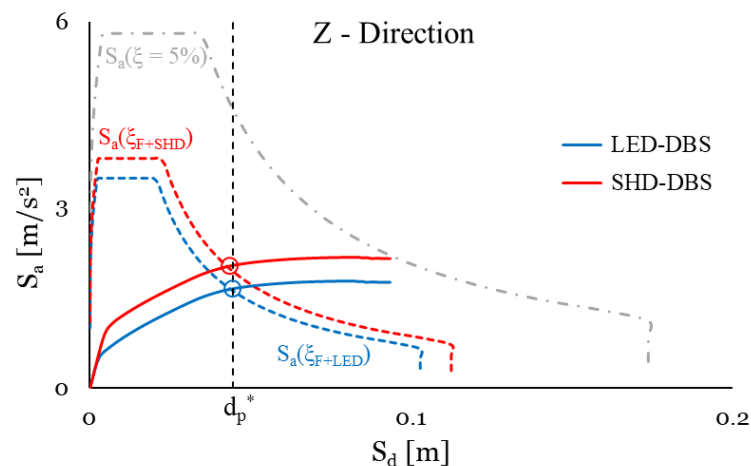


Figure 4-23: Comparison of the capacity curves in Z-direction of the case-study structure retrofitted with the LED-DBS and the SHD-DBS for dissipative frame behavior

#### 4 Assessment of the Lead Damper for the seismic rehabilitation of RC framed structures

---

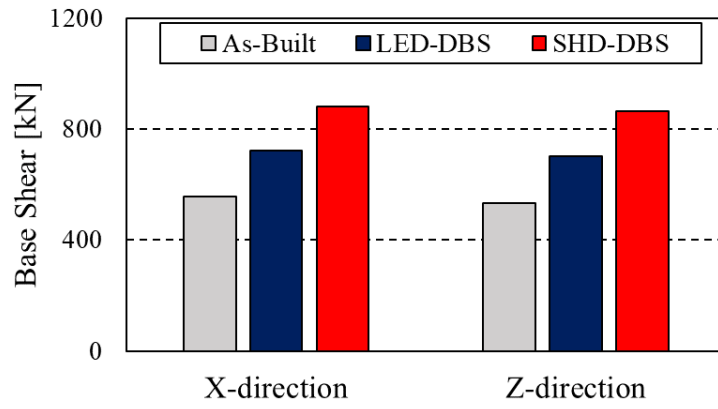


Figure 4-24: Comparison of the base shear force of the case-study structure retrofitted with either LED-DBS or SHD-DBS for dissipative frame behavior

## 4.2. Case-study 2: building in Pordenone

The same analysis performed in Section 4.1 is now applied to the second case-study structure located in Pordenone [8] already investigated in Section 3.3. Also in this case, the seismic retrofit is designed for two distinct performance levels, namely (i) an elastic behavior, and (ii) a partially dissipative behavior of the building. Both the numerical models used in the non-linear analyses (static and dynamic) and the accelerograms adopted in the bidirectional time histories are the same introduced in Chapter 3, and for this reason, they are not presented hereinafter.

### 4.2.1. Retrofit with elastic frame behavior

Eq. (3.5b) is applied to determine the performance displacement  $d_p$ , assuming  $\Delta_d$  equal to  $0.005 m/m$ , which results in  $d_p = 0.059 m$  in either direction. The properties of the equivalent SDOF system are reported in Table 4-8.

<i>Direction</i>	$\Gamma$	$d_y^*$	$V_y^{*F}$	$d_p^*$	$V_p^{*F}$	$\xi_F$	$m^*$
	[–]	[m]	[kN]	[m]	[kN]	[%]	[ton]
<b>X</b>	1.32	0.017	602.6	0.044	1387.4	2.2	958.1
<b>Z</b>	1.32	0.014	510.0	0.044	1368.1	2.4	955.9

Table 4-8: Properties of the equivalent SDOF system of case-2 structure in either horizontal direction

The retrofit is designed by assuming a LED-DBS characterized by  $\kappa_{DB} = 0.9$  and  $\mu_{DB} = 20$ , which correspond to  $\xi_{DB} = 55.0\%$  (Eq. (3.11)) and is validated by applying both NLSAs and BNLDAs, similarly to Chapter 3. The LED-DBS is modelled as discussed in the Section 4.1.1 (*truss element* with associated either *uniaxialMaterial* EPP [4] for NLSA and *uniaxialMaterial* EPPV for NLDA) with the properties reported in Table B.1 in Appendix B for the configuration of Figure 3-23, obtained at the 3<sup>rd</sup> iteration of the design procedure.

Figure 4-25 shows the capacity curves in X- and Z- directions of the upgraded structure in the ADRS plane. The design target is met with a shallow underestimation of the performance displacement in both directions.

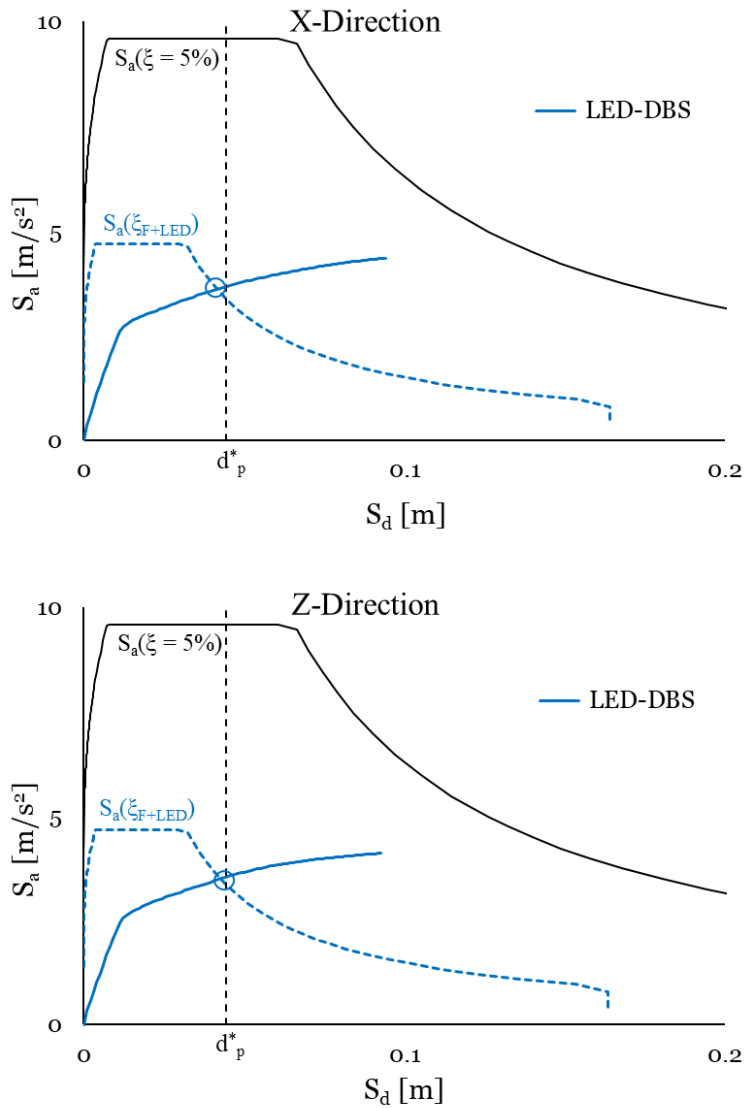


Figure 4-25: Capacity curves in X- and Z- direction of the case-2 structure retrofitted with the LED-DBS for elastic frame behavior

Figure 4-26 and Figure 4-27 report the seismic response of the upgraded structure in terms of maximum inter-story drift ratio  $\Delta$  and maximum shear force at each floor  $V$ . The inter-story drifts of the frame are significantly reduced, resulting in a regular deformed shape of the building and respecting the target  $\Delta_d = 0.005$  m/m at each floor (Figure 4-26), with only a slight increase of the shear forces  $V$ s with respect to the as-built situation (Figure 4-27).

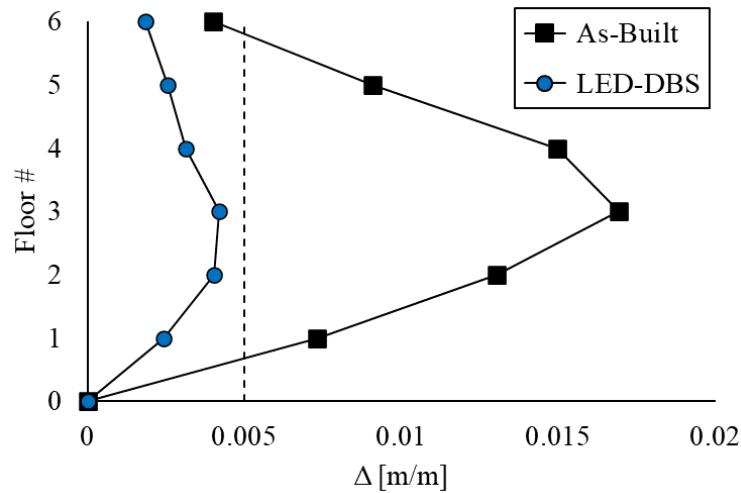


Figure 4-26: Maximum inter-story drift ratio  $\Delta$  of case-2 structure with and w/o LED-DBS for elastic frame behavior

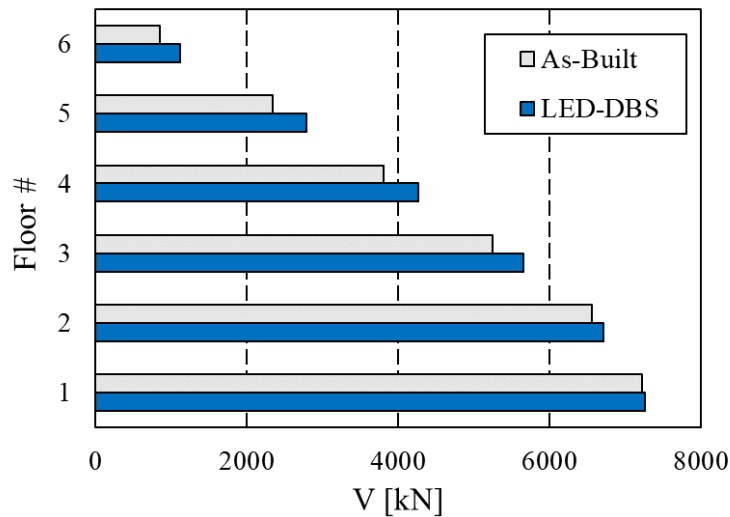


Figure 4-27: Maximum shear force  $V$  at each floor of case-2 structure with and w/o LED-DBS for elastic frame behavior

#### 4.2.2. Retrofit with dissipative frame behavior

Since the building in Pordenone has been designed with seismic detail according to the novel Italian Building Code [1], the performance displacement  $d_p$  is evaluated considering in the Eq. (3.5b) a ductility factor  $\mu_F = 2$ , in order to exploit the ability of the frame to resist larger plastic deformation than buildings designed according to updated codes without considerations of seismic actions. This target ductility corresponds to a displacement  $d_p = 0.120\text{ m}$  in both directions. The properties of the equivalent SDOF system corresponding to the assumed  $d_p^* = 0.089\text{ m}$  are reported in Table 4-9.

#### 4 Assessment of the Lead Damper for the seismic rehabilitation of RC framed structures

<i>Direction</i>	$\Gamma$	$d_y^*$	$V_y^{*F}$	$d_p^*$	$V_p^{*F}$	$\xi_F$	$m^*$
	[–]	[m]	[kN]	[m]	[kN]	[%]	[ton]
<b>X</b>	1.32	0.035	1222.9	0.089	2107.9	8.1	958.1
<b>Z</b>	1.32	0.034	1220.4	0.089	2020.4	9.6	955.9

Table 4-9: Main properties of the equivalent SDOF system of case-2 structure in either horizontal direction

Assuming a LED-DBS characterized by  $\kappa_{DB} = 0.9$  and  $\mu_{DB} = 20$ , correspondent to  $\xi_{DB} = 55.0\%$ , Eq. (3.11), leads to the convergence at the 3<sup>rd</sup> iteration and the properties of the LED-DBS units at each floor, for the configuration represented in Figure 3-23, are reported in Table B.2 in Appendix B.

NLSAs and BNLDAs are performed on the upgraded structure retrofitted for partially dissipative behavior of the bare frame, and the relevant results are reported in terms of: (i) capacity curves along X- and Z- directions (Figure 4-28); (ii) maximum inter-story drift ratio  $\Delta$  (Figure 4-29) and (iii) maximum shear force  $V$  at each floor (Figure 4-30). The retrofit design is effective, and the target performance is met by the upgraded structure with a shallow underestimation, as seen also in Figure 4-25 for the elastic design. At the third floor (the weak story) the inter-story drift ratio counts of  $\Delta = 0.0096 \text{ m/m}$ , corresponding to a ductility factor  $\mu_F = 1.92$ , in line with the target  $\mu_F = 2$  selected at the beginning of the design procedure. Moreover, at every floor (but for the last one) the shear forces  $V$  are even lower than those of the as-built structure.

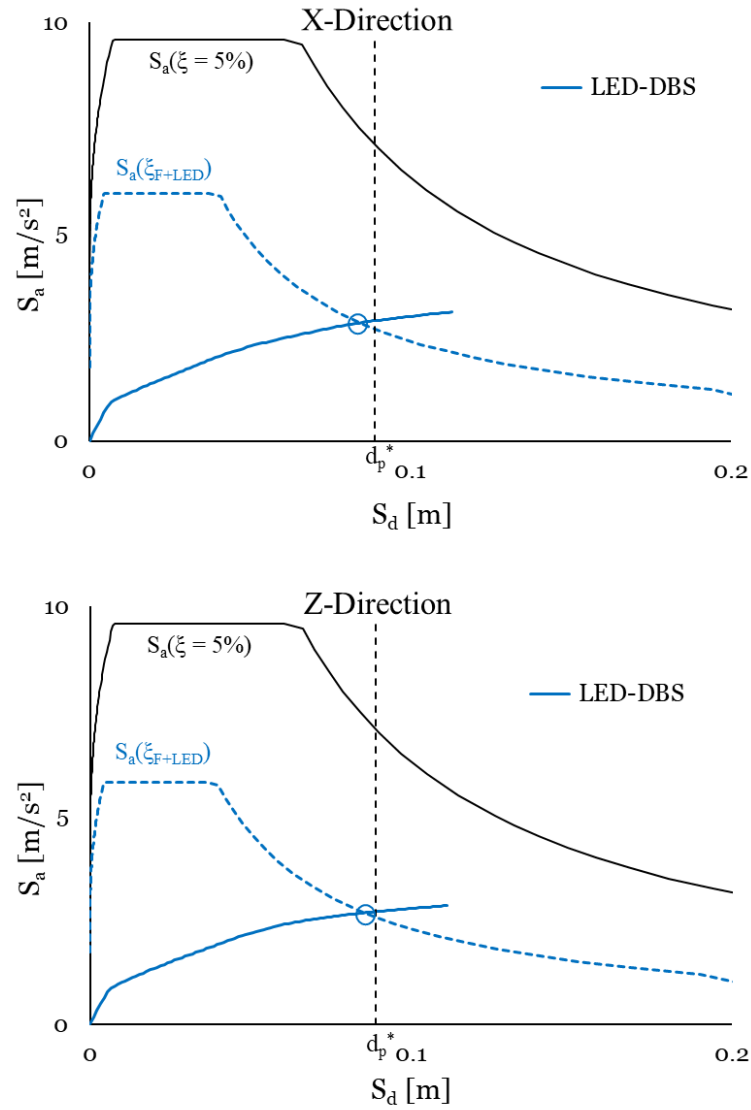


Figure 4-28: Capacity curves in X- and Z- direction of the case-study 2 structure retrofitted with the LED-DBS for dissipative frame behavior

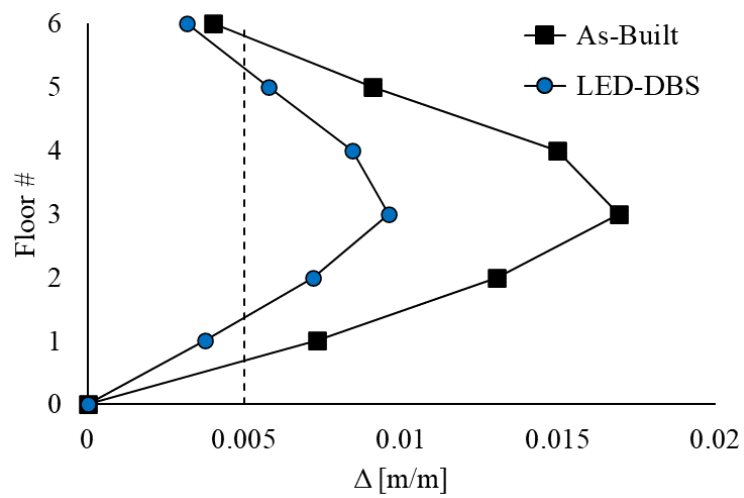


Figure 4-29: Maximum inter-story drift ratio  $\Delta$  of the case-2 structure with and w/o LED-DBS Comparison between LED- and SHD-DBS

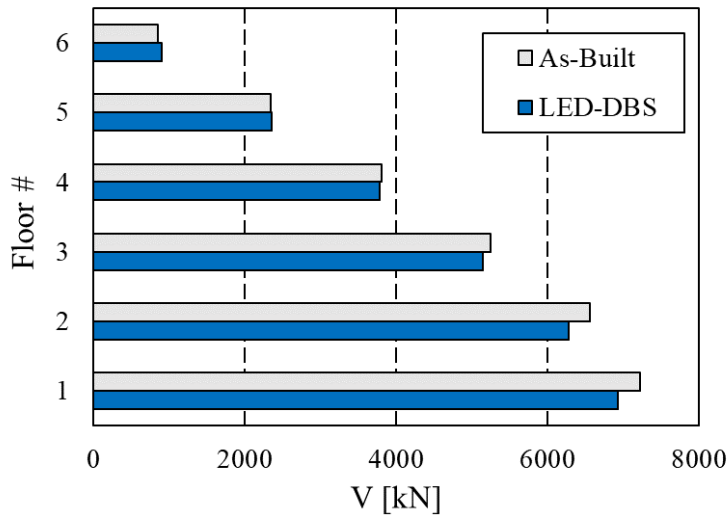


Figure 4-30: Maximum shear force  $V$  at each floor of the case-2 structure with and w/o LED-DBS for dissipative frame behavior

Unidirectional NLDAs are performed to determine the ductility demand  $\mu'_F$  of beams and columns, in order to assess the local damage of the RC frame members. As expected,  $\mu'_F$  is substantially decreased in each structural member and the upgraded structure seems to respect the principle of strong column / weak beam, forming plastic hinges only in the beams and not in the columns. Plastic hinges are triggered in beams up to the fourth floor, while the beams at the last two floors remain in the elastic regime. For this reason, Figure 4-31 refers only to the beams up to the fourth floor and the  $\varphi_{max}/\varphi_y$  ratios are reported as the mean and the maximum values calculated at the end sections of the girders at each story over the set of the 7 artificial accelerograms. In this graph, the  $F(AVG)$  and  $F+DB(AVG)$  tags refer to the ductility demand  $\varphi_{max}/\varphi_y$  averaged over all the beams at the floor, and the  $F(max)$  and  $F+DB(max)$  tags to the ductility demand of the most stressed beams at the floor.

Huge plastic deformations are experienced by the as-built configuration in either direction, especially at the third floor, where  $F(max)$  attains  $\mu'_F = 7.43$  along X-direction and  $\mu'_F = 6.54$  along Z-direction. Plots  $F+DB$  highlight that also in the retrofitted configuration the highest deformations are attained at the second and third floor, where  $F+DB(AVG)$  reaches the value  $\mu'_F = 2.74$  at the second floor along X-direction and  $\mu'_F = 2.61$  at the third floor along X-direction. It is worth noting that when the frame is subjected to unidirectional ground motions along either direction, all beams at floors are subjected to almost equivalent anelastic deformations.

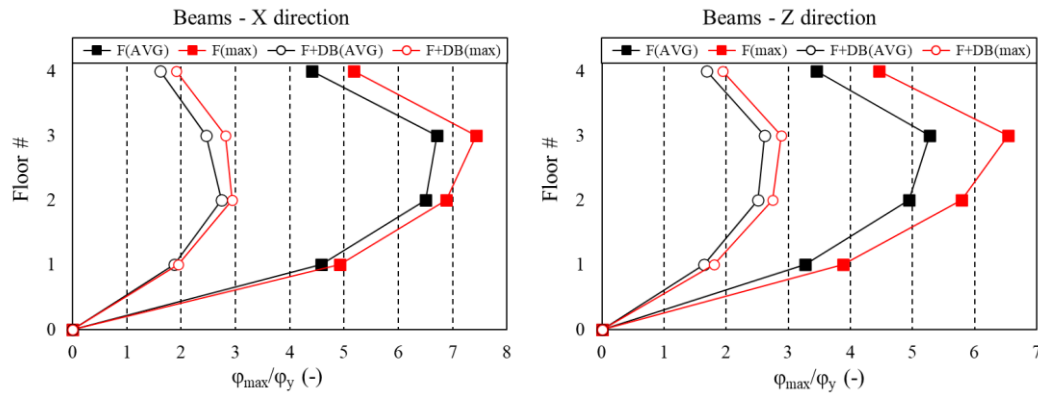


Figure 4-31: Average and maximum ductility demand  $\mu'_F$  of beams along X-direction (left) and Z-direction (right) at the first four floors

### 4.2.3. Comparison between LED- and SHD-DBS

In this section, the direct comparison between the performances of the case-study 2 structure retrofitted with either LED-DBS or with conventional SHD-DBS is performed, in line with Section 4.1.3 for case-study 1 structure.

#### 4.2.3.1. Elastic frame behavior

The retrofit design is performed with the aim of maintaining the structure behavior in the elastic range, by assuming the target displacement  $d_p = 0.059 m$  in either direction (Table 4-8). The retrofit with the Lead Damper brace system (LED-DBS) has been already presented in section 4.2.2. For the rehabilitation with steel hysteretic damped brace system (SHD-DBS), a device characterized by an equivalent viscous damping ratio  $\xi_{DB} = 24.4\%$  ( $\kappa_{DB} = 0.425$  and  $\mu_{DB} = 10$  as in [5]) is assumed. Resulting strength and stiffness of the damped brace units distributed at each story of the building are reported in Table B.3 of Appendix B. At each floor the ratio between the initial stiffnesses  $K_{yi}^{DB}$  of the LED-DBS and the SHD-DBS units counts 1.066, whereas the ratio between the axial forces  $N_{yi}^{DB}$  of the two systems is 0.533, which are the same values found in case-study 1. It is therefore confirmed that also in the case of a building designed with seismic details, when the target of the seismic rehabilitation is the elastic behavior of the structure, the strength demand for the LED-DBS is about 50% less than for the SHD-DBS.

Figure 4-32 and Figure 4-33 compare the capacity curves of the structure retrofitted with either DBS solution. In line with the results found for case-study 1, the capacity curve of the building upgraded with the SHD-DBS is stiffer than that of the building upgraded with the LED-DBS and presents a higher force at the performance point, specifically +35.8% along the X-direction and +27.6% along the Z-direction, see Figure 4-34. It is also worth reporting that the performance of the building with SHD-DBS is not fully compliant with the design target, as the lateral displacement along the Z-direction is about 9.0% higher than the target value selected for the design process.

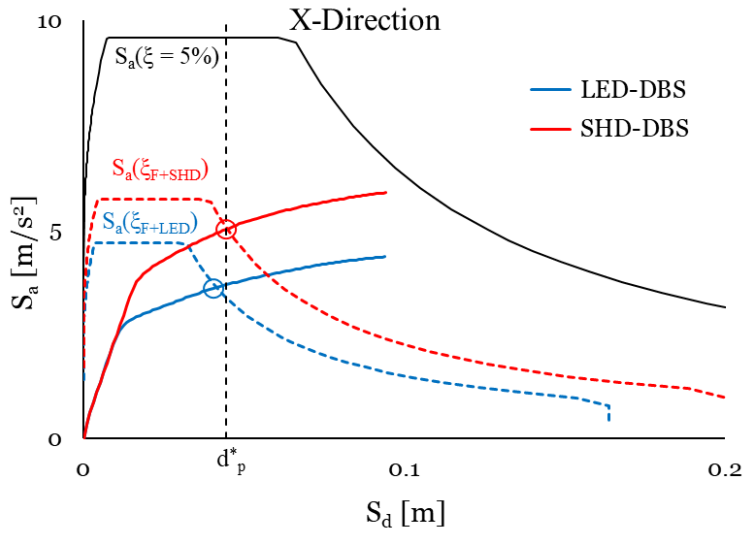


Figure 4-32: Comparison of the capacity curves in X-direction of the case-2 structure retrofitted with the LED-DBS and the SHD-DBS for elastic frame behavior

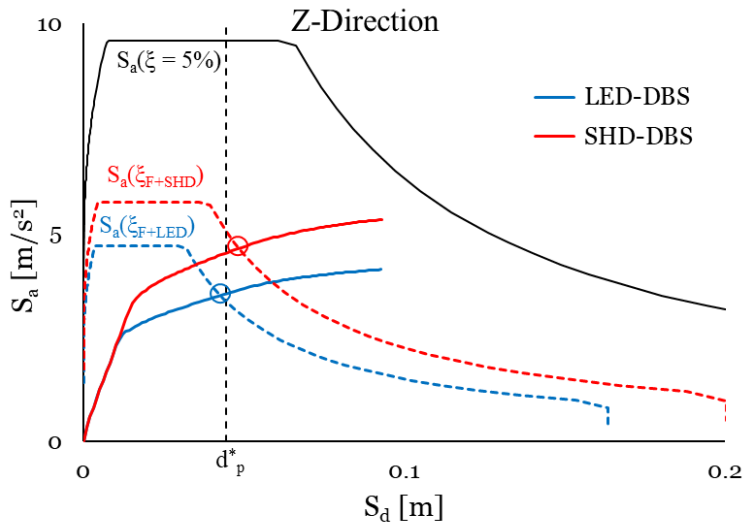


Figure 4-33: Comparison of the capacity curves in Z-direction of the case-2 structure retrofitted with the LED-DBS and the SHD-DBS for elastic frame behavior

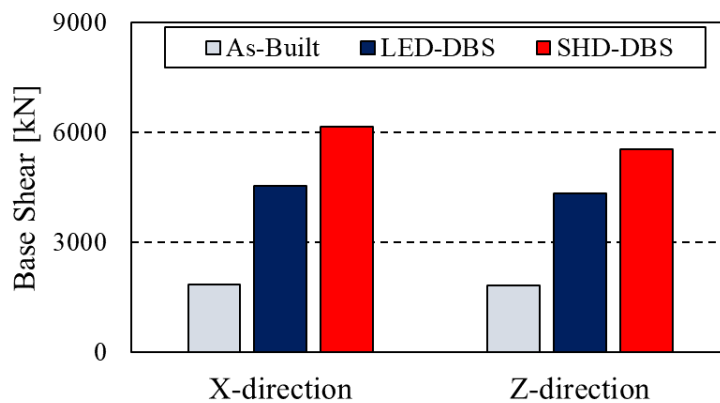


Figure 4-34: Comparison of the base shear force of the case-2 structure retrofitted with either LED-DBS or SHD-DBS for elastic frame behavior

4.2.3.2. Dissipative frame behavior

The retrofit design is now performed for dissipative frame behavior assuming a design ductility  $\mu_F = 2$  at the weak floor, which corresponds to a target displacement  $d_p = 0.12\text{ m}$  in both directions (Table 4-9). Strength and stiffness of the damped brace units at each story of the SHD- and the LED-DBS are reported in Table B.4 of Appendix B. Also in this case, at each floor the ratio between the initial stiffnesses  $K_{yi}^{DB}$  and the ratio between the axial forces  $N_{yi}^{DB}$  of the LED-DBS and the SHD-DBS are 1.066 and 0.533 respectively. Figure 4-35 to Figure 4-37 report the results of the NLSAs. As expected, the capacity curves of the buildings upgraded with the SHD-DBS shows a stiffer response, but, as already highlighted for case-study 1, the curves are closer to each other, and the differences in terms of base shear force at the performance point is of 21% along either direction, see Figure 4-37.

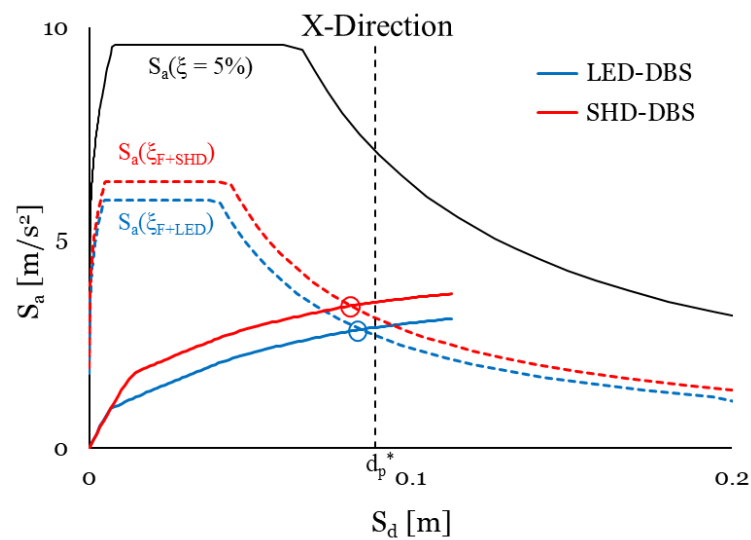


Figure 4-35: Comparison of the capacity curves in X-direction of the case-2 structure retrofitted with the LED-DBS and the SHD-DBS for dissipative frame behavior

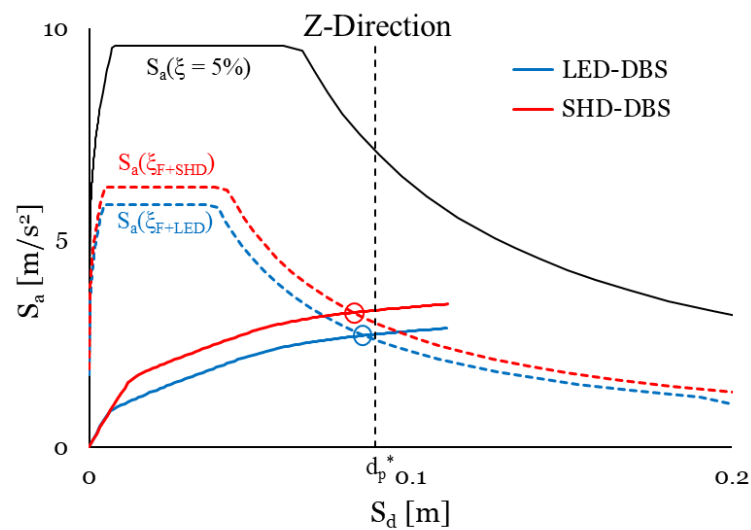


Figure 4-36: Comparison of the capacity curves in Z-direction of the case-2 structure retrofitted with the LED-DBS and the SHD-DBS for dissipative frame behavior

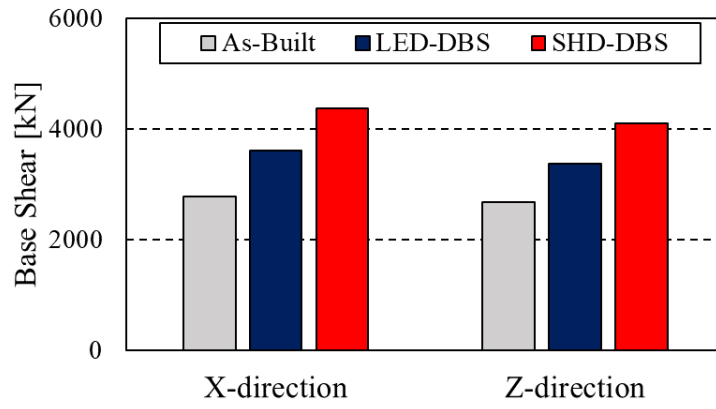


Figure 4-37: Comparison of the base shear force of the case-study structure retrofitted with either LED-DBS or SHD-DBS for dissipative frame behavior

### 4.3. Discussions and conclusions

In this Chapter, the displacement-based design procedure for the seismic upgrade of RC frame structures presented in Chapter 3 has been applied to the two already investigated case-study buildings. The Lead Damper (LED), a novel energy dissipation system investigated in Chapter 2, has been assumed for the design of the retrofit system, and its mechanical behavior has been modelled in OpenSees by means of a customized element object. In order to assess the suitability of the LED device for retrofitting RC frames and in particular to accommodate different performance requirements, the design has been performed considering two targets, namely the elastic behavior of the building under the design earthquake, and a partially dissipative frame behavior, with controlled formation of plastic hinges. Non-linear static and dynamic analyses have been performed to prove the effectiveness of the damped braced system equipped with the LED (LED-DBS). Moreover, a direct comparison between the retrofit with LED-DBS and a conventional SHD-DBS has been performed in order to evaluate the advantages introduced by the novel damper.

The design requirement is satisfied from structures upgraded with the LED device for both elastic frame behavior and dissipative frame behavior, showing a consistent reduction in terms of inter-story drift ratios  $\Delta$  with respect to the bare configuration; in case of elastic design, the drift of the weak story is smaller than the assumed elastic limit, whereas in case of plastic design, the lateral deformation of the weak story corresponds to a ductility factor  $\mu_F$  that respects the limit selected at the beginning of the design procedure.

A noteworthy result of the seismic rehabilitation with the LED-DBS, as far for the investigated case-studies, is that, in both cases, the upgraded frame shows a controlled activation of plastic hinges, which are triggered only in the beams at the lower floors, in accordance with the principle of strong column / weak beam prescribed by the performance-based design. Moreover, the insertion of the LED-DBS regularizes the behavior of the structure, reducing the dependency of the bending deformation of beams and columns on the features of the individual accelerogram.

Eventually, for both case-studies, a comparison is made between two different retrofit solutions, with either LED-DBS or SHD-DBS. By comparing the two DBS configurations, large differences in strength between the damper units are noticed, though they are characterized by the same initial stiffness at each floor (which allows to have the same first mode period for either DBS configuration). In both case-studies, at each floor the ratio between the initial stiffnesses  $K_{yi}^{DB}$  and the ratio between the axial forces  $N_{yi}^{DB}$  of the LED-DBS and the SHD-DBS counts 1.066 and 0.533 respectively. In fact, the energy dissipation capability of the LED-DBS is substantially higher (almost 55% more) than that of the SHD-DBS, producing similar decrease of the floor accelerations and of the internal forces of the structural elements of the main frame in the neighborhood of the sections where DBS were inserted. Consequently, LED outperforms SHD in significantly reducing the increasing of internal forces in structural members close to brace connections, in particular in columns of braced bays, which usually are among the most critical elements due to the large forces generated by damped braces [6], possibly requiring local strengthening of original RC elements. In this respect, it is noteworthy that the LED-DBS is more effective than the SHD-DBS in reducing the total base shear force when the seismic rehabilitation is designed for maintaining the frame behavior in the elastic

#### **4 Assessment of the Lead Damper for the seismic rehabilitation of RC framed structures**

---

range, resulting in about 30% decrease of the damper reaction force. In contrast, the decrease is on the order of 20% when the retrofit is designed for dissipative frame behavior, because of the contribution to the total damping provided by the inelastic deformation of the main frame which adds up to the contribution of the damped brace system.

#### 4.4. Symbols

$C_d$  damping coefficient of the *uniaxialMaterial ViscousDamper* object material in OpenSees associated to the EPPV model

$d_p$  target displacement of MDOF structure

$d_p^*$  target displacement of SDOF structure

$d_y^*$  yield displacement of the SDOF main structure

$K_d$  elastic stiffness of the internal spring of the *uniaxialMaterial ViscousDamper* object material in OpenSees associated to the EPPV model

$K_{EPP}$  elastic stiffness of the *uniaxialMaterial ElasticPP* object material in OpenSees associated to the EPPV model

$K_{yi}^{DB}$  stiffness of the damping braces at the  $i^{\text{th}}$  story (with  $i = 1 \div n$ , where  $n$  is the total number of stories)

$m^*$  equivalent mass of the SDOF structure

$N_{yi}^{DB}$  strength of the damped brace at the  $i^{\text{th}}$  story (with  $i = 1 \div n$ , where  $n$  is the total number of stories)

$V$  shear force across the frame

$V_{EPP}$  plastic force of the *uniaxialMaterial ElasticPP* object material in OpenSees associated to the EPPV model

$V_y^{*DB}$  yield strength of the SDOF damped brace system

$V_p$  maximum base shear force of the MDOF upgraded structure at the performance point

$V_p^{*F}$  ultimate strength of the SDOF damped brace system

$V_y^{*F}$  base shear force at yielding of the SDOF main structure

$\alpha_d$  velocity exponent of the *uniaxialMaterial ViscousDamper* object material in OpenSees associated to the EPPV model

$\Delta$  maximum inter-story drift ratio across the frame

$\Delta_0$  target inter-story drift ratio

$\Gamma$  participation factor

$\kappa_{DB}$  coefficient accounting for the energy dissipation capacity of the damped brace system

$\mu_{DB}$  ductility factor of the damped brace system

$\mu_F$  ductility factor of the main structure

$\mu'_F$  ductility demand attained at end sections of frame members

#### **4 Assessment of the Lead Damper for the seismic rehabilitation of RC framed structures**

---

$\xi_{DB}$  equivalent viscous damping ratio of the damped brace system

$\xi_F$  equivalent viscous damping ratio of the main structure (unbraced)

$\varphi_{max}$  average maximum curvature at either end section of structural member

$\varphi_y$  yielding curvature of structural member

#### 4.5. References

---

- [1] CSLLPP (Consiglio Superiore dei Lavori Pubblici). D.M. 17 gennaio 2018 in materia di “norme tecniche per le costruzioni”. Gazzetta ufficiale n.42 del 20 febbraio 2018, Supplemento ordinario n.8, Ministero delle Infrastrutture e dei trasporti, Roma; 2018, in Italian.
- [2] Di Cesare A, Ponzo FC. Seismic retrofit of reinforced concrete frame buildings with hysteretic bracing systems: design procedure and behaviour factor, *Hindawi, Shock and Vibration* 2017; Volume 2017, Article ID 2639361; DOI: 10.1155/2017/2639361.
- [3] Ponzo FC, Di Cesare A, Arleo G, Totaro P. Protezione sismica di edifici esistenti con controventi dissipativi di tipo isteretico: aspetti progettuali ed esecutivi, *Progettazione Sismica* 2010; II(1): 19-42.
- [4] OpenSeesWiki online manual. Available online at: [https://opensees.berkeley.edu/wiki/index.php/Main\\_Page](https://opensees.berkeley.edu/wiki/index.php/Main_Page) [last access: April 2021].
- [5] Gandelli E, Taras A, Disti J, Quaglini V. Seismic retrofit of hospitals by means of hysteretic braces: influence on acceleration-sensitive non-structural components. *Frontiers in Built Environment* 2019; 5(100); DOI:10.3389/fbuil.2019.00100.
- [6] Nuzzo I, Losanno D, Caterino N. Seismic design and retrofit of frames structures with hysteretic dampers: a simplified displacement-based procedure, *Bulletin of Earthquake Engineering* 2019; 17: 2787-2819; DOI: 10.1007/s10518-019-00558-8.
- [7] CEN (European Committee for Standardization). Design of structures for earthquake resistance - Part 3: Assessment and retrofitting of buildings. EN 1998–3 Eurocode 8; 2005.
- [8] Faleschini F, Zanini MA, Toska K. Seismic reliability assessment of code-conforming reinforced concrete buildings made with electric arc furnace slag aggregates, *Engineering Structures* 2019; 195: 324-339; DOI:10.1016/j.engstruct.2019.05.083.



# Conclusions

---

The Thesis aims at establishing design tools and practices for the seismic rehabilitation of reinforced concrete (RC) structures provided with energy dissipation devices. The retrofit of existing RC structures is an important issue for the Italian territory, where a large part of the building heritage is noted to be vulnerable to ground motions. In fact, the majority of the Italian stock, still fully in use today, dates back to the sixties up to the eighties of the last century, when it was designed without addressing the effects of seismic actions (as a matter of fact, only gravity loads were assumed for design from the codes in force at that time). Supplementary energy dissipation has indeed proved to be a viable solution for the rehabilitation of reinforced concrete structures, in order to prevent structural damage, increase life-safety and achieve a desired level of performance. However, nowadays the implementation of this technique for ordinary buildings is discouraged in practice by two main reasons:

- (i) practitioners still have little confidence in using energy dissipation strategies due to unavailability of design procedures ready to be adopted and of seismic codes that properly address specific provisions;
- (ii) current supplementary energy dissipation devices are bulky and architecturally invasive, get damaged from the dissipation of seismic energy, and need to be restated or even disposed after a seismic event; this poses safety issues, since after a major earthquake the structure is unprotected from future aftershocks until the dissipation devices are repaired or replaced, and increases life-cycle costs.

For this reason, the present work aims at presenting (i) a handy-to-use design procedure for the seismic upgrade of RC frame structures equipped with hysteretic dampers and (ii) a novel damper, expected to incorporate valuable characteristics, such as robustness, i.e., ability to accommodate multiple design strong motions without being damaged, high stiffness and damping capability, in a compact design with low manufacturing cost, which make it suitable for social housing.

This ultimate goal is achieved by pursuing intermediate objectives, which coincide with the milestones of the thesis.

- (i) The first achievement arises from the numerical investigation performed in *Chapter 1*, to define the best practices to model RC structures through concentrated plasticity models. Since both the literature and the codes present various modelling approaches for RC structures, comprising different formulas for estimating the plastic hinge length  $L_{pl}$  and accounting for the reduction of area moment of inertia  $I_{eq}$ , the numerical investigation aims at giving guidance to structural engineers who perform non-linear analyses on this type of structures. The results of the study suggest that, but for very low-rise frames, the adoption of distinct values of the area moment of inertia  $I_{eq}$  for either beams or columns, depending on the axial force applied to the structural members, provides a better estimate of structural response parameters such as inter-story drifts,

peak floor accelerations, maximum forces and maximum moments acting at the ground floor. Moreover, if a fixed (i.e., independent from the axial load) reduction of area moment of inertia  $I_{eq}$  is adopted, greater accuracy is obtained by adopting “long” plastic hinge lengths, like, e.g., the one recommended by the Italian Building Code.

- (ii) A second milestone is related to the characterization of the Lead Damper (LED), a novel energy dissipation device, experimentally investigated in *Chapter 2*. This damper provides huge energy dissipation through the friction force activated between a lead core and a shaft, and achieves a high specific output force by preloading the working material during the assembly. A prototype of the LED was tested at the Materials Testing Laboratory of Politecnico di Milano following the provisions of the European standard EN 15129 on anti-seismic device. The specimen provided a substantial energy dissipation capability, with an equivalent damping ratio  $\xi = 55\%$ ; moreover, the LED device was able to sustain multiple sequences of motion to the basic design earthquake displacement, demonstrating its ability to provide maintenance-free operation even in presence of repeated ground shakes. A refined constitutive model of the LED able to reproduce the essential characteristics of the damper, including the light dependency of the axial force on the velocity, was eventually formulated in OpenSees to perform non-linear dynamic analyses.
- (iii) In order to ease the use of energy dissipation systems, an effective and handy procedure for the seismic upgrade of existing frame structures by means of hysteretic damped braces has been presented. The procedure is suitable for professional applications and consists of two main parts: (i) a simple algorithm based on the Capacity Spectrum Method to define the global properties of the damped brace system, described by means of an equivalent SDOF system; and (ii) a strategy to determine the distribution of the properties of the equivalent SDOF damped brace along the height of the structure, by assuming that the lateral deformation of the retrofitted frame matches the first mode deformation of the main frame. The procedure is iterative and can be implemented in a spreadsheet, reaching the convergence in few steps. In addition, the graphical representation of the capacity curves in the ADRS plane has the added advantage of giving the engineer the opportunity to visualize at any iteration the relationship between demand and capacity.
- (iv) In the last part of the research, the use of the LED for the seismic rehabilitation of RC framed buildings is assessed. Two RC structures, designed according to either old codes that ignored seismic actions, or updated norms, are retrofitted with the LED system considering two different damage targets: (i) in the first case, the structure is retrofitted in order to behave elastically under the design earthquake; (ii) in the second case, a partially dissipative behavior of the structure is conceived, with activation of plastic hinges, and limited and repairable damage. The design requirement is satisfied for both case-study structures and for either design target, providing a consistent reduction of inter-story drift ratios with respect to the bare configurations, without significant increase of shear forces at the floors, thanks to the high energy dissipation capacity

of the LED device. A noteworthy result of the designed seismic rehabilitation with the LED system is that, in case of retrofit for dissipative frame behavior, the upgraded frame shows a controlled activation of plastic hinges, which are triggered only in the beams at the lower floors, in accordance with the principle of strong column / weak beam prescribed by the performance-based design. Finally, a comparison is performed between the retrofit with the LED device and the retrofit with a conventional steel hysteretic damper (SHD), demonstrating that the LED, thanks to its superior damping capacity, limits the increase in internal forces that usually affects frames equipped with SHDs, reducing the need of local strengthening of the columns and beams and the cost of the retrofit.

## Further developments and impacts

---

To the Writer's opinion, the outcome of this work has several practical impacts, even though some aspects require further investigations.

The first outcome lies in the definition of practices for formulating concentrated plasticity models of RC frames for non-linear dynamic analyses. The most striking result of the numerical investigation of *Chapter 1* is the evidence that the use of the area moment of inertia  $I_{eq}$  dependent upon the axial force acting through the structural member, provides a better estimate of the structural response. In this light, both the European and the Italian Building Codes should be aligned to the prescriptions of other standards, such as the Greek and the New Zealand standards, which prescribe different reduction factors for the gross area moment of inertia  $I_g$ , depending on the expected axial load ratio of the RC member under consideration. To this goal, it is necessary to extend the investigation performed in *Chapter 1*, in order to consider a large variety of practical conditions. The study should be extended to buildings irregular in plan and in elevation and a larger number of ground motions should be considered, in order to represent different site characteristics, comprising both near-fault and far-field events, and to avoid bias-related issues due to the low number of ground motions.

The novel friction damper, assessed in *Chapter 2* represents an emerging technology which is potentially suitable to overcome the main limits that characterize current supplementary energy dissipation devices. In particular, its ability to accommodate several strong motions at the design level without being damaged, and its high damping capability coupled to a compact design at low manufacturing cost, are the distinctive features that make it suitable for social housing. At the moment, only one prototype with 200 kN capacity has been assessed; the experimental campaign should be extended to other prototypes, characterized by different dimensions, in order to prove the absence of size-effects and to draft design charts which can be used by the manufacturers for a preliminary design of the device depending on the required performance.

Another important outcome is the development of a simple and handy methodology for practitioners for dimensioning the dissipation system to be installed in a building in order to achieve a target performance for considered limit state; the availability of this methodology is expected to enhance the confidence of structural designers and boost a wide spread of energy dissipation applications. In line with other norms,

## Conclusions

---

such as the FEMA 273 and FEMA 274, it is advisable that the future revisions of the European and the Italian Building Codes will include some practical indications to support structural engineers in the design of the seismic rehabilitation of buildings by means of energy dissipation devices. The procedure presented in this work, as well as the other methods reported in the State of Art of *Chapter 3*, can provide useful indications, that should be included in the norms. With this aim, some aspects related to the procedure developed in *Chapter 3* of the Thesis, require further investigations. In fact, this method has been initially conceived for regular RC buildings, and it should be extended to in-elevation irregular frames and unsymmetric-plan structures, as well as to steel structures and composite structures. Moreover, this procedure has been presented for the retrofit of buildings with dampers characterized by an elastic-perfectly plastic constitutive behavior, similar to the LED damper; it should be extended also to devices with a hardening parameter  $r \geq 0$ , in order to include also steel hysteretic dampers. Non-linear dynamic analyses have been performed in *Chapter 3* and *Chapter 4* considering artificial ground motions, because artificial accelerograms with smooth spectrum make the interpretation / comparison with NLSA simpler and more focused on the specific aspects that are analyzed in the work; in future developments the verification needs to be extended to include natural ground motions as well.

A last important development concerns the design of the installation of the LED device within the building; in fact, in *Chapter 4* the retrofit has been designed assuming the LED device encased in a brace, in order to provide both additional damping and stiffness to the existing structure. This does not overcome some of the main drawbacks related to the current energy dissipation devices, such as the architectural invasiveness and the heavy disturbance to the building occupants during the installation works. Since the LED damper is characterized by a compact size, a further improvement will investigate the installation of the device in convenient positions, such as at the beam-column connections, in order to adapt the retrofit system to the building layout and reduce the construction work, as well as to reduce the internal forces transmitted to the structural elements, with a consequent reduction of the invasiveness and the construction costs.

## Appendix A.

The procedure developed for tuning the parameters of the EPPV material, introduced to represent the hysteretic behavior of the Lead Damper (LED) in NLDA, is presented hereinafter. The procedure consists of two parts. The first part aims at establishing the target force-displacement hysteretic cycle of the LED when its design features are determined in terms of elastic stiffness, strength and ductility from design, and an experimental curve is not available. The second part of the procedure addresses the estimate of the parameters of the EPPV material in order to replicate the target design properties in terms of maximum force, maximum displacement and dissipated energy.

### (a) definition of the structure mock-up

Since, differently from the situation dealt with in Section 2.4, the reference force – displacement hysteretic loop may be not available from the experimentation, as a first step, the procedure aims at identifying the target hysteretic cycle by means of a mock-up of the structure to be upgraded.

The mock-up consists of a single-story shear type frame (Figure A.1). The model is coded in the OpenSees framework, where the frame is modelled with *elasticBeamColumn* elements, the beam is considered to be rigid, and the diagonal brace is modelled with a *truss* element with assigned *uniaxialMaterial* object material.

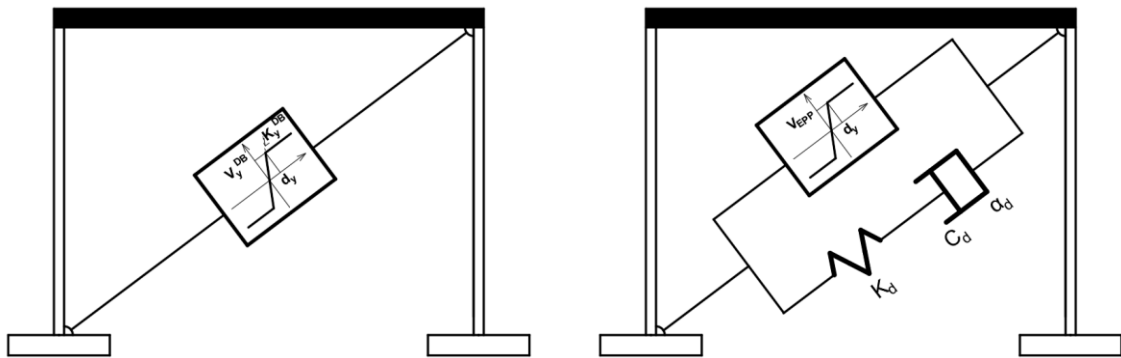


Figure A.1: Single-story shear frame for calibration of EPPV parameters: left, *uniaxialMaterial* EPP object material, used as benchmark; right, *uniaxialMaterial* EPPV object material

The frame is fixed at the base and has the same mass and fundamental period as the equivalent SDOF model of the MDOF building where the LED is installed

Once the material is assigned, the geometry of columns and beam is evaluated as a function of the mass and the fundamental period.

### (b) establishment of target properties

The target properties of the equivalent SDOF damped brace, namely the initial stiffness  $K_y^{DB}$  and the strength  $V_y^{DB}$  are calculated via the design procedure presented in Chapter 3 for an assigned ductility factor  $\mu_{DB}$ . The properties are implemented into an *uniaxialMaterial ElasticPP* object material that is used as benchmark.

### (c) determination of the target hysteretic cycle

## Appendix A

---

The structure mock-up, equipped with a diagonal brace modelled as a truss with associated the *uniaxialMaterial ElasticPP* object material with properties assigned in step (b) (Figure A.1, left) is subjected to the application of a sinusoidal ground excitation with amplitude equal to the Peak Ground Acceleration of the reference site, and the force – displacement hysteretic cycle of the damped brace is calculated. This plot is used as the target hysteretic cycle for tuning the parameters of the EPPV system.

(d) parameter setting

The EPPV system (Section 2.4) is described by five parameters (Figure A.1, right), namely

$K_{EPP}$  = elastic stiffness of linear spring to model the initial flexibility of the EPP material (e.g., combined stiffness of the supporting brace and initial stiffness of the elastic-perfectly plastic material)

$V_{EPP}$  = plastic strength of the EPP material

$K_d$  = elastic stiffness of linear spring to model the axial flexibility of the viscous damper (e.g., combined stiffness of the supporting brace and internal damper portion)

$C_d$  = damping coefficient of the viscous damper

$\alpha_d$  = velocity exponent of the viscous damper

The properties of the *uniaxialMaterial EPPV* object material are assigned as follows:

- the elastic stiffness  $K_{EPP}$  of the EPP material is set equal to the target initial stiffness  $K_y^{DB}$ , i.e.  $K_{EPP} = K_y^{DB}$ ; by this choice, the fundamental period of the mock-up is not affected by the adopted LED model (i.e., it is the same for both EPP and EPPV models);
- the strength  $V_{EPP}$  of the EPP material is set as a fraction  $\beta$  of the strength  $V_y^{DB}$ ; i.e.,  $V_{EPP} = \beta \cdot V_y^{DB}$ , where  $\beta$  is the partition coefficient;
- the elastic stiffness  $K_d$  is set as  $K_d \geq 20 \cdot K_{EPP}$ , in order to avoid significant elastic deflection of the viscous damper material (i.e., the whole displacement of the viscous damper portion is accommodated by the viscous dashpot);
- the damping coefficient  $C_d$  of the viscous damper is calculated as a function of the velocity exponent  $\alpha_d$  and the partition coefficient  $\beta$  according to the expression  $C_d = \frac{(1-\beta) \cdot V_y^{DB}}{(v_{max})^{\alpha_d}}$ , where  $v_{max}$  is the maximum velocity of deformation of the damped brace (i.e., the velocity of the dashpot)

In this way the tuning procedure is reduced to the estimation of two parameters only, namely the velocity exponent  $\alpha_d$  of the viscous damper portion and the partition coefficient  $\beta$ , which are adjusted by performing a least square fitting of the target hysteretic cycle defined in step (c).

The procedure was employed for the estimation of the parameters of the EPPV material for both case-study 1 and case-study 2 presented in Chapter 4. In both cases, regardless of the different characteristics of the frames (Table 3-2 and Table 3-5) and the different PGAs, the application of the procedure provides the same values of  $\beta$  and  $\alpha_d$  (Table A.1).

	Case-study 1	Case-study 2
$K_{EPP}$ [kN/mm]	54.02	397.14
$V_{EPP}$ [kN]	155.6	1411.6
$K_d$ [kN/mm]	2500.0	2500.0
$\alpha_d$ [-]	0.3	0.3
$C_d$ [kN $\left(\frac{s}{mm}\right)^{\alpha_d}$ ]	8.65	78.5

Table A.1: Parameters of the EPPV system for the two case-studies

The parameters  $K_{EPP}$ ,  $K_d$  and  $C_d$  are case-dependent and their values change at changing of the features of the equivalent damped brace for the case-study under exam;  $\beta$  and  $\alpha_d$  are independent on the specific case-study and express the dependency of the constitutive behavior of the device upon the velocity.

It is also worth noting that  $\beta = 0.8$  (80% of the total force is provided by the elastic-perfectly plastic portion and 20% by the velocity-dependent portion of the EPPV material), and  $\alpha_d = 0.30$ , are the same figures estimated for the LED in Section 2.4 based on experimental data.

As an example, Figure A.2 compares the force-displacement hysteretic cycles of the equivalent SDOF damped brace element calculated for case-study 1, modelled as a truss element with associated respectively the uniaxialMaterial EPP (black line) and the uniaxialMaterial EPPV (green dotted line) object materials.

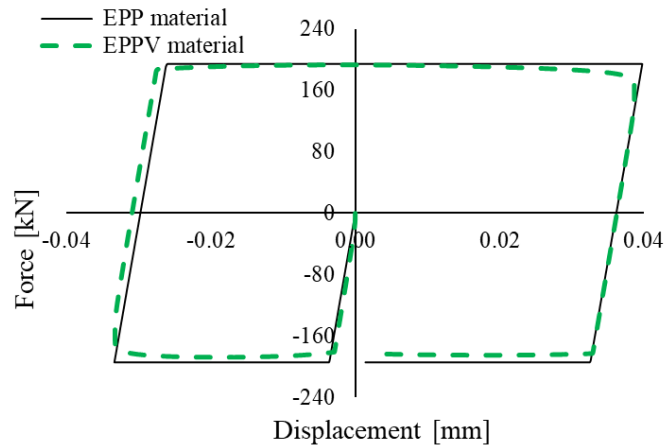


Figure A.2: Comparison between the force-displacement hysteretic curves of the damped brace element modelled as a truss with associated an EPP *uniaxialMaterial* (black line) and EPPV *uniaxialMaterial* (green dotted line)

The comparison between the two curves is evaluated in terms of maximum/minimum displacements ( $d_{max}, d_{min}$ ) induced by the dynamic excitation, maximum/minimum forces ( $F_{max}, F_{min}$ ) and energy dissipated in the cycle ( $A_{cycle}$ ), Table A.2.

	<i>EPP</i>	<i>EPPV</i>	<i>variation</i>
$d_{max}$ [m]	0.039	0.038	-2.8%
$d_{min}$ [m]	-0.033	-0.033	-0.3%
$F_{max}$ [kN]	194.35	193.2	-0.6%
$F_{min}$ [kN]	-194.35	-187.8	-3.4%
$A_{cycle}$ [kJ]	25.00	24.3	-2.8%

Table A.2: Parameters used to compare the force-displacement cyclic curves EPP and EPPV

Table A.2 shows that the calibration procedure is satisfied, with deviations less than 5% on each response parameter. It is worth to be noted that the hysteretic cycle provided by the EPPV material shows a smoother shape than the EPP material, with rounded corners at motion reversals, where the effect of the velocity is not negligible. This shape indeed resembles the actual shape observed in the experimental curves, as shown in Sections 2.3 and 2.4 of this Thesis. As a consequence, the energy dissipated per cycle provided by the EPPV model is expected to be slightly smaller (and closer to the actual value of a real LED units) than the one by the EPP model.

The tuning procedure is eventually evaluated by comparing the force-displacement curves of the LED – DBS modelled with either the EPP or the EPPV material within the MDOF case-study 1, for the case of elastic frame behavior. The retrofit design is performed considering the equivalent damped brace system with ductility  $\mu_{DB} = 20$ .

Figure A.3 compares the force-displacement curves of the LED-DBS, considering the damped brace installed in the frame X-direction at the base floor (LED-DBS 1) and at the fourth floor (LED-DBS 4). For sake of brevity, only the two damped braces at the lower and upper floors are reported, but similar results are found at the other floors and in the other frame direction. As expected, the EPPV model provides smoother curves though forces and displacements match very well. Figure A.3 confirms the fair agreement between the curves already observed in the analysis on the single-story shear type frame mock-up, demonstrating the reliability of the tuning procedure.

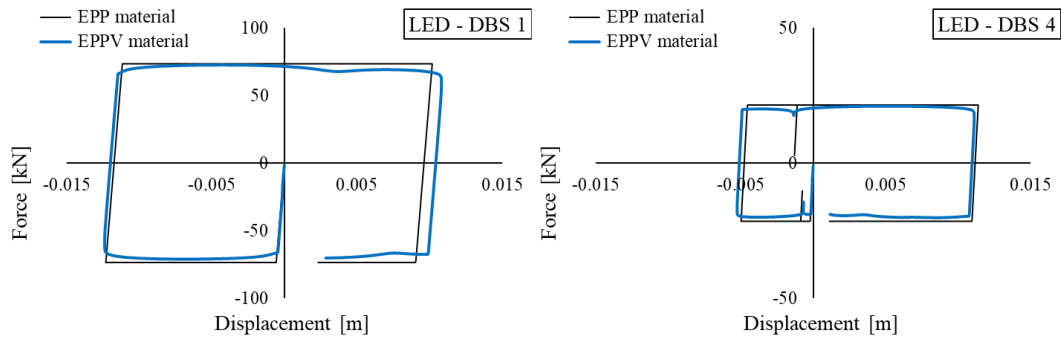


Figure A.3: Comparison between the force-displacement hysteretic curves of the LED-DBS modelled with EPP (black line) and EPPV (blue line) along X-direction at the base floor (left) and at the fourth floor (right) of the case-study 1



## Appendix B.

In Appendix B, the tables containing the properties of the EPPV for the case-study building in Potenza retrofitted for elastic frame behavior (Table B.1) and for dissipative frame behavior (Table B.2) are reported. Moreover, also the direct comparison in terms of strength and stiffness between the LED-DBS and the conventional SHD-DBS is reported in Table B.3 in case of elastic frame behavior and in Table B.4 in case of dissipative frame behavior.

<i>Direction</i>	<i>story</i>	$K_{EPP,i}$ [ $\frac{kN}{mm}$ ]	$V_{EPP,i}$ [ $kN$ ]	$\alpha_d$ [-]	$K_d$ [ $\frac{kN}{mm}$ ]	$C_{d,i}$ [ $kN(s/mm)^{\alpha_d}$ ]
X	1 <sup>st</sup>	2483.0	567.2	0.3	2500	31.5
	2 <sup>nd</sup>	1277.8	546.4	0.3	2500	30.4
	3 <sup>rd</sup>	949.9	488.7	0.3	2500	27.2
	4 <sup>th</sup>	919.0	389.5	0.3	2500	21.6
	5 <sup>th</sup>	900.0	254.3	0.3	2500	14.1
	6 <sup>th</sup>	703.1	95.1	0.3	2500	5.3
Z	1 <sup>st</sup>	2531.0	565.8	0.3	2500	31.5
	2 <sup>nd</sup>	1278.3	545.4	0.3	2500	30.3
	3 <sup>rd</sup>	949.0	488.3	0.3	2500	27.2
	4 <sup>th</sup>	911.9	389.6	0.3	2500	21.7
	5 <sup>th</sup>	888.3	254.6	0.3	2500	14.2
	6 <sup>th</sup>	679.6	95.4	0.3	2500	5.3

Table B.1: Properties of the EPPV for the case-study building in Pordenone retrofitted for elastic frame behavior

<i>Direction</i>	<i>story</i>	$K_{EPP,i}$ [ $\frac{kN}{mm}$ ]	$V_{EPP,i}$ [ $kN$ ]	$\alpha_d$ [-]	$K_d$ [ $\frac{kN}{mm}$ ]	$C_{d,i}$ [ $kN(s/mm)^{\alpha_d}$ ]
X	1 <sup>st</sup>	311.0	142.1	0.3	2500	7.9
	2 <sup>nd</sup>	160.0	136.9	0.3	2500	7.6
	3 <sup>rd</sup>	118.9	122.4	0.3	2500	6.8
	4 <sup>th</sup>	115.1	97.6	0.3	2500	5.4
	5 <sup>th</sup>	112.7	63.7	0.3	2500	3.5
	6 <sup>th</sup>	88.1	23.8	0.3	2500	1.3
Z	1 <sup>st</sup>	300.3	134.3	0.3	2500	7.5
	2 <sup>nd</sup>	151.7	129.4	0.3	2500	7.2
	3 <sup>rd</sup>	112.6	115.9	0.3	2500	6.4
	4 <sup>th</sup>	108.2	92.5	0.3	2500	5.1
	5 <sup>th</sup>	105.4	60.4	0.3	2500	3.4
	6 <sup>th</sup>	80.6	22.6	0.3	2500	1.3

Table B.2: Properties of the EPPV for the case-study building in Potenza retrofitted for dissipative frame behavior

<i>Direction</i>	<i>story</i>	SHD - DBS		LED - DBS	
		$K_{yi}^{DB}$	$N_{yi}^{DB}$	$K_{yi}^{DB}$	$N_{yi}^{DB}$
		$\left[\frac{kN}{mm}\right]$	$[kN]$	$\left[\frac{kN}{mm}\right]$	$[kN]$
<b>X</b>	1 <sup>st</sup>	2327.3	1329.1	2483.1	709.0
	2 <sup>nd</sup>	1197.6	1280.3	1277.8	683.0
	3 <sup>rd</sup>	890.3	1145.2	949.9	610.9
	4 <sup>th</sup>	861.4	912.6	919.0	486.8
	5 <sup>th</sup>	843.6	595.8	900.0	317.8
	6 <sup>th</sup>	659.0	222.8	703.1	118.9
<b>Z</b>	1 <sup>st</sup>	2372.2	1325.7	2531.0	707.2
	2 <sup>nd</sup>	1198.1	1278.0	1278.3	681.8
	3 <sup>rd</sup>	889.5	1144.1	949.0	610.4
	4 <sup>th</sup>	854.7	912.8	911.9	486.9
	5 <sup>th</sup>	832.6	596.6	888.3	318.3
	6 <sup>th</sup>	636.9	223.5	679.6	119.2

Table B.3: Comparison between design properties of the SHD-DBS and the LED-DBS at each story for elastic behavior

**Appendix B**

<i>Direction</i>	<i>story</i>	SHD - DBS		LED - DBS	
		$K_{yt}^{DB}$	$N_{yt}^{DB}$	$K_{yt}^{DB}$	$N_{yt}^{DB}$
		$\left[\frac{kN}{mm}\right]$	$[kN]$	$\left[\frac{kN}{mm}\right]$	$[kN]$
<b>X</b>	1 <sup>st</sup>	291.4	332.8	311.0	177.6
	2 <sup>nd</sup>	149.9	320.6	160.0	171.1
	3 <sup>rd</sup>	111.5	286.8	118.9	153.0
	4 <sup>th</sup>	107.9	228.5	115.1	121.9
	5 <sup>th</sup>	105.6	149.2	112.7	79.6
	6 <sup>th</sup>	82.5	55.8	88.0	29.8
<b>Z</b>	1 <sup>st</sup>	281.8	315.0	300.3	167.8
	2 <sup>nd</sup>	142.3	303.7	151.7	161.8
	3 <sup>rd</sup>	105.7	271.9	112.6	144.8
	4 <sup>th</sup>	101.5	216.9	108.2	115.6
	5 <sup>th</sup>	98.9	141.8	105.4	75.5
	6 <sup>th</sup>	75.7	53.1	80.6	28.3

Table B.4: Comparison between design properties of the SHD-DBS and the LED-DBS at each story for dissipative frame behavior